Perturbative Continuous Unitary Transformations: Spectral Properties of Low Dimensional Spin Systems

vorgelegt von

Christian Knetter

aus Troisdorf

Köln 2003

Contents

0. Introduction

Quantum mechanics was originally developed as a theory of non-relativistic charged particles interacting via the Coulomb force. It was successfully applied to a simple two-particle system like the hydrogen atom. The understanding of quantum mechanical systems composed of a few particles is important and the corresponding calculations are difficult. If the number of involved particles is very large, calculations seem to be impossible at first sight. However, amongst the most important applications of quantum mechanics is the description of $\sim 10^{23}$ interacting particles found in macroscopic matter. It is the objective of condensed-matter physicists to understand the electronic, magnetic and structural properties of matter on the grounds of quantum mechanics.

The physics of quantum many-particle systems is intriguing and beautiful, but apart from a few exceptions most of the theoretical models do not possess an exact solution and insight about the fundamental mechanisms is difficult to obtain. Because of the large number of open questions quantum many-particle systems are one of the most discussed problems in modern physics.

Quasi-Particles

Ground-breaking progress was achieved by introducing the concept of elementary excitations or quasi-particles. It allows the understanding of the *low-energy properties* of many-particle systems by considering the dynamics of essentially free, renormalised particles. All complicated interactions, experienced by the original particles, are stored in the properties of these new particles. It must be emphasised right away that these elementary excitations arise as a result of collective interactions between the particles of the system, so that they relate to the system as a whole, and not to individual particles. In particular, their number is by no means the same as the total number of particles in the system. To describe the low-energy spectrum it suffices to consider only a *few* quasi-particles.

The concept of quasi-particles was put on a firm theoretical footing in the 1950s by Landau's Fermi liquid theory (see e.g. Ref. [1]). The mathematical framework based on a diagrammatic approach was developed by Gor'kov et

al. (see e.g. Ref. [2]). The central postulate of the quasi-particle picture is that the ground state and the basic excitations of the interacting system are continuously related to the non-interacting system, if the interactions are introduced slowly. In other words, the quantum numbers characterising the states of the non-interacting system can be used to characterise the states of the interacting problem.

Let us briefly discuss two examples for which the quasi-particle concept can be used successfully. Our first example is Landau's Fermi liquid theory. This theory is based on the assumption that the excitation spectrum of a Fermi liquid has a similar type of structure to that of an ideal Fermi gas. The starting point is the proper identification of the (quantum) order in the ground state. Here the order is that implied by the distribution of plane wave states of electrons; the plane waves with small wavevectors are fully occupied, and there is an abrupt decrease in the average occupation number above a certain "Fermi wavevector". Landau then proceeds to describe the low-energy excited states by identifying the elementary excitations that perturb the order of the ground state in a fundamental way. Here these quasi-particles are electrons and holes in the vicinity of the Fermi wavevector. The theory can be used successfully to calculate observable quantities such as the specific heat, magnetic susceptibility, sound velocity and others.

Another well established example is given by three-dimensional quantum antiferromagnets. To be more specific we consider spin $1/2$ entities defined on the simple cubic lattice. For the construction of a quasi-particle picture one starts by considering the classical limit (no quantum fluctuations) for which the Néel state with total spin $S = 0$ is the ground state of the system. A basic excitation in the classical limit is given by flipping a single spin locally disturbing the Néel order. In our example this local excitation has total spin $S = 1$. Introducing quantum fluctuations the Néel state is no longer an eigenstate of the Hamiltonian. However, the quantum mechanical ground state is a singlet [3]; its total spin is $S = 0$ just as in the classical analogue. The elementary excitations are spin waves, i.e. collective excitations, with $S = 1$. They are referred to as magnons in the (quasi-)particle picture. One can thus use the same quantum numbers to characterise the states in both the simple classical model and the more complicated quantum mechanical analogue. A comprehensive introduction to the magnon picture can be found in Ref. [4] for instance.

There are various circumstances in which the quasi-particle picture breaks down. A phase transition in the system under study is perhaps the most apparent scenario. In this case the ground state is subject to a radical re-organisation. The definition of the original quasi-particles, which depends on

the observed order in the ground state, can no longer be hold up. Various mechanisms, such as strong fluctuations, strong interactions or topological deformations, can lead to phase transitions and thus to a breakdown of the quasi-particle picture.

The Fermi liquid theory for an ordinary metal for instance breaks down, if the metal becomes superconducting. In this case the electrons (or, more precisely, the electron-like quasi-particles) have paired due to an attractive interaction mediated by the sound waves in the solid [5]. The new entities (Cooper pairs) belong to a new class of elementary excitations – they are bosons.

Another example is given by reducing the dimension in the example of the three-dimensional antiferromagnet from above. In one dimension for instance quantum fluctuations are by far more important than in the three-dimensional counterpart. It turns out, that the antiferromagnetic spin $1/2$ chain should rather be described by elementary $S = 1/2$ excitation called spinons instead of the $S = 1$ magnons introduced for the three-dimensional model [6].

Spin Liquids

In this thesis we will focus on a particular class of many-particle systems – the spin liquids. Here we briefly introduce these systems and compile a short list of methods commonly used to tackle spin liquids.

Quantum antiferromagnets are strongly debated many-particle systems. Of particular interest are systems which do not have an ordered Néel-type ground state. Their ground state is a spin liquid without long-range spin order. Spin liquids are favoured by low spin ($S = 1/2$ mostly), low coordination number ($Z \in \{2, 3, 4\}$), i.e. low dimension, and strong geometrical frustration. Generically spin liquids are gapped. The antiferromagnetic spin $1/2$ chain, which is not gapped, can be seen as a marginal spin liquid.

Spin liquids exhibit interesting physics such as rich phase diagrams with quantum phase transitions, multi-particle continua, bound states and magnetisation plateaus to name but a few. The experimental realization of many spin liquids allows direct comparisons to theoretical findings and is another reason to consider these systems.

Now, what are the most common methods used to tackle this kind of spin systems? A prominent example is the Bethe *ansatz* which leads to a variety of exact solutions for the antiferromagnetic spin $1/2$ chain. A collection of relevant articles can be found in Ref. [7]. The elementary excitation is found to be the spinon (see preceding section.)

A very direct approach is given by (linear) spin wave theory (see e.g. Ref. [8]). Its application is straightforward and the magnon, introduced in

the preceding section, serves as an intuitive elementary particle. However, spin wave theory becomes problematic for low spin and (or) low dimension, when quantum fluctuations become increasingly important, which is also the case, if geometrical frustration is present. In this case it is difficult to obtain quantitative results.

Renormalisation techniques constitute very powerful approaches to extract the universal properties of spin systems. A comprehensive introduction can be found in Ref. [9]. They can be used to determine critical exponents and investigate the behaviour of the system in the vicinity of phase transitions, where it is often possible to identify the (fundamental) elementary excitations. While these methods lead to considerable insights they cannot be regarded as the optimal choice to *quantitatively* calculate measurable quantities like the ground state energy or energy gaps for instance.

In this sense perturbation theory can be considered as a complementary approach. Especially *high order* perturbation theories are well suited to quantitatively calculate measurable quantities. The (simple) unperturbed part of the full problem provides the elementary excitations, which become modified by introducing the perturbing part. However, starting from some simple limit also leads to a number of restrictions. The results might be biased by the chosen starting-limit. Furthermore, all calculations are restricted to the starting-regime, since in general the theory breaks down at the transition point (mode-softening). Only a single point of the neighbouring phase is reached. Phase transitions can thus be studied from one side only. Additional difficulties arise, if the system of interest is in the region where one cannot define a small perturbation parameter. Although it might be possible to use suitable extrapolations in this case, we still have to accept uncertainties.

Objective of this Thesis

We consider the possibility to quantitatively calculate measurable quantities as the main advantage of (high order) perturbation theory. In particular we regard quantitative comparisons to experimental data as a well suited approach to understand the physics of spin liquids.

The objective of this thesis is to construct a novel high order perturbation theory particularly suited to tackle gapped spin (liquid) systems at low temperatures. The essential idea is to systematically develop a "physical picture" for these systems by means of a controlled calculational method. In this thesis we illustrate the construction of the method and discuss its application to the Shastry-Sutherland model [10] which is a two-dimensional spin liquid.

Let us explain why there is a need for such a method by briefly summarising the status quo in the field of high order perturbation theory.

The first attempts to carry out high order expansions started in the early 1960s. These approaches were based on the cumulant method for which the general formalism can be found in Ref. [11] for instance. They were used in the context of the nearest-neighbour Heisenberg-Ising model

$$H = \sum_{\langle i,j \rangle} S_i^z S_j^z + x(S_i^x S_j^x + S_i^y S_j^y) \; , \tag{0.1}$$

with x as perturbation parameter, on bipartite lattices in one, two and three dimensions [12–16]. These calculations were rather technical and it was not before 1973 that correct results were obtained to 6th order in x for the sublattice magnetisation and two-point correlation functions [15].

In the late 1970s, Hamer et al. [17] generated series expansions for the gap between ground and lowest-excited state of one-dimensional quantum rotor models. The calculations went to order x^8 and relied on computer implementations to generate and evaluate the necessary diagrams.

Perturbation theory based on cumulant expansion can be used to calculate ground state energies and related quantities as well as quantities related to non-degenerate excited states. However, the necessary calculations are very technical. Cumulant expansion methods were overviewed in the context of lattice gauge theory in the mid 1980s by Hamer and Irving [18].

A more transparent and very successful high order perturbation theory is the linked-cluster expansion method. Relevant formalisms were first described in the early 1980s [19, 20]. This method has been applied to a wide variety of models.

Let us shortly describe the central ideas. There are two main steps in a cluster expansion. First is the identification of the finite number of relevant *connected* real-space clusters for the Hamiltonian under consideration. Then, for each cluster, one constructs the conventional Rayleigh-Schrödinger perturbation expansion for the *extensive* quantity (energy, correlation function) under consideration. The results for the various clusters are then combined (via "subgraph subtraction") so as to yield the quantity per site on the infinite lattice.[1] An overview of cluster expansions can be found in Ref. [21]

The separation of the problem in "small" clusters allows to optimise the calculational step. Computer implementations are rendered possible and yield high order results.

An important point is that linked-cluster expansions can only be applied for *extensive* properties. Consequently only ground state properties have been considered for a long time. However, there have been remarkable successes in

---

[1] We give some more details of the method on page 34.

this area. Amongst many others a cluster expansion about the Ising-limit of the two-dimensional spin 1/2 Heisenberg Hamiltonian on a square lattice (see Eq. (0.1)) led to 14th order results for the corresponding ground state energy per site and the staggered magnetisation [22].

It was not before 1996 that Gelfand [23] recognised that linked-cluster expansions can be constructed for "single-particle" excitation spectra and other excited-state properties such as spectral weights. An illustrative paper by Singh [24] shows how the Ising-limit can be used to calculate the spinon dispersion to 12th order in x for the antiferromagnet spin 1/2 chain by cluster expansions (see Eq. (0.1) again). Single-particle excitations for many other systems, for which no exact solutions are available, have been investigated since then, where also other starting-limits have been used, such as isolated dimer- or plaquette-limits to name but two.

Now, an important motivation for this thesis was the question of whether it is possible to quantitatively calculate and characterise *"two-particle" properties* and *spectral densities* for quantum spin (liquid) systems within a controlled perturbative framework. Considerations in this direction led to the construction of the novel perturbative approach which we will describe in this thesis. Before we give a brief introduction to this method in the next section we wish to shortly summarise the most recent advances of high order perturbation theory which came about during the development of this thesis.

In 2000 it became possible to use high order perturbation theory to calculate two-particle properties. We obtained high order results for the energies of two-particle bound states for the two-dimensional Shastry-Sutherland model [25]. We will illustrate these calculations in detail in this thesis. The two-leg spin 1/2 Heisenberg ladder is another example for which we obtained high order results for two-particle properties such as dispersive bound-states and two-particle continua (see e.g. Ref. [26]).

The key point is to use a transformation, which maps the initial Hamiltonian onto an *effective* Hamiltonian H_{eff} such that H_{eff} conserves the number of (quasi-)particles. Hence, H_{eff} is block-diagonal; the ground state sits in a block by itself, the one-particle states form another block, the two-particle states another block and so on.

Nearly at the same time Trebst et al. proved that the linked-cluster expansion method is also well suited for high order calculations of two-particle excitation spectra, if such a transformation is used [27, 28]. They calculated dispersive two-particle bound states for the Heisenberg-ladder and the antiferromagnetic alternating spin 1/2 Heisenberg-chain with next nearest neighbour coupling.

In a next step quantitative calculations of various energy and momentum

resolved one- and two-particle spectral densities based on high order perturbation theory became possible. Our calculations were done for the spin 1/2 Heisenberg ladder [26, 29–31]. They rely on high order series expansions of the Hamiltonian *and* the corresponding observables. In this thesis we consider the Raman operator and the inelastic neutron scattering operator of the Shastry-Sutherland model to calculate the corresponding one- and two-particle spectral densities.

In a very recent work Hamer et al. show that spectral densities can be obtained equally well with the cluster expansion method [32]. They consider the alternating Heisenberg chain and calculate the corresponding dynamic structure factor.

Perturbative Continuous Unitary Transformations

In this thesis we will construct and apply the method of perturbative continuous unitary transformations (perturbative CUTs). CUTs have been introduced by Wegner [33] as a general tool to tackle quantum many-particle problems. The basic idea is to unitarily map a given Hamiltonian, or another observable of interest, onto a simpler *effective* problem in a continuous fashion. In our case the transformation is constructed perturbatively and is exact to some given maximum order.

The concept of quasi-particles will enter our discussion: by giving a comprehensive introduction to the mathematical foundations of CUTs we will step by step promote this concept to a systematic calculational method, based on suitably defined "simple" quasi-particles. An important result will be that the transformation can be designed such that the resulting *effective Hamiltonian* conserves the number of quasi-particles. Seeking for a *perturbative* realization of the transformation will result in a versatile many-particle tool, which can straightforwardly be applied to spin (liquid) systems. All necessary details needed to implement the method on a computer will be given.

Our survey will show, that perturbative CUTs allow quantitative calculations for various spectral properties of many-particle systems by exploiting the quasi-particle conserving property of the effective Hamiltonian. The calculation of the ground state energy reduces to calculating the action of the effective Hamiltonian on the particle vacuum for instance. Similarly the lowest excitation energies are given by its action on the one-particle states. We will show that quantitative calculations are also possible in the two-particle sector, allowing the investigation of two-particle interactions.

We will also give a detailed description of how *effective observables* of interest (not necessarily the Hamiltonian) can be constructed by perturbative

CUTs. This will render quantitative comparisons to experimental data on the level of line shapes possible.

Similar to the calculations in the energy sector, the effective observables decompose into various parts characterised by the number of quasi-particles injected. We are thus in the position to calculate the relative contributions of one, two, three, etc. quasi-particles to the full weight of the considered process. This allows to judge the appropriateness of the chosen quasi-particle. If most of the spectral weight is captured by a small number of particles, the definition of the particle can be considered to constitute a suitable choice to describe the corresponding spectral properties.

This thesis also covers an extensively illustrated application to the anti-ferromagnetic spin 1/2 Shastry-Sutherland model, a two-dimensional system composed of orthogonally arranged dimers. A dimer is a unit composed of two spins interaction with each other via (dimer-)bonds of strength J_1. The dimers in turn interact with each other via inter-dimer bonds of strength J_2. The ratio $x := J_2/J_1$ is the perturbation parameter and the limit of isolated dimers ($x = 0$) will serve as perturbational starting point. Here the ground state is given by singlets on all dimers. An elementary excitation , the quasi-particle in our treatment, is given by a single triplet on one of the dimers. Since we are going to calculate bound states of these elementary excitations, which can bind to triplets again, we introduce the term *triplon* to differentiate the *elementary* triplet from triplets composed of two (or more) triplons.

We will calculate one- and two-triplon energies as high order series expansions in x. Similar series expansions will be calculated for the operators capturing the Raman and the inelastic neutron scattering processes for this system. This will lead to quantitative results for the corresponding spectral densities. Our findings are compared to actual experimental data for $SrCu_2(BO_3)_2$, a substance which constitutes an experimental realization of the Shastry-Sutherland model.

Thesis Outline

This thesis can be regarded to be composed of two parts. In the chapters 1 through 5 we introduce the method of perturbative CUTs on general grounds. All important concepts and practical tools accompanying a possible application are illustrated step by step. Chapter 6 contains the application of the method to the two-dimensional spin 1/2 Shastry-Sutherland model.

- Chapter 1 introduces the basic concepts of CUTs. We fix the notations and discuss simple examples to convey the underlying principles.

The problem of constructing reasonable generators, controlling the transformation, is discussed. Special attention is paid to the construction of a transformation leading to quasi-particle conserving effective Hamiltonians.

- Chapter 2 illustrates the mathematical structures of effective Hamiltonians and observables; in particular for the case, that the effective Hamiltonian conserves the number of quasi-particles. By showing that the effective operators decompose in n-particle irreducible operators, we prove that CUTs constitute a particular comprehensive and straightforward approach to many-particle systems. Another important result is the definition of cluster additivity on the level of operators, facilitating the perturbative calculation of results for the thermodynamic system on finite clusters. Our discussion is restricted to systems defined on a lattice.

- Chapter 3 formulates the perturbative realization of CUTs for a specific class of lattice systems. The perturbative transformations of Hamiltonians and observables are illustrated in detail. The corresponding effective operators are series expansions in terms of ladder operators. The application of these results to translational invariant systems is discussed in a separate section. We finally give a detailed description of how perturbative CUTs can be implemented on a computer, which allows to obtain high order results.

- Chapter 4 shows how spectral densities can be calculated as analytic expressions from the perturbatively obtain effective Hamiltonians and observables, by utilising the continued fraction expansion for zero-temperature Green's functions. A separate section elaborates on further considerations for one-dimensional systems.

- Chapter 5 addresses the problem of extrapolating the perturbative results obtained from the effective operators. We introduce and explain a novel extrapolation scheme based on the criterion of minimal sensitivity known from optimised perturbation theory. The method constitutes a robust and smooth extrapolation, well suited to simultaneously extrapolate a large number of quantities.

- Chapter 6 covers the application of a perturbative CUT to the two-dimensional antiferromagnetic spin 1/2 Shastry-Sutherland model, for which the recently synthesised $SrCu_2(BO_3)_2$ constitutes an experimental realization. We systematically investigate the low-energy spectral properties. Special attention is paid to the calculation of spectral densities

for the Raman and inelastic neutron scattering processes. The results render a quantitative comparison to experimental findings possible. This chapter will lead to both a proof for the applicability of perturbative CUTs in two dimensions and interesting and partly unprecedented result for the model.

- Chapter 7 summarises our findings by separately considering the achievements for the methodical part and the results obtained for the application.

1. CUT – Prologue

In this first chapter we want to give a conceptual introduction to the method of continuous unitary transformations (CUT). The discussion is presented on general grounds and the results obtained apply to all quantum mechanical systems which can be represented in a Hamiltonian description.

Following Wegner's ideas [33] we introduce the method as a general tool to tackle quantum many particle problems. In the following chapters the method will be refined and customised to serve our needs to work for quantum spin lattice systems. We should mention that Głazek and Wilson [34, 35] independently developed a related method based on similarity transformations.

1.1. Basics

The simplification of a given quantum mechanical problem can be achieved on different routes. One possibility is to perform a suitable change of basis. Since quantum mechanical observables are hermitian, a unitary transformation might be most comfortable. If the transformation is engendered by an anti-hermitian generator S the initial problem A is mapped onto the simplified problem B by

$$B = e^S A e^{-S} \ . \tag{1.1}$$

We call this procedure a *one-step transformation*. The right hand side of Eq. (1.1) can be expanded with the Baker-Hausdorff formula to give

$$B = A + [S, A] + \frac{1}{2}[S, [S, A]] + \mathcal{O}(S^3) \ . \tag{1.2}$$

Although the one-step transformation can be motivated by physical considerations and can lead to a deeper physical understanding, there is a considerable drawback. The choice of the transformation depends on the given initial problem. There may be cases where one is not able to find a suitable transformation at all. We can put this in a more concise form: there is no possibility to give an algorithm telling us which transformation will in fact simplify the initial problem.

This problem can be overcome by performing a series of unitary transformations. We successively rotate the basis by a *discrete* number of transformations

$$
\begin{aligned}
A &= A_0 \rightarrow A_1 \rightarrow \ldots \rightarrow A_m \ , \\
A_i &= U_i A_{i-1} U_i^\dagger \quad i = 1, 2, \ldots m \ .
\end{aligned}
\tag{1.3}
$$

All transformations U_i may differ from each other. If the matrix A is hermitian, as is the case in our consideration, we can formulate algorithms which lead to a matrix B, from which the eigen-values and eigen-vectors can be extracted more easily than from matrix A

$$
B = A_m = U A U^\dagger, \qquad U := U_1 U_2 \ldots U_m \ .
\tag{1.4}
$$

Since U is unitary, matrix B yields the same eigen-values as matrix A. The eigen-vectors of A, $\mathbf{v}_a$, are connected to those of B, $\mathbf{v}_b$, by $\mathbf{v}_a = U^\dagger \mathbf{v}_b$.

Established methods following this procedure are the Householder- and the Jacobi-Algorithm to name but two. The latter diagonalises a given (finite dimensional) hermitian matrix by means of an infinite series of unitary transformations. The Househoulder-Algorithm turns an initial finite dimensional hermitian matrix into a tridiagonal matrix in a finite number of steps. The reader can find further details and proofs in Ref. [36].

In contrast to the one-step transformation the sketched method allows the formulation of a systematic algorithm leading to a considerable simplification independent of the (possibly complicated) structure of the initial problem.

However, this numerical approach has two main drawbacks. To obtain reliable results for typical quantum many particle systems one has to consider a large finite subspace of the system's Hilbert space. This is particularly true for strongly correlated systems. Even with the use of computers an implementation covering very large matrices may be insufficient. More important is the fact that this rather mathematical procedure is not based on physical considerations. The physics of the treated system cannot be tracked in the course of the transformation. One does not gain a new (possibly simpler) picture leading to a better understanding of the underlying processes in the system.

Let us now outline a method which combines the favourable aspects of the two approaches sketched above: the method should allow an automation in the sense that it can be successfully applied to a large number of problems without dramatic rearrangements, and it should be physically motivated leading to a comprehensive understanding of the system's underlying mechanisms. The latter can be realised elegantly by introducing suitable quasi-particles as we will see later.

The basic idea is to unitarily transform the initial problem in a *continuous* fashion. To this end we need a continuous label for the observable A under inspection

$$A \to A(\ell), \quad \ell \in \mathbb{R}_0^+ , \tag{1.5}$$

where $A(0) = A$ is the initial observable. We further introduce a unitary transformation $U(\ell)$ as function of the continuous parameter (one-parameter unitary group) and define

$$A(\ell) = U(\ell)A(0)U^\dagger(\ell) . \tag{1.6}$$

We proceed by analysing how $A(\ell + d\ell)$ is connected to $A(\ell)$. A small manipulation yields

$$A(\ell + d\ell) = U(\ell + d\ell)U^\dagger(\ell)A(\ell)U(\ell)U^\dagger(\ell + d\ell) . \tag{1.7}$$

So far we have been very abstract. To make further progress we need to introduce an infinitesimal anti-hermitian generator $\eta = -\eta^\dagger$, which governs the evolution of $U(\ell)$ locally.[1] In general, and this is an important point, η may also be a function of ℓ, therefore

$$\frac{dU(\ell)}{d\ell} = \eta(\ell)U(\ell) . \tag{1.8}$$

For infinitesimal $d\ell$ a first order analysis is sufficient and gives

$$
\begin{aligned}
U(l + d\ell) &= U(\ell) + \eta(\ell)U(\ell)d\ell \\
\Rightarrow U(\ell + d\ell)U^\dagger(\ell) &= \mathbf{1} + \eta(\ell)d\ell \\
\Rightarrow U(\ell)U^\dagger(\ell + d\ell) &= \mathbf{1} - \eta(\ell)d\ell ,
\end{aligned}
\tag{1.9}
$$

where we used the fact that $\eta(\ell)$ is anti-hermitian. Substituting these findings in Eq. (1.7) gives to first order in $d\ell$

$$
\begin{aligned}
A(\ell + d\ell) &= \big(\mathbf{1} + \eta(\ell)d\ell\big)A(\ell)\big(\mathbf{1} - \eta(\ell)d\ell\big) \\
&= A(\ell) + [\eta(\ell), A(\ell)]d\ell ,
\end{aligned}
\tag{1.10}
$$

which is the equivalent to the so-called *flow equation* [33]

$$\boxed{\frac{dA(\ell)}{d\ell} = [\eta(\ell), A(\ell)]} . \tag{1.11}$$

---

[1] The generator needs to be anti-hermitian, since we want the transformation to be unitary.

The flow equation resembles the equation of motion of an observable transferred to the Heisenberg picture, where the generator is the Hamiltonian of the system and the time t plays the role of the continuous parameter ℓ. The flow equation is a first order differential equation for operators. In general, ℓ does not appear explicitly so that the equation is autonomous. The initial condition is defined by the above mentioned convention that $A(\ell = 0) = A$. The objective is to solve this differential equation for $A(\ell)$ and to examine the limit $\ell \to \infty$. The resulting *effective* observable will be denoted by

$$A_{\text{eff}} = \lim_{\ell \to \infty} A(\ell) \ . \tag{1.12}$$

We can further elaborate on the structure of continuous unitary transformations. A formal integration of Eq. (1.8) yields ($U(0) = \mathbf{1}$)

$$U(\ell) = \mathbf{1} + \int_0^\ell \eta(\ell')U(\ell')d\ell' \ . \tag{1.13}$$

Recursive substitutions lead to a von Neumann series for $U(\ell)$, which can be put in the concise form

$$U(\ell) = T_\ell \exp\left(\int_0^\ell \eta(\ell')d\ell'\right) \ . \tag{1.14}$$

Here, T_ℓ denotes the ℓ-order operator in analogy to Dyson's time-order operator.

An interesting perspective arises through the so-called Magnus expansion [37]

$$U(\ell) = e^{\Omega(\ell)}, \quad \Omega(\ell) = \sum_{k=1}^\infty \Omega_k(\ell) \ , \tag{1.15}$$

where in our case the first two operators read

$$\Omega_1(\ell) = \int_0^\ell \eta(\ell_1)d\ell_1 \tag{1.16}$$

$$\Omega_2(\ell) = \frac{1}{2}\int_0^\ell d\ell_1 \int_0^{\ell_1} [\eta(\ell_1), \eta(\ell_2)] \ . \tag{1.17}$$

The operators Ω_k can be obtained by a recursive procedure [38]. They involve multi-variant integrals of nested commutators of $\eta(\ell)$.[2] Note that in general

---

[2] Ω_3 and Ω_4 are given in the appendix of Ref. [38]. There has been considerable interest in this kind of expansion. For instance, Blanes et al. [39] established the ℓ-domain of convergence for the Ω-series.

$\eta(\ell_1)$ and $\eta(\ell_2)$ do not commute for different ℓ_1 and ℓ_2. In other words, the transformation at some ℓ-value depends on all infinitesimal transformations at smaller ℓ-values. Moreover, if $\eta(\ell)$ in turn depends on $H(\ell)$, which is the case in standard approaches (see next section), we have a self-controlling flow: at some arbitrary but fixed value of ℓ $H(\ell)$ determines the next infinitesimal transformation to be performed on itself by the indicated feedback structure. Although this mechanism is complicated, it should be clear that the method offers a great potential to control the mapping to an effective system.

Now, the expansion (1.15) allows a contact to the one-step transformation to be established by identifying (cf. Eq. (1.1))

$$S = \lim_{\ell \to \infty} \Omega(\ell) \ \Leftrightarrow e^S = \lim_{\ell \to \infty} U(\ell). \tag{1.18}$$

Thus, we could always express a continuous transformation by a one-step transformation. However, and this is important, it is virtually impossible to find all the complicated terms of the Magnus expansion which constitute the generator S, but this would be necessary to construct the corresponding one-step transformation from scratch. The continuous transformation, however, automatically generates all these terms in form of nested commutators, as we have seen. The continuous transformation automatizes this task for *any* initial problem A. This is a strong simplification.

Let us examine an example to further illustrate this issue. The Fröhlich transformation [40] constitutes a prominent example of a one-step transformation. Fröhlich considered a system of electrons (created) annihilated by $c^{(\dagger)}$ coupled to phonons $a^{(\dagger)}$

$$H = H_d + H_{\text{ep}}(\alpha). \tag{1.19}$$

The first part is considered to be diagonal

$$H_d = \sum_k \epsilon_k c_k^\dagger c_k + \sum_q \omega_q a_q^\dagger a_q \ . \tag{1.20}$$

Additionally, $H_{\text{ep}}(\alpha)$ comprises electron-phonon interactions of the form

$$\sum_{k,q} (\alpha_q a_{-q}^\dagger + \alpha_{-q}^* a_q) c_{k+q}^\dagger c_q \ . \tag{1.21}$$

As described by Eq. (1.1), Fröhlich uses a one-step transformation to map H onto an effective Hamiltonian H_{eff}. By S^F we denote his choice for the generator. Assuming small values for α, Fröhlich eliminates all interaction terms from H_{eff} in second order in α by requiring (see Eq. (1.2))

$$\left[S^F, H_d \right] = -H_{\text{ep}}(\alpha) \ . \tag{1.22}$$

This requires S^F to be linear in α. The remaining commutators in Eq. (1.2) proportional to α^2 are

$$\left[S^F, H_{\text{ep}}\right] + \frac{1}{2}\left[S^F, [S^F, H_d]\right] = \frac{1}{2}\left[S^F, H_{\text{ep}}\right] \; . \tag{1.23}$$

For a suitable choice of S^F this last expression no longer contains electron-phonon interaction terms. However, electron-electron interactions of the form

$$\sum_{k,k',q} V_{k,k',q} c^{\dagger}_{k+q} c^{\dagger}_{k'-q} c_{k'} c_k \tag{1.24}$$

emerge. Therefore, up to second order in α, Fröhlich's one-step transformation exactly maps the interacting electron-phonon system to an effective decoupled electron-phonon system with phonon-induced effective electron-electron interaction, which was not present in the initial problem. This constitutes a significant simplification and leads to interesting physical insights.

Now, In Ref. [41] Lenz and Wegner re-investigated the electron-phonon Hamilton (1.19) by means of a continuous unitary transformation. This transformation also leads to a suppression of the electron-phonon interaction part, i.e. $H_{\text{ep}}(\infty) = 0$, and generates electron-electron interactions $V_{k,k',q}$. However, expressing everything up to second order in α as Fröhlich did, they find that the explicit form of $V_{k,k',q}$ differs considerably from what Fröhlich found; it is less singular.[3] Their analysis shows that the difference can be understood on the level of Eq. (1.18). Fröhlich's one-step generator S^F is nothing else but the first term in the expansion of S, i.e. $S^F = \Omega_1(\infty)$. Thus, the differences rely on the non-commutivity of η at different ℓ-values. The η guided adjustments of $U(\ell)$ at each infinitesimal step of the transformation allow a controlled and smooth suppression of unwanted processes. In this perspective, Fröhlich's one-step transformation is not able to track the subtle interplay of processes on *all* energy scales, which can lead to singularities in the effective quantities in an uncontrolled way. The continuous approach seems to be capable of dealing with this important kind of subtleties.

So far we expressed everything in general terms. In fact, we just reformulated the problem of simplification. Any further progress is based on making a choice for the infinitesimal generator $\eta(\ell)$. This choice is by no means unique. There is no prescription which tells us how the generator has to be constructed

---

[3] To be more precise, the differences show up for virtual processes only; i.e. processes which are not directly observable. All observable processes in the electron-electron interaction do not show any difference to Fröhlich's results, as it should: observable processes are invariant under unitary transformations. They should therefore not depend on the specific form of the transformation.

to obtain a significant simplification. In fact, the construction of a suitable generator is a highly intuitive task. In principal, a vast number of generators differing in appearance and effect is conceivable. Though there has been some work on this issue (see e.g. Refs. [42] and [43]), further investigations are necessary, but this is not the topic of this thesis. The following two sections are intended to convey the ideas of generator-construction. They are guided by the intention to simplify the Hamiltonian. We identify $A(\ell) = H(\ell)$ in the following.

1.2. Standard Generator

To construct a method which is as independent as possible of the specific form of the Hamiltonian one seeks a functional form for the generator in accordance with

$$\eta(\ell) = \eta[H(\ell)] . \tag{1.25}$$

Wegner, in his original work on this topic (Ref. [33]), proposed the following generator

$$\eta(\ell) = [H_d(\ell), H(\ell)] . \tag{1.26}$$

The operator $H_d(\ell)$ denotes the diagonal part of the Hamiltonian $H(\ell)$ with respect to a particular basis. With a little consideration we can already see what the effect of this generator will be. In the beginning of the transformation $H_d(\ell = 0)$ and $H(\ell = 0)$ will not commute in general. The right hand side of Eq. (1.11) is not zero and $H(\ell)$ starts to change its appearance. The flow of $H(\ell)$ stops, i.e. $\eta(\ell)=0$, either if $H(\ell)$ becomes zero, the uninteresting case, or if $H_d(\ell)$ commutes with $H(\ell)$. If we consider the elements of the diagonal part H_d to be sorted according to their value, we see, that the transformation terminates when H has reached a block-diagonal appearance. The dimension of each block is given by the multiplicity of the corresponding (degenerate) eigen-value of H_d. As we show in the following paragraphs, this structure is reached in the limit $\ell \to \infty$.

According to our definition above we call the resulting block-diagonal Hamiltonian H_{eff}. All matrix elements of H_{eff} connecting states with different diagonal energies have vanished, which is a considerable simplification. This block-diagonality is of essential interest to us and will play an important role in the rest of this thesis. In particular, the results of the next chapter rely on this property of H_{eff}.

To explicitly prove the block-diagonalising properties of Wegner's generator we need to take a look at the matrix elements of $H(\ell)$ (see also Ref. [33]). Let $\{|\mu_i\rangle\}$ be the basis of the Hilbert space in which H_d is diagonal. We then have

$h_{ij}(\ell) = \langle \nu_i | H(\ell) | \nu_j \rangle$ where we wish to highlight the diagonal elements $\epsilon_i(\ell) = \langle \nu_i | H(\ell) | \nu_i \rangle$. The matrix elements of η in this basis are $\eta_{ij}(\ell) = \langle \nu_i | \eta(\ell) | \nu_j \rangle$ and from Eq. (1.26) we get

$$\eta_{ij} = (\epsilon_i - \epsilon_j) h_{ij} . \tag{1.27}$$

Using this result the flow equation (1.11) becomes

$$
\begin{aligned}
\frac{\partial h_{ij}}{\partial \ell} &= \sum_k \eta_{ik} h_{kj} - \sum_k h_{ik} \eta_{kj} \\
&= \sum_k (\epsilon_i + \epsilon_j - 2\epsilon_k) h_{ik} h_{kj} .
\end{aligned}
\tag{1.28}
$$

Further progress is made by inspection of the transformation-invariant trace of $H^2(\ell)$

$$\mathrm{Tr} H^2(\ell) = \sum_{k,i} h_{ki} h_{ik} = \sum_k \epsilon_k^2 + \sum_{i \neq k} h_{ki} h_{ik} = \mathrm{const.}$$

$$\Rightarrow \frac{\partial \mathrm{Tr} H^2(\ell)}{\partial \ell} = 0 . \tag{1.29}$$

We therefore have

$$\sum_k \frac{\partial \epsilon_k^2}{\partial \ell} = -\sum_{i \neq k} \frac{\partial}{\partial \ell} (h_{ki} h_{ik}) . \tag{1.30}$$

Finally we make use of the flow equation for the diagonal elements

$$
\begin{aligned}
\sum_k \frac{\partial \epsilon_k^2}{\partial \ell} &= 2 \sum_k \epsilon_k \frac{\partial \epsilon_k}{\partial \ell} \\
&\overset{\mathrm{Eq.\ (1.28)}}{=} 2 \sum_k \left(\epsilon_k \cdot 2 \sum_i (\epsilon_k - \epsilon_i) h_{ki} h_{ik} \right) \\
&= 2 \sum_{k,i} (\epsilon_k - \epsilon_i)^2 h_{ki} h_{ik} .
\end{aligned}
\tag{1.31, 1.32}
$$

The last equation follows from a simple re-summation. As a result we find in which way the *non*-diagonal elements of $H(\ell)$ behave in the flow of the transformation

$$-\sum_{k,i \neq k} \frac{\partial}{\partial \ell} |h_{ki}|^2 = 2 \sum_{k,i} (\epsilon_k - \epsilon_i)^2 |h_{ki}|^2 . \tag{1.33}$$

Eq. (1.33) expresses the fact that the sum of the absolute values of the non-diagonal elements of $H(\ell)$ decrease with increasing ℓ as long as the right hand side is larger than zero. As soon as all non-diagonal elements h_{ij}, connecting states of *non-equal* diagonal elements ϵ_i and ϵ_j, vanish, the transformation terminates. Non-diagonal elements, connecting *equal* diagonal elements, need not vanish. Thus, the limit $\ell \to \infty$ leads to a block-diagonalisation of H. The dimension of each block is equal to the multiplicity of its corresponding degenerate eigen-value of $H_d(\infty)$. From Eq. (1.27) we additionally see, that the corresponding elements η_{ij} vanish in any case, so that we find

$$\lim_{\ell\to\infty} \eta(\ell) = \lim_{\ell\to\infty} [H_d(\ell), H(\ell)] = 0 \;, \tag{1.34}$$

i.e. H_{eff} commutes with its diagonal part.

It is rewarding to have a closer look at the precise behaviour of the matrix elements in the flow of the transformation. Eq. (1.33) shows that non-diagonal matrix elements h_{ik} connecting states with a large difference in the diagonal energies $\epsilon_k - \epsilon_i$ decay faster than those with a smaller difference. In this sense the method shows a *renormalisation behaviour* as known from standard renormalisation schemes [44], where high energy processes connected to large momenta are successively suppressed, while energies connected to small momenta are renormalised. However, in contrast to this "standard" renormalisation scheme the continuous unitary transformation preserves the full Hilbert space. No information is lost. All energy scales are taken into account, none is discarded. Thus, in contrast to standard renormalisation schemes, the continuous transformation gives rise to an effective Hamiltonian which is not only valid in the low energy sector but on all energy scales (see also Ref. [45]).

We therefore obtain an intuitive and physical understanding of how the simplification is realised. The method suppresses processes involving a change of diagonal energy by renormalising processes of constant diagonal energy. The investigation of H can thus be split into investigations of the smaller blocks, each associated with a specific "diagonal energy". In the next section we will assign a physically reasonable quantity to the phrase "diagonal energy".

The proof above, however, also reveals a disadvantage of the chosen generator. Non-zero matrix elements may be generated in $H(\ell)$ for intermediate ℓ where there have been zeros initially. In other words, a possible simple structure in the initial Hamiltonian will be destroyed in the flow of H, building up a complicated intermediate problem which may not be simplified until the very end of the transformation. To see this we consider a band-diagonal Hamiltonian according to

$$h_{ij}(\ell = 0) = 0 \;, \text{ for } |i - j| > M \;. \tag{1.35}$$

From the flow equation (1.28) we see, that the derivative of elements outside the band depend on non-zero elements within the band and may thus be subject to changes even if their initial value was zero.

Although the presented generator meets the requirement for a systematic and physically comprehensible simplification we introduce another generator in the next section. This modified generator removes the deficiency of an artificially increased use of the system's Hilbert space. This increased use can be considered as a drawback if one thinks of a possible computer implementation, where one would try to keep the number of states to be stored as small as possible.

1.3. Quasi-Particles – Modified Generator

In this section we introduce a modified generator which will lead to a considerable advancement. As outlined in the introduction, we would like to be able to describe the system under study by suitably defined quasi-particles. Let us assume, that we were able to define these particles. It might be necessary to use a whole family of quasi-particles. To be more precise we introduce an operator Q which counts the number of these particles in a given state of the system. Let $|n\rangle$ be such an eigen-state of Q containing n quasi-particles, then

$$Q|n\rangle = n|n\rangle \ . \tag{1.36}$$

If there are k different kinds of quasi-particles involved, n becomes a vector $(n_1, n_2, \ldots, n_k)$, where the ith-entry is the number of quasi-particles of kind i in the state $|n_1, n_2, \ldots, n_k\rangle$, i.e. $\sum_i n_i = n$. Generally the eigen-values n are degenerate, i.e. there may be different states comprising the same number of quasi-particles.

Our aim is to achieve a simplification by mapping the initial Hamiltonian onto an effective problem, which *conserves* the number of quasi-particles. From what we have learned in the section on Wegner's generator this can be achieved by

$$\eta(\ell) = [Q(\ell), H(\ell)] \ . \tag{1.37}$$

Now, since this leads to an effective Hamiltonian H_{eff} which commutes with Q the whole physics of interest can be expressed in terms of the conserved quasi-particles. We can use the common eigen-states of Q and H_{eff} to calculate the matrix elements of H_{eff}.

We again choose to examine the flow equation on the level of matrix elements. Let i count the eigen-states of Q such that $Q|i\rangle = q_i|i\rangle$, where q_i is the number of quasi-particles in the state $|i\rangle$. We express all operators in terms of

their matrix elements with respect to the basis $\{|i\rangle\}$. In this case Eq. (1.37) reads

$$\eta_{ij}(\ell) = (q_i - q_j)h_{ij}(\ell) \ . \tag{1.38}$$

Before we prove that the new generator leads to a block-diagonalisation as in the case of Wegner's generator we want to add another feature that will warrant a structure conserving behaviour of the resulting transformation.

Now, what would be a reasonable initial form of a generic multi-particle Hamiltonian in the $\{|i\rangle\}$ basis? The initial Hamiltonian H does not conserve the number of quasi-particles and will thus not be block-diagonal. A reasonable assumption is, that H creates or destroys a *finite* number of quasi-particles when acting on a given state $|i\rangle$, which leads to a block band structure as depicted in Fig. 3.1 on page 47. We can formally express this by

$$h_{ij}(\ell = 0) = 0, \quad \text{for} \ \ |q_i - q_j| > \Delta Q_{\max} \ , \tag{1.39}$$

where $\Delta Q_{\max}$ is the maximum change of quasi-particles the initial Hamiltonian is able to produce.

We now add a feature to our generator which will warrant the conservation of this block band structure in the flow of the Hamiltonian. We introduce the modification on the level of matrix element notation. Instead of the full difference of the number of quasi-particles $q_i - q_j$ in Eq.(1.38) we merely take the signum of this difference. It is understood that $\text{sgn}(0) = 0$

$$\eta_{ij} = \text{sgn}(q_i - q_j)h_{ij} \ . \tag{1.40}$$

Independently from our considerations Mielke found a similar generator [42]. He considered an initial true band structure. Substituting Eq. (1.40) in the flow equation (1.11) yields

$$\begin{aligned}
\frac{\partial h_{ij}}{\partial \ell} &= \sum_k \left[\text{sgn}(q_i - q_k) - \text{sgn}(q_k - q_j) \right] h_{ik} h_{kj} \tag{1.41} \\
&= -\text{sgn}(q_i - q_j)(h_{ii} - h_{jj})h_{ij} \\
&\quad + \sum_{k \neq i,j} \left[\text{sgn}(q_i - q_k) - \text{sgn}(q_k - q_j) \right] h_{ik} h_{kj} \ . \tag{1.42}
\end{aligned}$$

For $|q_i - q_j| > \Delta Q_{\max}$ the first term in Eq. (1.42) vanishes, since $h_{ij} = 0$ in this case. The second term vanishes, too. This is because either $|q_i - q_k|$ or $|q_j - q_k| > \Delta Q_{\max}$, therefore h_{ik} or $h_{kj} = 0$, or $\text{sgn}(q_i - q_k) - \text{sgn}(q_k - q_j) = 0$. This means that the derivatives of the initially zero matrix elements h_{ij}, with

$|q_i - q_j| > \Delta Q_{\mathrm{max}}$, vanish. Thus, they remain to be zero for all ℓ, which proves that the modified generator preserves the initial block band structure.

We now turn to prove that the modified generator (1.40) indeed leads to a block diagonalisation. To this end we inspect the flow of diagonal elements of $H(\ell)$. From Eq. (1.42) we get

$$\frac{\partial h_{ii}(\ell)}{\partial \ell} = 2 \sum_{k \neq i} \mathrm{sgn}(q_i - q_k)|h_{ik}(\ell)|^2 \ . \tag{1.43}$$

We assume without loss of generality that the basis $\{|i\rangle\}$ of eigen-states of Q is ordered such that $q_i = \langle i|Q|i\rangle \geq \langle j|Q|j\rangle = q_j$ for $i > j$. Then, the sum of the first r diagonal elements (r arbitrary, but fixed) reads

$$\frac{\partial}{\partial \ell} \sum_{i=1}^{r} h_{ii} = 2 \sum_{i=1}^{r} \sum_{k>r} \mathrm{sgn}(q_i - q_k)|h_{ik}|^2 \ . \tag{1.44}$$

Because we have ordered the basis beforehand, the right hand side of Eq. (1.44) is non-positive for all ℓ. Thus, the sum on the left hand side is a continuous monotonically decreasing function with ℓ. We now have to make a last important assumption. If we know, that the sum on the left hand side is bounded from below we conclude that the sum converges. Therefore, its derivative vanishes in the limit $\ell \to \infty$. Since we have chosen r to be arbitrary this implies

$$\lim_{\ell \to \infty} |h_{ik}(\ell)| = 0, \quad \text{for } q_i \neq q_k \ , \tag{1.45}$$

which is equivalent to

$$\boxed{[Q, H_{\mathrm{eff}}] = 0} \ . \tag{1.46}$$

The boundedness of $H(\ell)$ is a crucial point. Due to a generalised variational principle, the sum of the first r diagonal elements is also bounded from below by the sum of the r lowest eigen-values of $H(\ell)$. Note that the eigen-values of H are invariant under the unitary transformation, so that the r lowest eigen-values of $H(\ell)$ are identical to those of the initial Hamiltonian $H(0)$. In all reasonable physical circumstances H should have a finite ground state energy. At this stage of our discussion, however, we try to be as rigorous as possible, and there might be occasions where the Hamiltonian is not renormalisable in the sense that its spectrum decreases below all bonds at some point of the flow. In this case the argument leading to Eq. (1.45) breaks down.

This concludes our formal discussion of the modified generator. Eq. (1.46) is of vast importance in the rest of this thesis. Its consequences will be discussed in great detail in the next chapter.

1.4. Next steps

From what we have derived so far and excluding the existence of an exact solution an application of continuous unitary transformations to physical systems can follow two possible routes. In this thesis we pursue a perturbative realisation. For completeness we make a short excursion to shed some light on the other possible route, the so-called self-similar renormalisation, which has been applied to several problems by various authors [33, 45–50].

The generators we have discussed are commutators of some operator R with the Hamiltonian

$$\eta = [R, H] . \tag{1.47}$$

Therefore, the flow equation contains the square of the Hamiltonian

$$\frac{\partial H}{\partial \ell} = [[R, H], H] , \tag{1.48}$$

and is a non-linear first order differential equation for $H(\ell)$. By means of the commutator the flow equation gives rise to new terms not present in the initial Hamiltonian. The objective is to compare the coefficients of equal operators on both sides of the flow equation, which gives rise to a set of first order differential equations for these coefficients. This can only be done, if the renormalisation is self-similar, i.e. the left and the right and side of the flow equation comprise the same operators. Thus, we have two possibilities to deal with the newly generated terms, not appearing in the initial Hamiltonian:

(a) Omit these terms completely and risk a crude approximation.

(b) Keep (some of) these terms by including them in the initial Hamiltonian by setting their initial coefficients to zero.

In general, it is difficult to know beforehand which terms are relevant, for the renormalisation procedure. The choice is not unique and depends on the system under study and the goals one seeks to achieve.

This difficulty can be overcome by implementing the transformation in a perturbative way. The details of the perturbative implementation are the subject of chapter 3. We will illustrate the assets and drawbacks of this approach.

However, before we turn to a detailed discussion, the next chapter is intended to present some interesting *general* aspects of perturbatively obtained observables. By defining cluster additivity on the level of operators we show that the properties of infinite systems can be calculated on *finite* portions of the system as long as the perturbation order stays finite. Remember, that we needed the Hamiltonian to be bounded from below for the proof of the

block diagonalising property of the modified generator. In this light, the next chapter leads to an a posteriori justification of our preliminary assumption: if the Hamiltonian needs to be evaluated on finite portions of the system for finite orders only, it *will* be bounded from below. By elaborating on the mathematical background, the following chapter leads to other interesting properties which show, that the perturbative CUT approach naturally leads to a very systematic and physical understanding of the studied systems.

1.5. Chapter Summary

CUTs are introduced as a sequence of infinitely many unitary transformations $U(\ell)$, $\ell \in \mathbb{R}_0^+$, performed on a *flowing* Hamiltonian $H(\ell)$ (or observable $\mathcal{O}(\ell)$ more generally). The initial Hamiltonian is identified by $H = H(\ell = 0)$, while the *effective*, fully transformed Hamiltonian is obtained in the limit $\ell \to \infty$, $H_{\text{eff}} = H(\ell = \infty)$.

The infinitesimal difference between two successive transformations $U(\ell)$ and $U(\ell + d\ell)$ is proportional to $d\ell$ and controlled by an anti-hermitian generator $\eta(\ell)$. Generically, $\eta(\ell)$ in turn depends on $H(\ell)$, which guarantees a model independent and self-adjusting transformation. This must be seen in contrast to one-step transformations, which are constructed to work for *one* Hamiltonian at a time. We show that the flow of the Hamiltonian (or observable) is governed by the *flow equation*

$$\frac{\partial H(\ell)}{\partial \ell} = [\eta(\ell), H(\ell)] \ , \tag{1.49}$$

a first order differential equation for operators.

The construction of suitable generators is illustrated by two examples. We introduce the standard generator suggested by Wegner and a modified generator, which preserves a possible block-band structure of the initial Hamiltonian for all values of ℓ. The latter has the important property to yield an effective Hamiltonian which *conserves* the number of quasi-particles. The identification or definition of suitable quasi-particles depends on the model under study and might be a difficult issue for some systems. However, once a suitable set of quasi-particles is found, the transformation unitarily maps the possibly complicated initial Hamiltonian onto an effective problem, for which the conserved particles render a more transparent description possible.

In the last section we indicate two possible implementations of CUTs for concrete systems, both of which rely on a comparison of operators on both sides of the flow equation. The *self-similar* implementation is hampered by the necessity to identify relevant operators, which cannot be discarded without risking crude approximations. Generally it is difficult to judge in which sense the resulting theory is controlled. If the problem under investigation contains a small parameter x, the discussed difficulties can be avoided by using a *perturbative* implementation. The effective theory is controlled by the assumed smallness of x. However, the results will be given as series expansions, which have to be truncated at some finite order in x.

2. Mathematical Structure of Effective Operators

In this chapter we start to reduce the set of considered models. We will focus on lattice models with Hamiltonians exhibiting a finite interaction range. We assume that we are able to calculate the corresponding effective Hamiltonian and the effective observables in one way or the other, such that H_{eff} conserves the number of quasi-particles (see Eq. (1.46))

$$[Q, \mathcal{H}_{\mathrm{eff}}] = 0 \ . \tag{2.1}$$

By exploiting this property of H_{eff} we will elaborate on global mathematical structures hidden within the effective Hamiltonian and observables. It will be shown that the determination of these effective operators is facilitated by a decomposition into n-particle irreducible parts. We set up such a classification at zero temperature for *strong-coupling* situations, i.e. no weak-coupling limit is needed and no non-interacting fermions or bosons are required. Generically, we deal with hard-core bosons.

The necessity for the decomposition into n-particle irreducible parts arises in perturbative calculations of the effective Hamiltonians because only the n-particle irreducible interactions are independent of the system size. For them the linked cluster property holds. Therefore the effective operators which hold in the thermodynamic limit can be computed in finite systems.

2.1. Model Requirements

We consider models which are defined on a lattice Γ. At each site of the lattice the system can be in a number d of states spanning the local Hilbert space. Let us assume that d is finite. The dynamics of the system is governed by a Hamiltonian H acting in the tensor-product space of the local Hilbert spaces. For simplicity we do not consider antisymmetric, fermionic situations although this is also possible. So we are focusing on physical systems which can be described in terms of hard-core bosons.

The Hamiltonian H is assumed to be of finite range. This means that it is composed of *local* operators h_ν acting on a *finite* number of sites in the vicinity of the site ν

$$H = \sum_{\nu \in \Gamma} h_\nu \ . \tag{2.2}$$

We further assume, that H can be split according to

$$H(x) = U + xV \ , \tag{2.3}$$

such that the spectrum of U is simple (see below) and that the system does not undergo a phase transition from $x = 0$ to the range of values we are finally interested in. These requirements do not necessarily imply that x has to be small. But it is helpful if this is the case.

The ground state $|0\rangle$ of U and its lowest lying eigen-states shall be known. The latter will be viewed as elementary excitations from which the whole spectrum can be built. We assume that we can view the elementary excitations above $|0\rangle$ as (quasi-)particles above the vacuum. For simplicity, we will drop the prefix 'quasi-'; it is understood that 'particle' is a synonym for elementary excitation.

We assume that the physical picture sketched for $H(x = 0) = U$ is linked *continuously* to the range $0 \leq x \leq x_c$ where x_c is the critical value at which a phase transition occurs. At the critical value x_c the picture breaks down and cannot be used beyond $x = x_c$. Generically, a mode of $H(x)$ will become soft at x_c.

Furthermore, the particles for $x = 0$ shall be local in the sense that we can assign a site to each of them. Let Q be the operator that counts the number of particles.

As a concrete example, the reader may think of an antiferromagnetic Heisenberg model made up from strongly coupled (coupling J) pairs of spins ('dimers') which are weakly coupled (coupling xJ) among themselves. At $x = 0$, the ground state is the product state with singlets on all dimers; the elementary excitations are local triplets. The number of these local triplets, i.e. the number of dimers which are not in the singlet state, shall be given by the operator Q.

2.2. Effective Hamiltonian

We assume that we are able to construct a mapping such that H_{eff} fulfils Eq. (2.1). The eigen-states of the quasi particle operator Q serve as a basis for the Hilbert space of the system. If the mapping is realised perturbatively, the matrix elements of H_{eff} and $\mathcal{O}_{\text{eff}}$ are polynomials in x.

2.2.1. Global Structure

We will show that H_{eff} can be written as

$$H_{\text{eff}} = H_0 + H_1 + H_2 + H_3 + \dots \;, \tag{2.4}$$

where H_n is an n-particle irreducible operator, i.e. H_n measures n-particle energies. Moreover, each thermodynamic matrix element of any of the components H_n can be obtained on finite clusters for a given order in x if the original Hamiltonian is of finite range. The components H_n can be defined recursively in ascending order in n.

Eq. (2.4) already comprises a route to determine the properties of H_{eff} in a sequence of approximate treatments. The very first step is to know the ground state energy which defines H_0. The second level is to describe the dynamics of a single particle (elementary excitations) correctly which is possible by knowing H_1. The third level is reached if H_2 is included which contains the information on the interaction of two particles. True three-particle interactions are contained in H_3 and so on. From the generic experience in condensed matter theory, the three- and more particle terms can very often be neglected. So the first three terms in Eq. (2.4) provide the systematically controlled starting point of a broad class of problems.

Let us clarify some notation. We define the following eigen-states of the particle-counting operator Q

$$
\begin{aligned}
&|0\rangle && \text{ground state (particle vacuum)} \\
&|i\rangle && \text{state with 1 particle on site } i \\
&|i_1 i_2\rangle && \text{state with 2 particles on sites } i_1 \text{ and } i_2 \\
&\quad\vdots &&
\end{aligned}
\tag{2.5}
$$

i.e. $Q|0\rangle = 0|0\rangle$, $Q|i\rangle = 1|i\rangle$ and $Q|ij\rangle = 2|ij\rangle$ and so on. These states span the global Hilbert space $\mathcal{E}$ of the physical system under study. Dealing with (hardcore) bosons $|i_1 i_2\rangle$ and $|i_2 i_1\rangle$ are identical states. This indistinguishability causes a certain ambiguity. This ambiguity can be remedied for instance by assuming that coefficients depending on several indices $i_1 i_2 \dots i_n$ are even under permutation of any pair of these indices.[1] For simplicity, the ground state $|0\rangle$ is assumed to be unique.

---

[1] Another way to deal with the ambiguity would be to introduce a certain ordering among the indices. Then only one representative of the two (or more) identical states needs to be kept. We will make use of this concept in the application chapter later on.

Let $\mathcal{R}$ be an arbitrary operator acting on $\mathcal{E}$ and conserving the number of particles $[\mathcal{R}, Q] = 0$. By $\mathcal{R}|_n$ we denote the restricted operator acting on $\mathcal{E}_n \subset \mathcal{E}$ spanned by all states with exactly n particles.

Now we define the operators H_n (recall, that H_n conserves the number of particles)

$$
\begin{aligned}
H_0 &:= E_0 \mathbf{1} \\
H_1 &:= \sum_{i;j} t_{j;i} e_j^\dagger e_i \\
H_2 &:= \sum_{i_1 i_2; j_1 j_2} t_{j_1 j_2; i_1 i_2} e_{j_1}^\dagger e_{j_2}^\dagger e_{i_2} e_{i_1} \\
&\vdots \\
H_n &:= \sum_{i_1 \ldots i_n; j_1 \ldots j_n} t_{j_1 \ldots j_n; i_n \ldots i_1} e_{j_1}^\dagger \ldots e_{j_n}^\dagger e_{i_n} \ldots e_{i_1}. \qquad (2.6)
\end{aligned}
$$

where $\mathbf{1}$ is the identity operator. Note that these operators are defined on the full Hilbert space $\mathcal{E}$. The operators $e_i^{(\dagger)}$ are *local* operators that annihilate (create) particles at site i. They are bosonic operators. Their definition can be tailored to include a hard-core repulsion between the particles to account for the common situation that at maximum one of the particles may be present at a given site i. If the particles have additional internal quantum numbers, i.e. if there can be different particles at each site, the indices i and j are substituted by multi-indices $\mathbf{i}$ and $\mathbf{j}$.

As an example let us consider that there are three kinds of particles per site, but that at maximum only one of these particles can occupy a given site. Then each site corresponds to a four-level system; the particles are hard-core bosons. Such a situation arises in antiferromagnetic dimerized spin systems where each dimer represents a four-level system. The ground state is the unique singlet while the three particles are given by the three-fold degenerate triplet states. In this case we have the multi-indices $\mathbf{i} = (i, \alpha)$, where i denotes the site and α takes for instance the three values of the S^z component $\alpha \in \{-1, 0, 1\}$. In the local basis $\{|i, s\rangle, |i, -1\rangle, |i, 0\rangle, |i, 1\rangle\}$, where s denotes the singlet, the local

creation operators $e^\dagger_{i,\alpha}$ are the 4×4-matrices

$$
e^\dagger_{i,-1} = \begin{pmatrix} 0 & 0 & 0 & 0 \\ 1 & 0 & 0 & 0 \\ 0 & 0 & 0 & 0 \\ 0 & 0 & 0 & 0 \end{pmatrix},
$$

$$
e^\dagger_{i,0} = \begin{pmatrix} 0 & 0 & 0 & 0 \\ 0 & 0 & 0 & 0 \\ 1 & 0 & 0 & 0 \\ 0 & 0 & 0 & 0 \end{pmatrix},
$$

$$
e^\dagger_{i,1} = \begin{pmatrix} 0 & 0 & 0 & 0 \\ 0 & 0 & 0 & 0 \\ 0 & 0 & 0 & 0 \\ 1 & 0 & 0 & 0 \end{pmatrix}. \tag{2.7}
$$

It is understood that the action at all other sites but i is the identity so that the operators in (2.7) are defined on the whole Hilbert space. The annihilation operators $e_{i,\alpha}$ are given by the hermitian conjugate matrices. All possible commutators can easily be computed within the matrix representation. Finite matrix elements in the lower right 3×3 block can be viewed as combined annihilation & creation processes: the matrix $M_{\alpha,\beta}$ with all elements zero except the one at (α, β) corresponds to the process $e^\dagger_{i,\alpha} e_{i,\beta}$. A finite matrix element in the upper left 1×1 block, i.e. the singlet-singlet channel, can be expressed in normal-ordered fashion as $\mathbf{1}_4 - \sum_\alpha e^\dagger_{i,\alpha} e_{i,\alpha}$. In this way the operators (2.7) and their hermitian conjugate define a complete algebra which in turn enables us to classify contributions of the Hamiltonian according to the number of particles affected as done in Eqs. (2.4) and (2.6).

The decomposition (2.4) is physically very intuitive. Yet the next important question is whether and how the operators H_n are unambiguously defined. This issue is addressed by noting that $H_n|_m$ vanishes for $m < n$. This follows directly from the normal-ordering of the creation and annihilation operators in Eq. (2.6). Then we can proceed iteratively by requiring that H_{eff} applied to n particles corresponds to $H_0 + H_1 + \ldots + H_n$ (n arbitrary but fixed). Solving

for H_n yields the recursions

$$
\begin{aligned}
H_0|_0 &:= H_{\text{eff}}|_0 \\
H_1|_1 &:= H_{\text{eff}}|_1 - H_0|_1 \\
H_2|_2 &:= H_{\text{eff}}|_2 - H_0|_2 - H_1|_2 \\
&\vdots \\
H_n|_n &:= H_{\text{eff}}|_n - \sum_{i=0}^{n-1} H_i|_n \ .
\end{aligned}
\tag{2.8}
$$

Assuming that H_{eff} is calculated beforehand one starts by evaluating E_0 using the first definition. The result entirely defines H_0. The restriction $H_0|_1$ is then used in the second equation to extract the $t_{j;i}$ of H_1 and so on. Generally, H_n is defined on the full many-particle Hilbert space, not only for n particles. But it is sufficient to know the action of H_n on the subspace of n particles to determine all its matrix elements in (2.6). It is the essential merit of the notation in second quantisation (2.6) that it provides the natural generalisation of the action of a part of the Hamiltonian on a *finite* number of particles to an *arbitrary* number of particles. Since Eq. (2.8) holds for any number of particles and since $H_n|_m$ vanishes for $m < n$ we obtain Eq. (2.4), neglecting the precise definition of convergence which is beyond the scope of this chapter.

In conventional many-body language, H_n stands for the n-particle irreducible interaction. The subtractions in Eq. (2.8) ensure that H_n contains no reducible contributions, i.e. contributions which really act only on a lower number of particles. It should be emphasised that the formalism above does not require that a simple *free* fermionic or bosonic limit exists. It is possible to start from any type of elementary particles counted by some operator Q.

Moreover, the formalism presented in this section does not depend on how H_{eff} is obtained. It does not matter whether a perturbative, a renormalising procedure or a rigorously exact method was used to obtain H_{eff}.

2.2.2. Cluster Additivity

Here we focus on formal aspects of a perturbative approach generalising results obtained previously for zero-particle properties [51] and for one-particle properties [23]. This is achieved by lifting the definition of cluster additivity on the level of operators. The feature that the Hamiltonian is of finite range on the lattice is exploited. Then the Eqs. (2.8) can be evaluated on finite subsystems

(clusters, see below). Still, the thermodynamically relevant matrix elements of the operators H_n are obtained as we show in the following paragraphs.

To proceed further definitions are needed. A *cluster C* of the thermodynamic system is a *finite* subset of sites of the system and their linking bonds. By $\mathcal{R}^C$ we denote an operator which acts only on the Hilbert space $\mathcal{E}^C$ of C. If $\overline{C}$ denotes the sites of the total system which are not included in C, the restricted operator $\mathcal{R}^C$ is lifted naturally to an operator $\mathcal{R}$ in the total Hilbert space $\mathcal{E} = \mathcal{E}^C \otimes \mathcal{E}^{\overline{C}}$ by

$$\mathcal{R} := \mathcal{R}^C \otimes \mathbf{1}^{\overline{C}} . \tag{2.9}$$

Note that it is not possible to define a restricted operator $\mathcal{R}^C$ from an arbitrary operator $\mathcal{R}$ acting on $\mathcal{E}$ since $\mathcal{R}$ will not have the product structure (2.9) in general.

Two clusters A and B are said to form a *disconnected cluster $C = A \cup B$* iff they do not have any site in common $A \cap B = 0$ *and* there is no bond linking sites from A with sites from B. Otherwise the clusters A and B are said to constitute together a *linked cluster $C = A \cup B$*. Given a disconnected cluster $C = A \cup B$ an operator $\mathcal{R}^C$ is called *cluster additive* iff it can be decomposed as

$$\mathcal{R}^C = \mathcal{R}^A \otimes \mathbf{1}^B + \mathbf{1}^A \otimes \mathcal{R}^B . \tag{2.10}$$

With these definitions we show that H_{eff} and H_n are cluster additive. But $H_{\text{eff}}|_n$ is not! This will turn out to be another important reason to introduce the operators H_n.

The cluster additivity of H_{eff}^C is obvious since A and B are assumed to be disconnected. So they can be viewed as physically independent systems. Hence

$$H_{\text{eff}}^C = H_{\text{eff}}^A \otimes \mathbf{1}^B + \mathbf{1}^A \otimes H_{\text{eff}}^B . \tag{2.11}$$

Similarly, we deduce from (2.8) the operators H_n^A and H_n^B which act on $\mathcal{E}^A$ and $\mathcal{E}^B$, respectively. Then it is straightforward to verify that the operators

$$H_n^C = H_n^A \otimes \mathbf{1}^B + \mathbf{1}^A \otimes H_n^B \tag{2.12}$$

fulfil the recursion (2.8) for the operators defined for the cluster C. Hence the operators H_{eff} and H_n are indeed cluster additive.

It is instructive to see that $H_{\text{eff}}|_n$ is *not* cluster additive, contrary to what one might have thought. Let us consider the tentative identity

$$H_{\text{eff}}^C|_n = H_{\text{eff}}^A|_n \otimes \mathbf{1}^B + \mathbf{1}^A \otimes H_{\text{eff}}^B|_n . \tag{2.13}$$

This equation cannot be true since on the left hand side the number of particles is fixed to n while on the right hand side the number of particles to which the

identities $\mathbf{1}^A$ and $\mathbf{1}^B$ are applied is not fixed. So no cluster additivity is given for the $H_{\text{eff}}|_n$.

The fact that cluster additivity holds only for particular quantities was noted previously for $n = 1$ [23]. For $n = 2$, the subtraction procedure was first applied in the calculations in Ref. [52] (though not given in detail). In Refs. [25, 27, 28, 53] the subtractions necessary to obtain the irreducible two-particle interaction were given in more detail. The general formalism presented here shows on the *operator* level why such subtractions are necessary and where they come from. Thereby, it is possible to extend the treatment to the general n-particle irreducible interaction.

The notation in terms of second quantisation (2.6) renders the cluster additivity almost trivial. This is so since the creation and annihilation operators are defined locally for a certain site. It is understood that the other sites are not affected. Hence the same symbol $e_i^\dagger$ can be used independent of the cluster in which the site i is embedded. In particular, one automatically identifies $e_i^{\dagger,C}$ with $e_i^{\dagger,A} \otimes \mathbf{1}^B$ if $i \in A$ and with $\mathbf{1}^A \otimes e_i^{\dagger,B}$ if $i \in B$. Hence cluster additivity is reduced to trivial statements of the kind that

$$
\begin{aligned}
H_1^A &= \sum_{i,j \in A} t_{j;i} e_j^\dagger e_i \\
H_1^B &= \sum_{i,j \in B} t_{j;i} e_j^\dagger e_i
\end{aligned}
\tag{2.14}
$$

implies

$$
\begin{aligned}
H_1^C &= \sum_{i,j \in C} t_{j;i} e_j^\dagger e_i \\
&= \sum_{i,j \in A} t_{j;i} e_j^\dagger e_i + \sum_{i,j \in B} t_{j;i} e_j^\dagger e_i \\
&= H_1^A \otimes \mathbf{1}^B + \mathbf{1}^A \otimes H_1^B \ .
\end{aligned}
\tag{2.15}
$$

In this sense, the notation in second quantisation is the most natural (or canonical) way to think of cluster additivity.

Following Gelfand and co-workers [21, 23, 51] we conclude that the cluster additive quantities possess a (linked-)cluster expansion. Hence all the irreducible matrix elements $t_{j;i}$ possess a cluster expansion and can be computed on finite clusters.

Let us briefly sketch the fundamental ideas of this argument. Suppose we could calculate the series expansions for a certain property (the ground state

energy for instance) of all possible clusters of a given thermodynamic system. The central idea of the cluster expansion method is to express the expansion coefficients for the property of a large cluster in terms of the expansion coefficients for the property of smaller clusters. Thus, even for an infinite system, the expansion coefficients to a given order are obtained from separate series expansions done for a finite number of finite clusters. The role of the infinite lattice is to provide the number and types of different small clusters that can be embedded in it. To a given order one has to consider all clusters that differ by their topology. It can be shown, and this is an important point, that to a given order only the number of *linked* clusters is finite [21], the number of differing *disconnected* clusters of an infinite system is obviously infinite. Now, cluster additivity of the property under study ensures that only the *linked* clusters have to be considered so that the method can be used successfully [21].

In conclusion we see that the finite range of the interactions in the considered problem together with the cluster additivity of the considered quantity allow to correctly calculate finite series expansions of this quantity for the thermodynamic lattice on finite clusters.

2.2.3. Computational Aspects

Since H_{eff} conserves the number of particles, i.e. Eq. (2.1), its action is to shift existing particles. Let us denote the relevant matrix elements for a linked cluster A by

$$
\begin{aligned}
E_0^A &:= \langle 0|H_{\text{eff}}^A|0\rangle \\
a_{j;i}^A &:= \langle j|H_{\text{eff}}^A|i\rangle \\
a_{j_1 j_2;i_1 i_2}^A &:= \langle j_1 j_2|H_{\text{eff}}^A|i_1 i_2\rangle \\
&\;\;\vdots \quad ,
\end{aligned}
\tag{2.16}
$$

where the indices $i, j, \ldots$ may be multi-indices from now on. Put differently, E_0^A is the matrix element of $H_{\text{eff}}^A|_0$, the $a_{j;i}^A$ are the matrix elements of $H_{\text{eff}}^A|_1$, the $a_{j_1 j_2;i_1 i_2}^A$ those of $H_{\text{eff}}^A|_2$ and so on. The number E_0^A is the ground state

energy of cluster A. The recursive definitions (2.8) imply

$$t^A_{j;i} = a^A_{j;i} - E^A_0 \delta_{ji}$$

$$t^A_{j_1 j_2; i_1 i_2} = a^A_{j_1 j_2; i_1 i_2} - E^A_0 \delta_{j_1 i_1} \delta_{j_2 i_2} - E^A_0 \delta_{j_1 i_2} \delta_{j_2 i_1}$$

$$-t^A_{j_2; i_2} \delta_{j_1 i_1} - t^A_{j_1; i_2} \delta_{j_2 i_1} - t^A_{j_2; i_1} \delta_{j_1 i_2} - t^A_{j_1; i_1} \delta_{j_2 i_2}$$

$$t^A_{j_1 j_2 j_3; i_1 i_2 i_3} = a^A_{j_1 j_2 j_3; i_1 i_2 i_3} - A_0 - A_1 - A_2 \tag{2.17}$$

$$\vdots \, ,$$

where A_0 comprises six terms resulting from H_0, A_1 comprises 18 terms res-ulting from H_1 and A_2 comprises 36 terms resulting from H_2. The explicit for-mulae are given in appendix A. The recipe for deriving the above equations is straightforward. For a given n-particle process $\{i_m\} \rightarrow \{j_m\}$ ($m \in \{1, \ldots, n\}$) one has to subtract all possible processes which move less than n particles. The procedure is recursive since the m-particle processes with $m < n$ have been computed before. Note that all coefficients must be computed for the *same* cluster.

The cluster additivity or, equivalently, the existence of a cluster expansion can be exploited to compute the irreducible matrix elements on finite clusters given that the Hamiltonian is of finite range. There are two strategies to do so.

The first strategy is to choose a cluster large enough to perform the intended computation without finite-size effects. This strategy works particularly well if the dimensionality of the problem is low. Let us assume for simplicity that the Hamiltonian links only nearest-neighbour sites. Aiming at a given matrix element, for instance $t^A_{j_1 j_2; i_1 i_2}$, which shall be computed in a given order k, the large enough cluster C_l contains all possible subcluster C_s with two properties: (i) they have k or less bonds, (ii) they link the concerned sites j_1, j_2, i_1, i_2 among themselves.[2] Clearly, C_l depends on the order k. But it depends also on the sites j_1, j_2, i_1, i_2 under study so that the notation $C^{(k)}_l(\{j_1, j_2, i_1, i_2\})$ is appropriate. Note that the sequence of the sites does not matter.

If some sites are omitted the constraints for the subclusters C_s are dimin-ished since less sites must be linked. This implies in particular

$$C^{(k)}_l(\{j_1, j_2, i_1, i_2\}) \subset C^{(k)}_l(\{j_1, i_1\}) \, . \tag{2.18}$$

---

[2] Depending on the details of the interaction on the bonds it may be sufficient to consider smaller clusters than mentioned in the main text, for instance a pure nearest-neighbour spin exchange reduces the range of virtual excursions. Frustration is another mechanism which reduces the range of the effective processes, see e.g. the Shastry-Sutherland model discussed in chapter 6.

Hence there can be a cluster A which contains $C_l^{(k)}(\{j_1, j_2, i_1, i_2\})$ but does *not* contain $C_l^{(k)}(\{j_1, i_1\})$ so that the hopping matrix element $t_{j_1;i_i}^A$ is *not* the thermodynamic one, but the interaction $t_{j_1j_2;i_1i_2}^A$ is without finite-size correction. So intermediate steps in the calculations (2.17) can display finite-size effects although the final result does not.

The second strategy is to compute for a given order k the *net* contributions of all clusters C with $m \leq k$ bonds which link the sites under study. The advantage of this approach is that only smaller clusters need to be treated ($\leq k$ bonds). The price to pay is an overhead in determining the *net* contribution. This requires to deduct from the brutto contribution of C the contributions of all subcluster of C with less bonds which link the points under study. This must be done in order to avoid double counting. More details on this strategy can be found in Ref. [21].

For Hamiltonians with relatively simple topology, the second strategy is more powerful. For more complicated Hamiltonians, however, the task to implement the overhead without flaw can quickly become impracticable while the first strategy can still be used, at least up to a certain order of the perturbation.

2.3. Effective Observable

An effective Hamiltonian conserving the number of particles is useful to determine characteristic energies of the considered systems. But it is not sufficient to determine physical quantities which require more knowledge than the eigen-energies of the system. In particular, we aim at determining dynamic correlations such as $\langle \mathcal{O}(t)\mathcal{O}(0)\rangle$. Then the mapping of the original Hamiltonian H to the effective Hamiltonian H_{eff} must be extended to a mapping of the original observable $\mathcal{O}$ to the effective observable $\mathcal{O}_{\text{eff}}$. Here we will assume that this has been achieved by an appropriate unitary transformation, for instance in a continuous fashion as described in the Introduction.

2.3.1. Global Structure

The structure of the observables can be described best by using the notation of second quantisation again. Thereby it can be denoted clearly how many particles are involved. The most important difference compared to the Hamiltonian is that there is no particle conservation. We can construct the mapping such that the effective Hamiltonian conserves the particle number. Generally, an observable does not conserve the particle number: generically it

creates and annihilates excitations, i.e. particles. Hence we define the operators

$$\mathcal{O}_{d,n} := \sum_{i_1 \cdots i_n; j_1 \cdots j_{n+d}} w_{j_1 \cdots j_{n+d}; i_1 \cdots i_n} e^{\dagger}_{j_1} \cdots e^{\dagger}_{j_{n+d}} e_{i_n} \cdots e_{i_1}. \qquad (2.19)$$

The local operators e_i have been described after Eq. (2.6). Again they shall appear normal-ordered, i.e. all creation operators are sorted to the left of the annihilation operators. The first index d indicates how many particles are created ($d \geq 0$) or annihilated ($d < 0$) by application of $\mathcal{O}_{d,n}$. The second index $n \geq 0$ denotes how many particles have to be present before the operator $\mathcal{O}_{d,n}$ becomes active. The result of $\mathcal{O}_{d,n}$ acting on a state with less than n particles is zero.

In analogy to Eq. (2.4) the effective observables can be decomposed into partial observables like

$$\mathcal{O}_{\text{eff}} = \sum_{d=-\infty}^{\infty} \left(\mathcal{O}_{d,0} + \mathcal{O}_{d,1} + \mathcal{O}_{d,2} + \mathcal{O}_{d,3} + \ldots \right) . \qquad (2.20)$$

The additional feature in comparison to Eq. (2.4) is the sum over d. Tab. 2.1 sketches the structure of the terms appearing in the partial observables $\mathcal{O}_{d,n}$

$d \downarrow / n \rightarrow$	0	1	2	3
$\cdots$	$\cdots$	$\cdots$	$\cdots$	$\cdots$
-3	0	0	0	eee
-2	0	0	ee	$e^{\dagger}eee$
-1	0	e	$e^{\dagger}ee$	$e^{\dagger}e^{\dagger}eee$
0	1	$e^{\dagger}e$	$e^{\dagger}e^{\dagger}ee$	$e^{\dagger}e^{\dagger}e^{\dagger}eee$
1	$e^{\dagger}$	$e^{\dagger}e^{\dagger}e$	$e^{\dagger}e^{\dagger}e^{\dagger}ee$	$e^{\dagger}e^{\dagger}e^{\dagger}e^{\dagger}eee$
2	$e^{\dagger}e^{\dagger}$	$e^{\dagger}e^{\dagger}e^{\dagger}e$	$e^{\dagger}e^{\dagger}e^{\dagger}e^{\dagger}ee$	$e^{\dagger}e^{\dagger}e^{\dagger}e^{\dagger}e^{\dagger}eee$
$\cdots$	$\cdots$	$\cdots$	$\cdots$	$\cdots$

Table 2.1.: List of terms appearing in the partial observables $\mathcal{O}_{d,n}$ which form together the effective observable $\mathcal{O}_{\text{eff}}$ according to Eq. (2.20). No prefactors or indices are given for clarity.

Let us assume that we computed $\mathcal{O}_{\text{eff}}$ by some technique, for instance by a

CUT. Then the partial observables can be determined recursively by

$$\mathcal{O}_{d,0}|_{0\to0+d} := \mathcal{O}_{\text{eff}}|_{0\to0+d}$$

$$\mathcal{O}_{d,1}|_{1\to1+d} := \mathcal{O}_{\text{eff}}|_{1\to1+d} - \mathcal{O}_{d,0}|_{1\to1+d}$$

$$\mathcal{O}_{d,2}|_{2\to2+d} := \mathcal{O}_{\text{eff}}|_{2\to2+d} - \mathcal{O}_{d,0}|_{2\to2+d} - \mathcal{O}_{d,1}|_{2\to2+d}$$

$$\vdots$$

$$\mathcal{O}_{d,n}|_{n\to n+d} := \mathcal{O}_{\text{eff}}|_{n\to n+d} - \sum_{i=0}^{n-1} \mathcal{O}_{d,i}|_{n\to n+d} . \tag{2.21}$$

Here $|_{n\to n+d}$ denotes the restriction of an operator to act on the n-particle subspace $\mathcal{E}_n$ (domain) and to yield states in the $(n+d)$-particle subspace $\mathcal{E}_{n+d}$ (co-domain). The recursion is set-up in analogy to (2.8). It is again used that an operator $\mathcal{O}_{d,n}$ effectively vanishes if it is applied to *less* than n particles. Barring possible problems to define convergence, the validity of the recursion (2.21) for all d and n implies the decomposition (2.20).

As for the Hamiltonian the partial observables $\mathcal{O}_{d,n}$ can be viewed as the n-particle irreducible part of the particular observable. The notation in second quantisation elegantly resolves the question of how the observables act on clusters as was explained in the section 2.2.2. Hence the definition (2.19) ensures cluster additivity and there exist cluster expansions for the partial observables. So they can be computed on finite clusters.

If dynamical correlations at zero temperature $T = 0$ shall be described, the observables are applied to the ground state $|0\rangle$ which is the particle vacuum [45]. Then only the partial observables $\mathcal{O}_{d,0}$ with $d \geq 0$ matter. According to (2.21) no corrections are necessary, i.e. the structure of the relevant part of the effective observable is given by

$$\mathcal{O}_{\text{eff}}^{T=0} = \mathcal{O}_{0,0} + \mathcal{O}_{1,0} + \mathcal{O}_{2,0} + \mathcal{O}_{3,0} + \dots . \tag{2.22}$$

This structure has been used so far in a number of investigations of spectral weights [54, 55] and spectral densities [26, 29, 32]. It turned out that it is indeed sufficient to consider a restricted number of particles [26, 29, 55]. But the question of how many particles are required to describe a certain physical quantity sufficiently well depends on the considered model, the chosen basis (What do we call a particle?) and the quantity under study.

At finite temperatures a certain number of particles will already be present in the system due to thermal fluctuations. Then the action of the partial observables $\mathcal{O}_{d,n}$ with $n \geq 1$ will come into play as well. This constitutes an interesting route to extend the applicability of effective models, which were derived in the first place at zero temperature, to finite temperatures.

2.3.2. Computational Aspects

The recursive equations for matrix elements which can be derived from (2.21) are very similar to those obtained for the Hamiltonian (2.17). We illustrate this for the matrix elements of $\mathcal{O}_{1,n}$. Let the bare matrix elements on a cluster A be

$$
\begin{aligned}
v_j^A &:= \langle j | \mathcal{O}_{\text{eff}}^A | 0 \rangle \\
v_{j_1 j_2; i}^A &:= \langle j_1 j_2 | \mathcal{O}_{\text{eff}}^A | i \rangle
\end{aligned}
\tag{2.23}
$$

$$\vdots \quad .$$

From (2.21) we obtain the irreducible elements as

$$
\begin{aligned}
w_j^A &= v_j^A \\
w_{j_1 j_2; i}^A &:= v_{j_1 j_2; i}^A - w_{j_1}^A \delta_{j_2 i} - w_{j_2}^A \delta_{j_1 i}
\end{aligned}
\tag{2.24}
$$

$$\vdots \quad .$$

As for the irreducible interactions the strategy is straightforward. One has to subtract from the reducible n-particle matrix elements v^A the contributions which come from the m-particle irreducible matrix elements w^A with $m < n$. With this strategy also other irreducible matrix elements can be determined in a straightforward manner.

So far our considerations were rather general. Next we focus on the actual *perturbative* evaluation of the matrix elements on finite clusters. For simplicity, we assume as before that the perturbative part of the Hamiltonian links only nearest-neighbour sites. Let us consider for instance $w_{j_1 j_2; i}^A$. We assume that the observable $\mathcal{O}$ is also local, i.e. acts on a certain site only, or is a sum of such terms. If the observable is a sum of local terms, the transformation of each term separately and subsequent summation yields the result. So without loss of generality we consider $\mathcal{O}$ to affect only site p. Then we have to compute the matrix elements for clusters linking the *four* sites j_1, j_2, i, p. If $\mathcal{O}$ itself is a product of operators affecting several sites p_i, then the observable $\mathcal{O}$ itself links these sites p_i. Apart from this difference compared to the matrix elements of the effective Hamiltonian, we may copy the remaining steps from there:

There are again the two strategies. Either the calculation in order k is performed on a cluster C_l large enough so that all subclusters of k bonds linking the relevant sites j_1, j_2, i, p are comprised in C_l [26, 29, 31, 56]. Or one has to add the *net* contributions of all different clusters with k or less bonds

which link the relevant sites j_1, j_2, i, p [32]. In either way the results for spectral densities can be obtained.

The next chapter shows how an actual mapping, providing the effective operators, can be constructed. This mapping will be perturbative. The structure of the differential equations, which have to be solved to obtain the effective operators, will allow a computer implementation, rendering high order results possible.

2.4. Chapter Summary

In this chapter we focus on quantum multi-particle systems defined on a lattice. We assume the existence of a mapping of the original problem to an effective one in which the number of elementary excitations, or (quasi-)particles, is conserved. The general structure of the effective Hamiltonians and the observables is analysed.

We find that a classification of the various contributions in terms of the number of particles concerned is possible. To this end we introduced a notation in second quantisation which does not, however, require non-interacting fermions or bosons. Generically, hard-core bosons are involved. We find the effective operators to decompose into n-particle *irreducible operators*, which display *cluster additivity*. The effective Hamiltonian, for instance, decomposes into irreducible operators according to

$$H_{\text{eff}} = H_0 + H_1 + H_2 + \dots .$$

The individual operators H_n are determined recursively in ascending order in n, and are defined in second quantisation

$$H_n = \sum_{i_1 \dots i_n; j_1 \dots j_n} t_{j_1 \dots j_n; i_1 \dots i_n} e_{j_1}^\dagger \dots e_{j_n}^\dagger e_{i_n} \dots e_{i_1} .$$

The operators $e_i^{(\dagger)}$ (create) annihilate a particle on site i and are defined on the *whole* Hilbert space of the system. The coefficients t denote the *thermodynamic n-particle hopping amplitudes*. The recursive definition of the H_n implies that the thermodynamic amplitude for the n-particle process $\{i_m\} \to \{j_m\}$ is calculated by subtracting all processes that move less than n particles (see further down for an example). A similar decomposition holds for effective operators.

Since the irreducible interactions and vertex corrections are cluster additive, they possess a cluster expansion so that they can be computed on finite clusters provided that the Hamiltonian is of finite range. This property is the basis for a real-space treatment of many spin systems. Since H_{eff} and thus all H_n conserve the number of particles, the real-space states are unambiguously defined by the number of particles and their position. For instance, if A denotes a cluster large enough to calculate the thermodynamic one-particle hopping amplitudes $t_{j;i}$ to some finite order, the generic procedure is captured by

$$a_{j;i}^A := \langle j | H_{\text{eff}} | i \rangle \text{ followed by}$$

$$t_{j;i} = a_{j;i}^A - E_0^A \delta_{ji} \ .$$

The cluster index can be dropped from the thermodynamic amplitude.

The irreducible operators are defined on the whole Hilbert space, i.e. not only for a small number of particles. The matrix elements of the n-particle irreducible operators can be computed considering only n-particles. But the resulting operators hold for an arbitrary number of particles.

The formulation in second quantisation is particularly intuitive. It facilitates the definition of the irreducible quantities and cluster additivity on the *operator level* in a natural way. We would like to emphasise that the definition of irreducible operators is not a trivial task if a strong-coupling situation is considered as was done here. No limit of non-interacting bosons or fermions is assumed. Since the definition of irreducible operators is completely general it allows the computation of the n-particle contribution for arbitrary n.

Let us finally emphasise that our findings suggest a very systematic way to treat quantum multi-particle systems. After the effective operators are calculated, one can successively investigate the sectors of different particle numbers. Canonically one would start with the ground state (H_0). In a next step one might analyse the one-particle dynamics (H_1). If particle correlations are important one includes the two- and possibly also the three-particle irreducible interactions (H_2 and H_3) and so on. The investigation of other observables follows a similar route.

3. Perturbative CUT

So far we did not presume any particular property of the transformation which leads to the effective operators H_{eff} and $\mathcal{O}_{\text{eff}}$. The only prerequisites were the existence of a counting operator Q, which counts the number of elementary excitations, i.e. particles, and the conservation of this number by H_{eff}: $[H_{\text{eff}}, Q] = 0$.

In this chapter we specify a particular perturbative continuous unitary transformation. For simplicity we restrict the set of considered models once more. The first section, illustrating the perturbative transformation of the Hamiltonian, is a brief summary of earlier descriptions, see e.g. Ref. [57] or Ref. [58]. This section is necessary to fix the notation for the subsequent section dealing with the transformation of general observables.

The block diagonality of H_{eff} with respect to the number of particles is reconsidered for translational invariant systems in section 3.4. Elaborating on the one- and two-particle blocks will show that translational invariance leads to a strongly simplified appearance of H_{eff} in a suitably defined momentum basis. Section 3.4 also covers the appearance of effective observables in momentum space.

Finally we give a detailed description of how the perturbative transformations can be implemented on a computer in section 3.5.

3.1. Hamiltonian

Suppose the problem can be formulated as perturbation problem as in Eq. (2.3) with the two additional properties

(A) The unperturbed part U has an equidistant spectrum bounded from below. The difference between two successive levels is the energy of a particle, i.e. $Q = U$.

(B) There is a number $\mathbb{N} \ni N > 0$ such that the perturbing part V can be split according to $V = \sum_{n=-N}^{N} T_n$ where T_n increments (or decrements, if $n < 0$) the number of particles by n: $[Q, T_n] = nT_n$.

Condition (A) allows the introduction of the particularly simple and intuitive choice $Q = U$. Note that the restrictions of (A) are not too serious in practice since very often the deviations from an equidistant spectrum can be put into the perturbation V. Conditions (A) and (B) together imply that the starting Hamiltonian H has a block-band-diagonal structure as depicted in Fig. 3.1 on page 47. The perturbation V connects states of different particle numbers only if the difference is a finite number $\leq N$. Note that very many problems in physics display this property, for a discussion of interacting fermions see Refs. [45, 50]. We find $N = 1$ for the particular application, which we shall discuss in section 6. We also treated systems with $N = 2$ [26, 29, 31, 56, 57, 59]. Systems with $N = 2$ have been considered by other authors, too [52, 55, 60]. Calculations for higher N are also possible [61].

We solve the flow equation (1.11)

$$\frac{dH(\ell)}{d\ell} = [\eta(\ell), H(\ell)] \, , \tag{3.1}$$

for Hamiltonians $H(x) = U + xV$ obeying the conditions (A) and (B) perturbatively, that means up to a certain order in the expansion parameter x. The *ansatz* used is

$$H(x; \ell) = U + xV(\ell) = U + \sum_{k=1}^{\infty} x^k \sum_{|\underline{m}|=k} F(\ell; \underline{m}) T(\underline{m}), \tag{3.2}$$

with unknown real functions $F(\ell; \underline{m})$ for which the flow equation (3.1) yields non-linear recursive differential equations. The notation comprises

$$
\begin{aligned}
\underline{m} &= (m_1, m_2, m_3, \ldots, m_k) \quad \text{with} \\
m_i &\in \{0, \pm 1, \pm 2, \ldots, \pm N\} \\
|\underline{m}| &= k \\
T(\underline{m}) &= T_{m_1} T_{m_2} T_{m_3} \cdots T_{m_k} \\
M(\underline{m}) &= \sum_{i=1}^{k} m_i \, .
\end{aligned}
\tag{3.3}
$$

The second sum in ansatz (3.2) runs over all indices $\underline{m}$ of length $|\underline{m}| = k$. Thereby, $H(x; \ell)$ includes all possible virtual excitation processes $T(\underline{m})$ in a given order x^k multiplied by the weight $F(\ell; \underline{m})$.

As we have discussed in chapter 1, the optimum choice for the infinitesimal generator η of the unitary transformation in the given situation reads

$$\eta(x;\ell) = \sum_{k=1}^{\infty} x^k \sum_{|\underline{m}|=k} \text{sgn}\left(M(\underline{m})\right) F(\ell;\underline{m}) T(\underline{m}). \tag{3.4}$$

One easily confirms, that in the eigen-basis $\{|n\rangle\}$ of Q, i.e. $Q|n\rangle = q_n|n\rangle$, the matrix elements of the generator η read

$$\eta_{i,j}(x;\ell) = \text{sgn}(q_i - q_j) H_{i,j}(x;\ell) \ , \tag{3.5}$$

with the convention $\text{sgn}(0) = 0$, just as introduced in chapter 1. Recall, that η keeps the flowing Hamiltonian block-band diagonal also at intermediate values of ℓ. For $\ell \to \infty$ the generator (3.5) eliminates all parts of $H(x;\ell)$ changing the number of particles so that $[H_{\text{eff}}, Q] = 0$ with $H_{\text{eff}} := H(\ell = \infty)$.

For the functions $F(\ell;\underline{m})$ a set of coupled differential equations is determined by inserting Eqs. (3.2) and (3.4) in the flow equation (3.1) and comparing coefficients in the resulting expression

$$x\frac{\partial V(\ell)}{\partial \ell} = x[\eta(\ell), V(\ell)] \ - \ \sum_{k=1}^{\infty} x^k \sum_{|\underline{m}|=k} F(\ell;\underline{m}) \text{sgn}(M(\underline{m})) \underbrace{[U, T(\underline{m})]}_{=M(\underline{m})T(\underline{m})}$$

$$\Rightarrow \sum_{k,|\underline{m}|=k} x^k \frac{\partial F(\ell;\underline{m})}{\partial \ell} \cdot T(\underline{m}) \ =$$

$$\sum_{\substack{k_1,k_2 \\ |\underline{m}_1|=k_1 \\ |\underline{m}_2|=k_2}} x^{k_1+k_2} F(\ell;\underline{m}_1) F(\ell;\underline{m}_2) \text{sgn}(M(\underline{m}_1))[T(\underline{m}_1), T(\underline{m}_2)]$$

$$- \sum_{k,|\underline{m}|=k} x^k F(\ell;\underline{m})|M(\underline{m})|T(\underline{m}) \ . \tag{3.6}$$

Comparing the coefficients of equal operators in equal orders yields

$$\frac{\partial}{\partial \ell} F(\ell;\underline{m}) \ = \ -|M(\underline{m})|F(\ell;\underline{m}) + \tag{3.7}$$

$$\sum_{\{\underline{m}_1,\underline{m}_2\}=\underline{m}} [\text{sgn}(M(\underline{m}_1)) - \text{sgn}(M(\underline{m}_2))] \ F(\ell;\underline{m}_1) F(\ell;\underline{m}_2) \ .$$

The summation condition $\{\underline{m}_1, \underline{m}_2\} = \underline{m}$ means that one sums over all possible nontrivial breakups of $\underline{m}$

$$\underline{m}_1 = (m_1) \quad \text{and} \quad \underline{m}_2 = (m_2, \ldots, m_k)$$

$$\underline{m}_1 = (m_1, m_2) \quad \text{and} \quad \underline{m}_2 = (m_3, \ldots, m_k)$$

$$\underline{m}_1 = (m_1, m_2, m_3) \quad \text{and} \quad \underline{m}_2 = (m_4, \ldots, m_k)$$

$$\vdots$$

$$\underline{m}_1 = (m_1, \ldots, m_{k-2}) \quad \text{and} \quad \underline{m}_2 = (m_{k-1}, m_k)$$

$$\underline{m}_1 = (m_1, \ldots, m_{k-1}) \quad \text{and} \quad \underline{m}_2 = (m_k) \ . \tag{3.8}$$

The starting conditions read

$$F(0; \underline{m}) = 1 \quad \text{for} \quad |\underline{m}| = 1$$

$$F(0; \underline{m}) = 0 \quad \text{for} \quad |\underline{m}| > 1 \ . \tag{3.9}$$

For the solution of Eq. (3.7) we observe that the first term on the right hand side just generates an exponential prefactor

$$F(\ell; \underline{m}) = \exp(-|M(\underline{m})|\ell) f(\ell; \underline{m}) \ . \tag{3.10}$$

The rest of the Eq. (3.7) is recursive and can thus be directly found by integration beginning from the starting conditions. The simplified differential equation reads

$$\frac{\partial}{\partial \ell} f(\ell; \underline{m}) = \sum_{\{\underline{m}_1, \underline{m}_2\}=\underline{m}} e^{(|M(\underline{m})|-|M(\underline{m}_1)|-|M(\underline{m}_2)|)l} \ .$$

$$[\operatorname{sgn}(M(\underline{m}_1)) - \operatorname{sgn}(M(\underline{m}_2))] f(\ell; \underline{m}_1) f(\ell; \underline{m}_2) \ . \tag{3.11}$$

Note that $|M(\underline{m})| - |M(\underline{m}_1)| - |M(\underline{m}_2)| \leq 0$ holds so that no exponential growth occurs in the $f(\ell; \underline{m})$.

Let us give two examples. Since there is no non-trivial breakup in the case $\underline{m} = (m_1)$, the derivative of the function $f(\ell; (m_1))$ is zero. From the initial conditions (3.9) we get $f(0; (m_1)) = 1$ and thus $f(\ell; (m_1)) = 1$. Finally Eq. (3.10) gives

$$F(\ell; (m_1)) = e^{-|m_1|\ell} \ . \tag{3.12}$$

For the second example we consider $f(\ell; (-2, 1))$, for which the differential equation (3.11) yields

$$\partial_\ell f(\ell; (-2, 1)) = e^{(+1-2-1)\ell}[\operatorname{sgn}(-2) - \operatorname{sgn}(1)] \cdot 1 = -2e^{-2\ell} \ . \tag{3.13}$$

Integration with $f(0, (-2, 1)) = 0$ yields $f(\ell; (-2, 1)) = \exp(-2\ell) - 1$. We finally obtain

$$F(\ell; (-2, 1)) = e^{-3\ell} - e^{-\ell} \ . \tag{3.14}$$

Note that the differential equations are recursive, because of the sum over all possible breakups of $\underline{m}$. The functions f of order k, i.e. $f(\ell; \underline{m})$ with $|\underline{m}| = k$, are determined by the functions f of order $< k$. The functions are sums of monomials with structure $(p/q)\ell^i \exp(-2\mu\ell)$, where $p, q, i, (\mu > 0)$ are integers. This allows the implementation of a computer-aided iterative algorithm for the computation of the functions F. We will turn to this issue in section 3.5.

Figure 3.1.: Block-band diagonal Hamilton matrix for $N = 1$ in the eigen-basis $\{|n\rangle\}$ of the operator Q which counts the number of particles. The unperturbed Hamiltonian $H(x = 0) = U$ and the effective Hamiltonian H_{eff} have matrix elements in the blue (dark grey) areas only: $[H_{\text{eff}}, Q] = 0$. For a non-degenerate ground state H_{00} is a 1×1 matrix. The dimension of H_{nn} grows roughly like L^n with system size L. The perturbation V can lead to overlap matrices indicated as red (light grey) boxes. The empty boxes contain vanishing matrix elements only.

The following symmetry relations hold

$$F(\ell; \underline{m}) = F(\ell; (-m_k, \ldots, -m_1)) \tag{3.15}$$

$$F(\ell; \underline{m}) = F(\ell; (-m_1, \ldots, -m_k))(-1)^{k+1} \ . \tag{3.16}$$

Relation (3.15) reflects the hermitecity of the Hamiltonian. The block-band diagonality for all ℓ implies

$$F(\ell; \underline{m}) = 0 \quad \text{for} \quad |M(\underline{m})| > N \ . \tag{3.17}$$

In the limit $\ell \to \infty$ the coefficients $C(\underline{m}) := F(\infty; \underline{m})$ are obtained. The leading coefficients can be found in appendix B. Coefficients of higher orders can be obtained from our websites [62]. The effective Hamiltonian is given by the general form

$$H_{\text{eff}}(x) = U + \sum_{k=1}^{\infty} x^k \sum_{\substack{|\underline{m}|=k \\ M(\underline{m})=0}} C(\underline{m}) T(\underline{m}) \ , \tag{3.18}$$

where $M(\underline{m}) = 0$ reflects the conservation of the number of particles. The action of H_{eff} can be viewed as a weighted sum of particle-number conserving virtual excitation processes each of which is encoded in a monomial $T(\underline{m})$. In this way the effective Hamiltonian creates the polarisation cloud of the dressed quasi-particles, which are the *true* excitation. This is a simple and effective picture for the possibly complicated initial quantum multi-particle problem. We want to emphasise that the effective Hamiltonian H_{eff} with known coefficients $C(\underline{m})$ can be used straightforwardly in all perturbative problems that meet conditions (A) and (B).

Evaluation of H_{eff}

The evaluation of H_{eff} can be done most conveniently by calculating its action on real space states, for which we need to specify the number of particles and their positions on the lattice only. With $|0\rangle$ denoting the particle vacuum, the ground state energy E_0 is given by

$$E_0 = \langle 0|H_{\text{eff}}|0\rangle = \langle 0|H_0|0\rangle \ . \tag{3.19}$$

Note that $|0\rangle$ is the ground state of $H_{\text{eff}}(x = 0) = U$. In appendix H we prove, that $|0\rangle$ remains to be the ground state of $H_{\text{eff}}(x)$ for finite (not too large) x. The one-particle hopping amplitudes $a_{j;i}$ are given by

$$a_{j;i} = \langle j|H_{\text{eff}}|i\rangle = \langle j|(H_0 + H_1)|i\rangle \ , \tag{3.20}$$

where $|i\rangle$ and $|j\rangle$ denote the states with exactly one particle at site i and j respectively. It is obvious how one has to proceed for higher particle numbers. Note that the hopping amplitudes $t_{j;i}$ of the *thermodynamic* systems are obtained by subtracting the ground state energy appropriately. The same applies for higher particle numbers. The necessary procedures are given in section 2.2.3.

3.2. Observable

To calculate physical quantities which do not only depend on the eigen-energies the relevant observables must also be known. The conceptual simplicity of unitary transformations implies that the observables must be subject to the *same* unitary transformation as the Hamiltonian. In this section we describe how the perturbative CUT method can be extended to serve this purpose.

Consider the observable $\mathcal{O}$. It is mapped according to the flow equation

$$\frac{\partial \mathcal{O}(x; \ell)}{\partial \ell} = [\eta(x; \ell), \mathcal{O}(x; \ell)] , \tag{3.21}$$

where the *same* generator $\eta(x; \ell)$ as given in Eq. (3.4) is to be used to generate the transformation. In analogy to Eq. (3.2) we employ the ansatz

$$\mathcal{O}(x; \ell) = \sum_{k=0}^{\infty} x^k \sum_{i=1}^{k+1} \sum_{|\underline{m}|=k} G(\ell; \underline{m}; i) \mathcal{O}(\underline{m}; i), \tag{3.22}$$

where the $G(\ell; \underline{m}; i)$ are real-valued functions for which the flow equation (3.21) yields recursive differential equations. The operator products $\mathcal{O}(\underline{m}; i)$ are given by

$$\mathcal{O}(\underline{m}; i) := T_{m_1} \cdots T_{m_{i-1}} \mathcal{O} T_{m_i} \cdots T_{m_k} , \tag{3.23}$$

where we use the notation of the Eqs. (3.3). The integer i denotes the position in $\mathcal{O}(\underline{m}, i)$ at which the operator $\mathcal{O}$ is inserted in the sequence of the T_m. The starting condition is $\mathcal{O}(x; 0) = \mathcal{O}(x)$ and the final result is found at $\ell = \infty$: $\mathcal{O}_{\text{eff}}(x) := \mathcal{O}(x; \infty)$.

Inserting the ansatz (3.23) for $\mathcal{O}(x; \ell)$ and the generator $\eta(x; \ell)$ from (3.4) into the flow equation (3.21) yields

$$\sum_{k=0}^{\infty} x^k \sum_{|\underline{m}|=k} \sum_{i=1}^{k+1} \frac{\partial}{\partial \ell} G(\ell; \underline{m}; i) \mathcal{O}(\underline{m}; i) =$$

$$\sum_{k_1=1}^{\infty} \sum_{k_2=0}^{\infty} x^{k_1+k_2} \sum_{\substack{|\underline{m}'|=k_1 \\ |\underline{m}''|=k_2}} \sum_{i=1}^{k_2+1} F(\ell; \underline{m}') G(\ell; \underline{m}''; i) \times$$

$$\times \text{sgn}(M(\underline{m}')) [T(\underline{m}'), \mathcal{O}(\underline{m}''; i)] . \tag{3.24}$$

The functions $F(\ell; \underline{m})$ are known from the calculations described in the preceding section pertaining to the transformation of the Hamiltonian. The sums

denoted by expressions of the type $|\underline{m}| = k$ run over all multi-indices $\underline{m}$ of length k.

Comparing coefficients in Eq. (3.24) yields a set of recursive differential equations for the functions $G(\ell; \underline{m}, i)$. To ease the comparison of coefficients we split a specific $\underline{m}$ with k fixed in two parts as defined by i

$$\underline{m} = (\underline{m}_l, \underline{m}_r) \ , \tag{3.25}$$

with $|\underline{m}_l| = i - 1$ and $|\underline{m}_r| = k - i + 1$ such that the splitting reflects the structure of $\mathcal{O}(\underline{m}; i)$ in (3.23). Then the explicit recursions can be denoted by

$$\frac{\partial}{\partial \ell} G(\ell; \underline{m}; i) =$$

$$\sum_{\substack{\underline{m}_l = (\underline{m}_a, \underline{m}_b) \\ \underline{m}_a \neq 0}} \mathrm{sgn}(M(\underline{m}_a)) F(\ell; \underline{m}_a) G(\ell; (\underline{m}_b, \underline{m}_r); i - |\underline{m}_a|)$$

$$- \sum_{\substack{\underline{m}_r = (\underline{m}_a, \underline{m}_b) \\ \underline{m}_b \neq 0}} \mathrm{sgn}(M(\underline{m}_b)) F(\ell; \underline{m}_b) G(\ell; (\underline{m}_l, \underline{m}_a); i) \ . \tag{3.26}$$

Note that these differential equations for the functions G are linear for known functions F, in contrast to the non-linear differential equations for F (see Eq. (3.7) on page 45). The recursive nature of these equations becomes apparent by observing that the summations $\underline{m}_l = (\underline{m}_a, \underline{m}_b)$ and $\underline{m}_r = (\underline{m}_a, \underline{m}_b)$ are performed over all non-trivial breakups of $\underline{m}_l$ and $\underline{m}_r$. For instance, the restriction

$$\underline{m}_l = (m_1, m_2, \ldots, m_{i-1}) \doteq (\underline{m}_a, \underline{m}_b) \tag{3.27}$$

with $\underline{m}_a \neq 0$ means, that one has to sum over the breakups

$$\underline{m}_a = (m_1) \qquad \text{and} \quad \underline{m}_b = (m_2, \ldots, m_{i-1})$$

$$\underline{m}_a = (m_1, m_2) \qquad \text{and} \quad \underline{m}_b = (m_3, \ldots, m_{i-1})$$

$$\vdots \qquad\qquad\qquad \vdots$$

$$\underline{m}_a = (m_1, m_2, \ldots, m_{i-1}) \quad \text{and} \quad \underline{m}_b = () \ . \tag{3.28}$$

This implies that the $G(\ell; \underline{m}; i)$ appearing on the right side of Eq. (3.26) are of order $k - 1$ or less. Once they are known the function on the left hand side of order k can be computed. By iteration, all functions can be determined. The initial conditions follow from $\mathcal{O}(x; \ell = 0) = \mathcal{O}$ and read

$$G(0; \underline{m}; 1) \ = \ 1 \text{ for } |\underline{m}| = 0$$

$$G(0; \underline{m}; i) \ = \ 0 \text{ for } |\underline{m}| > 0 \ . \tag{3.29}$$

By iteration of (3.26), all functions can be determined.

We briefly discuss two examples to illustrate how the Eqs. (3.26) work. Let us assume $N = 2$. All zero order functions $G(\ell; (), 1)$ are equal to 1. Since there is no breakup of (), as would be required by the sums on the right hand side of Eqs. (3.26), the right hand sides vanish identically, whence $G(\ell; (); 1) = 1$ for all values of ℓ.

The first order function $G(\ell; (1); 2)$ is given by

$$\frac{\partial}{\partial \ell} G(\ell; (\underbrace{1}_{m_l}); 2) = \text{sgn}\left[M((1))\right] F(\ell; (1)) \cdot G(\ell; (); 1)$$

$$= e^{-\ell} \cdot 1 , \tag{3.30}$$

where $F(\ell; (1)) = e^{-\ell}$ is taken from Eq. (3.12). With the initial condition $G(0; (1); 2) = 0$ from (3.29) the differential equation (3.30) yields

$$G(\ell; (1); 2) = 1 - e^{-\ell} \xrightarrow[\ell \to \infty]{} 1 . \tag{3.31}$$

As a second example we consider a second order function where we can use the above result

$$\frac{\partial}{\partial \ell} \quad G(\ell; (\underbrace{-2, 1}_{m_l}); 3) =$$

$$\text{sgn}\left[M((-2, 1))\right] F(\ell; (-2, 1)) G(\ell; (), 1)$$

$$+ \text{sgn}\left[M((-2))\right] F(\ell; (-2)) G(\ell; (1), 2)$$

$$= -\left(e^{-3\ell} - e^{-\ell}\right) \cdot 1 - e^{-2\ell} \cdot \left(1 - e^{-\ell}\right)$$

$$= e^{-\ell} - e^{-2\ell} . \tag{3.32}$$

The results for the functions $F(\ell; (-2, 1))$ and $F(\ell; (-2))$ are taken from the Eqs. (3.14) and (3.12) respectively. Integrating the result (3.32) using the initial condition (3.29) leads to

$$G(\ell; (-2, 1); 3) = -e^{-\ell} + \tfrac{1}{2} e^{-2\ell} + 1 - \tfrac{1}{2} \xrightarrow[\ell \to \infty]{} \tfrac{1}{2}. \tag{3.33}$$

This kind of calculation carries forward to higher orders. The functions G – like the functions F – are sums of simple monomials $(p/q)\ell^i \exp(-2\mu\ell)$, where $p, q, i, (\mu > 0)$ are integers.

In analogy to Eqs. (3.16) for F two symmetry relations hold for G. With $\underline{m} = (m_1, \ldots, m_k)$ they read

$$G(\ell; \underline{m}; i) = G(\ell; (-m_k, \ldots, -m_1); k - i + 2) \tag{3.34}$$

$$G(\ell; \underline{m}; i) = G(\ell; (-m_1, \ldots, -m_k); i)(-1)^k \tag{3.35}$$

as can be shown by induction. The first symmetry (3.34) holds if $\mathcal{O}$ is hermitian. Unfortunately, there is no equivalence to Eq. (3.17) so that a possible initial block-band structure in $\mathcal{O}(x; 0)$ is generically lost in the course of the transformation, i.e. for $\ell > 0$.

In the limit $\ell \to \infty$ the coefficients $\tilde{C}(\underline{m}; i) := G(\infty; \underline{m}; i) \in \mathbb{Q}$ are obtained as rational numbers. So we retrieve finally

$$\mathcal{O}_{\text{eff}}(x) = \sum_{k=0}^{\infty} x^k \sum_{i=1}^{k+1} \sum_{|\underline{m}|=k} \tilde{C}(\underline{m}; i)\mathcal{O}(\underline{m}; i) \tag{3.36}$$

similar to Eq. (3.18). The leading coefficients $\tilde{C}(\underline{m}; i)$ in this operator expansions for $N = 2$ are given in appendix B. All calculated coefficients can be found on our websites [62]. Note that $\mathcal{O}_{\text{eff}}$ is *not* a particle-conserving quantity as is obvious from the fact that the sum over $|\underline{m}|$ is not restricted to $M(\underline{m}) = 0$. In order to see the net effect of $\mathcal{O}_{\text{eff}}(x)$ on the number of particles explicitly it is helpful to split the bare operator according to $\mathcal{O} = \sum_{n=-N'}^{N'} T'_n$, where T'_n increments (or decrements, if $n < 0$) the number of particles by n: $[Q, T'_n] = nT'_n$.

The difference between the bare initial observable $\mathcal{O}$ and the representation (3.36) must be viewed as vertex correction which comes into play since the bare initial excitations are not the true eigen-excitations of the interacting system. In fact, as discussed for the effective Hamiltonian, the excitations (particles) injected by $\mathcal{O}_{\text{eff}}$, are subject to Hamiltonian dynamics, as is clear from the definition of the processes $\mathcal{O}(\underline{m}; i)$ in Eq. (3.22). Again, the *true* excitations are dressed particles, which the effective operators provide by a cloud of additional virtual excitations taking place in a vicinity (perturbation order) of the point of injection.

We would like to stress that the formalism presented introduces the notions of n-particle irreducibility, vertex correction and so on *without* starting from the limit of *non-interacting* conventional particles such as bosons or fermions.

Evaluation of $\mathcal{O}_{\text{eff}}$

The evaluation of $\mathcal{O}_{\text{eff}}$ can again be done by calculating its action on real space states, for which we need to specify the number of particles and their positions on the lattice only. For the action on the ground state we find

$$\mathcal{O}_{\text{eff}}|0\rangle = (\mathcal{O}_{0,0} + \mathcal{O}_{1,0} + \mathcal{O}_{2,0} + \ldots)|0\rangle$$

$$= const. + \sum_i w_i|i\rangle + \sum_{i_1,i_2} w_{i_1,i_2}|i_1, i_2\rangle + \ldots , \tag{3.37}$$

where the amplitudes w are the thermodynamic amplitudes. No subtractions are necessary (cf. section 2.3.1).

3.3. Effective Lattice

In this short section we introduce the effective lattice Γ_{eff} on which the effective operators act. A simple spin model is used to show, that Γ_{eff} may differ from the original lattice Γ used to define the initial problem on. The illustration remains on the level of the Hamiltonian. A generalisation to observables is straightforward.

We consider the dimerized spin chain depicted in Fig. 3.2

$$H = J \sum_{i=1}^{2N} (1 + \delta(-1)^i) S_i S_{i+1}$$

$$= U + xV = \tilde{J} \sum_{j=1}^{N} S_{2j} S_{2j+1} + x\tilde{J} \sum_{j=1}^{N} S_{2j} S_{2j-1} \ , \tag{3.38}$$

where we used $\tilde{J} = J(1 + \delta)$ and $x = (1 - \delta)/(1 + \delta)$. The summation index i counts the sites in the original lattice Γ, depicted as small black circles in Fig. 3.2, while j counts the dimers, i.e. the sites of the effective lattice Γ_{eff}, depicted as big grey circles. The ground state of the fully dimerized system,
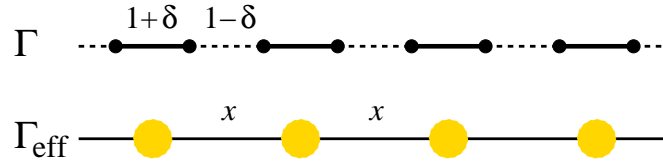
Figure 3.2.: A simple example to illustrate the difference between the original lattice Γ, on which the initial Hamiltonian H is defined, and the effective lattice Γ_{eff} derived from Γ. Small black circles denote the sites of Γ, on which we consider spin entities to be defined. Two sites connected by a solid line are referred to as dimer. The sites of Γ_{eff} are denoted by big yellow (grey) circles. They resume the dimers in the original lattice. It suffices to consider Γ_{eff} to calculate the action of the effective Hamiltonian H_{eff}.

i.e. U, is given by singlets on all dimers. An elementary excitation of U, the quasi-particle here, is a single triplet on one of the dimers, which is to say on one of the sites of Γ_{eff}. Thus, U has an equidistant spectrum and, barring a constant factor, counts the number of quasi-particles – condition (A) at the

beginning of this chapter is fulfilled. It is easily verified that V meets condition (B) with $N = 2$ (see Ref. [57]). We can thus use the effective Hamiltonian H_{eff} as derived in section 3.1.

The effective Hamiltonian H_{eff} conserves the number of triplets. The important point is that H_{eff} engenders a hopping of these triplets from dimer to dimer, i.e. from site to site in Γ_{eff}. In other words, it suffices to study the action of H_{eff} on Γ_{eff}, which comprises only half of the number of sites of the original lattice Γ. From know on it is understood that the action of H_{eff} is evaluated on the corresponding effective lattice Γ_{eff}.

3.4. Translational Invariance

In section 3.1 we derived an effective Hamiltonian H_{eff} which is block diagonal (to the calculated order) with respect to the number of particles. A sketch of the situation is depicted in Fig. 3.1. In this section we elaborate on the one- and two-particle block. They can be simplified considerably, if the model under inspection exhibits translational invariance. In this case it is advantageous to introduce a momentum basis. It is the objective of the first subsection to calculate the matrix representing the one- and two-particle blocks of H_{eff} in this basis. The structure of the corresponding one- and two-particle matrices of $\mathcal{O}_{\text{eff}}$ is inspected in the second subsection. The results obtained are important for the concrete application presented in chapter 6.

With respect to this application we assume the quasi-particles for each site of Γ_{eff} to be triplets t^i, where $i \in \{-1, 0, 1\}$ denotes the z-component, defined above a singlet (s) ground state (triplet-vacuum). The sites of Γ_{eff} can be considered to be dimers, just as illustrated in the preceding section (see also Fig. 3.2). We introduce the term *triplon* to denote the *elementary triplets* defined for the dimers. All quantities associated with with these elementary triplets will be called triplon quantities from now on.

3.4.1. Hamiltonian-Matrix

We consider the effective Hamiltonian H_{eff}, acting on a lattice Γ_{eff}, to be invariant under translations of Γ_{eff}. By $|\mathbf{r}\rangle$ we denote the state where one triplon is located at the site $\mathbf{r}$ of Γ_{eff}, while all other sites are in the singlet state. For the case of two triplons present we introduce the states $|\mathbf{r}, \mathbf{r}'\rangle^{S,m}$, with one triplon at site $\mathbf{r}$ and another at site $\mathbf{r}'$. Here S is the total spin and m is the S^z component of the two-triplon state. For the rest of this section we assume the effective Hamiltonian to conserve S and m.

It will be helpful to additionally consider the two-triplon states $|S, m\rangle$, *neglecting* the actual position of the triplons. Tab. 3.1 summarises all states $|S, m\rangle$ that can be constructed for zero, one and two triplons.

S	m	$|S, m\rangle$, 0 triplon
0	0	$|s, s\rangle$
S	m	$|S, m\rangle$, 1 triplon
1	-1	$|s, t^{-1}\rangle$
1	0	$|s, t^0\rangle$
1	-1	$|s, t^1\rangle$
S	m	$|S, m\rangle$, 2 triplons
2	2	$|t^1, t^1\rangle$
2	1	$1/\sqrt{2}(|t^0, t^1\rangle + |t^1, t^0\rangle)$
2	0	$1/\sqrt{6}(|t^{-1}, t^1\rangle + 2|t^0, t^0\rangle + |t^1, t^{-1}\rangle)$
2	-1	$1/\sqrt{2}(|t^{-1}, t^0\rangle + |t^0, t^{-1}\rangle)$
2	-2	$|t^{-1}, t^{-1}\rangle$
1	1	$1/\sqrt{2}(|t^1, t^0\rangle - |t^0, t^1\rangle)$
1	0	$1/\sqrt{2}(|t^1, t^{-1}\rangle - |t^{-1}, t^1\rangle)$
1	-1	$1/\sqrt{2}(|t^0, t^{-1}\rangle - |t^{-1}, t^0\rangle)$
0	0	$1/\sqrt{3}(|t^0, t^0\rangle - |t^1, t^{-1}\rangle - |t^{-1}, t^1\rangle)$

Table 3.1.: The $|S, m\rangle$ states. The notation is a short form of the tensor product state of any two sites situated somewhere in Γ_{eff}.

We will see, that the simple structure of H_{eff} in the momentum-basis is mainly due to the decomposition (see section 2.2.1)

$$H_{\text{eff}} = H_0 + H_1 + H_2 + \dots \,, \tag{3.39}$$

and the fact that H_{eff}, and thus all H_n, conserve the number quasi-particles (here triplons).

One-Particle Sector

The case of one triplon present is particularly simple to treat. We introduce the momentum states

$$|\mathbf{k}\rangle = \frac{1}{\sqrt{N}} \sum_{\mathbf{r}} e^{i\mathbf{k}\mathbf{r}} |\mathbf{r}\rangle \,, \tag{3.40}$$

where N is the total number of sites in Γ_{eff}. Since only one triplon is present in the states $|\mathbf{k}\rangle$ we can measure the ground state energy E_0 with H_0 or the

one-triplon energy with H_1. We focus on the latter. Since H_1 conserves the number of triplons we have

$$H_1|\mathbf{r}\rangle = \sum_{\mathbf{d}} t_{\mathbf{d}}|\mathbf{r}+\mathbf{d}\rangle \ , \qquad (3.41)$$

where we use the thermodynamic one-triplon hopping amplitudes $t_{\mathbf{r}}$ defined in section 2.2.1. They are calculated perturbatively to some maximum order by means of the effective Hamiltonian H_{eff} (cf. Eq. (3.18)). They are thus given by polynomials in x with rational coefficients. One index suffices to denote a hopping amplitude unambiguously due to the translation invariance. Furthermore, since the original Hamiltonian was considered to act on a finite number of neighbouring sites, the triplon can move a finite distance for a finite order only. Thus, the sum over $\mathbf{d}$ is restricted in a way that depends on the geometry of the problem. Calculating the action of H_1 on the states $|\mathbf{k}\rangle$ yields

$$H_1|\mathbf{k}\rangle = \frac{1}{\sqrt{N}}\sum_{\mathbf{r},\mathbf{d}} e^{i\mathbf{k}\mathbf{r}} t_{\mathbf{d}}|\mathbf{r}+\mathbf{d}\rangle \qquad (3.42)$$

$$= \frac{1}{\sqrt{N}}\sum_{\mathbf{r},\mathbf{d}} e^{i\mathbf{k}(\mathbf{r}-\mathbf{d})} t_{\mathbf{d}}|\mathbf{r}\rangle \qquad (3.43)$$

$$= \underbrace{\sum_{\mathbf{d}} e^{-i\mathbf{k}\mathbf{d}} t_{\mathbf{d}}}_{\omega(\mathbf{k};x)} \underbrace{\frac{1}{\sqrt{N}}\sum_{\mathbf{r}} e^{i\mathbf{k}\mathbf{r}}|\mathbf{r}\rangle}_{|\mathbf{k}\rangle} \ . \qquad (3.44)$$

If H_{eff} exhibits an additional inversion symmetry about points in Γ_{eff} such that $t_{\mathbf{r}} = t_{-\mathbf{r}}$ the matrix elements of H_1 in the $\{|\mathbf{k}\rangle\}$-basis are real. We end up with

$$\omega(\mathbf{k};x) = \langle\mathbf{k}|H_1(x)|\mathbf{k}\rangle = t_{\mathbf{0}}(x) + 2\sum_{\mathbf{d}>0} t_{\mathbf{d}}(x)\cos(\mathbf{d}\mathbf{k}) \ . \qquad (3.45)$$

A suitable definition of $\mathbf{d}>0$ will be given in the next section (see Eq. (3.48)). Thus, for fixed $\mathbf{k}$ the action of the one-triplon part H_1 of H_{eff} is given as a polynomial in x for $\omega(\mathbf{k})$ in the one-triplon sector.

Note that we calculate the action of $H_{\text{eff}} - H_0 = H_1$ on the one-triplon momentum states and not the action of $H_0 + H_1$ to obtain the one-triplon dispersion. This is because an actual experiment could also measure the energy difference from the ground state energy only.

Two-Particle Sector

The case of two triplons present is more involved. It will be convenient to work in the centre of mass reference frame, where we write

$$|\mathbf{r}, \mathbf{r}'\rangle \longrightarrow |\mathbf{r}, \mathbf{r} + \mathbf{d}\rangle \ , \tag{3.46}$$

with $\mathbf{d}$ denoting the distance between the two triplons. Translational invariance of H_{eff} implies the conservation of *total* crystal momentum, which we shall denote by $\mathbf{K}$. Note that only $\mathbf{K}$, the Fourier transformed of $\mathbf{r}$, is conserved. The relative momentum $\mathbf{q}$, the Fourier transformed of $\mathbf{d}$, will not be conserved in general. In fact, the remaining degree of freedom $\mathbf{q}$ generically leads to the formation of a two-particle continuum. We formally distinguish the total momentum $\mathbf{K}$ for two triplons present from the one-triplon momentum $\mathbf{k}$ of the last subsection.

The two-triplon momentum states can be defined according to

$$|\mathbf{K}, \mathbf{d}\rangle^S = \frac{1}{\sqrt{N}} \sum_{\mathbf{r}} e^{i\mathbf{K}(\mathbf{r}+\mathbf{d}/2)} |\mathbf{r}, \mathbf{r} + \mathbf{d}\rangle^S \ . \tag{3.47}$$

Note that, if H_{eff} conserves the total spin S, the triplon-exchange parity is fixed and we have $|\mathbf{r}, \mathbf{r} + \mathbf{d}\rangle^S = (-1)^S |\mathbf{r} + \mathbf{d}, \mathbf{r}\rangle^S$ (see also Tab. 3.1). Thus, we should rather consider only one half of all possible distances $\mathbf{d}$.[1] In one dimension we can most conveniently use the restriction $d > 0$. A suitable generalisation to two dimensions is given by

$$\mathbf{d} = (d_1, d_2) > 0, \quad \text{iff } (d_1 > 0) \text{ or } (d_1 = 0 \text{ and } d_2 > 0) \tag{3.48}$$

(see also Fig. 6.14 on page 117). For the rest of this section one might always think of a suitable separation if we write $\mathbf{d} > 0$.

The fixed parity with respect to exchange translates to the momentum

---

[1] If we were to allow all distances $\mathbf{d}$, the basis $\{|\mathbf{r}, \mathbf{d}\rangle\}$ would be over-complete. The quantum mechanical indistinguishability of the triplons does not allow to specify which of the two triplons is the one that is say left to the other one or vice versa.

states according to

$$
\begin{aligned}
|\mathbf{K}, \mathbf{d}\rangle^S &= \frac{1}{\sqrt{N}} \sum_{\mathbf{r}} e^{i\mathbf{K}(\mathbf{r}+\mathbf{d}/2)} |\mathbf{r}, \mathbf{r}+\mathbf{d}\rangle^S \\
&= (-1)^S \frac{1}{\sqrt{N}} \sum_{\mathbf{r}} e^{i\mathbf{K}(\mathbf{r}+\mathbf{d}/2)} |\mathbf{r}+\mathbf{d}, \mathbf{r}\rangle^S \\
&\stackrel{\mathbf{r}\to\mathbf{r}+\mathbf{d}}{=} (-1)^S \frac{1}{\sqrt{N}} \sum_{\mathbf{r}} e^{i\mathbf{K}(\mathbf{r}-\mathbf{d}/2)} |\mathbf{r}, \mathbf{r}-\mathbf{d}\rangle^S \\
&= (-1)^S |\mathbf{K}, -\mathbf{d}\rangle^S ,
\end{aligned}
\tag{3.49}
$$

where we omitted the magnetic quantum number m for clarity. We will also do so for the rest of the section.

For two triplons present we can measure the ground state energy (H_0), the pure one-triplon energies (H_1) and the pure two-triplon interaction energies (H_2). The action of H_0 on the two particle momentum states is trivial

$$
H_0 |\mathbf{K}, \mathbf{d}\rangle = E_0 |\mathbf{K}, \mathbf{d}\rangle , \tag{3.50}
$$

where E_0 is the ground state energy. We thus start by analysing how H_1 acts on $|\mathbf{K}, \mathbf{d}\rangle^S$ and consider H_2 thereafter.

We use the fact that H_1 only shifts triplons, i.e. here

$$
H_1 |\mathbf{r}, \mathbf{r}+\mathbf{d}\rangle^S = \sum_{\mathbf{d}'} t_{\mathbf{d}'} \left[|\mathbf{r}+\mathbf{d}', \mathbf{r}+\mathbf{d}\rangle^S + |\mathbf{r}, \mathbf{r}+\mathbf{d}+\mathbf{d}'\rangle^S \right] . \tag{3.51}
$$

Note that only one triplon can be moved at a time. Additionally assuming inversion symmetry, the action of H_1 on $|\mathbf{K}, \mathbf{d}\rangle^S$ is given by

$$
H_1 |\mathbf{K}, \mathbf{d}\rangle^S = 2 \sum_{\substack{\mathbf{d}' \\ \mathbf{d}' \neq \mathbf{d}}} t_{\mathbf{d}'} \cos\left(\mathbf{K}\frac{\mathbf{d}'}{2}\right) [\operatorname{sgn}(\mathbf{d}-\mathbf{d}')]^S |\mathbf{K}, |\mathbf{d}-\mathbf{d}'|\rangle^S . \tag{3.52}
$$

Since we restricted $\mathbf{d} > 0$ the signum function and the absolute value $|\mathbf{d} - \mathbf{d}'|$ (see Eq. (3.48) for the definition of $\mathbf{d} > 0$) enter the result. The full calculation can be found in appendix C. Note that the matrix elements of H_1 are real in the basis $\{|\mathbf{K}, \mathbf{d}\rangle\}$ due to the assumed inversion symmetry.

For fixed $\mathbf{K}$ we find H_1 to be a semi-infinite band matrix in the relative distance $\mathbf{d}$. Independent of how large the initial-distance $\mathbf{d} > 0$ between the two triplons is, H_1 will produce states where the two triplons are pushed apart or pushed together by a maximum amount $\mathbf{d}_{\max}$, which depends on the order

to which we calculated the hopping amplitudes $t_{\mathbf{d}'}$. (Recall, that the sum over $\mathbf{d}'$ is finite for finite perturbation order.)

As soon as the initial distance $\mathbf{d}$ is larger than $|\mathbf{d}_{\mathrm{max}}|$, H_1 continues to produce the same matrix elements on and on for all $\mathbf{d} > |\mathbf{d}_{\mathrm{max}}|$. The situation is sketched in Fig. 3.3. If the initial distance is smaller than $|\mathbf{d}_{\mathrm{max}}|$, H_1 generates states with negative relative distances, which have to be inverted and then added to the states with a positive relative distance. These states can be found in the head of the matrix (see Fig. 3.3). The tail of the matrix, i.e. the matrix elements between states with $\mathbf{d} > |\mathbf{d}_{\mathrm{max}}|$, is build up from identical raws, since here no negative relative distances are produces. These identical raws are depicted as solid lines in Fig. 3.3. In conclusion, the matrix representing H_1 in the chosen basis for fixed K is a semi-infinite band-matrix with a repeated pattern in the tail. The matrix H_1 comprises the thermodynamic one-triplon dynamics in the two-triplon sector to the given order.

Let us turn to H_2. Now both of the triplons can be moved at the same time. Consider the following example. Let the initial state be $|\mathbf{r}, \mathbf{r}+\mathbf{d}\rangle^S$ which becomes $|\mathbf{r}'', \mathbf{r}'' + \mathbf{d}'\rangle^S$ under the action of H_2 with amplitude $t^S_{\mathbf{r},\mathbf{r}+\mathbf{d};\mathbf{r}'',\mathbf{r}''+\mathbf{d}'}$. Since Γ_{eff} is translational invariant we can shift the whole process such that $\mathbf{r} = \mathbf{0}$

$$|\mathbf{r}, \mathbf{r} + \mathbf{d}\rangle^S \xrightarrow{H_2} |\mathbf{r}'', \mathbf{r}'' + \mathbf{d}'\rangle^S \text{ with amplitude } t^S_{\mathbf{r},\mathbf{r}+\mathbf{d};\mathbf{r}'',\mathbf{r}''+\mathbf{d}'}$$

is equivalent to

$$|\mathbf{0}, \mathbf{d}\rangle^S \xrightarrow{H_2} |\mathbf{r}'' - \mathbf{r}, \mathbf{r}'' - \mathbf{r} + \mathbf{d}'\rangle^S$$
$$= \quad |\mathbf{r}', \mathbf{r}' + \mathbf{d}'\rangle^S \text{ with amplitude } t^S_{\mathbf{d};\mathbf{r}',\mathbf{d}'} \, . \tag{3.53}$$

Three indices suffice to label the corresponding hopping amplitude unambiguously. In contrast to the one-triplon amplitudes, the two-triplon amplitudes can have differing total spin S and depend on it. Thus we write

$$H_2|\mathbf{r}, \mathbf{r} + \mathbf{d}\rangle^S = \sum_{\mathbf{r}',\mathbf{d}'} t^S_{\mathbf{d};\mathbf{r}',\mathbf{d}'}|\mathbf{r} + \mathbf{r}', \mathbf{r} + \mathbf{r}' + \mathbf{d}'\rangle^S \, . \tag{3.54}$$

The thermodynamic amplitudes $t^S_{\mathbf{d};\mathbf{r}',\mathbf{d}'}$ are again calculated by means of the effective Hamiltonian H_{eff} and are given as polynomials in x with rational coefficients. We proceed and calculate the action of H_2 on the states $|\mathbf{K}, \mathbf{d}\rangle^S$. We again exploit translational and inversion symmetry[2] and the fact, that H_2

---

[2] It might be necessary, that the inversion symmetry for H_{eff} also holds for points $\notin \Gamma_{\mathrm{eff}}$. An additional inversion symmetry about the points of the lattice with primitive vectors $\mathbf{a}/2$, $\mathbf{b}/2$, $\mathbf{c}/2$, ..., if $\mathbf{a}$, $\mathbf{b}$, $\mathbf{c}$, ... are the primitive vectors of Γ_{eff}, might be necessary.

conserves the number of triplons. The full calculation is more involved and can be found in appendix C. The result reads

$$^S\langle \mathbf{K}, \mathbf{d}'|H_2|\mathbf{K}, \mathbf{d}\rangle^S = t^S_{\mathbf{d};(\mathbf{d}-\mathbf{d}')/2,\mathbf{d}'}$$

$$+ 2 \sum_{\mathbf{r}'>(\mathbf{d}-\mathbf{d}')/2} t^S_{\mathbf{d};\mathbf{r}',\mathbf{d}'} \cos\left[\mathbf{K}\left(\mathbf{r}' - \frac{\mathbf{d}-\mathbf{d}'}{2}\right)\right] . \qquad (3.55)$$

Note that the sum runs over $\mathbf{r}' \in \mathbb{Z}$ only. Again, all matrix elements are real in the basis $\{|\mathbf{K}, \mathbf{d}\}$ due to the assumed inversion symmetry.

The sum over $\mathbf{r}'$ is finite because of the finite maximum perturbation order. Thus, in contrast to H_1 the matrix representing H_2 in $\{|\mathbf{K}, \mathbf{d}\}$ for fixed $\mathbf{K}$ is of finite dimension. Fig. 3.3 sketches the situation. The sum of the two matrices H_1 and H_2 comprises the complete two-triplon dynamics.

The constructed picture is physically justified. At large distances $\mathbf{d}$ the two-triplon dynamics is governed by independent one-triplon hopping, which is represented by the infinite tail of H_1 when $\mathbf{d}$ is the only remaining quantum number. At smaller distances an additional two-particle interaction occurs.
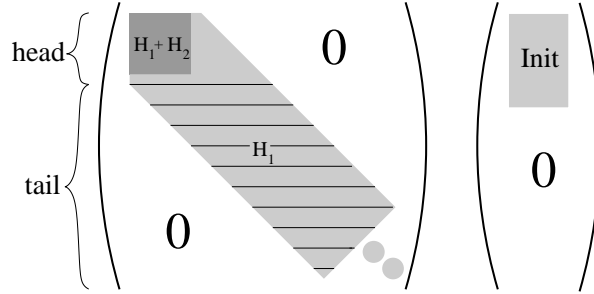
Figure 3.3.: The left part of the figure schematically shows the matrix representation of H_1 and H_2 in the two-triplon $\{|\mathbf{K}, \mathbf{d}\rangle\}$ basis for fixed $\mathbf{K}$. The matrix H_1 has elements in the whole grey area, while H_2 has elements in the dark grey area only, when the perturbation is terminated at some maximum order. The sum of H_1 and H_2 represents H_{eff} in the two-triplon sector to the given order. The horizontal lines in H_1 indicate the fact, that H_1 has a repeated pattern in the tail. Each line is identical to the other lines. The right part shows the initial vector $|\text{Init}\rangle = \mathcal{O}_{2,0}|0\rangle$. The effective Green's function $\mathcal{G}$ is calculated by tridiagonalising the Hamilton matrix with the initial vector $|\text{Init}\rangle$ leading to a continued fraction. More information is given in chapter 4.

This is captured by the finite matrix H_2 in $\mathbf{d}$. Finally, the sum $H_1 + H_2$ gives the combined effect of one-triplon hopping and two-triplon interaction. For the model, which we consider in the application chapter, we can show that the interaction amplitudes $\langle K, d|H_2|K, d\rangle$ drop rapidly for larger distances, so that the truncation at a certain $|\mathbf{d}|$ is justified (see Tab. 6.2 on page 118).

3.4.2. Matrix of the Observable

The effective Hamiltonian H_{eff} acts on each site of the full effective lattice Γ_{eff}. In this sense H_{eff} is a *global* operator. The situation might be different for other observables. In many circumstances it is more convenient to model a specific measurement by a *local* observable in a first step. A local observable acts on a finite number of (neighbouring) sites in Γ_{eff} only. Since we focus on low temperature physics in this thesis we consider the decomposition (see section 2.3.1, Eq. (2.22))

$$\mathcal{O}_{\text{eff}}^{T=0} = \mathcal{O}_{0,0} + \mathcal{O}_{1,0} + \mathcal{O}_{2,0} + \mathcal{O}_{3,0} + \ldots \, . \tag{3.56}$$

While $\mathcal{O}_{0,0}$ is just a constant, the effect of the locally defined observable $\mathcal{O}_{1,0}$ acting on the triplon vacuum ground state $|0\rangle$ is to inject one triplon on site $\mathbf{r} \in \Gamma_{\text{eff}}$. The injected triplon can acquire an additional motion, since $\mathcal{O}_{\text{eff}}$ contains parts of H_{eff} (see Eq. (3.36) and text thereafter). We are thus led to define

$$\mathcal{O}_{1,0}(\mathbf{r})|0\rangle = \sum_{\mathbf{d}} w_{\mathbf{d}}|\mathbf{r} + \mathbf{d}\rangle \, , \tag{3.57}$$

where the thermodynamic hopping amplitudes $w_{\mathbf{d}}$ have been introduced in section 2.3.1. They are calculated by means of the effective observable $\mathcal{O}_{\text{eff}}$ and are thus given by polynomials in x with rational coefficients. The action of $\mathcal{O}_{2,0}$ on $|0\rangle$ is captured by

$$\mathcal{O}_{2,0}(\mathbf{r})|0\rangle = \sum_{\mathbf{d}',\mathbf{d}''} w_{\mathbf{d}',\mathbf{d}''}^{S}|\mathbf{r} + \mathbf{d}', \mathbf{r} + \mathbf{d}''\rangle^{S} \, , \tag{3.58}$$

where we have to take additional care of the total spin of the generated two-triplon states. Generally, the amplitudes w also depend on S. The amplitudes $w_{\mathbf{d}',\mathbf{d}''}^{S}$ are again calculated from $\mathcal{O}_{\text{eff}}$. They are rational polynomials in x, too.

If we assume translational invariance, the observables, defined by their local action in *real-space*, have a *momentum-space* representation

$$\mathcal{O}_{\mu,0}(\mathbf{K}) = \frac{1}{\sqrt{N}} \sum_{\mathbf{r}} e^{i\mathbf{K}\mathbf{r}} \mathcal{O}_{\mu,0}(\mathbf{r}) \, . \tag{3.59}$$

This identity is defined for all observables on the right hand site of the decomposition (3.56). In the case of one triplon being injected we identify $\mathbf{K} = \mathbf{k}$ for the total momentum $\mathbf{K}$. We will frequently call the observables in their momentum-space representation *global observables* $\mathcal{O}_{\mu,0}(\mathbf{K})$ in contrast to the observables $\mathcal{O}_{\mu,0}(\mathbf{r})$ which are defined by their *local* action in real-space.

The one- and two-triplon cases are treated separately in the following two subsections.

One-Particle Space

The action of $\mathcal{O}_{1,0}(\mathbf{k})$ on the ground state is given by

$$\mathcal{O}_{1,0}(\mathbf{k})|0\rangle = \frac{1}{\sqrt{N}} \sum_{\mathbf{r},\mathbf{d}} e^{i\mathbf{k}\mathbf{r}} w_{\mathbf{d}} |\mathbf{r} + \mathbf{d}\rangle$$

$$= \sum_{\mathbf{d}} w_{\mathbf{d}} e^{-i\mathbf{k}\mathbf{d}} \frac{1}{\sqrt{N}} \sum_{\mathbf{r}} e^{i\mathbf{k}\mathbf{r}} |\mathbf{r}\rangle$$

$$= \sum_{\mathbf{d}} w_{\mathbf{d}} e^{-i\mathbf{k}\mathbf{d}} |\mathbf{k}\rangle \ . \tag{3.60}$$

A more compact notation can be introduced by

$$\mathcal{O}_{1,0}(\mathbf{k})|0\rangle = A_{\mathbf{k}}|\mathbf{k}\rangle \quad \text{with}$$

$$A_{\mathbf{k}} := \sum_{\mathbf{d}} w_{\mathbf{d}} e^{-i\mathbf{k}\mathbf{d}} \ . \tag{3.61}$$

If we further assume inversion symmetry about the point of injection $\mathbf{r}$, we have $w_{\mathbf{d}} = w_{-\mathbf{d}}$, which yields the real result

$$A_{\mathbf{k}} = w_{\mathbf{0}} + 2 \sum_{\mathbf{d}>0} w_{\mathbf{d}} \cos(\mathbf{k}\mathbf{d}) \ . \tag{3.62}$$

The sum over $\mathbf{d}$ is finite, if the perturbation is truncated at some finite order. Thus, the action of the effective observable on the ground state into the one-triplon subspace is captured by a polynomial in x with real coefficients for fixed $\mathbf{k}$.

Two-Particle Space

The corresponding calculation for the two-triplon injecting observable $\mathcal{O}_{2,0}$ is similar, but more involved, and can be found in appendix D. Here we confine ourselves to give the result

$$\mathcal{O}_{2,0}(\mathbf{K})|0\rangle = \sum_{\mathbf{r}',\mathbf{d}} w^S_{\mathbf{r}',\mathbf{r}'+\mathbf{d}} e^{-i\mathbf{K}(\mathbf{r}'+\mathbf{d}/2)} |\mathbf{K}, \mathbf{d}\rangle^S \ . \tag{3.63}$$

We can project on the resulting momentum states, which yields

$$A^S_{\mathbf{K},\mathbf{d}} = {}^S\langle \mathbf{K}, \mathbf{d}|\mathcal{O}_{2,0}(\mathbf{K})|0\rangle = \sum_{\mathbf{r}'} w^S_{\mathbf{r}',\mathbf{r}'+\mathbf{d}} e^{-i\mathbf{K}(\mathbf{r}'+\mathbf{d}/2)} \ . \tag{3.64}$$

If we assume inversion symmetry, we again obtain real results (calculation in appendix D)

$$A_{\mathbf{K},\mathbf{d}}^{S} = \sum_{\mathbf{r}'} w_{\mathbf{r}',\mathbf{r}'+\mathbf{d}}^{S} \cos[\mathbf{K}(\mathbf{r}' + \mathbf{d}/2)] \ . \tag{3.65}$$

We might also restrict $\mathbf{d} > 0$ now. For fixed $\mathbf{K}$ we find that $\mathcal{O}_{2,0}(\mathbf{K})|0\rangle$ is a vector with a finite number of non-zero components in the remaining quantum number $\mathbf{d}$ for finite perturbation order. All other components are zero. Its components are denoted by $A_{\mathbf{K},\mathbf{d}}$, which are polynomials in x with real coefficients. Fig. 3.3 depicts this vector on the right hand site. Non-vanishing components can be found in the grey shaded area (Init) only. The length of the depicted block depends on the perturbation order.

3.5. Implementation

This section is intended to present the basic ideas of implementing perturbative CUTs on a computer. The readers who are not interested in these details may skip the section.

To begin with, we note that the method naturally splits into two distinct steps. As was outlined in sections 3.1 and 3.2, the coefficients $C(\underline{m})$ and $\tilde{C}(\underline{m}; i)$, appearing in H_{eff} and $\mathcal{O}_{\text{eff}}$ respectively, are calculated by solving recursive differential equations. This first calculational step does not depend on the specific model under consideration. In this sense the coefficients can be applied universally. Their computer-aided calculation is described in the first subsection.

The second step is the evaluation of the action of the effective operators on the relevant states of the considered model. Since the implementation of this action follows the same pattern in all possible applications it will be useful to briefly sketch the fundamental ideas, which will be done in the second subsection.

In both cases we start by illustrating the procedure for the effective Hamilton operator. The implementations for effective observables will be obtained by suitable modifications.

3.5.1. Universal Coefficients

We begin by illustrating the computer implementation allowing the calculation of the coefficients $C(\underline{m})$ appearing in the series expansion of the effective

Hamiltonian (see Eq. (3.18))

$$H_{\text{eff}}(x) = U + \sum_{k=1}^{\infty} x^k \sum_{\substack{|\underline{m}|=k \\ M(\underline{m})=0}} C(\underline{m})T(\underline{m}) \ . \tag{3.66}$$

The $C(\underline{m})$ are the $\ell \to \infty$ limit values of the function $F(\ell, \underline{m})$ appearing in the *ansatz* for the ℓ-dependent Hamiltonian (see Eq. (3.2))

$$H(x; \ell) = U + \sum_{k=1}^{\infty} x^k \sum_{|\underline{m}|=k} F(\ell; \underline{m})T(\underline{m}) \ . \tag{3.67}$$

The functions F are calculated by solving the recursive differential Eqs. (3.7) or more conveniently by solving the equivalent Eqs. (3.11) for the functions $f(\ell; \underline{m})$

$$\frac{\partial}{\partial \ell} f(\ell; \underline{m}) = \sum_{\{\underline{m}_1, \underline{m}_2\}=\underline{m}} e^{(|M(\underline{m})|-|M(\underline{m}_1)|-|M(\underline{m}_2)|)l} \ .$$

$$[\text{sgn}(M(\underline{m}_1)) - \text{sgn}(M(\underline{m}_2))] \ f(\ell; \underline{m}_1) f(\ell; \underline{m}_2) \ . \tag{3.68}$$

Recall, that

$$F(\ell; \underline{m}) = \exp\left(-|M(\underline{m})|\ell\right) \ f(\ell; \underline{m}) \ . \tag{3.69}$$

In Fig. 3.4 we give a flow-diagram of the implementation of Eqs. (3.68). The algorithm starts by initialising the functions $f(\ell; \underline{m})$ of order $k = |\underline{m}| = 1$ according to the starting conditions (3.9). Recall that the functions F and therefore the functions f are sums of monomials with structure $(p/q)\ell^i \exp(-2\mu\ell)$, where $p, q, i, (\mu > 0)$ are integers. These integers can be stored in interlaced chains of suitable data-structures, each representing one of the monomials.

The flow-diagram is self-explanatory. Operations are enclosed in rectangles, control structures are denoted by elliptic symbols and loops can be followed by arrows. The outermost loop (step 2) through step 15)) controls the order k. Since all calculated functions f have to be stored in memory, a finite maximum order k will be reached depending on the memory capacity of the used computer system. Two GB RAM should suffice to calculate all $C(\underline{m})$ to 10th order for $N = 2$ and to 15th order for $N = 1$, where N is the maximum number of particles which can be created or destroyed by a single application of the perturbation part V of the initial Hamiltonian $H = U + xV$ (see also point (B) at the beginning of section 3.1).

For each order k there are numerous $\underline{m}$ fulfilling $|\underline{m}| = k$ and $|M(\underline{m})| \leq N$ (recall, that functions $f(\ell; \underline{m})$, with $|M(\underline{m})| > N$ are zero)). Let us assume

1) initialize $f(l;\underline{m})$, $|\underline{m}|=1$

2) order: $k=2$

3) generate list of all $\underline{m}^i$ with $|\underline{m}^i|=k$ and $|M(\underline{m}^i)| < N+1$

$Mk[n]:$ $Mk[0]=\underline{m}^1$
$Mk[1]=\underline{m}^2$
$\vdots$
$Mk[n_{max}(k)]=\underline{m}^{n_{max}(k)}$

4) $n = 0$

5) generate list of all breakups of $\underline{m}^n$

$B[b][2]:$ $B[0][0]=(\underline{m}^n_1)$
$B[0][1]=(\underline{m}^n_2, ... ,\underline{m}^n_k)$
$B[1][0]=(\underline{m}^n_1,\underline{m}^n_2)$
$\vdots$
$B[b_{max}(n)][1]=(\underline{m}^n_k)$

6) $b=0$

7) $f(l;Mk[n])=0$

8) $f(l;Mk[n])=f(l;Mk[n]) + [\ e^{(|M(Mk[n])|-|M(B[b][0])|-|M(B[b][1])|)l}$
$[sgn(M(B[b][0]))-sgn(M(B[b][1]))]$
$f(l;B[b][0])*f(l;B[b][1])\ ]$

9) if $b < b_{max}(n)$ ⟶ $b=b+1$

10) $f(l;Mk[n])=$ INTEGRATE $[\ f(l;Mk[n])\ ]$

11) if $|M(Mk[n])| = 0$

12) $C(Mk[n])=$ LIMIT $[\ f(l;Mk[n])\ ]$
$l -> \infty$

13) save $C(Mk[n])$ to disc

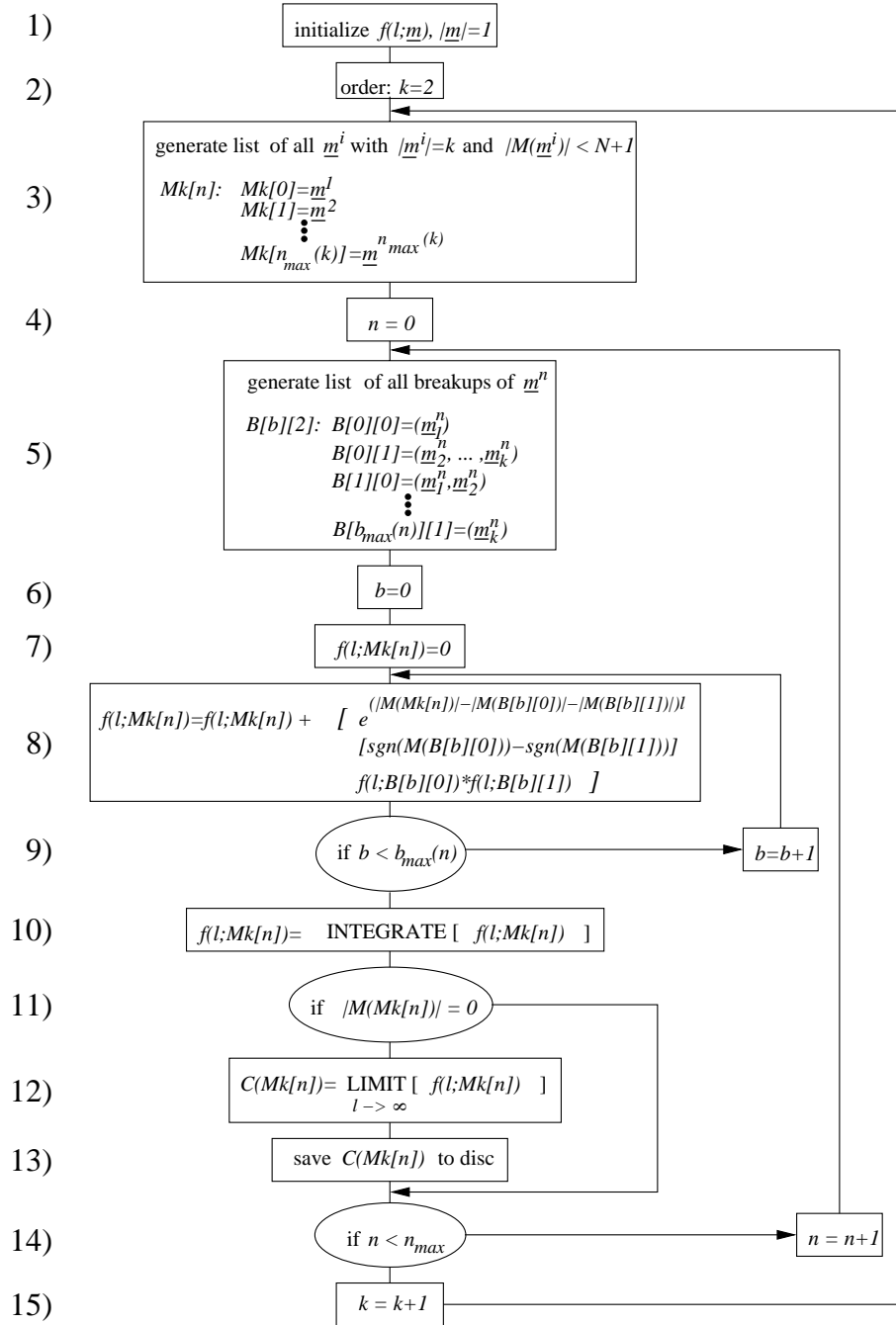14) if $n < n_{max}$ ⟶ $n = n+1$

15) $k = k+1$

Figure 3.4.: Flow-diagram: Implementation of the differential equations (3.11) allowing the computation of the coefficients in the operator series expansion of H_{eff}.

we have $n_{max}(k)$ of these $\underline{m}$ in order k. They are stored in the list $Mk[n]$ at step 3). The n-loop (step 4) through step 14)) controls the calculation of the functions $f(\ell; \underline{m})$. For each n, i.e. for each $\underline{m}$, the sum over all breakups is controlled by the b-loop (step 6) through step 9)). After the sum has been calculated the result is integrated (step 10)). If $|M(\underline{m})| = 0$ we additionally take the limit $\ell \to \infty$ in step 12) and save the resulting coefficient $C(\underline{m})$ to a file for later use (step 13)).

There are three different operations on the functions f to be implemented. The multiplication of functions f in step 8) can be easily transferred to the representing interlaced chains. The integration in step 10) is achieved by

$$\int_0^\ell d\ell' \ell'^i = \frac{1}{i+1} \ell^{i+1} \tag{3.70}$$

$$\int_0^\ell d\ell' \ell'^i e^{-2\mu\ell'} = \frac{i!}{2\mu} \left[\frac{1}{(2\mu)^i} - e^{-2\mu\ell} \sum_{j=0}^i \frac{\ell^j}{j!(2\mu)^{i-j}} \right] . \tag{3.71}$$

Finally, one has to calculate the limit $\ell \to \infty$ for those $f(\ell; \underline{m})$ with $|M(\underline{m})| = 0$ in step 12). Note that in this case one always has $\mu > 0$ in Eq. (3.71). Thus, taking the limit reduces to omitting the term proportional to $e^{-2\mu\ell}$ in Eq. (3.71).

The functions $G(\ell; \underline{m}; i)$, which upon taking the limit $\ell \to \infty$ ultimately yield the coefficients $\tilde{C}(\underline{m}; i)$ in the operator expansion of $\mathcal{O}_{\text{eff}}$

$$\mathcal{O}_{\text{eff}}(x) = \sum_{k=0}^\infty x^k \sum_{i=1}^{k+1} \sum_{|\underline{m}|=k} \tilde{C}(\underline{m}; i) \mathcal{O}(\underline{m}; i) \tag{3.72}$$

obey similar recursive differential equations (cf. Eq. (3.26)) and have the same monomial structure as the functions $F(\ell; \underline{m})$. Thus, only minor corrections of the given algorithm are necessary to calculate the $\tilde{C}(\underline{m}; i)$. We assume that the functions f or F have been calculated and that they are stored in RAM before the modified algorithm starts. The modifications will be addressed step by step.

- In step 3) we do not have the restriction $|M(\underline{m})| \leq N$ any more, since a possible band-diagonal structure in the initial observable might be lost in the course of the transformation (see section 3.2). However, we can exclude those $\underline{m}$, which lead to intermediate negative index-sums like $\underline{m} = (1, 1, -2, -1, 2)$, if we are interested in the action of $\mathcal{O}_{\text{eff}}$ on the ground state only. Although the process corresponding to this multi-index leads to the creation of one particle in the end, it intermediately

leads to the destruction of one-particle. Therefore, starting from the ground state, the particle vacuum, we can neglect the full process.

- Within the n-loop (step 4) through step 14)) we introduce yet another loop i just before step 5) controlling the left-right splitting of $\underline{m} = (\underline{m}_l, \underline{m}_r)$.

- Then, steps 5) through 9) are run twice. Once for the left part of the splitting, representing the operation of taking the first sum on the right hand side of Eq. (3.26) and once for the second sum. Thus, before we enter step 10), we have calculated two functions, which we denote by $G_l(\ell; i; Mk[n])$ and $G_r(\ell; i; Mk[n])$. They represent the two sums on the right hand side of Eq. (3.26). Steps 5) and 8) have to be modified accordingly: the breakups are different for step 5). The multiplications in step 8) are different according to Eq. (3.26). In step 8) the functions F computed beforehand enter.

- Before the integration in step 10) is performed, we have to add G_l and G_r to obtain the representation of the full right hand side of Eq. (3.26).

- The short-cut in step 11) does not hold anymore, since the effective observable does not conserve the number of particles. We thus have to store all $\tilde{C}(\underline{m}; i)$ to disc. The operation to take the limit in step 12) does not change.

- Before we re-enter the n-loop we increment the control-variable of the inserted i-loop to calculate the next splitting of the current $\underline{m} = Mk[n]$. The n-loop does not advance until all possible splittings i have been considered for the current $\underline{m}$.

Since the transformation leading to the effective observables does not conserve a possible simple initial structure and because of the extra splitting, the number of functions G exceeds the number of functions f in a given order k. Typically, the demand on memory capacity is more than doubled. (Recall, that we have to store the functions F in RAM, too). As a rule of thumb, one can calculate the coefficients $\tilde{C}(\underline{m}; i)$ to one or two orders less than the coefficients $C(\underline{m})$.

Since the calculations are done with integers, the algorithm is fast and exact. There are no numerical rounding errors. The prepared output file contains all multi-indices $\underline{m}$ with corresponding coefficients $C(\underline{m})$ for H_{eff}, and $\underline{m}$, i and $\tilde{C}(\underline{m}, i)$ for $\mathcal{O}_{\text{eff}}$. The coefficients are rational numbers. We store the denominator and the numerator as two separate integers. The output file serves as input in the next section.

3.5.2. Operator Action

We now turn to the implementation of the action of the effective Hamiltonian H_{eff} on some specific initial state $|\psi_{\text{init}}\rangle$ of the system. We will illustrate that a *symbolic* implementation is possible. Thus, the results of the algorithm depend analytically on all the parameters contained in the model under inspection.

As we have explained in detail in chapter 2, all calculations to finite order can be done on finite clusters of the thermodynamic lattice Γ_{eff}. For simplicity we assume, that cluster C suffices for our considerations. Since the original Hamiltonian $H = U + xV$ is a sum of local operators, acting only within a finite range of sites, we expect the operators T_n in the decomposition of V to be sums over local operators $\mathcal{T}(\nu)$, too. We write

$$V = \sum_{n=-N}^{N} T_n \ , \ \text{with } T_n = \sum_{\nu=1}^{\nu_{\text{max}}} \mathcal{T}_n(\nu) \ . \tag{3.73}$$

Here ν denotes a set of sites in C. For simplicity we assume that a single ν is a pair of adjacent sites (see also Fig. 3.5) and that we have ν_{max} different pairs on C. The sum in Eq. (3.73) runs over all adjacent pairs ν in C. A local operator $\mathcal{T}_n(\nu)$ creates (annihilates) n quasi-particles for $n > 0$ ($n < 0$) on the pair ν.

To ensure a transparent description we will use the example model depicted in Fig. 3.5. The model comprises two different kinds of bonds denoted by α
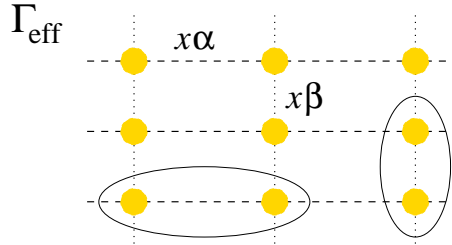

Figure 3.5.: An example of an effective lattice. The perturbation parameter is x. There are two different kinds of bonds distinguished by α and β. Excited states are described by quasi-particles located at the sites denoted by filled circles. They acquire dynamics due to the effective Hamiltonian $H = U + xV$. The *global* ladder operators $T_n = \sum_\nu \mathcal{T}_n(\nu)$ in the perturbation part $V = T_{-N} T_{-N+1} \dots T_N$ create, destroy or move particles in the lattice. Here we assume, that a single *local* operator $\mathcal{T}_n(\nu)$ acts on a pair ν of adjacent sites only. Two such pairs are depicted as ovals. The application of a single $\mathcal{T}_n$ operator on some state produces a new state which has to be multiplied by α or β.

and β. Two different pairs of adjacent sites are highlighted by ovals. The cluster C is a finite portion of the full lattice Γ_{eff}.

Let us start by implementing the action of the local operators $\mathcal{T}_n(\nu)$ on the states of the pair ν. We assume that each *site* $\gamma \in C$ can be in a variety of basis-states $|\phi_i^\gamma\rangle$. To reach high orders we need an efficient representation of these states. A possible way is to encode the states of each site γ by a set of bits

$$|\phi_1^\gamma\rangle = |00\ldots00|$$
$$|\phi_2^\gamma\rangle = |00\ldots01|$$
$$|\phi_3^\gamma\rangle = |00\ldots10|$$
$$\vdots \; . \tag{3.74}$$

The state of a pair $\nu = (\nu_1, \nu_2)$ is then given by two such bit-sets, i.e.

$$x = |\phi^\nu\rangle = |\phi^{\nu_1}, \phi^{\nu_2}\rangle = \underbrace{|01\ldots11|}_{\phi^{\nu_1}}\underbrace{|10\ldots01|}_{\phi^{\nu_2}} \in \mathbb{N} \; , \tag{3.75}$$

for instance. The action of $\mathcal{T}_n(\nu)$ on $x = |\phi^\nu\rangle$ is most conveniently captured by a matrix representing $\mathcal{T}_n$ in the basis spanned by all states of the pairs ν. As an example we assume that the pairs ν can be in four different states represented by the four integers x_j, $j = 1, \ldots, 4$. In this case Tab. 3.2 gives an example for a matrix representation of the local operator $\mathcal{T}_n$.

initial state of ν	final state of ν
x_1	x_2
x_2	$x_1 \oplus x_3$
x_3	$x_2 \oplus x_4$
x_4	x_3

Table 3.2.: Matrix representing the local operator $\mathcal{T}_n$ in the four dimensional basis spanned by all possible states of the pairs ν. The action of $\mathcal{T}_n$ on a pair can result in linear combinations of the four basis-states of ν. The operation of linearly combining basis-states is denoted by $\oplus$. It is important to understand, that this operation is *not* given by adding the integer values representing the basis-states.

We advance and show in which way one can implement the action of the locally acting operator $\mathcal{T}_n(\nu)$ on a basis-state $|\psi^i\rangle$ of the *full* cluster C

$$|\psi^i\rangle = \underbrace{|00\ldots01|}_{|\phi^1\rangle}\underbrace{|00\ldots10|}_{|\phi^2\rangle}\ldots\underbrace{|01\ldots11|}_{|\phi^{\nu_1}\rangle}\ldots\underbrace{|10\ldots01|}_{|\phi^{\nu_2}\rangle}\ldots\underbrace{|10\ldots11|}_{|\phi^L\rangle} \; . \tag{3.76}$$

Here L is the number of sites in C. First we need to extract the integer value x representing the state of the specific pair ν from $|\psi^i\rangle$. To this end we define the bit-mask

$$|\text{mask}^{\nu_{1/2}}\rangle = 0\ldots0 \underbrace{|11\ldots1|}_{\text{bits of } \nu_{1/2}} \overbrace{0\ldots0}^{n_{1/2} \text{ bits}} , \qquad (3.77)$$

with all bits set to zero except those representing the sites ν_1 or ν_2 of ν. With $|\gamma|$ denoting the number of bits necessary to represent the state of a single site $\gamma \in C$, x is given by

$$x = 2^{|\gamma|}x_1 + x_2 , \quad \text{with} \qquad (3.78)$$

$$x_{1/2} = \xrightarrow{n_{1/2}} \left(|\psi^i\rangle \text{ AND } |\text{mask}^{\nu_{1/2}}\rangle \right) . \qquad (3.79)$$

Arrows denote the operation of displacing all bits by the given number in the direction indicated, while zeros are filled in from the opposite site.

From Tab. 3.2 we deduce the action of $\mathcal{T}_n(\nu)$ on the state x, which leads to the final state y given by the right hand side of Tab. 3.2. The state y may be a linear combination of the basis-states of ν.

We finally need to embed the resulting state(s) y in the full cluster-state $|\psi^i\rangle$. This can be done be decomposing y in its individual components y_1 and y_2 representing the states of the individual sites ν_1 and ν_2 of ν respectively in analogy to Eq. (3.78)

$$y = 2^{|\gamma|}y_1 + y_2 . \qquad (3.80)$$

In a last step the bit-sets y_1 and y_2 have to be displaced to the positions representing the sites ν_1 and ν_2 in the full basis-state $|\psi^i\rangle$. The action of $\mathcal{T}_n(\nu)$ on $|\psi^i\rangle$ is thus given by

$$\mathcal{T}_n(\nu)|\psi^i\rangle = \left(|\psi^i\rangle \text{ AND } \neg|\text{mask}^{\nu_1}\rangle \text{ AND } \neg|\text{mask}^{\nu_1}\rangle \right)$$

$$\text{OR } \left(\xleftarrow{n_1} (y_1) \right) \text{ OR } \left(\xleftarrow{n_2} (y_2) \right) , \qquad (3.81)$$

where $\neg$ denotes the inversion of a bit-pattern ($0 \to 1$ and $1 \to 0$). If y is a linear combination the procedure has to be applied for each *pair* basis-state appearing in y. In this case $\mathcal{T}_n(\nu)|\psi^i\rangle$ leads to a linear combination of *cluster* basis-states.

We see that the actual eigen-states $|\psi\rangle$ of H_{eff} acting on C will be linear combinations

$$|\psi\rangle = \sum_i a_i|\psi^i\rangle . \qquad (3.82)$$

Thus, a representation of $|\psi\rangle$ is given by an interlaced chain of suitable data structures containing the states $|\psi^i\rangle$ and the prefactors a_i.

Now that we have explained how the action of a *local* operator $\mathcal{T}_n(\nu)$ can be implemented we advance and show how the action of the *full* operator $T_n = \sum_\nu \mathcal{T}_n(\nu)$ on some initial state $|\psi_{\text{in}}\rangle$ can be implemented. The state $|\psi_{\text{in}}\rangle$ can be a linear combination of cluster basis-states as indicated in Eq. (3.82).

To organise all possible pairs ν we most conveniently create a global list P of all pairs $\nu = (\nu_1^i, \nu_2^i)$, with $\nu_1^i, \nu_2^i \in C$ and $i = 1, \ldots, \nu_{\text{max}}$

$$P[\nu_{\text{max}}][2]: \quad P[0][0] = \nu_1^1$$

$$P[0][1] = \nu_2^1$$

$$P[1][0] = \nu_1^2$$

$$\vdots$$

$$P[\nu_{\text{max}} - 1][1] = \nu_2^{\nu_{\text{max}}} . \tag{3.83}$$

This list must be organised such that the pairs $\nu^i = (\nu_1^i, \nu_2^i)$ are *oriented* in the sense that ν_2^i is always to the right of or below ν_1^i for instance to avoid an over-counting of bonds (see Fig. 3.5). The list P can be customised to suit more complicated interactions.

The algorithm to calculate the action of a single T_n on some state $|\psi_{\text{in}}\rangle = \sum_i a_i |\psi^i\rangle$ is depicted in Fig. 3.6. The outer loop i (step 2) through step 7)) assures, that the action is calculated for each addend $a_i |\psi^i\rangle$. The inner loop m (step 3) through step 6)) represents the sum $T_n = \sum_\nu \mathcal{T}_n(\nu)$. The + in step 5) denotes the operation of concatenating two interlaced chains of the data structures needed to represent states of type $\sum_i a_i |\psi^i\rangle$ (see also Eq. (3.82) and text below).

Following these steps we see, that the resulting state $T_n |\psi_{\text{in}}\rangle$ is calculated as a new interlaced chain of basis states. In the final step 8) $|\psi_{\text{out}}\rangle$ is renamed in $|\psi_{\text{in}}\rangle$. The algorithm can be re-entered to start the calculation for the next T_n.

We can finally show how the action of the full effective Hamiltonian (3.18) can be implemented. Fig. 3.7 depicts the algorithm needed to calculate the matrix element $\langle\psi_{\text{final}}|H_{\text{eff}}|\psi_{\text{init}}\rangle$ for a given order k. If $|\psi_{\text{init}}\rangle$ is the state of one particle at a fixed site $\gamma_1 \in C$ and $|\psi_{\text{final}}\rangle$ the state of one particle at $\gamma_2 \in C$ for instance, the depicted algorithm can be used to calculated the amplitude for one particle hopping from site γ_1 to site γ_2 in order k.

In step 1) we initialise some variables and define the state $|\psi_{\text{final}}\rangle$. In step 2) the first multi-index $\underline{m}$ and its corresponding coefficient $C(\underline{m})$ are loaded
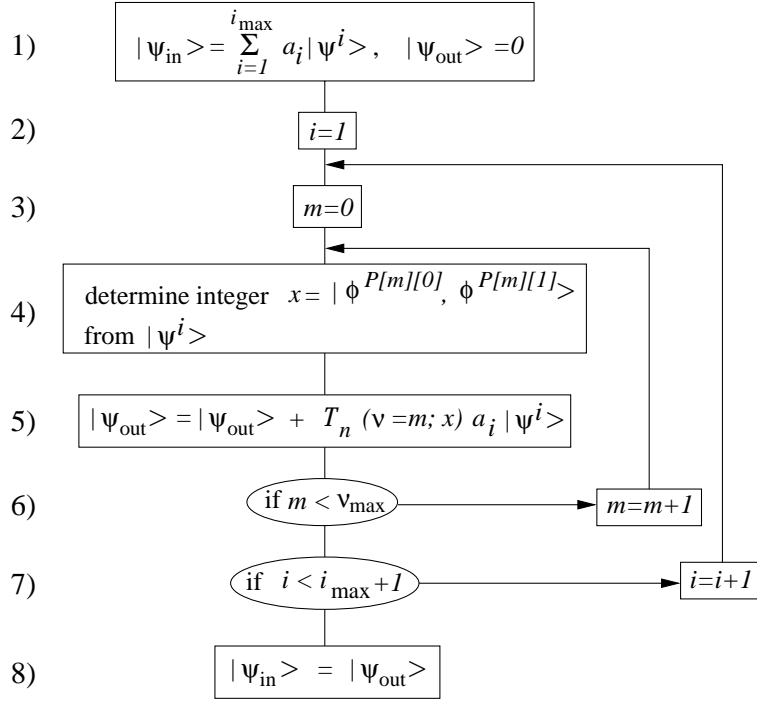
Figure 3.6.: Flow-diagram: Implementation of the action of a single operator T_n on some state $|\psi_{\text{in}}\rangle$ of C. The generated new state is denoted by $|\psi_{\text{out}}\rangle$.

from the file computed by the algorithm described in the preceding section. The outer loop is repeated until all multi-indices and coefficients of the given order have been considered. In step 4) we fix the initial state $|\psi_{\text{init}}\rangle$. The inner loop i (step 5) through step 7)) ensures that every single operator T_n of $T(\underline{m})$ is applied to $|\psi_{\text{init}}\rangle$ according to the current multi-index $\underline{m}$. After the full operator product $T(\underline{m})$ has acted on $|\psi_{\text{init}}\rangle$ the resulting state is multiplied by the corresponding rational coefficient $C(\underline{m})$ in step 8). Finally, we add the projection $\langle\psi_{\text{final}}|\psi_{\text{init}}\rangle$ to the current k^{th} order result.

After all $\underline{m}$ of the given order k have been considered, the full k^{th} order result can be transferred to a computer algebra programme such as MAPLE, where it is multiplied by x^k and stored. The algorithm then progresses to the next order calculating the $(k+1)^{\text{th}}$ result, which is again transferred to MAPLE where it is multiplied by x^{k+1}, added to the old result and so on. Thereby we obtain the one-particle hopping amplitudes or the two-particle interaction matrix elements as a polynomial in x,

Let us now turn to the issue of a *symbolic* implementation by using our example model depicted in Fig. 3.5 again. The action of a local operator $\mathcal{T}_n(\nu)$
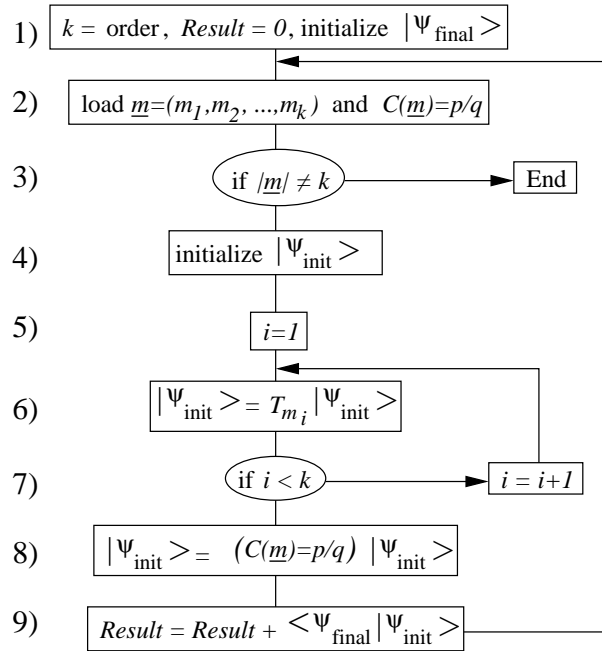
Figure 3.7.: Flow-diagram: This algorithm calculates the matrix element $\langle \psi_{\text{final}} | H_{\text{eff}} | \psi_{\text{init}} \rangle$ in order k.

to a cluster basis-state $|\psi^i\rangle$ leads to a new state, which has to be multiplied by α or β, if the specific pair ν is a horizontal or vertical pair respectively. The application of a single $T_n = \sum_{\nu} \mathcal{T}_n(\nu)$ to a cluster basis-state $|\psi^i\rangle$ produces a linear combination of basis-states, each multiplied by α or β. Applying a product $T(\underline{m}) = T_{m_1} \cdots T_{m_k}$ of k operators T_n to a cluster basis-state $|\psi^i\rangle$ leads to a linear combination of basis-states, each multiplied by a monomial $p\alpha^s\beta^t$ with $s + t = k$. The additional integer prefactor p is necessary, since a single cluster basis-state might have been produced several times with the same monomial $\alpha^s\beta^t$. Finally the coefficients $C(\underline{m})$ have to be multiplied. They are fractions of integers, such that a full cluster basis-state reads

$$a_i|\psi^i\rangle = \frac{p}{q}\alpha^s\beta^t|\psi^i\rangle \ . \tag{3.84}$$

Thus, a symbolic implementation is possible by using the data structure BAS_EL depicted in Fig. 3.8 to represent a single cluster basis-state. Linear combinations of basis-states are interlaced chains as indicated on the right side of Fig. 3.8. All calculations can be done with integers. Thus, the results are exact to the given order and hence analytical in the model parameters although the computer is used.

```
BAS_EL:

very_long_integer   |ψⁱ>
integer             s
integer             t
integer             p
integer             q
next                *BAS_EL
```

$$|\Psi\rangle = \boxed{\text{BAS\_EL 1}} \rightarrow \boxed{\text{BAS\_EL 2}} \cdots \boxed{\text{BAS\_EL X}} \rightarrow \text{NULL}$$
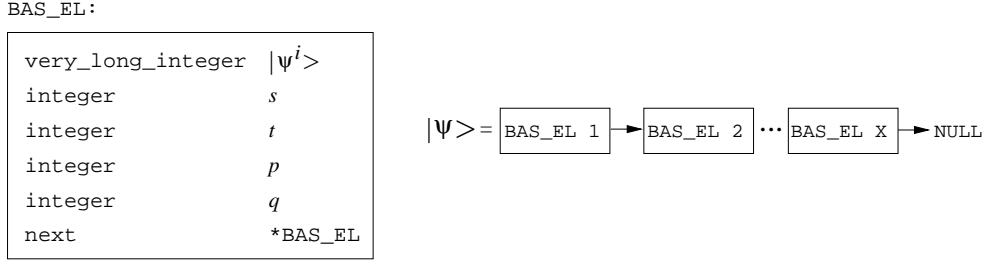
Figure 3.8.: A suitable data structure representing the basis-states $a_i|\psi^i\rangle$ which linearly add up to the full state $|\psi\rangle = \sum_i a_i|\psi^i\rangle$ of the system. Here very_long_int denotes a suitably defined data type, which comprises enough bits to encode the basis states of the considered cluster C; see main text. The integers s and t encode the powers of α and β, while p and q encode the coefficient $C(\underline{m}) = p/q$ appearing in the prefactors a_i, see Eq. (3.84). The vector next is needed to build an interlaced chain of the depicted data structure. This chain finally represents the full state $|\psi\rangle$.

The calculation of the action of effective observables

$$\mathcal{O}_{\text{eff}}(x) = \sum_{k=0}^{\infty} x^k \sum_{j=1}^{k+1} \sum_{|\underline{m}|=k} \tilde{C}(\underline{m};j)\mathcal{O}(\underline{m};j) , \quad \text{with} \tag{3.85}$$

$$\mathcal{O}(\underline{m};j) = T_{m_1} \cdots T_{m_{j-1}}\mathcal{O}T_{m_j} \cdots T_{m_k} , \tag{3.86}$$

can be done with slight modifications. The operators T_n already appeared in the effective Hamiltonian. As we have seen in section 3.4.2 it suffices to calculate the locally acting effective observable $\mathcal{O}_{\text{eff}}(\mu; x)$. In this case the operator $\mathcal{O}$ in Eq. (3.86) is a local operator acting on a finite number of sites denoted by μ. To pursue our particular example we assume μ to be a fixed pair of adjacent sites.

An obvious modification on the algorithm is, that one has to load the coefficients $\tilde{C}(\underline{m}, j)$ with corresponding multi-indices $\underline{m}$ including the position j of the observable $\mathcal{O}$ in step 2) of Fig. 3.7 instead of the coefficients $C(\underline{m})$. Extra attention has to be paid to step 6). Before we advance to calculate the action of T_{m_i} with $i = j$ within the i-loop, we have to include an additional step, in which the action of $\mathcal{O}$ is calculated. Again, this can be done with the algorithm depicted in Fig. 3.6. However, the m-loop, representing the sum over all pairs μ can be dropped. Steps 4) and 5) need to be executed only once and only for the pair μ to which we consider the operator $\mathcal{O}$ to be attached. We would like to mention that it suffices to consider a single site γ for some observables instead of a pair ν.

Experience has shown that the performance of the presented algorithm suf-

fices to calculate the action of effective observables to the same order to which the corresponding coefficients can be obtained. Two points deserve attention. Operator products $T(\underline{m})$, likewise products $\mathcal{O}(\underline{m}; j)$, intermediately creating a large number of particles, are particularly memory demanding. This becomes clear from the following consideration. We separate the Hilbert space $\mathcal{H}$ in sub-spaces $\mathcal{H}_n$ classified by the number n of particles. The dimension of $\mathcal{H}_i$ is larger than the dimension of $\mathcal{H}_j$, if $L/2 > i > j$, where L is the total number of sites in the considered finite cluster C. The most difficult sub-space is $\mathcal{H}_{N/2}$. Although the $T(\underline{m})$ or $\mathcal{O}(\underline{m}; j)$ will not generate all possible states in the largest subspace accessible for a given order, the argument gives a good approximation. Additionally, all clusters needed to calculate a specific quantity, should be chosen as small as possible, to keep the binary-representations small.

We wish to conclude this section by drawing the reader's attention to appendix B, where we compiled some coefficients C and $\tilde{C}$.

3.6. Chapter Summary

In this chapter we consider the initial problem to read $H = U + xV$ and present a perturbative CUT, leading to a (quasi-) particle conserving effective Hamiltonian H_{eff}. For simplicity we restrict the class of considered lattice models. The unperturbed part U must have an equidistant spectrum bounded from below. The difference between two levels of U is called a quasi-particle. The perturbing part V must allow a decomposition $V = \sum_{n=-N}^{N} T_n$, with $N \in \mathbb{N}$ and $[U, T_n] = nT_n$.

The resulting effective Hamiltonian and observables act on real-space states for which we need to specify the number of quasi-particles and their position in the lattice only. The particles are not the true excitations of the effective systems. However, the effective operators are expressed as series expansions of

the ladder operators T_n acting on these particles

$$H_{\text{eff}}(x) = U + \sum_{k=1}^{\infty} x^k \sum_{\substack{|\underline{m}|=k \\ M(\underline{m})=0}} C(\underline{m})T(\underline{m}) \,, \quad \text{with}$$

$$T(\underline{m}) = T_{m_1}T_{m_2}T_{m_3}\cdots T_{m_k} \,, \quad \text{and}$$

$$\mathcal{O}_{\text{eff}}(x) = \sum_{k=0}^{\infty} x^k \sum_{i=1}^{k+1} \sum_{|\underline{m}|=k} \tilde{C}(\underline{m};i)\mathcal{O}(\underline{m};i) \,, \quad \text{with}$$

$$\mathcal{O}(\underline{m};i) = T_{m_1}\cdots T_{m_{i-1}}\mathcal{O}T_{m_i}\cdots T_{m_k} \,.$$

While H_{eff} conserves the number of particles (the sum on the right hand side is restricted by $M(\underline{m}) = m_1 + m_2 + \ldots + m_k = 0$) and is thus block diagonal with respect to the number of particles, no such conservation is found for $\mathcal{O}_{\text{eff}}$. The action of the effective operators is captured by virtual particle excitations $T(\underline{m})$ ($\mathcal{O}(\underline{m};i)$) weighted by *rational* coefficients $C(\underline{m})$ ($\tilde{C}(\underline{m};i)$). Higher expansion orders are accompanied by longer virtual excitations, reflecting the way in which the effective operators create the polarisation clouds dressing the original quasi-particles.

We explain in detail how a computer implementation is realised, which allows the calculation of the coefficients $C(\underline{m})$ and $\tilde{C}(\underline{m})$ up to high orders; (e.g. $C(\underline{m})$: 15th (10th) order for $N = 1$ ($N = 2$) on conventional computer systems). The coefficients are obtained as exact fractions of integers.

The ladder operators T_n have to be specified for the specific model under investigation. Assuming that this problem has been solved, we present a computer implementation allowing to *symbolically* calculate the action of H_{eff} and $\mathcal{O}_{\text{eff}}$ on the real-space states specified above. In other words, the implementation is designed in such a way that the computed results analytically depend on the model parameters. Generically, one obtains series expansions to the same order in x as specified for the coefficients.

The appearance of H_{eff} and $\mathcal{O}_{\text{eff}}$, which we consider to be calculated to some finite maximum order in x, is simplified considerably, if one assumes translational invariance for the system under study. In the one-particle momentum basis $\{|\mathbf{k}\rangle\}$ the one-particle part H_1 of $H_{\text{eff}} = H_0 + H_1 + H_2 + \ldots$ is given by a (truncated) polynomial in x for fixed one-triplon momentum $\mathbf{k}$. The polynomial coefficients are real, if one assumes inversion symmetry in addition. In the two-particle momentum basis $\{|\mathbf{K}, \mathbf{d}\rangle\}$ H_1 is a semi-infinite band matrix with a repeated pattern in the tail for fixed total momentum $\mathbf{K}$; the relative distances $\mathbf{d}$ between the two particles are the remaining quantum

numbers between which the matrix elements are defined. Each matrix element is a polynomial in x with real (inversion symmetry) coefficients. The pure two-particle matrix H_2 is captured by a finite matrix in $\{|\mathbf{K}, \mathbf{d}\rangle\}$ for fixed $\mathbf{K}$. Again, the matrix elements are polynomials, with real coefficients if inversion symmetry holds.

In the case of translational invariance it is convenient to define momentum-space representations of the effective observables which produce momentum states, if they act on the ground state of the system (particle vacuum). The action of the momentum-state representation $\mathcal{O}_{1,0}(\mathbf{k})$ of the one-particle injecting part $\mathcal{O}_{1,0}$ in $\mathcal{O}_{\mathrm{eff}} = \mathcal{O}_{0,0} + \mathcal{O}_{1,0} + \mathcal{O}_{2,0} + \ldots$ produces the one-particle momentum states $|\mathbf{k}\rangle$. For fixed $\mathbf{k}$ the amplitude for this process is given by a polynomial in x with real (inversion symmetry) coefficients. The two-particle injecting part $\mathcal{O}_{2,0}(\mathbf{K})$ produces two-particle momentum states $|\mathbf{K}, \mathbf{d}\rangle$. For fixed $\mathbf{K}$ the amplitudes can be viewed to constitute a vector, the components of which correspond to the different relative distances $\mathbf{d}$.

4. Effective Green's Function – Spectral Densities

In this chapter we tackle the problem of calculating $T = 0$ spectral densities from the effective Hamiltonian and observables derived in the last chapter. Though not essential for the proposed method to work, we will assume translational invariance of H_{eff} and $\mathcal{O}_{\text{eff}}$ to ease the description. As we have seen in section 3.4, the appearance of H_{eff} and $\mathcal{O}_{\text{eff}}$ is strongly simplified in this case (see Fig. 3.3 for a sketch of our findings). The calculation of one- and two-particle spectral densities is explained in detail.

4.1. General Considerations

For some given observable $\mathcal{O}$, modelling a specific measurement, the $T = 0$ momentum and energy resolved spectral density $\mathcal{S}$ is given by

$$\mathcal{S}(\mathbf{K}, \omega) = -\frac{1}{\pi} \text{Im} \mathcal{G}^{\mathcal{O}}(\mathbf{K}, \omega) , \qquad (4.1)$$

where $\mathcal{G}^{\mathcal{O}}(\mathbf{K}, \omega)$ is the retarded zero temperature Green's function

$$\mathcal{G}^{\mathcal{O}}(\mathbf{K}, \omega) = \left\langle 0 \left| \mathcal{O}^{\dagger}(\mathbf{K}) \frac{1}{\omega - (H(\mathbf{K}) - E_0) + i0^+} \mathcal{O}(\mathbf{K}) \right| 0 \right\rangle . \qquad (4.2)$$

The ground state of the system is denoted by $|0\rangle$. We subtract the ground state energy E_0 to account for the fact that an actual experiment can measure energy-differences from the ground state only.

Spectral densities provide information on the density of elementary excitations, on their interaction, and on how the particular excitation operator couples to them. The spectral density is a measure for the density of states "visible" for the measurement modelled by $\mathcal{O}$. It is thus proportional to the momentum and energy resolved intensity of scattering experiments. We are going to exploit this fact in the application chapter.

Since the eigen-values of quantum mechanical observables are conserved quantities under unitary transformations, $\mathcal{S}$ will not be changed if we substitute the operators appearing in $\mathcal{G}$ by the perturbatively obtained effective operators discussed in the preceding chapter.[1] Note that H_{eff} and $\mathcal{O}_{\text{eff}}$ are obtained by the *same* transformation.

In the case of translational invariance the calculation of the spectral density in the one-particle sector is particularly simple. Using Dirac's identity

$$\frac{1}{x - x_0 \pm i0^+} = \mathcal{P}\frac{1}{x - x_0} \mp i\pi\delta(x - x_0) \; , \tag{4.3}$$

where $\mathcal{P}$ denotes Cauchy's principal value, we find (see Eqs. (4.1) and (4.2))

$$\mathcal{S}(\mathbf{k}, \omega) = \left\langle 0 \left| \mathcal{O}_{1,0}^\dagger(\mathbf{k})\delta(\omega - H_1)\mathcal{O}_{1,0}(\mathbf{k}) \right| 0 \right\rangle$$

$$= |A_{\mathbf{k}}|^2 \left\langle \mathbf{k} \left| \delta(w - H_1) \right| \mathbf{k} \right\rangle$$

$$= |A_{\mathbf{k}}|^2 \delta\left(\omega - \omega(\mathbf{k})\right) \; . \tag{4.4}$$

The one-particle dispersion $\omega(\mathbf{k})$ and the observable amplitude $A_{\mathbf{k}}$ are readily given by Eqs. (3.45) and (3.62) respectively. At each point $(\mathbf{k}, \omega(\mathbf{k}))$ the corresponding weight is given by the square of the modulus of $A_{\mathbf{k}}$ which is a polynomial in x. The result is thus obtained by assigning a δ-function with corresponding weight to each point $(\mathbf{k}, \omega(\mathbf{k}))$.

For the two-particles case we choose to evaluate the effective Green's function by tridiagonalisation. This leads to the continued fraction expression ([63–65], for overviews see Refs. [66, 67])

$$\mathcal{G}_{2,0}^{\mathcal{O}}(\mathbf{K}, \omega) = \tag{4.5}$$

$$\cfrac{\langle 0|\mathcal{O}_{2,0}^\dagger(\mathbf{K})\mathcal{O}_{2,0}(\mathbf{K})|0\rangle}{\omega - a_0 - \cfrac{b_1^2}{\omega - a_1 - \cfrac{b_2^2}{\omega - \cdots}}} = \cfrac{\sum_{\mathbf{d}} |A_{\mathbf{K},\mathbf{d}}|^2}{\omega - a_0 - \cfrac{b_1^2}{\omega - a_1 - \cfrac{b_2^2}{\omega - \cdots}}} \; .$$

The amplitudes $A_{\mathbf{K},\mathbf{d}}$ are given by Eq. (3.65) on page 63. The coefficients a_i and b_i^2 are calculated by repeated application of $H_{\text{eff}} - H_0 = H_1 + H_2$ on the initial two-particle momentum state $|\text{Init}\rangle = |f_0\rangle = \mathcal{O}_{2,0}(\mathbf{K})|0\rangle$. Setting the states $|f_{n<0}\rangle$ to zero the recursion

$$|f_{n+1}\rangle = (H_1 + H_2)|f_n\rangle - a_n|f_n\rangle - b_n^2|f_{n-1}\rangle \tag{4.6}$$

---

[1] The transformation amounts to inserting identities of the form $U \; U^\dagger$.

generates a set of orthogonal states, if the coefficients are defined according to

$$a_n = \frac{\langle f_n|(H_1 + H_2)|f_n\rangle}{\langle f_n|f_n\rangle} \quad , \qquad b_{n+1}^2 = \frac{\langle f_{n+1}|f_{n+1}\rangle}{\langle f_n|f_n\rangle} \quad .$$

In the generated $\{|f_n\rangle\}$-basis H_{eff} is a tridiagonal matrix, where the a_i are the diagonal matrix elements and the b_i are the elements on the second diagonal. All other matrix elements are zero.

Fig. 3.3 on page 60 illustrates the procedure for the two-particle sector. For fixed $\mathbf{K}$ the relative (positive) distance $\mathbf{d}$ between the two injected particles is the only remaining quantum number. In this basis $H_1 + H_2$ is represented as a matrix (left side). Its matrix elements are polynomials in the perturbation parameter x. We have to evaluate the repeated application of this matrix on the vector representing $|f_0\rangle = |\text{Init}\rangle$ (right side), whose components $A_{\mathbf{K},\mathbf{d}}$ are also polynomials in x for fixed $\mathbf{K}$.

The general case of more than two particles can be treated similarly. For n particles we have to consider the conserved total momentum $\mathbf{K}$ and $n - 1$ relative distances. Then, for fixed $\mathbf{K}$ $|\text{Init}\rangle$ and H_{eff} are still represented by a vector and matrices respectively, but there appearance becomes more complicated. For three particles we obviously have to apply $H_1 + H_2 + H_3$ to $|\text{Init}\rangle$. For four particles H_4 is added and so on.

We come back to the two-particle case. Here we have $H_1 + H_2$. The pure two-particle interaction part H_2 is represented by a finite matrix of dimension d_{max} mixing the first d_{max} components in the states $|f_n\rangle$ only. On the other hand, H_1 is a semi-infinite matrix generating finite components in the state $|f_{n+1}\rangle$ for larger $\mathbf{d}$ where there have been zeros in the previous state $|f_n\rangle$ (see Fig. 3.3). The range of non-zero components in $|f_n\rangle$ grows with each application of H_1. The amount of non-zero elements additionally generated in each application depends on the width of the band matrix representing H_1, which in turn depends on the order to which we have calculated H_1.

The described procedure is realised for fixed x and $\mathbf{K}$ leaving a purely numerical problem. For the $S = 1/2$ two-leg spin ladder for instance (see e.g. Refs. [26, 29, 30, 68]), we calculated H_{eff} to 14th order. While H_2 mixes the first 14 components in each state $|f_n\rangle$ only, H_1 continues to produce non-zero components in the $|f_n\rangle$ in each application. For the given example we were able to implement a maximum relative distance of ≈ 10000, allowing to repeat the recursion about 650 times giving the first 650 coefficients a_i and b_i^2. For a comparable two-dimensional application one can assume the square root of the given numbers.

Thus, and we would like to stress this point, the chosen method to evaluate the effective Green's function introduces no quantitative finite size effects. The

problem of calculating the spectral densities for given effective Hamiltonians and observables comprises the two quantum numbers $\mathbf{K}$ and $\mathbf{d}$ in the two-particle sector. (For every particle more, there is one more relative distance to be considered, see above). Our calculations are in the thermodynamic limit (to the given order) for the total momentum $\mathbf{K}$. It is only for $\mathbf{d}$, that an approximation enters the calculations.

The main error for $\mathbf{d}$ is caused by the finiteness of the perturbative calculations. The true many-particle interactions are accounted for, only if all involved particles are within a certain finite distance to each other. This approximation is controlled, since one generically observes a rather sharp drop of the interaction matrix elements with increasing distances. Especially gapped systems with finite correlation lengths are well suited to be tackled by our method. Difficulties arise if the correlations drop slowly with increasing distances. In this case the truncations in real-space might introduce crude approximations.

Another error for $\mathbf{d}$ is introduced by truncating the continued fraction expansion of the Green's function. However, allowing 10000 distances as in the ladder example should guarantee, that this additional error is very small in comparison to the error introduced by truncating the perturbative expansion as discussed in the preceding paragraph.

The finiteness of the continued fraction can be partly compensated by suitable terminations as shall be shown in the following section for the two-particle sector of generic, gapped one-dimensional models.

4.2. Terminators for Gapped 1d-Systems

In this section we especially consider the two-particle spectral density of a gapped one-dimensional system. The spectral density $\mathcal{S}(\omega)$ obtained from the continued fraction (4.5) representation of the effective Green's function has poles at the zeros of the denominator. Thus, in principle, $\mathcal{S}$ is a collection of sharp peaks. A slight broadening of $\mathcal{S}$ via $\omega \to \omega + i\delta$ (δ small) in $\mathcal{G}$ will smear out all poles to give a continuous function for all practical purposes (see Fig. 4.1). However, we aim to increase the resolution of $\mathcal{S}$ to a smooth function by introducing proper terminations of the continued fraction exploiting the one-dimensionality of the considered model.

To this end we note, that for fixed total momentum K the (upper) lower band edges (ϵ_{ub}) ϵ_{lb} of the two-particle continuum (see also our discussion in section 3.4.1 below Eq. (3.46)) can be calculated from the one-particle disper-

sion ω_1 (3.45). All energies of the two-triplon continuum are seized by

$$\omega_2(k,q) = \left(\omega_1\left(\frac{K}{2}+q\right) + \omega_1\left(\frac{K}{2}-q\right)\right) , \tag{4.7}$$

where $q \in [-\pi, \pi]$ denotes the relative momentum. Therefore, we can calculate ϵ_{ub} and ϵ_{lb} from the one-triplon dispersion

$$\epsilon_{\mathrm{ub}}(K) = \max_q(\omega_2(K,q))$$

$$\epsilon_{\mathrm{lb}}(K) = \min_q(\omega_2(K,q)) . \tag{4.8}$$

For fixed K the upper and lower band edges ϵ_{ub} and ϵ_{lb} give the values to which the continued fraction coefficients a_i and b_i should converge for $i \to \infty$. One finds $a_\infty = (\epsilon_{\mathrm{ub}} + \epsilon_{\mathrm{lb}})/2$ and $b_\infty = (\epsilon_{\mathrm{ub}} - \epsilon_{\mathrm{lb}})/4$ [66], which also serves as an independent check for the highest calculated coefficients.

Further, if we assume the system under study to be gapped we have massive elementary excitations showing quadratic behaviour at the dispersion extrema, and the one-particle dispersion $\omega_1(k)$ is two-fold continuously differentiable. Obviously $\omega_2(K,q)$ then has this property with respect to q, too. Hence, we have square root singularities in the density of states at the edges of the continuum (the problem is one-dimensional). The two particles, giving rise to the continuum of states, are assumed to be asymptotically free. In conclusion, a square root termination for the continued fraction is appropriate: all listed properties lead to a convergent behaviour of a_i and b_i^2 [67], so that from some finite fraction depth on the coefficients can be considered to be constant. This naturally leads to the following terminations. With

$$D = 4b_\infty^2 - (\omega - a_\infty)^2 \tag{4.9}$$

we define the continued fraction terminations for three distinct cases

$$\tau_{\mathrm{a}} = \frac{1}{2b_\infty^2}\left(\omega - a_\infty - \sqrt{-D}\right) , \text{ above continuum}$$

$$\tau_{\mathrm{i}} = \frac{1}{2b_\infty^2}\left(\omega - a_\infty - i\sqrt{D}\right) , \text{ within continuum}$$

$$\tau_{\mathrm{b}} = \frac{1}{2b_\infty^2}\left(\omega - a_\infty + \sqrt{-D}\right) , \text{ below continuum.} \tag{4.10}$$

The last calculated b_i^2 in Eq. (4.5) is multiplied by the appropriate terminator, depending on which energy range is investigated. Taking the imaginary part

of the resulting expression for the case within the continuum yields the continuous part of the spectral density $\mathcal{S}$ in the thermodynamic limit. We want to emphasise that the result is a continuous function displaying the full weight of the continuum correctly, limited by the extent of the perturbative expansion order only.

As an illustrative example we consider the elliptic spectral density

$$\mathcal{S}(\omega) = \frac{1}{2\pi b^2} \sqrt{4b^2 - (\omega - a)^2} \, , \tag{4.11}$$

depicted as solid black curve in Fig. 4.1. The corresponding Green's function $\mathcal{G}(\omega)$ can be expressed as

$$\mathcal{G}(\omega) = \cfrac{1}{\omega - a - \cfrac{b^2}{\omega - a - \cfrac{b^2}{\ldots}}} = \frac{1}{\omega - a - b^2 \tau_i(\omega)} \, , \quad \text{with}$$

$$\tau_i(\omega) = \mathcal{G}(\omega) = \frac{1}{2b^2} \left(\omega - a - i\sqrt{4b^2 - (\omega - a)^2} \right)$$

$$\Rightarrow \mathcal{S}(\omega) = -\frac{1}{\pi} \mathrm{Im} \mathcal{G}(\omega) \quad \checkmark \, . \tag{4.12}$$

This simple example illustrates how the terminator τ_i for the continued fraction within a continuum is used. The resulting spectral density is the solid black line in Fig. 4.1. For more complicated systems the leading coefficients a_i and b_i display fluctuations. It is only for larger indices i that they converge to constant values. In this case one calculates as many coefficients as possible and multiplies the terminator to the last obtained b_i^2.

A truncated continued fraction for $\mathcal{G}(\omega)$ would lead to the δ-peaks indicated as vertical lines in Fig. 4.1. A broadening of $\mathcal{S}$ via $\omega \to \omega + i\delta$ leads to the wavy grey curve.

In the case of bound states we note that the Green's function can be written as (K is assumed fixed)

$$\mathcal{G}^{\mathcal{O}}(\omega) = \frac{\langle 0|\mathcal{O}_{2,0}^\dagger \mathcal{O}_{2,0}|0\rangle}{\omega - f(\omega)} \, , \tag{4.13}$$

where the function $f(\omega)$ is real-valued (see terminations τ_a and τ_b). The position of possible bound states is given by the zeros of $g(\omega) = \omega - f(\omega)$. Let ω_0 be such a zero of g. We expand g about ω_0 in $\omega - \omega_0$ to first order, which is sufficient for small deviations from ω_0. This gives

$$\mathcal{G}^{\mathcal{O}}(\omega) \approx \frac{\langle 0|\mathcal{O}_{2,0}^\dagger \mathcal{O}_{2,0}|0\rangle}{(\omega - \omega_0)(1 - \partial_\omega f(\omega_0))} \, . \tag{4.14}$$
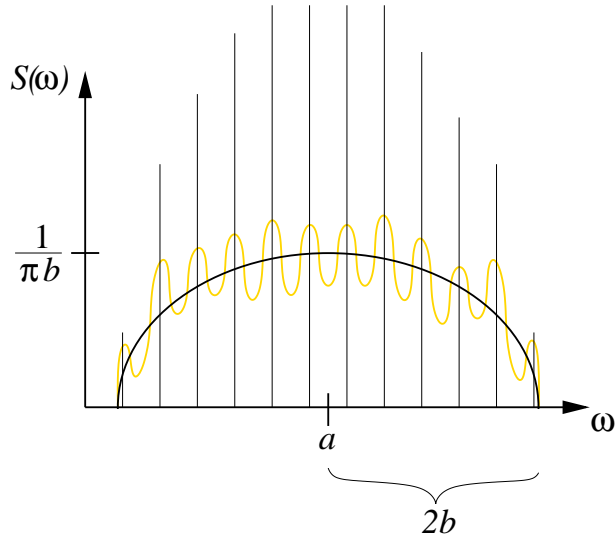
Figure 4.1.: An elliptic spectral density $\mathcal{S}(\omega)$, considered as an example. The true spectral density is the solid black curve, for which we illustrate the use of a square-root terminator in the corresponding Green's function. The vertical lines indicate the appearance of $\mathcal{S}(\omega)$, if the continued fraction expansion of the Green's function was terminated at some finite depth. The yellow (grey) curve is the spectral density which results from a terminated Green's function by introducing a broadening via $\omega \to \omega + i\delta$.

If $\mathcal{G}^{\mathcal{O}}$ is the retarded Green function the Dirac-identity yields

$$\mathcal{S}(\omega)|_{\omega \approx \omega_0} = -\frac{1}{\pi} \mathrm{Im} \mathcal{G}^{\mathcal{O}}(\omega) = \frac{\langle 0| \mathcal{O}_{2,0}^{\dagger} \mathcal{O}_{2,0} |0\rangle}{1 - \partial_\omega f(\omega_0)} \delta(\omega - \omega_0) , \qquad (4.15)$$

clarifying that a possible bound state shows up as a δ-function. Its spectral weight is given by

$$I_{\mathrm{bound}}^{-1} = \partial_\omega \left(\mathcal{G}^{\mathcal{O}}(\omega)^{-1} \right) |_{\omega = \omega_0} , \qquad (4.16)$$

which is easy to calculate once the Green's function $\mathcal{G}$ is evaluated.

4.3. Chapter Summary

In this chapter we illustrate, how spectral densities can be calculated from an effective Hamiltonian and an effective observable. Assuming translation invariance the one-particle spectral density can be calculated straightforwardly from the results of the preceding chapter. For the calculation of two-particle spectral densities we utilise the continued fraction technique. A generalisation

to many-particle spectral densities is indicated. The technical details of the approach are explained in detail. Note that translational invariance is not a necessary prerequisite for the method to work.

The case of a gapped one-dimensional system is investigated in more detail to show how an analytical expression for the two-particle spectral density can be achieved by introducing suitable continued fraction terminators.

An important point is, that if H_{eff} and $\mathcal{O}_{\text{eff}}$ are calculated in the thermodynamic limit to a given order, the continued fraction technique allows the calculation of the corresponding spectral density in the thermodynamic limit, too. We argue, that the finiteness of the continued fraction introduces negligible errors for the quantum number $\mathbf{d}$ only. No additional errors enter for the quantum number $\mathbf{K}$.

It should be emphasised that the dominant error for $\mathbf{d}$ is caused by the finiteness of the maximum perturbation order. In actual applications we may encounter situations, where it becomes necessary to extrapolate the matrix elements of H_{eff} and $\mathcal{O}_{\text{eff}}$ to reach quantitative agreements with experimental findings. We will address this problem in the next chapter.

5. Optimised Perturbation Theory

Our approach to calculate the effective operators H_{eff} and $\mathcal{O}_{\text{eff}}$ is perturbative. Results for physical quantities will thus be truncated series in the perturbation parameter x. The theory is controlled in the sense that it is correct for $x \to 0$, but we do not have information on the radius of convergence. It might be necessary to find results for larger x-values, where we cannot rely on the truncated series. Suitable extrapolation schemes have to be considered.

A standard way to extrapolate polynomials is the use of Padé - or Dlog-Padé - approximants and other techniques. An overview can be found in Ref. [69]. These techniques pose a feasible task if one is dealing with a *few* polynomials. However, parts of the effective Hamiltonian, in particular the two-particle interaction H_2, are (possibly large) matrices of which each element is a polynomial in x. Clearly, the task of extrapolating these matrices has to be automatized. The Padé-methods do not allow a simple automatization, since the resulting approximants are not robust, i.e. there is no algorithmic criterion judging the quality of the approximant.

To overcome these difficulties we propose the use of optimised perturbation theory (OPT) which is based on the principle of minimal sensitivity [70].

For the illustration of OPT to start we need to go back to the very beginning of our perturbational approach where we assumed that the Hamiltonian can be split into an unperturbed part U and a perturbation V

$$H(x) = U + xV \ . \tag{5.1}$$

The fundamental idea of optimised perturbation theory (OPT) is to add an auxiliary variable a, which allows a self-adjusting splitting into unperturbed and perturbation part, without modifying the Hamiltonian

$$H(x; a) = (1 + a)U + xV - aU$$

$$= (1 + a)\tilde{H}(\tilde{x}; \tilde{a})$$

$$\tilde{H}(\tilde{x}; \tilde{a}) = U + \tilde{x}(V + \tilde{a}U) \ , \quad \text{with } \tilde{x} = \frac{x}{1 + a} \ \text{ and } \tilde{a} = -\frac{a}{x} \ . \tag{5.2}$$

We consider $\tilde{x}$ to be the new expansion parameter. The Hamiltonian $H(x;a) = (1+a)\tilde{H}(\tilde{x};\tilde{a})$ leads to the same *true* eigen-energies $\Delta(x)$ as Hamiltonian $H(x)$ (we regard the energy-gap Δ as an universal example). However, the truncated series expansion $\Delta_{\mathrm{trunc}}(x;a)$ of the eigen-values of $H(x;a)$ will depend on a. We write

$$\Delta_{\mathrm{trunc}}(x;a) = (1+a)\mathcal{T}\Big|^{n}_{\tilde{x}=0} \tilde{\Delta}(\tilde{x};\tilde{a}) \;, \tag{5.3}$$

where $\tilde{\Delta}(\tilde{x};\tilde{a})$ denotes the eigen-values of $\tilde{H}(\tilde{x};\tilde{a})$ and $\mathcal{T}\Big|^{n}_{x=x_0} f(x)$ is the nth order Taylor expansion of $f(x)$ in x about $x = x_0$.

Now, since $\Delta_{\mathrm{trunc}}(x;a)$ depends on a, although it should not, we shall at least demand stationarity in this unphysical parameter. This leads to the criterion of minimal sensitivity

$$\partial_a \Delta_{\mathrm{trunc}}(x;a)|_{a=a_{\mathrm{opt}}} = 0 \;. \tag{5.4}$$

In general $\Delta_{\mathrm{trunc}}(x;a_{\mathrm{opt}})$ converges faster than the corresponding series expansions of $\Delta(x)$, since the additional degree of freedom can be used to optimise the splitting into an unperturbed and a perturbing part [70]. In other words the system has the freedom to choose the best splitting depending on what kind of quantity we are interested in. Moreover, in some cases a convergent series expansion can be enforced by OPT even if the original series diverges. In Ref. [70] (see also references therein) the harmonic oscillator perturbed by a quartic potential is given as an example, whose standard series expansion for the ground state energy diverges [71].

To be more specific we rewrite

$$\tilde{H}(\tilde{x};\tilde{a}) = U + \tilde{x}(V + \tilde{a}U) = (1 + \tilde{a}\tilde{x})\left[U + \frac{\tilde{x}}{1 + \tilde{a}\tilde{x}}V\right] \;. \tag{5.5}$$

One clearly sees, that we can obtain the corresponding eigen-energies $\tilde{\Delta}(\tilde{x};\tilde{a})$ by simply substituting $x \to \tilde{x}/(1 + \tilde{a}\tilde{x})$ in $\Delta(x)$

$$\tilde{\Delta}(\tilde{x};\tilde{a}) = (1 + \tilde{a}\tilde{x})\Delta\left(\frac{\tilde{x}}{1 + \tilde{a}\tilde{x}}\right) \;. \tag{5.6}$$

Now, consider we had already calculated $\Delta(x)$ as a truncated series $\Delta_{\mathrm{trunc}}(x)$ from H_{eff}. We then obtain $\Delta_{\mathrm{trunc}}(x;a)$ by a simple re-expansion (note that $\tilde{x}$

is the small parameter in $\tilde{\Delta}(\tilde{x}; \tilde{a}))$

$$\Delta_{\text{trunc}}(x; a) = (1 + a)\mathcal{T}\bigg|_{\tilde{x}=0}^{n_{\max}} \tilde{\Delta}(\tilde{x}; \tilde{a})$$

$$= (1 + a)\mathcal{T}\bigg|_{\tilde{x}=0}^{n_{\max}} \left\{ (1 + \tilde{a}\tilde{x})\Delta_{\text{trunc}}\left(\frac{\tilde{x}}{1 + \tilde{a}\tilde{x}}\right) \right\} , \qquad (5.7)$$

where $n_{\max}$ is the maximum order to which we obtained $\Delta_{\text{trunc}}(x)$ before. We finally re-substitute $\tilde{x}$ and $\tilde{a}$ by their definitions in Eq. (5.2). In order to be able to do all steps in one we introduce an auxiliary variable λ for the derivation. Then, the Taylor expansion in $\tilde{x}$ can be replaced by an expansion in λ

$$\tilde{x} = \frac{\lambda x}{1 + a} \quad \text{and} \quad \tilde{a} = -\frac{a}{x} , \qquad (5.8)$$

where it is understood, that the final result is obtained for $\lambda = 1$. Thus we obtain

$$\Delta_{\text{trunc}}(x; a) = \left[\mathcal{T}\bigg|_{\lambda=0}^{n_{\max}} (1 + a(1 - \lambda))\Delta_{\text{trunc}}\left(\frac{\lambda x}{1 + a(1 - \lambda)}\right) \right]_{\lambda=1} . \qquad (5.9)$$

We are thus able to use optimised series expansions without any new calculations. We take the direct expansions for the eigen-energies $\Delta_{\text{trunc}}(x)$ obtained from the effective Hamiltonian and substitute and re-expand according to Eq. (5.9) to get the optimised expansions $\Delta_{\text{trunc}}(x; a_{\text{opt}})$, where a_{opt} is given by the minimal sensitivity criterion (5.4).

From the discussion above it should be clear, that any other quantity $A_{\text{trunc}}(x)$ obtained as a truncated series expansion in x from some effective observable (not the Hamiltonian) can be optimised analogously

$$A_{\text{trunc}}(x; a) = \left[\mathcal{T}\bigg|_{\lambda=0}^{n_{\max}} A_{\text{trunc}}\left(x \to \frac{\lambda x}{1 + a(1 - \lambda)}\right) \right]_{\lambda=1} . \qquad (5.10)$$

The prefactor $(1 + a(1 - \lambda))$ has to be dropped since A is not measured in unit of energy in contrast to Δ.

We use the criterion of minimal sensitivity to further elaborate on the structure of a_{opt}. In the following paragraphs we will show that we can always write

$$a_{\text{opt}} = \alpha_{\text{opt}}x . \qquad (5.11)$$

Let $R_{\text{trunc}}(x; a)$ be the truncated series expansion of the quantity for which we want to find the optimum value a_{opt}. In the following discussion R is an eigen-energy Δ or some other quantity A. To ease the description we introduce the function

$$g(u, v) = \begin{cases} v\Delta_{\text{trunc}}(u/v) & \text{for energies,} \\ A_{\text{trunc}}(u/v) & \text{otherwise.} \end{cases} \tag{5.12}$$

The derivative of g with respect to v is denoted by $f(u, v) = \partial_v g(u, v)$. Now, the problem of calculating a_{opt} reduces to (for clarity we suppress the notation for $\lambda = 1$ in the end)

$$0 \doteq \partial_a R_{\text{trunc}}(x; a) = \mathcal{T}\Big|^n_{\lambda=0} \partial_a g(\lambda x, 1 + a(1 - \lambda))$$

$$= \mathcal{T}\Big|^n_{\lambda=0} f(\lambda x, 1 + a(1 - \lambda))(1 - \lambda) . \tag{5.13}$$

For the following argument it is important to see that we can write

$$\mathcal{T}\Big|^n_{\lambda=0} f(\lambda x, 1 + a(1-\lambda))(1-\lambda) = f_n\lambda^n + (1-\lambda)\mathcal{T}\Big|^{n-1}_{\lambda=0} f(\lambda x, 1 + a(1-\lambda)) , \tag{5.14}$$

where f_n denotes the nth coefficient in the Taylor expansion of f

$$f_n = \frac{1}{n!}(\partial_\lambda)^n f(\lambda x, 1 + a(1 - \lambda)) . \tag{5.15}$$

For $\lambda = 1$ in the end, the second term on the right hand side of Eq. (5.14) vanishes. In addition, the structure of f is such, that with every derivative with respect to λ we obtain an x or an a as internal derivative of the chain rule. Thus, setting $\lambda = 1$ in the end, we find $\partial_a R_{\text{trunc}}(x; a)$ to be a homogeneous polynomial in the variables x and a. In an nth order expansion the criterion of minimal sensitivity reads

$$0 \doteq \partial_a R_{\text{trunc}}(x; a)|_{a=a_{\text{opt}}} = \sum_{i=0}^{n} R_{i,n-i} a^i x^{n-i}|_{a=a_{\text{opt}}} , \tag{5.16}$$

which clearly shows, that we can always write $a_{\text{opt}} = \alpha_{\text{opt}} x$. This proves the assertion.

The proposed OPT procedure can be performed for all physical quantities of interest in particular for the matrix elements of H_1 and H_2. We do not

have to start any new calculations. Instead, we can use our plain results and promote them to OPT-results by simple substitutions and re-expansion.

In some circumstances we will use the OPT method by assuming that an optimal α exists and fix its value by simultaneously optimising some simple quantities like the one-triplon gap, a bound state energy and others with respect to the best Dlog-Padé approximant of these quantities. This approach is based on the plausible assumption that all considered quantities (here: energy levels) are governed by the same model specific singularities. This is supported by the fact that all energy expansions we will calculate in the application chapter start to deviate from their best extrapolations at about the same x-value for a given model. Thus, in contrast to the original spirit of the OPT method, we propose that α_{opt} essentially depends on the model and the order of the expansions only, but not on the particular quantity under study.

The matrix elements of H_1 and H_2 may also be functions of the total momentum $\mathbf{K}$. This does not impose any difficulties for the OPT method, since all arguments from above hold true, if the quantities under inspection depend on auxiliary variables. However, Padé approximations would have to be calculated for every momentum separately. This is obviously not possible. The standard way out is to retreat to sliding techniques, where one calculates approximants for a discrete set of momenta.

Even more, the procedure is linear additive: let $O[\cdot]$ denote the OPT procedure such that

$$f(x; a_{\text{opt}}) = O[f(x)] \tag{5.17}$$

is the optimised series obtained from the direct series $f(x)$. Then, for a linearly composed quantity $F(x) = \sum_i a_i f_i(x)$ we find

$$F(x; a_{\text{opt}}) = O\left[\sum_i a_i f_i(x)\right]$$

$$= \sum_i a_i\, O\left[f_i(x)\right]\ , \tag{5.18}$$

as long as all f_i are given to the same order. For the two-particle interaction part H_2 of H_{eff} in the case of translational invariance for instance, this means, that we can choose to optimise the matrix elements of H_2 directly, or we optimise the two-particle hopping amplitudes before we sum them to yield the Fourier transformed elements (see Eq. (3.55) in section 3.4.1).

We would like to stress that OPT does not yield the best approximants one could think of. This approach is rather a compromise between feasibility and quality. The OPT method represents a very robust and smooth approximation scheme in the sense that none of the approximants diverges or produces

unexpected pathologies. Its additivity makes it particular appropriate for the treatment of Fourier transformed matrix elements.

Chapter Summary

In this chapter we address the problem of extrapolating perturbatively obtained quantities. Standard techniques can be used successfully for a small number of quantities. However, they become an infeasible task, if one needs to extrapolate a *large* number of quantities. To resolve this difficulty, we propose and illustrate the use of optimised perturbation theory (OPT) as an extrapolation scheme for truncated series expansions. The method allows an automatized and synchronous extrapolation (optimisation) of a large number of quantities, if all these quantities belong to the same physical class (for instance all matrix elements of the pure two-particle interaction H_2.)

Having calculated all quantities to be optimised as truncated series expansions in x, OPT is realised by a simple substitution and re-expansion. No new calculations are necessary. The underlying idea is to introduce an auxiliary, "unphysical" parameter a, not changing the *true* result. The truncated result, however, depends on a. The *criterion of minimal sensitivity* demands stationarity in a and yields the *optimal* value a_{opt}. We show that a_{opt} can always be written as $a_{\mathrm{opt}} = \alpha_{\mathrm{opt}} x$.

A comfortable way of using OPT is to adjust α_{opt} by comparing a *small* set of optimised simple quantities (the one- and two-particle gap for instance) to the corresponding approximants obtained by standard techniques such as Dlog-Padé for instance. Then, the α_{opt}-value found for this small set of quantities is assumed to work equally well for all other quantities. This approach is justified by the generic observation that all quantities of a physical system are governed by the same system-specific singularities.

OPT does not necessarily yield the best extrapolations. It should rather be understood as a trade-off between feasibility and quality. However, OPT represents a robust and smooth extrapolation scheme allowing an automatized and simultaneous optimisation of a a large number of quantities.

6. Shastry-Sutherland Model

The perturbative CUT method allows to tackle a large class of physical systems which can be written in the form $H = U + xV$ and which obey the requirements (A) and (B) given at the beginning of section 3.1.

An ideal testing and working ground is given by spin lattice systems. Despite their formal simplicity they exhibit interesting and complex physics, such as true quantum multi-particle effects and rich phase diagrams with quantum phase transitions. They allow to study effects introduced by geometrical frustration and dimensional crossover, to name but a few. In addition a large number of theoretical publications and experimental data is available for various dimensions and topologies.

Especially quantum antiferromagnets are at the centre of research not only because of their relation to high T_c superconductors. Of particular interest are systems which do not have an ordered, Néel-type ground state. Their ground state is a spin liquid without long-range spin order. Spin liquids are favoured by low spin ($S = \frac{1}{2}$ mostly), low coordination number ($Z \in \{2, 3, 4\} \Rightarrow$ dimension $\in \{1, 2\}$), and strong geometric frustration.

We have studied various spin liquids, such as the antiferromagnetic dimerized and frustrated $S = 1/2$ spin chain [57], a two-dimensional model for the dimerized phase of $CuGeO_3$ [59] and two-leg spin ladders [26, 29, 30, 56, 68]. The limit of isolated dimers serves as starting point. In the ladder system, for instance, we choose U to denote the sum of isolated rungs such that the product state of singlets on all rungs is the ground state of U. An elementary excitation of U is given by promoting one singlet to a triplet (triplon). It is easily verified, that U meets prerequisite (A) of section 3.1. The leg-couplings $J_\parallel$ yield V, and their relative strength compared to the rung-couplings $J_\perp$ is an appropriate small parameter $x := J_\parallel / J_\perp$.

In this thesis we want to focus on particularly transparent spin liquids, the so-called dimer solids. In one dimension, the generic example is the Majumdar-Ghosh model [72] of which Shastry and Sutherland found a two-dimensional generalisation [10]. The latter shall be the model for which we will present a detailed illustration of how the perturbative CUT method can be applied to

spin systems.

   We will systematically investigate the spectral properties of the model by exploiting high order results for its effective Hamiltonian and two different effective observables. A large number of interesting results will be obtained.

6.1. Introduction to the Model and to SrCu$_2$(BO$_3$)$_2$

Geometrical frustration is essential in the Majumdar-Ghosh model and its two-dimensional generalisation, the Shastry-Sutherland model. They are constructed in such a way, that each spin is coupled to pairs of spins (dimers). If these pairs form singlets the couplings between dimers is without effect and the singlet-on-dimers product state is always an eigen-state. It is the ground-state for certain parameter-values [10, 73, 74]. The situation is sketched in Fig. 6.1. Solid lines represent the dimers composed of two spins (circles) each. The spins
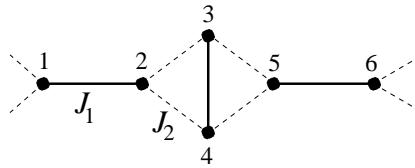

Figure 6.1.: Illustration of a dimer solid. Spins are denoted by circles. Two spins interacting via J_1 couple to a dimer. The dimers interact via J_2. The singlet-on-dimers state is always an eigenstate (see main text).

on dimers are connected by bonds of strength J_1. Each spin interacts with a dimer via two bonds J_2. The Hamiltonian reads

$$H = J_1(\ldots+S_1S_2+S_3S_4+S_5S_6+\ldots)+J_2(\ldots+S_2(S_3+S_4)+S_5(S_3+S_4)+\ldots) \,.$$

All terms proportional to J_2 can be put in the form $S_i(S_n+S_m)$, where S_n and S_m are spins on the *same* dimer. Assuming all dimers to be in the singlet state the total spin of all $(S_n + S_m)$ is zero and all the products $S_i(S_n + S_m)$ vanish. Hence, the inter-dimer coupling is without effect. The remaining couplings $\ldots + S_1S_2 + S_3S_4 + S_5S_6 + \ldots$ proportional to J_1 give $-L3/4$ for the singlet-on-dimer state, where L is the number of dimers in the system.

   The dimer-phase, where the singlet-on-dimer state is the ground state, is gapped. The elementary excited states are dressed $S = \frac{1}{2}$ (one dimension) [74] or $S = 1$ (two dimensions) entities. They interact strongly and form bound and anti-bound states in various spin channels.

The two-dimensional $S = 1/2$ Shastry-Sutherland model [10] is depicted in Fig. 6.2. The Hamiltonian reads

$$H = J_1 \sum_{[i,j]} S_i S_j + J_2 \sum_{\langle i,j \rangle} S_i S_j \; , \qquad (6.1)$$

where the S_i are $S = 1/2$ spin vector-operators and $\langle i, j \rangle$ denotes nearest neighbours (dashed bonds) while $[i, j]$ denotes next- nearest neighbours (solid bonds), which we will call dimers from now on. Because of the particular geometry the system is sometimes called orthogonal dimer model [75]. The dashed bonds in Fig. 6.2 induce a strong geometrical frustration in the antiferromagnetic regime. Without these diagonal bonds we retrieve the two-dimensional Heisenberg model. The latter attracts great attention since it is the magnetic model of the undoped copper-oxide planes in high T_c superconductors.
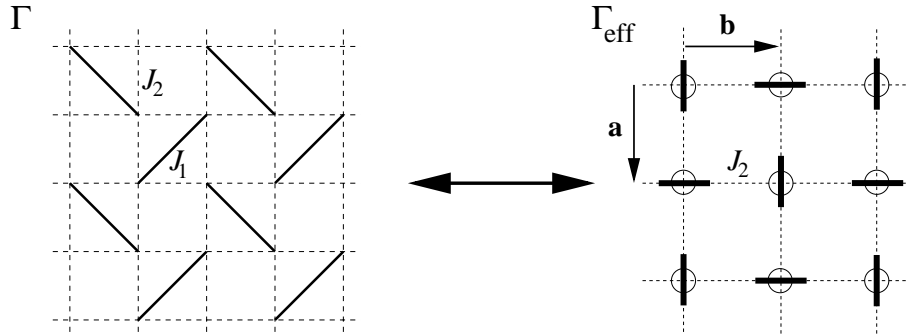

Figure 6.2.: The left figure shows the Shastry-Sutherland model with spins of size $S = 1/2$ on the vertices. In the antiferromagnetic regime the lattice is frustrated. Spins interact via the dimer-bonds J_1 (solid lines) and via residual bonds J_2 (broken lines). The product state of singlets is the exact ground state for J_2 not too large; details can be found in the main text. We denote the depicted lattice by Γ. The right side shows Γ_{eff}, which results from Γ by interpreting one dimer as a single site (circle) and a rotation by $\pi/4$. Only the bonds J_2 remain visible. Note that Γ_{eff} has an A-B sublattice structure due to the pairwise orthogonal structure of the original dimers indicated as solid lines. Γ_{eff} is spanned by the primitive vectors **a** and **b**.

In their original work [10] in 1981 Shastry and Sutherland designed this model in an effort to create a two- (and three-) dimensional system exhibiting an exact ground state made from a product of singlets. Shastry and Sutherland show, that the dimer-singlet state is the exact ground state for $x = J_2/J_1 < 1/2$ (spin $S = 1/2$) and for $x < 1/(2S+2)$ (spin $S \geq 1$). The elementary excitations above the dimer-singlet ground state are given by promoting one of the singlets

to a triplet (triplon).[1]

The Shastry-Sutherland model has experienced a sudden revival of interest by the synthetization of the orthoborate $SrCu_2(BO_3)_2$ by Smith and Keszler [76] in 1991. The schematic crystal structure is depicted in Fig. 6.3. $SrCu_2(BO_3)_2$ is a layered compound consisting of slightly buckled $Cu(BO_3)$-
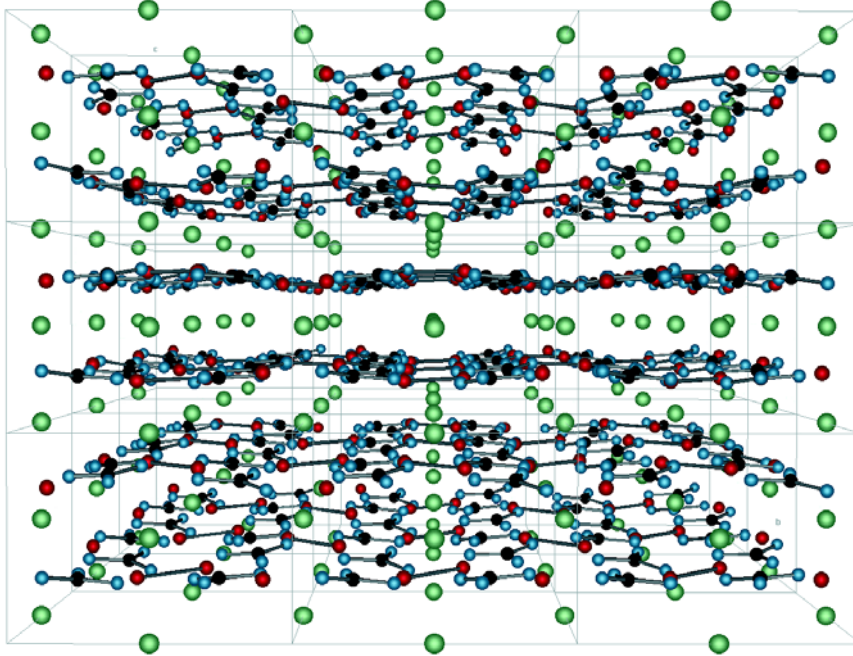

Figure 6.3.: Crystal structure of $SrCu_2(BO_3)_2$, which is a layered compound with slightly buckled $Cu(BO_3)$-planes separated by Sr-Atoms: green spheres; Cu: red, B: black, O: blue.

planes separated by Sr-Atoms. Fig. 6.4 gives a top-view onto an isolated $Cu(BO_3)$-plane. One clearly identifies two Cu^{2+}-ions (red circles) close to each other, which we choose to emphasise by connecting lines. These are the dimers. The magnetic properties of the crystal are dominated by the $S = 1/2$ spins which we consider to be situated on the Cu^{2+}-sites. Setting the interaction-strength of two adjacent spins to J_1 and assuming a (probably complicated)

---

[1] For $S = 1/2$ the product singlet state remains the ground state even in the anisotropic case, where $J^x \neq J^y \neq J^z$ in $S_i S_j = J^x S_i^x S_j^x + J^y S_i^y S_j^y + J^z S_i^z S_j^z$ [10]. In this case we have the peculiar but interesting situation that an eigen-state has higher symmetry (rotational invariance of singlets) than the system itself. In the language of particles one might say, that the symmetry of the vacuum (here: no triplons) is larger than the symmetry of the Hamiltonian.

exchange path J_2 over the borate-groups BO_3^{3-}, we see that a single $Cu(BO_3)$-plane can be mapped onto the Shastry-Sutherland model. This was first observed by Miyahara and Ueda [77] in 1999.
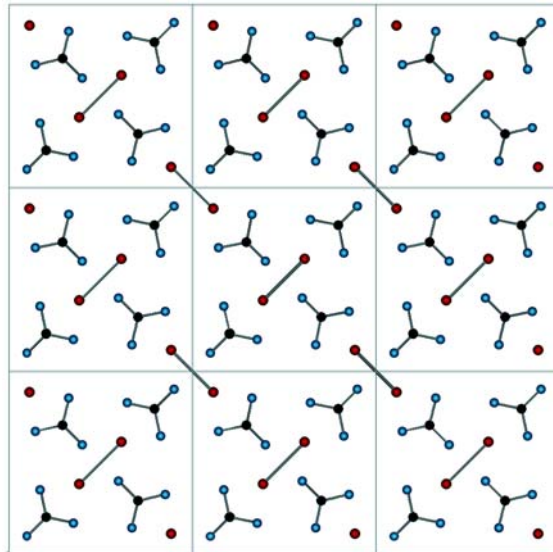

Figure 6.4.: A finite portion of a single $Cu(BO_3)$-plane in $SrCu_2(BO_3)_2$. The magnetism is governed by $S = 1/2$ spins located on the Cu^{2+} ions denoted by red circles. By geometry we find two Cu^{2+} ions close to each other and we connect them by lines. They form the dimers with interaction strength J_1. We assume another spin-exchange path via the borate groups (boron: black circles, oxygen: blue circles). These couplings are modelled by the J_2 bonds in Fig. 6.2. Thus, the depicted model-plane can be mapped onto the $S = 1/2$ Shastry-Sutherland model. Experiments show, that the exchange couplings must be considered to be positive. The crystal is an antiferromagnet. The ratio $x = J_2/J_1$ is sufficiently small so that the system is in the dimer state.

Every second $Cu(BO_3)$-plane is rotated by $\pi/2$ about one of the dimer centres, so that each dimer has a rotated dimer above and below. The resulting tetrahedral inter-plane interaction geometry is fully frustrated: the four spins of two dimers stacked atop of each other interact according to $(S_1+S_2)(S'_1+S'_2)$, where the S_i belong to the dimer in the lower plane and the S'_i belong to the dimer in the upper plane for instance. We see that both dimers must be excited for this interaction to be relevant. We thus expect the interactions perpendicular to the planes to be weak or ineffective (see also Ref. [78]) and we concentrate on the in-plane physics.

Before we summarise the experimental findings for $SrCu_2(BO_3)_2$ we wish to convey a preliminary understanding of the two-dimensional Shastry-Sutherland

model by taking a closer look at its $T = 0$ phase diagram. Fig. 6.5 shows a reprint of Fig. 2 in Ref. [79]. We will use the depicted phase diagrams to shed some light on the various phases of the model.

The classical phase diagram ($S \to \infty$) is depicted in the left part of Fig. 6.5 and has been derived in Ref. [10] already. It is no surprise that one finds a long range ordered Néel phase for large $J_2 > 0$ and a ferromagnetic ordering for large $J_2 < 0$. At $|J_2| = J_1$ there are crossovers to a helical phase with a pitch angle of $\Theta = \pi \pm \arccos(J_2/J_1)$ between two adjacent spins [10]. Along the line $J_2 = 0$ we find what one might call an isolated antiferromagnetic dimer state for $J_1 > 0$ and an analogous ferromagnetic dimer state for $J_1 < 0$.
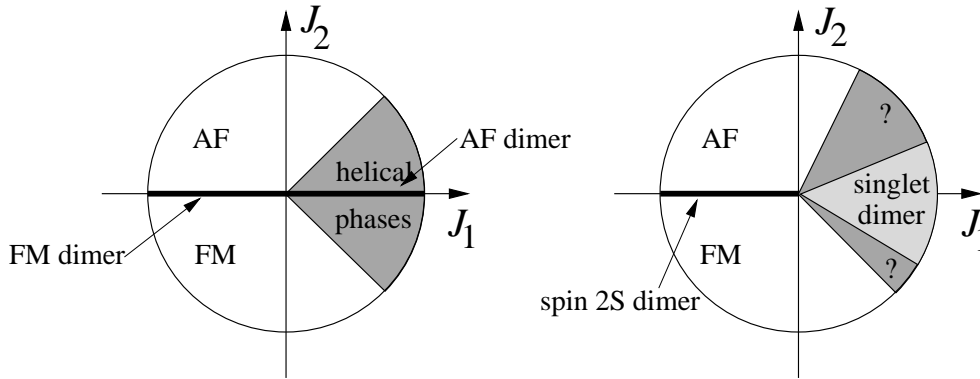

Figure 6.5.: The left part shows the classical phase diagram of the two-dimensional Shastry-Sutherland model. The phase transition lines can be calculated exactly. The right part depicts the phase diagram in the quantum mechanical case ($S < \infty$). The singlet dimer phase covers a finite region. The nature of the adjacent phases is not understood yet. (Figure kindly provided by U. Löw, published in [79].)

As soon as one enters the quantum mechanical regime ($S < \infty$), the above discussed short-ranged dimer-singlet product state becomes the exact ground state for $J_1 > 0$ and J_2 not too large. The situation is sketched in the right part of Fig. 6.5. One might picture these singlets to be the transmuted isolated antiferromagnetic dimer states of the last paragraph. In this perspective it is surprising, that quantum fluctuations seem to protect the dimer phase against the neighbouring phases. We will come back to this point later on. The quantum dimer phase extends over a larger area than its classical analogue. The quantum mechanical (anti-) ferromagnetic regimes persist, although they are slightly shifted. The phase diagram does not change on the $J_1 < 0$ side.

Löw and Müller-Hartmann [79] use variational arguments and consider the ground state to identify the individual phases. For the antiferromagnetic side ($J_2 > 0$) they find an exact lower critical ratio $x = J_2/J_1$ of $x_c = 1/(2S + 1)$

to which the dimer phase exists in any case for all finite spin values S. Note that for $S > 1/2$ this constitutes a better estimate than the original bound of Shastry and Sutherland. They also use exact diagonalisation to improve their estimates further. For $S = 1/2$ they calculate a (conservative) lower bond of $x_c \approx 0.59$. Finite size scaling turns out to be difficult, since not only the size of a cluster but also the shape seems to be important. Note that one always finds an intermediate regime for finite $J_2 > 0$.

For $J_2 < 0$ Löw and Müller-Hartmann find an analogous lower bond of $x_c = -1/S$ to the neighbouring phase. For $S = 1/2$, there is no intermediate phase. The system directly passes from the dimer phase to the long-range ordered ferromagnetic regime. In this case, $-1/S$ is the exact transition point. For larger S the intermediate phase re-appears.

A very intriguing issue is the nature of the intermediate phases next to the short-ranged dimer phase. A reasonable first guess is to assume a quantum mechanical equivalent to the classical helical phase. Using Schwinger boson mean field theory Albrecht and Mila [80] indeed find such a regime. For $S = 1/2$ and $J_2 > 0$ the Néel phase vanishes in favour of a helical phase in a second order transition at $x \approx 0.91$. They further find the system to undergo a first order transition from the intermediate helical regime to the dimer phase at $x \approx 0.606$.

Since then a large number of publications have appeared which address the problem of finding quantitative estimates for the phase boundaries and of identifying the nature of the intermediate phase. Since we will also touch on this subject later we give a compilation of results obtained by other authors here.

Sachdev et al. [81] construct a symplectic $\text{Sp}(2N)$-group invariant field theory which yields two different intermediate phases. Within this theory these phases appear as Bose condensates. According to their argument the intermediate regime exhibits helical and collinear phases. Another field theory by Carpentier and Balents [82] based on a Bose-dimer representation shows a weakly incommensurable spin density wave as intermediate phase. They additionally argue that there *must* be an intermediate regime on the antiferromagnetic side. A direct dimer to Néel transition cannot appear.

The remaining publications we focus on the $S = 1/2$ case. In an earlier work Miyahara and Ueda [77] use exact diagonalisation and fourth order perturbation theory. They find a direct dimer to Néel transition of first order (the ground state energies cross at a finite angle). The transition occurs at $x \approx 0.7$, which is a broadly accepted value. Large scale exact diagonalisations (32 sites) were performed by Läuchli et al. [83]. By comparing ground state energies they find an upper critical value of $x_c = 0.67$ for the dimer phase. They claim that

an intermediate phase has to lie within the interval $0.67 < x < 0.70$ and argue in favour of an intermediate plaquette phase. They exclude the possibility of an intermediate columnar phase. Another numerical study based on a novel operator variational method [84] supports a helical intermediate phase again.

Perturbational studies do not seem to yield a better understanding. Various publications support different pictures. Koga and Kageyama [85] argue in favour of a plaquette phase in the interval $0.677 < x < 0.861$. Their calculations are based on perturbation theory with different starting points: isolated plaquettes, isolated dimers and Ising-limit. A series of publications by Zengh et al. [86, 87] however excludes the scenarios of an intermediate plaquette or helical phase. They employ high order perturbation theory and compare the ground states of various phases and find that only a columnar phase might apply in the range $0.67 < x < 0.83$. Unfortunately, their investigation of the staggered magnetisation, which vanishes as soon as one left the Néel ordered phases, is hampered by large errors bars in the region of interest. They also investigate the one-triplon gap above the singlet ground state in the dimer phase. This gap vanishes at $x = 0.691$ defining a very precise upper bound for the dimer phase.

In conclusion, the community seems to agree on an upper critical value slightly below $x_c = 0.7$ for the dimer phase in the two-dimensional Shastry-Sutherland model with spin $S = 1/2$. There are very strong hints on an intermediate phase between the dimer and the Néel regime in the antiferromagnetic domain $J_1, J_2 > 0$. The nature of the intermediate phase is not understood and is an issue of intensive current research.

Before we start to present our results, we should briefly summarise the experimental findings for SrCu$_2$(BO$_3$)$_2$. Comparing theoretical results to the real substance will illuminate the situation considerably.

Kageyama et al. [88] were the first to publish data on the magnetic response of SrCu$_2$(BO$_3$)$_2$. The magnetic susceptibility measured on powder shows a maximum at around 20 K and a rapid drop towards zero with decreasing temperature, indicating an energy gap in the magnetic spectrum. An exponential low temperature fit gives a gap of ≈ 19 K $= 1.6$ meV. The high temperature tail gives a Weiss temperature of about -92.5 K with an effective value $g = 2.14$. They further performed a spin echo experiment (copper nuclear quadrupole resonance) measuring the relaxation time after an external perturbation. They confirm the existence of a singlet ground state. An exponential fit to the spin-lattice relaxation time gives a magnetic gap of ≈ 30 K $= 2.6$ meV to the first excitation. They conclude, that SrCu$_2$(BO$_3$)$_2$ is a realization of the Shastry-Sutherland model in the dimer phase.

A year later Kageyama et al. published inelastic neutron scattering (INS)

data obtained from a large crystal [89]. They confirmed the existence of a small gap of ≈ 3 meV at momentum $\mathbf{K} = (0, 0)$. The lowest observed mode is nearly dispersionless. We will come back to this measurement in section 6.6, where we will also show a plot of their findings in the momentum-energy plane, Fig. 6.45 on page 174.

Other experiments like electron spin resonance [90], far infrared studies [91] and nuclear magnetic resonance [92] give further evidence for a singlet ground state above which a triplon excitation with gap 2.9 meV can be found.

Further support of this scenario comes from a Raman experiment [93], which shows interesting multi-triplon resonances in addition (see Fig. 6.29 on page 150). We will come back to this point in section 6.5.3.[2]

One can find various fits of the model parameters to the experimental data. Generally they are based on a simultaneous fit of the one-triplon gap and the magnetic susceptibility. The earliest fit by Miyahara and Ueda [77] gives $x = 0.68$ and $J_1 = 100$ K $= 8.617$ meV. In a later and improved calculation they find $x = 0.635$ and $J_1 = 85$ K $= 7.325$ meV [96]. Other values in this range are e.g. $x = 0.664$ and $J_1 = 83$ K $= 7.15$ meV [86] or $x = 0.65$ and $J_1 = 87$ K $= 7.50$ meV [84]. The range of given x-values is rather close to the critical value of $x_c \approx 0.69$. There are experimental considerations to push $SrCu_2(BO_3)_2$ towards the critical value by means of pressure or chemical substitutions. A direct observation of a real substance at or close to a quantum critical point would indeed be very interesting, but has so far not been accomplished.

The $S = 1/2$ Shastry-Sutherland model is challenging in two ways. On the one hand, the fascinating phase diagram with its unresolved structures is of great theoretical interest and may give rise to insights into the largely unknown and complex physics of two-dimensional spin liquids. On the other hand, the realization of the model in the experimentally accessible $SrCu_2(BO_3)_2$ allows a direct comparison of theoretical findings to a large collection of real data.

Starting with the next section we present an extensive survey of these issues by applying the perturbative CUT method with isolated dimers as starting point. In this case the ground state is given by the product state of singlets on the dimers. An elementary excitation, or quasi-particle, is given by promoting one singlet to a triplon which we call a *triplon*. Although we are limited to the dimer phase for all our calculations[3], we will be able to produce strong

---

[2] $SrCu_2(BO_3)_2$ shows magnetisation plateaus for higher external magnetic fields at 1/8, 1/4 and 1/3 of the full magnetisation. We refer the reader to Ref. [94], where we present a theory for these plateaus. Another interesting work on this issue can be found in Ref. [95].

[3] The dimer phase extends at maximum to the x-value where one of the gaps of the model vanishes. At the same time this value marks the point up to which our approach can be

predictions. We start by investigating the low-lying energy levels including the two-triplon sector. This will lead to a new upper critical value x_c for the dimer phase and yield values for J_1 and J_2 by fitting our findings to various experimental $T = 0$ data simultaneously.

By means of the perturbative CUT method we are also in the position to calculate spectral densities. We will identify the relevant Raman and INS observables for the Shastry-Sutherland and calculate the corresponding line shapes. Comparing these results to the experimental findings will lead to a considerable advance in understanding the system.

6.2. One-Triplon Energies

We begin by calculating the one-triplon dispersion. In subsection 6.2.1 we show how the effective Hamiltonian H_{eff} can be constructed from the original Hamiltonian (6.1). In subsection 6.2.2 we investigate the symmetries of H_{eff} and deduce some interesting consequences for the one-triplon hopping amplitudes. Finally, the one-triplon dispersion is calculated in subsection 6.2.3.

6.2.1. CUT-Implementation

To begin with we show that Hamiltonian (6.1) meets the conditions (A) and (B) repeated at the beginning of this chapter. To this end we rewrite the Hamiltonian

$$\frac{H}{J_1} = U + xV \ , \quad \text{with } x = \frac{J_2}{J_1} \ \text{ and}$$

$$U = \sum_{[i,j]} S_i S_j \ ,$$

$$V = \sum_{\langle i,j \rangle} S_i S_j \ . \tag{6.2}$$

Note that U merely counts the number of excited dimers or, equivalently, the number of triplons in the system. Thus, in the limit of isolated dimers, $x = 0$, H is bounded from below and has an equidistant energy spectrum. The quasi-particles are triplons on the dimers and we can identify $Q = U$ to be the operator which counts these particles.

The perturbation part V can be decomposed in operators, increasing or decreasing the number of triplons, according to (potential $T_{\pm 2}$ operators cancel

used (cf. section 2)

out due to the frustration)

$$V = T_{-1} + T_0 + T_1 , \quad \text{with} \tag{6.3}$$

$$T_{\pm 1,0} = \frac{1}{2} \sum_\nu \mathcal{T}_{\pm 1,0}(\nu) , \tag{6.4}$$

where ν denotes pairs of adjacent dimers. Thus, the Shastry-Sutherland Hamiltonian meets the conditions (A) and (B) of section 3.1 and we can use the effective operators H_{eff} (Eq. (3.18)) and $\mathcal{O}_{\text{eff}}$ (Eq. (3.36)). They act on the effective lattice Γ_{eff} depicted on the right hand side of Fig. 6.2.

Let us elaborate on the local operators $\mathcal{T}_n(\nu)$, which sum up to give the global ladder operators T_n. A specific pair of adjacent dimers ν is depicted in Fig. 6.6. Note that all other pairs are related to the depicted one by simple symmetries. The state of the depicted pair is determined by $|x_1, x_2\rangle$, where $x_1, x_2 \in \{s, t^1, t^0, t^{-1}\}$ are singlets or one of the triplons occupying the vertical and horizontal dimer, respectively. The superscript $n \in \{0, \pm 1\}$ in t^n stands for the S^z component. The action of the local operators $\mathcal{T}_i$ on the states $|x_1, x_2\rangle$
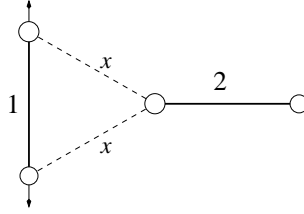
Figure 6.6.: A pair of adjacent dimers (intra-dimer coupling-constant set to unity) connected by the perturbing interaction x. The local operators $\mathcal{T}_i$ as defined in Tab. 6.1 acquire a global minus, if we reflect the pair on the indicated axis and keep the notation $|x_1, x_2\rangle$ as defined in the text. This is due to the singlet antisymmetry under reflection.

is given in Tab. 6.1. The remaining matrix elements can be constructed by using $\mathcal{T}_n^\dagger = \mathcal{T}_{-n}$ (H_{eff} is hermitian). Note that we need to fix the orientation for singlets, say spin up with positive sign always at the right (upper) site of the dimers. Hence $\mathcal{T}_1$ and $\mathcal{T}_{-1}$ acquire a global minus for oppositely oriented dimer pairs (reflection of the dimer pair in Fig. 6.6 about the vertical dimer). Instead of Hamiltonian (6.1) we use the effective Hamiltonian H_{eff} (Eq. (3.18)) with the T_i defined in Eqs. (6.3,6.4) from now on. The effective Hamiltonian (3.18) simplifies the computations considerably. Since $[H_{\text{eff}}, U] = 0$, H_{eff} is block diagonal allowing triplon conserving processes only. Thus the effective Hamiltonian acts in a much smaller Hilbert space than the original problem.

$\mathcal{T}_0$		
$\lvert t^{\pm 1}, t^{\pm 1}\rangle$	$\longrightarrow$	$\lvert t^{\pm 1}, t^{\pm 1}\rangle$
$\lvert t^{\pm 1}, t^0\rangle$	$\longrightarrow$	$\lvert t^0, t^{\pm 1}\rangle$
$\lvert t^{\pm 1}, t^{\mp 1}\rangle$	$\longrightarrow$	$\lvert t^0, t^0\rangle - \lvert t^{\pm 1}, t^{\mp 1}\rangle$
$\lvert t^0, t^0\rangle$	$\longrightarrow$	$\lvert t^1, t^{-1}\rangle + \lvert t^{-1}, t^1\rangle$
$\mathcal{T}_1$		
$\lvert t^{\pm 1}, s\rangle$	$\longrightarrow$	$\mp\lvert t^0, t^{\pm 1}\rangle \pm \lvert t^{\pm 1}, t^0\rangle$
$\lvert t^0, s\rangle$	$\longrightarrow$	$\lvert t^1, t^{-1}\rangle - \lvert t^{-1}, t^1\rangle$

Table 6.1.: The action of the local operators $\mathcal{T}_0$ and $\mathcal{T}_1$ as they appear in Eq. (6.4) on all relevant states of the dimer pair depicted in Fig. 6.6. These operators conserve the total S^z component. Note that $\mathcal{T}_1$ can only create another triplon on the horizontal dimer if one already exists on the vertical dimer. This has also been noted in Ref. [10]. Potential $\mathcal{T}_{\pm 2}$ operators cancel out due to the frustration. Matrix elements not listed are zero.

In addition to this simplification the explicit form of H_{eff} provides a simple and comprehensive picture of the physics involved. Imagine we put a triplon on one of the dimers in the lattice. In the real substance this local excitation would polarise its environment due to the exchange couplings and must be viewed as a quasi-particle dressed by a cloud of virtual excitations fluctuating in space and time. The effective Hamiltonian includes these fluctuations as virtual processes $T(\underline{m})$, each weighted by the factors $C(\underline{m})$. Each process ends with a state having the same number of triplons as the initial state. Other quantum numbers such as the total spin are also conserved. As the order k is increased longer processes are allowed for and the accuracy of the results will be enhanced. Inspecting the weight factors $C(\underline{m})$ shows that longer processes have less influence (see appendix B).

Let us follow one of the possible virtual processes and understand why the observed triplon dispersion of $SrCu_2(BO_3)_2$ is rather flat (cf. Fig. 6.11 on page 113 or Fig. 6.45 on page 174). Suppose we begin with one triplon in the lattice as depicted in the upper left corner of Fig. 6.7. By applying T_1 once we can create another triplon only on one of the two *horizontally* adjacent dimers as is clear from Tab. 6.1. From there we create another one and so on till we can close a circle (bottom left state in Fig. 6.7). We now start de-exciting triplons by T_{-1} processes and end up with the shifted triplon. The amplitude for this hopping is $\propto x^6$. It is the leading amplitude (see also Ref. [97]). Therefore the triplons are rather localised leading to a flat dispersion.

Examining the two-triplon sector in the next section we will show that *correlated* hopping processes already occur in second order. The actual dispersion,
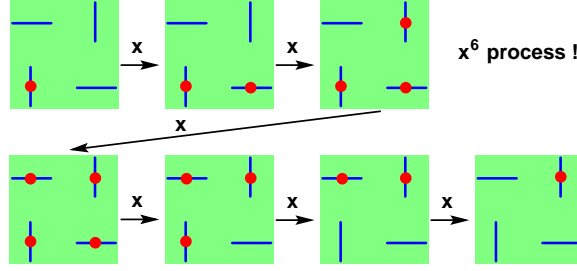
Figure 6.7.: Leading (virtual) process for one-triplon hopping corresponding to $x^6 T(\underline{m}) = x^6 T_{-1} T_{-1} T_{-1} T_1 T_1 T_1$. Red (dark) dots are triplons, bars are dimers. There is no lower order process leading to one-triplon motion.

however, sets in only in third order. This much lower order (x^3 instead of x^6) explains the much stronger two-triplon dispersion (see Fig. 6.45 again).

To quantify the picture constructed let $|\mathbf{r}\rangle = |r_1, r_2\rangle$ denote the state of the system with one triplon at $\mathbf{r} \in \Gamma_{\text{eff}}$ (see Fig. 6.2) and singlets on all other sites. These states span the one-particle sub-space of the full Hilbert space of H_{eff}. Recall, that we can calculate the thermodynamic one-triplon hopping amplitudes by the action of $H_1 = H_{\text{eff}} - H_0$ on these states. Now, as long as we are in the singlet dimer phase, H_0 gives the *constant* ground state energy, which we set to zero. Therefore, the thermodynamic amplitude $t_{\mathbf{r}', \mathbf{r}}^{\pi(\mathbf{r})}$ for a one triplon-hopping from site $\mathbf{r}$ to site $\mathbf{r}'$ can be obtained from

$$t_{\mathbf{r}', \mathbf{r}}^{\pi(\mathbf{r})} = \langle \mathbf{r}' | H_{\text{eff}} | \mathbf{r} \rangle = t_{\mathbf{d}}^{\pi(\mathbf{r})} , \quad \text{with } \mathbf{d} = \mathbf{r}' - \mathbf{r} , \tag{6.5}$$

where the upper index $\pi(\mathbf{r}) \in \{v, h\}$ allows to distinguish whether the hopping started on a vertically oriented (v) or a horizontally oriented dimer (h). Furthermore we choose to split the hopping amplitudes into a net part $\bar{t}_{\mathbf{d}}$ and a deviation part $dt_{\mathbf{d}}$

$$t_{\mathbf{d}}^{\pi(\mathbf{r})} = \bar{t}_{\mathbf{d}} + e^{i\mathbf{Q}\mathbf{r}} dt_{\mathbf{d}} , \tag{6.6}$$

with $\mathbf{Q} = (\pi, \pi)$. The net and deviation parts are given by

$$\bar{t}_{\mathbf{d}} = \left(t_{\mathbf{d}}^v + t_{\mathbf{d}}^h \right) / 2$$

$$dt_{\mathbf{d}} = \left(t_{\mathbf{d}}^v - t_{\mathbf{d}}^h \right) / 2 , \tag{6.7}$$

respectively.

The computer implementation, allowing the calculation of the hopping amplitudes $t_{\mathbf{d}}^v$ and $t_{\mathbf{d}}^h$ as polynomials in x, follows our illustrations in section 3.5. We calculated all amplitudes up to and including order 15.

The cluster needed to obtain the *thermodynamic* amplitudes is easily constructed. As has been shown above, the motion of a single triplon by virtue of the operators $T_{\pm 1}$ can be pictured to follow a zig-zag path. The operator T_0 does not lead to any motion. Consider the triplon to be placed on a vertical dimer initially. Then, a new triplon can be created on one of the horizontal dimers to its left or right. Nothing else is possible. In a next step yet another triplon can be created on the dimers to the top or to the bottom and so on. In 15th order this can happen 7 times, since we need enough T_{-1} operators to annihilate all triplons but one. All processes $T(\underline{m})$ *must* conserve the number of triplons! Now, a sufficiently large cluster for all amplitudes up to 15th order can be constructed by assuming the initial triplon to be placed on the middle dimer and including all dimers that could be visited by all zig-zag paths of lengths 7.

Fig. 6.8 illustrates the construction of the cluster for 9th order. All paths of length 4 have to be considered. The set of all depicted dimers is the resulting cluster. Two zig-zag paths of length 4 are indicated by arrows. Each path starts at the dimer in the centre of the cluster.
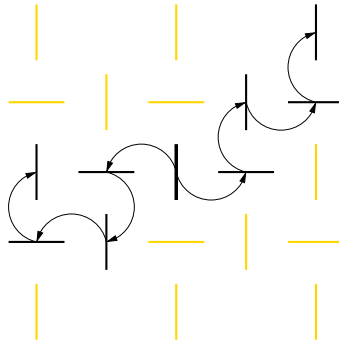
Figure 6.8.: The construction of a sufficient cluster to calculate one-triplon hopping amplitudes in ninth order. We need to consider all zig-zag paths of length four. Two of them are indicated by arrows. All possible paths start at the dimer in the centre of the cluster. Considering all these paths of length four leads to the depicted cluster.

The restricted motion of triplons is due to the geometrical frustration of the Shastry-Sutherland lattice. In this perspective frustration helps to reduce the size of the clusters needed for thermodynamic relevant calculations (cf. footnote on page 36).

The cluster constructed in the described way contains 57 dimers. Since each dimer can be in four different states, we need to reserve four bits per dimer. The full state of the cluster can thus be stored in eight integers, each composed of four bytes. Since triplons will always be created in chain-like structures, the

actual number of encountered states stays well below the maximum number of states possible on the cluster in 15th order. A memory capacity of about 2 GB and a CPU time of about 20h suffice to calculate all hopping amplitudes.[4]

6.2.2. Symmetries

Before we calculate the one-triplon dispersion quantitatively in the next section it is worthwhile to look at the symmetries of the model. The two-dimensional space group of the model can be identified to be p4mm as can be verified in Fig. 6.9. The underlying point group is 4mm, of which the irreducible representations are $\Gamma_1(1)$, $\Gamma_2(x^2 - y^2)$, $\Gamma_3(xy)$, $\Gamma_4(xy(x^2 - y^2))$ and $\Gamma_5(x, y)$. Simple polynomials are given in brackets to show the transformation behaviour (see Fig. 6.9). The two-dimensional representation Γ_5 is represented by a vector. We will use these representations later on to classify the momentum eigen-states in the one- and two-triplon sector. We will not treat all symmetry
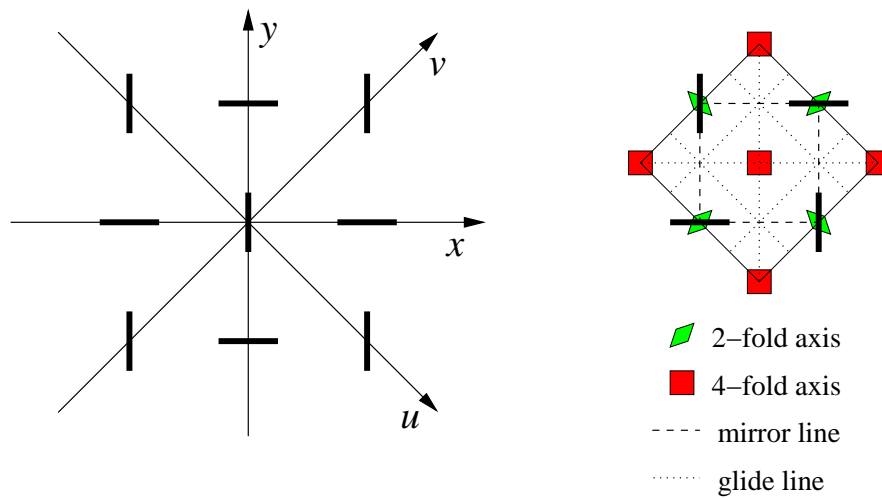
Figure 6.9.: The left figure illustrates how we choose the coordinate system. In the right figure we depict a possible unit cell of the Shastry-Sutherland model with the dimers arranged at the sides of the cell. All symmetries are depicted. The two-dimensional crystallographic space group is p4mm.

aspects here but concentrate on those that will be of use later on.

---

[4] Note that all hopping amplitudes can be calculated in a single run of the algorithm illustrated in section 3.5 because the clusters can be chosen large enough for all hopping amplitudes. So H_{eff} can be applied to one initial state (triplon at the origin) and all possible finite states can be read-off from the result.

We choose the coordinate system parallel to the dimers such that one dimer (horizontal or vertical) lies in the origin and introduce two diagonals u and v crossing the origin with slope -1 and 1, respectively (see Fig. 6.9). The distance between the centres of two adjacent dimers is set to unity.

Several relations between different hopping amplitudes can be deduced. To this end we define six symmetry operations which map the lattice onto itself. Note that the fixed singlet orientation can lead to negative phase factors

- $m_{x/y}$: Reflection about x/y-axis

$$m_{x/y}|r_1, r_2\rangle = (-1)^{r_1+r_2}|\pm r_1, \mp r_2\rangle \ ,$$

- I: Inversion about the origin

$$I|r_1, r_2\rangle = |-r_1, -r_2\rangle \ ,$$

- $\sigma_{v/u}$: Reflection about the diagonals v/u plus translation by $(0, -1)$

$$\sigma_{v/u}|r_1, r_2\rangle = |\pm r_2, \pm r_1 - 1\rangle \ ,$$

- R: Rotation of $\pi/2$ about one of the 4-fold axes (see Fig. 6.9)

$$R|r_1, r_2\rangle = (-1)^{r_1+r_2}|-r_2, r_1 + 1\rangle \ .$$

Since these operations leave H unchanged they all commute with H_{eff}. Applying m_x to Eq. (6.5) we find

$$
\begin{aligned}
t^{\pi(\mathbf{r})}_{\mathbf{r},\mathbf{r}'} &= \langle r_1', r_2'|H_{\text{eff}}|r_1, r_2\rangle \\
&= (-1)^{r_1+r_2+r_1'+r_2'}\langle r_1', -r_2'|H_{\text{eff}}|r_1, -r_2\rangle \\
&= (-1)^{r_1+r_2+r_1'+r_2'}\ t^{\pi(\mathbf{r})}_{(r_1', -r_2'),(r_1, -r_2)} \\
\Leftrightarrow t^{\pi(\mathbf{r})}_{\mathbf{d}} &= (-1)^{d_1+d_2}\ t^{\pi(\mathbf{r})}_{(d_1, -d_2)} \ .
\end{aligned}
\qquad (6.8)
$$

Analogously using m_y, I, σ_u, σ_v and R we find

$$t_{\mathbf{d}}^{\pi(\mathbf{r})} = (-1)^{d_1+d_2} t_{(-d_1,d_2)}^{\pi(\mathbf{r})} \tag{6.9}$$

$$= t_{-\mathbf{d}}^{\pi(\mathbf{r})} \tag{6.10}$$

$$= t_{(-d_2,-d_1)}^{\pi(\mathbf{r}-(0,1))} \tag{6.11}$$

$$= t_{(d_2,d_1)}^{\pi(\mathbf{r}-(0,1))} \tag{6.12}$$

$$= (-1)^{d_1+d_2} t_{(-d_2,d_1)}^{\pi(\mathbf{r}+(0,1))} \tag{6.13}$$

respectively. In particular, Eqs. (6.9) and (6.10) together yield

$$t_{(d_1,0)}^{\pi(\mathbf{r})} = (-1)^{d_1} t_{(-d_1,0)}^{\pi(\mathbf{r})} = (-1)^{d_1} t_{(d_1,0)}^{\pi(\mathbf{r})}$$

$$\Rightarrow t_{(d_1,0)}^{\pi(\mathbf{r})} = 0, \text{ if } d_1 \text{ odd; analogously} \tag{6.14}$$

$$\Rightarrow t_{(0,d_2)}^{\pi(\mathbf{r})} = 0, \text{ if } d_2 \text{ odd,} \tag{6.15}$$

describing the interesting fact, that hopping along one of the axes has non-zero amplitude only if this hopping moves the triplon by an even number of sites in Γ_{eff}.

6.2.3. Dispersion

Since Γ_{eff} is translational invariant, the calculation of the one-triplon dispersion follows our discussion presented in section 3.4. However, we have to take care of the A-B sublattice structure of Γ_{eff}. This can be taken into account by the following substitutions (N is the number of sites in Γ_{eff})

$$\mathbf{k} \rightarrow \mathbf{k} + \sigma \mathbf{Q} , \quad \text{with } \mathbf{Q} = (\pi, \pi) \text{ and } \sigma \in \{0,1\} \tag{6.16}$$

$$|\mathbf{k}\rangle \rightarrow |\sigma, \mathbf{k}\rangle = \frac{1}{\sqrt{N}} \sum_{\mathbf{r}} e^{i(\mathbf{k}+\sigma\mathbf{Q})\mathbf{r}} |\mathbf{r}\rangle , \quad \mathbf{k} \in \text{MBZ and} \tag{6.17}$$

$$t_{\mathbf{r}',\mathbf{r}} \rightarrow t_{\mathbf{r}',\mathbf{r}}^{\pi(\mathbf{r})} = \bar{t}_{\mathbf{r}',\mathbf{r}} + e^{i\mathbf{q}\mathbf{r}} dt_{\mathbf{r}',\mathbf{r}} . \tag{6.18}$$

The substitution for the hopping amplitudes has already been discussed at the end of section 6.2.1. The introduction of the extra quantum number σ is guided by the following consideration, which can be easily reproduced by means of Fig. 6.31 on page 155. In part (a) we depict the direct lattice Γ_{eff} spanned by the primitive vectors $\mathbf{a}$ and $\mathbf{b}$. Any position vector $\mathbf{r}$ of a triplon in

Γ_{eff} is a linear combination of integer multiples of $\mathbf{a}$ and $\mathbf{b}$. Yet, Γ_{eff} is mapped onto itself by *those* translations only, which are linear combinations of integer multiples of $\tilde{\mathbf{a}}$ and $\tilde{\mathbf{b}}$, spanning the lattice Γ_{AF}. Thus, the crystal momenta $\mathbf{k}$ take unique values only in the magnetic Brillouin zone (MBZ), which is the first Wigner Seitz cell of the reciprocal lattice of Γ_{AF} (see Fig. 6.31(b)). However, the number of states in the MBZ is only half as large as the number of states contained in the first Brillouin zone B_{eff} of the primarily considered lattice Γ_{eff}. This loss of states is compensated by the additional quantum number σ, which is allowed to take two values. Thus, the number of states $|\mathbf{r}\rangle$ equals the number of states $|\sigma, \mathbf{k}\rangle$.

The action of the one-triplon part $H_1 = H_{\text{eff}} - H_0$ on the one-triplon momentum states is rapidly calculated. Inversion symmetry holds for Γ_{eff}. With $\bar{\sigma} = 1 - \sigma$ we obtain

$$\langle \sigma, \mathbf{k}|\mathcal{H}_{\text{eff}}|\sigma, \mathbf{k}\rangle = \bar{t}_{\mathbf{0}} + 2\sum_{\mathbf{d}>0} \bar{t}_{\mathbf{d}} \cos((\mathbf{k}+\sigma Q)\mathbf{d}) \equiv a_\sigma$$

$$\langle \bar{\sigma}, \mathbf{k}|\mathcal{H}_{\text{eff}}|\sigma, \mathbf{k}\rangle = dt_{\mathbf{0}} + 2\sum_{\mathbf{d}>0} dt_{\mathbf{d}} \cos((\mathbf{k}+\bar{\sigma} Q)\mathbf{d}) \equiv b \ . \qquad (6.19)$$

Apart from minor changes the calculation is similar to the one presented in section 3.4.1. In appendix E we show that $dt_{\mathbf{0}} = 0$ and $dt_{\mathbf{r}} = 0$ for $r_1 + r_2$ odd. Hence b does not depend on $\bar{\sigma}$

$$b = 2\sum_{\substack{\mathbf{r}>0 \\ r_1+r_2 \text{ even}}} dt_{\mathbf{r}} \cos(\mathbf{k}\mathbf{r}) \ , \qquad (6.20)$$

and $\mathcal{H}_{\text{eff}}$ is symmetric in the new states. The remaining 2×2 problem can be solved easily to yield the dispersion

$$\omega_{1/2}(\mathbf{k}) = \underbrace{\frac{a_0 + a_1}{2}}_{\omega_0(\mathbf{k})} \pm \frac{1}{2}\sqrt{(a_0 - a_1)^2 + 4b^2} \ . \qquad (6.21)$$

The one-triplon dispersion splits into two branches. We want to point out, however, that at $\mathbf{k} = \mathbf{0}$ and at the borders of the MBZ (i.e. $|k_1 + k_2| = \pi$ or $|k_2 - k_1| = \pi$) the two branches fall onto each other leading to a two-fold degenerate dispersion. An analogous degeneracy is noticed in the two-triplon sector as we will show in the next section. In appendix F we demonstrate that the degeneracy is due to the point symmetry R in combination with the glide line symmetry $\sigma_{u/v}$ and show that $(a_0 - a_1)$ and b both vanish. Moreover, $(a_0 + a_1)$ is a sum over $\mathbf{r}$ with $r_1 + r_2$ even and thus contains "even" hopping

amplitudes only. At $\mathbf{k} = \mathbf{0}$ and at the border of the MBZ we therefore find that one-triplon hopping takes place on one species of the two sublattices A/B in Γ_{eff} only. In other words, the triplons live either on the horizontal or on the vertical dimers for these $\mathbf{k}$-values.

It is interesting to see that the one-triplon eigen-states at the degenerate point $\mathbf{k} = \mathbf{0}$ fall into the two-dimensional Γ_5 representation. To see this we consider the m_y symmetry operation as an example. At $\mathbf{k} = \mathbf{0}$ we have the two states

$$|0\rangle = |\sigma = 0, \mathbf{k} = \mathbf{0}\rangle = \sum_{\mathbf{r} = r_1, r_2} |\mathbf{r}\rangle$$

$$|1\rangle = |\sigma = 1, \mathbf{k} = \mathbf{0}\rangle = \sum_{\mathbf{r} = r_1, r_2} (-1)^{r_1 + r_2} |\mathbf{r}\rangle \ . \tag{6.22}$$

Applying the m_y symmetry to $|0\rangle$ for instance gives

$$m_y |0\rangle = \sum_{r_1, r_2} (-1)^{r_1 + r_2} |-r_1, r_2\rangle = \sum_{r_1, r_2} (-1)^{r_1 + r_2} |r_1, r_2\rangle = |1\rangle \ . \tag{6.23}$$

Similarly we find $m_y |1\rangle = |0\rangle$. Thus, under the action of m_y the two states transform like the vector $(y + x, y - x)$, which is an element of Γ_5. The one-triplon momentum states being Γ_5 at $\mathbf{k} = \mathbf{0}$ will be of interest in the section on the two-triplon spectrum again.

Expanding the square root in Eq. (6.21) about the limit of vanishing x produces a term $\propto x^{10}$ in leading order. Hence the energy splitting starts in 10th order and is negligible for all reasonable values of x. The fact that the splitting starts four orders later than the dispersion may be understood by observing that $(a_0 - a_1)$ is a sum over $\mathbf{r}$ with $r_1 + r_2$ odd. From the discussion at the end of section 6.2.2 it is clear that $t_{\pm 1, 0}^{\pi(\mathbf{r})}$ and $t_{0, \pm 1}^{\pi(\mathbf{r})}$ vanish so that the leading odd process is $t_{\pm 2, \pm 1}^{\pi(\mathbf{r})}$ or $t_{\pm 1, \pm 2}^{\pi(\mathbf{r})}$ (knight moves), which start in 10th order only. One may object that b contains $dt_{1,1}$, which could be larger, but from relation (E.5) in appendix E follows that $dt_{1,1} = 0$. The amplitudes $dt_{\pm 2, 0}$ and $dt_{0, \pm 2}$ in b also start in 10th order only. Hence the almost degeneracy in the one-triplon sector can be understood on the basis of the symmetries of the lattice.

Since the corrections introduced by the square root on the right hand side of Eq. (6.21) are very small, we henceforth consider $\omega_0(\mathbf{k})$ only. Evaluating our exact results (fractions) for $\omega_0(\mathbf{k})$ to floats we obtain the decimal numbers computed by Zheng et al. [98].

Let us focus on the one-triplon gap $\omega_0(\mathbf{0})$. We give the first eight orders

$$\omega_0(\mathbf{0}) = -x^2 - \frac{1}{2} x^3 - \frac{1}{8} x^4 + \frac{5}{32} x^5 - \frac{7}{384} x^6 - \frac{2051}{4608} x^7 - \frac{39091}{55296} x^8 \ . \tag{6.24}$$

The full 15$^{\text{th}}$ order result is depicted as solid black line in Fig. 6.10. The use of Dlog-Padé approximants (dashed lines) allows to precisely fix the value $x_c = 0.697$ where the one-triplon gap vanishes. The result obtained by using optimised perturbation theory (OPT) with $\alpha = -0.2$ is depicted as grey solid curve, very close the direct series result. OPT does not lead to an improvement for the one-triplon dispersion. However, OPT will become important in the chapters 6.5 and 6.6 on spectral densities.
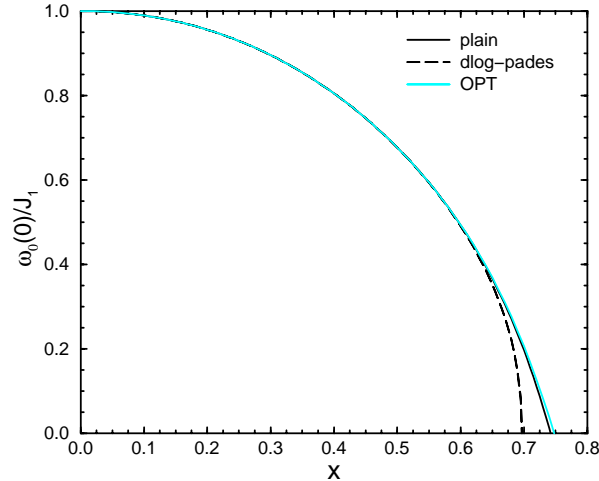
Figure 6.10.: One-triplon gap $\omega_0(\mathbf{k} = \mathbf{0})$ in units of J_1 as function of x. The plain series result is depicted as solid black line. The dashed lines are the Dlog-Padés [7,7], [8,6] and [6,8]. They coincide perfectly and yield $x_c = 0.697$ as the value were the gap vanishes. The solid cyan (grey) line is the result obtained by using optimised perturbation theory with $\alpha = -0.2$.

The critical value x_c is in complete accordance with the finding in Ref. [86]. The vanishing of Δ indicates the definite breakdown of the dimer phase. It may happen that another excitation becomes soft before the triplon vanishes or that a first order transition takes place. These possibilities will be of interest in the next section, where we investigate the two-triplon sector.

Let us turn to a comparison of the theoretical dispersion to experimental data for $SrCu2(BO_3)_2$. To fit the dispersion we make use of the parameter dependence of our results by requiring the curves to go through certain points and solve the resulting set of equations. At $\mathbf{k} = (0,0)$ ESR [90], FIR [91] and INS [89] data suggest a value of $\omega(0,0) = (2.98 \pm 0.01)$meV (the approximate error applies for ESR and FIR). At finite $\mathbf{k}$ we have to rely on the INS meas-

urement [89], which contains rather large errors. In Fig. 6.11 we show the INS data (bullets and error bars) and three of our fitted curves. For the parameter values given we get an excellent agreement. There are two bands for each parameter set. However, the difference is so small that they cannot be distinguished optically. Because of the flatness of the dispersion and the comparably
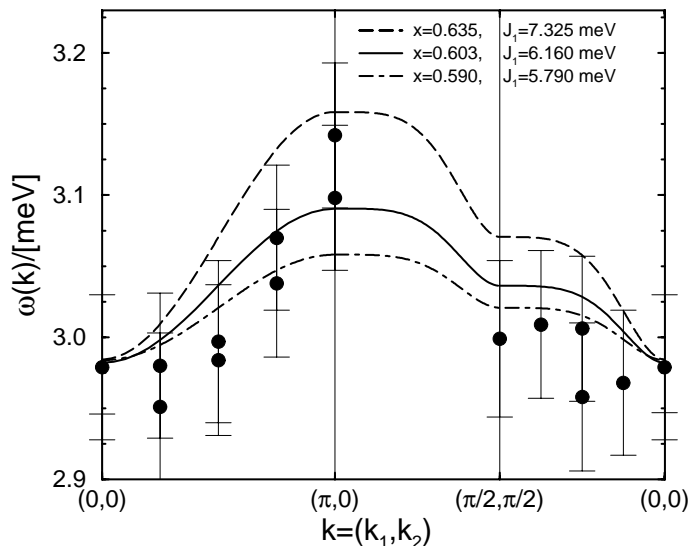
Figure 6.11.: One-triplon dispersion. Our theoretical results fitted to INS data (bullets, experimental errors at least as large as error bars). Due to the large errors it is not possible to fit the model parameters unambiguously. The set $(x, J_1) = (0.635, 7.325 \text{ meV})$ is taken from Ref. [96].

large error bars it is not possible to fix the model parameters unambiguously. As sketched in Fig. 6.11 one can lower x and J_1 simultaneously without losing reasonable agreement. On the basis of the one-triplon dispersion alone it is not possible to fix the model parameters quantitatively. This issue will be left to the next section.

We also considered a generalised Shastry-Sutherland model, where we introduced an additional coupling J_3 preserving the exact dimer singlet ground state. We choose to not present any results for this model. However, results for the one-triplon dispersion in the generalised model can be found in Ref. [99]. In Ref. [94] we present the phase diagram of the generalised model and comment on its magnetisation plateaus.

6.3. Two-Triplon Bound states

We now turn to the two-triplon part of the spectrum of $SrCu_2(BO_3)_2$. The basic implementational details have already been discussed in the preceding section. Let us begin by focusing on a qualitative understanding of the two-triplon dynamics. By what might be called *correlated* hopping a finite motion in the two-triplon sector sets in in second order already. The leading processes are depicted in Fig. 6.12. Compared to the one-triplon dynamics, the motion

Figure 6.12.: Leading processes of correlated two-triplon hopping. Red (dark) dots are triplons, bars are dimers.
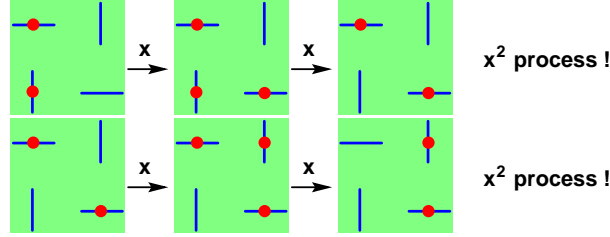
of two triplons together is much less restricted. Matrix elements occur in x^2 as first observed for total spin $S = 2$ [100] and more generally in Ref. [25]. But the dispersion (band width) of bound states starts only in x^3 (and not in x^4 as claimed in Ref. [93]). By means of the operator T_0 in the first order of H_{eff} two adjacent triplons interact linearly in x.[5] The energy of the initial and final state in each row in Fig. 6.12 differ by an amount $\sim x$. Hence both rows must be combined, making it an $(x^2)^2/x = x^3$ process eventually. Fig. 6.13 illustrates the situation. It suffices to consider a three level system. Without any interaction the two two-triplon states $|2\rangle$ and $|2'\rangle$ are degenerate. The degeneracy is lifted by introducing a finite interaction x, which leads to a splitting $\sim x$. The state $|2'\rangle$ has higher energy and corresponds (for $S = 0, 1$) to the state at the right (left) of the upper (lower) row in Fig. 6.12. The intermediate three-triplon state is denoted by $|3\rangle$. The process leading from the upper left state to the lower right state in Fig. 6.12 is translated to the level diagram in Fig. 6.13. Each process a through d is $\sim x$. But, second order degenerate perturbation theory gives an energy denominator $\sim x$ for process b while the denominators of all other processes are ~ 1. Thus *abcd* divided by the energy denominator is proportional to $(x/1)(x/x)(x/1)(x/1) = x^3$.

---

[5] With the two-triplon states $|S, m\rangle$ given in Tab. 3.1 one can easily verify that the action of T_0 on two adjacent triplons in the state $|S, m\rangle$ gives $-x$ for $S = 0$, $-x/2$ for $S = 1$ and $x/2$ for $S = 2$.
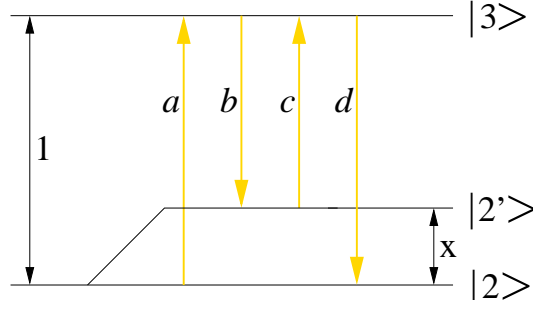
Figure 6.13.: Level-diagram to illustrate that the two-triplon dispersion starts in third order.

This applies for each of the eight (anti-) bound states that can be constructed from two triplons on nearest neighbour or next nearest neighbour dimers. The dispersion of any other state sets in at even higher order.

We now turn to quantitative results. We again use momentum states (see section 3.4.1) to make use of the translational invariance of Γ_{eff}. As in the one-triplon case (cf. beginning of section 6.2.3) we have to take care of the sublattice structure, which here is accounted for by

$$|\mathbf{K}, \mathbf{d}\rangle^S \to |\sigma, \mathbf{K}, \mathbf{d}\rangle^S = \frac{1}{\sqrt{N}} \sum_{\mathbf{r}} e^{i(\mathbf{K}+\sigma\mathbf{Q})(\mathbf{r}+\mathbf{d}/2)} |\mathbf{r}, \mathbf{r}+\mathbf{d}\rangle^S \qquad (6.25)$$

$$t_{\mathbf{d};\mathbf{r}',\mathbf{d}'} \to t^{\pi(\mathbf{r})}_{\mathbf{d};\mathbf{r}',\mathbf{d}'} = \bar{t}_{\mathbf{d};\mathbf{r}',\mathbf{d}'} + e^{i\mathbf{Q}\mathbf{r}} dt_{\mathbf{d};\mathbf{r}',\mathbf{d}'} \ . \qquad (6.26)$$

Recall, that $\mathbf{K}$ is the total momentum within the MBZ. As outlined in section 3.4.1 we restrict to $\mathbf{d} > 0$. The action of the one-triplon part H_1 and the two-triplon part H_2 of H_{eff} on these states can be calculated in an analogous fashion as in section 3.4.1. Using the inversion symmetry of Γ_{eff} to obtain real matrix elements is more involved. The necessary calculations can be found in appendix C. For H_1 the result reads

$$H_1|\sigma, \mathbf{K}, \mathbf{d}\rangle^S =$$

$$2 \sum_{\substack{\mathbf{d}' \\ \mathbf{d}' \neq \mathbf{d}}} \bar{t}_{\mathbf{d}'} \cos\left[(\mathbf{K}+\sigma\mathbf{Q})\mathbf{d}'/2\right] \left[\text{sgn}(\mathbf{d}-\mathbf{d}')\right]^S |\sigma, \mathbf{K}, |\mathbf{d}-\mathbf{d}'|\rangle^S + \qquad (6.27)$$

$$2 \sum_{\substack{\mathbf{d}' \\ \mathbf{d}' \neq \mathbf{d}}} dt_{\mathbf{d}'} \cos\left[(\mathbf{K}+\bar{\sigma}\mathbf{Q})\mathbf{d}'/2 - \mathbf{Q}\mathbf{d}(\sigma-1/2)\right] \left[\text{sgn}(\mathbf{d}-\mathbf{d}')\right]^S |\bar{\sigma}, \mathbf{K}, |\mathbf{d}-\mathbf{d}'|\rangle^S \ .$$

Note again, that H_1 is constructed by one-triplon amplitudes alone. No new calculations have to be started.

From our discussion in section 3.4.1 it should be clear, that H_1 is a semi-infinite band-matrix for fixed $\mathbf{K}$ in the basis $\{|\sigma, \mathbf{K}, \mathbf{d}\rangle\}$ with remaining quantum number $\mathbf{d}$.[6] As discussed in the last section, the one-triplon amplitudes $t_{\mathbf{d}}^{v/h}$, giving $\bar{t}_{\mathbf{d}}$ and $dt_{\mathbf{d}}$, have been calculated as 15th order polynomials in x. Thus, the width of the band in the matrix representing H_1 is fixed. Let us picture the remaining quantum numbers $\mathbf{d}$ as points in a two-dimensional plane. To each point we attach dimers to be able to track the lattice structure. The resulting plane is depicted in Fig. 6.14. Here we concentrate on part (b). Consider H_1 to act on the state $|\sigma, \mathbf{K}, \mathbf{d}_i\rangle$ ($\mathbf{K}$ fixed). The initial distance $\mathbf{d}_i$ is depicted in the centre of Fig. 6.14(b). It turns out, that having calculated all one-triplon amplitudes to 15th order means, that only those distances can be reached, which we depict as grey dimers. If the initial distance happens to be small enough, such that some of the reached distances under the action of H_1 are negative (see Eq. (3.48) for the definition of negative in this context), we reflect these distances back to the positive part by inversion. This procedure leads to the absolute values in Eq. (6.27). Note that the order, in which the two triplons are arranged changes under inversion, such that we have to interchange them. This introduces an extra minus sign in the total spin $S = 1$ case, which is accounted for by the signum-function in Eq. (6.27).

In a similar fashion, we can calculate the action of H_2 on the states $|\sigma, \mathbf{K}, \mathbf{d}\rangle^S$, which yields

$$^S\langle\sigma, \mathbf{K}, \mathbf{d}'|H_2|\sigma, \mathbf{K}, \mathbf{d}\rangle^S = \bar{t}_{\mathbf{d};(\mathbf{d}-\mathbf{d}')/2,\mathbf{d}'}^S +$$

$$2 \sum_{\mathbf{r}'>(\mathbf{d}-\mathbf{d}')/2} \bar{t}_{\mathbf{d};\mathbf{r}',\mathbf{d}'}^S \cos\left[(\mathbf{K}+\sigma\mathbf{Q})\left(\mathbf{r}'+(\mathbf{d}'-\mathbf{d})/2\right)\right] ,$$

$$^S\langle\bar{\sigma}, \mathbf{K}, \mathbf{d}'|H_2|\sigma, \mathbf{K}, \mathbf{d}\rangle^S = dt_{\mathbf{d};(\mathbf{d}-\mathbf{d}')/2,\mathbf{d}'}^S \cos(\mathbf{Q}\mathbf{d}/2) + \qquad (6.28)$$

$$2 \sum_{\mathbf{r}'>(\mathbf{d}-\mathbf{d}')/2} dt_{\mathbf{d};\mathbf{r}',\mathbf{d}'}^S \cos\left[(\mathbf{K}+\bar{\sigma}\mathbf{Q})\left(\mathbf{r}'+(\mathbf{d}'-\mathbf{d})/2\right) - \mathbf{Q}\mathbf{d}(\sigma-1/2)\right] .$$

Recall, that the two-triplon amplitudes depend on the total spin S. The full calculation can again be found in appendix C. The matrix representing H_2 in $\{|\sigma, \mathbf{K}, \mathbf{d}\rangle\}$ for fixed $\mathbf{K}$ is finite. We are able to calculate all two-triplon amplitudes $t_{\mathbf{d};\mathbf{r}',\mathbf{d}'}^{v/h}$ as polynomials in x up to and including 14th order. For fixed $\mathbf{K}$ Fig. 6.14(a) shows all distances $\mathbf{d}$, which give finite matrix elements in H_2 up to order 14. We count 42 distances. However, the quantum number $\sigma \in \{0, 1\}$ doubles the number of states, such that H_2 is represented by a

---

[6] For fixed $\mathbf{K}$ we picture the basis sorted according to $\{|\sigma = 0, \mathbf{d}\rangle, |\sigma = 1, \mathbf{d}\rangle\}$, with some convenient order defined for the distances $\mathbf{d}$.
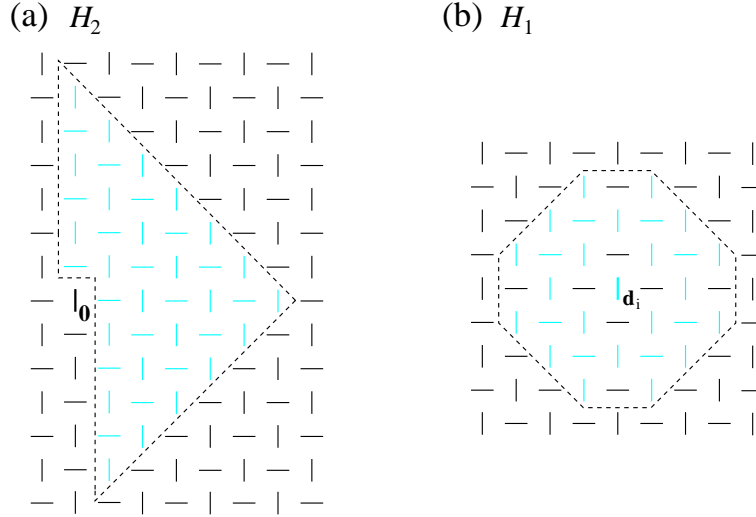
(a) H_2 (b) H_1

Figure 6.14.: If H_1 and H_2 act on the two-triplon momentum states $|\sigma, \mathbf{K}, \mathbf{d}\rangle$ at fixed momentum $\mathbf{K}$, the relative distance $\mathbf{d}$ between the two triplons is the remaining quantum number ($\sigma \in \{0, 1\}$). We picture the distances $\mathbf{d}$ to be points in a two-dimensional plane. To each point we attach a dimer to keep track of the dimer orientation. Up to 14th order non-zero matrix elements in H_2 can only be found for the 42 positive distances (cyan/grey dimers) within the triangle in part (a). Thus, up to 14th order H_2 is represented by a finite 84×84 matrix in $\{|\sigma, \mathbf{K}, \mathbf{d}\rangle\}$ for fixed $\mathbf{K}$ (cf. Eq. (6.28)). Part (a) also shows in which way our definition of $\mathbf{d} > 0$ (see Eq. (3.48)) divides the plane into positive and negative distances. In part (b) we illustrate, which distances can be reached from an initial distance $\mathbf{d}_i$, in the middle of the depicted cluster, under the action of H_1 (cf. Eq. (6.27)). For a calculation up to order 15 it turns out that only the distances in the oval shaped area (cyan/grey dimers) can be reached from $\mathbf{d}_i$. "Odd" hoppings along the axes are forbidden by symmetry (cf. section 6.2.2). This fixes the width of the band of finite elements in H_1, which is represented by a semi-infinite band matrix in $\{|\sigma, \mathbf{K}, \mathbf{d}\rangle\}$ for fixed $\mathbf{K}$. The splitting $H_{\text{eff}} = H_1 + H_2$ in the two-triplon sector is important for the calculation of the effective Green's function at fixed $\mathbf{K}$, where the iterative application of H_{eff} on the states $|\sigma, \mathbf{K}, \mathbf{d}\rangle$ has to be calculated. One clearly sees that H_2 mixes the finite set of 84 states symbolised by part (a). On the other hand, H_1 continues to produce states $|\sigma, \mathbf{K}, \mathbf{d}\rangle$, where the distances $\mathbf{d}$ grow in each application. The manner, in which the $\mathbf{d}$ grow, can be recognised by moving the oval structure in part (b) onto a specific active (cyan/grey) dimer in part (a), where we use a fixed reference frame. One clearly sees, in which way the number of non-vanishing distances increases in a given pattern.

84×84 matrix in $\{|\sigma, \mathbf{K}, \mathbf{d}\rangle\}$ for fixed $\mathbf{K}$. Also visible in Fig. 6.14(a) is the way, in which our definition of $\mathbf{d} > 0$ (see Eq. (3.48)) splits the full plane of distances $\mathbf{d}$ into two parts.

Practically we calculate the *combined* action of $H_1 + H_2 = H_{\text{eff}} - H_0$ on the two triplon states $|\mathbf{r}, \mathbf{r} + \mathbf{d}\rangle^S$. The zero-triplon part H_0 can again be neglected,

$\mathbf{d} = (d_1, 0)$	$\lvert\langle 0, \mathbf{0}, \mathbf{d}\rvert H_2\lvert 0, \mathbf{0}, \mathbf{d}\rangle\rvert$; $x = 0.4$	$\lvert\langle 0, \mathbf{0}, \mathbf{d}\rvert H_2\lvert 0, \mathbf{0}, \mathbf{d}\rangle\rvert$; $x = 0.6$
1	$2.98 \cdot 10^{-1}$ $(3.01 \cdot 10^{-1})$	$5.25 \cdot 10^{-1}$ $(2.32 \cdot 10^{-1})$
2	$6.72 \cdot 10^{-2}$ $(7.19 \cdot 10^{-2})$	$3.04 \cdot 10^{-1}$ $(2.11 \cdot 10^{-1})$
3	$9.33 \cdot 10^{-6}$ $(2.73 \cdot 10^{-5})$	$4.80 \cdot 10^{-3}$ $(8.27 \cdot 10^{-4})$
4	$3.29 \cdot 10^{-5}$ $(1.88 \cdot 10^{-6})$	$7.35 \cdot 10^{-3}$ $(9.25 \cdot 10^{-5})$
5	$3.31 \cdot 10^{-5}$ $(1.97 \cdot 10^{-6})$	$7.38 \cdot 10^{-3}$ $(9.61 \cdot 10^{-5})$
6	$3.31 \cdot 10^{-5}$ $(1.97 \cdot 10^{-6})$	$7.38 \cdot 10^{-3}$ $(9.61 \cdot 10^{-5})$

Table 6.2.: The pure two-triplon interaction energies drop rapidly with increasing distances. The table shows the diagonal elements of H_2 for total spin $S = 0$ at $\sigma = 0$ and $\mathbf{K} = \mathbf{0}$. In the left column we choose $x = 0.4$ and in the right column $x = 0.6$. The given numbers result from the plain series expansions. The numbers in parentheses are the corresponding results obtained by using optimised perturbation theory with $\alpha = 1.0$ (see section 6.5.3 for further explanations). Non diagonal elements are even smaller.

such that we can calculate the two-triplon amplitudes $a^S_{\mathbf{d};\mathbf{r}',\mathbf{d}'}$ of combined one- and two-triplon dynamics via

$$a^S_{\mathbf{d};\mathbf{r}',\mathbf{d}'} = {}^S\langle \mathbf{r}', \mathbf{r}' + \mathbf{d}'\rvert H_{\text{eff}} \lvert \mathbf{r}, \mathbf{r} + \mathbf{d}\rangle^S . \tag{6.29}$$

If we represent H_{eff} and H_1 (composed of the previously calculated one-triplon amplitudes) in the 84 states that suffice to represent H_2 up to 14th order, the simple matrix subtraction $H_2 = H_{\text{eff}} - H_1$ yields the pure two-triplon interaction matrix. Alternatively, one can obtain the two-triplon amplitudes $t^S_{\mathbf{d};\mathbf{r}',\mathbf{d}'}$ by subtracting the one-triplon amplitudes $t_{\mathbf{d}}$ from the amplitudes $a^S_{\mathbf{d};\mathbf{r}',\mathbf{d}'}$ as outlined in section 2.2.3. The H_2 matrix can then be constructed "manually" by means of the Eqs. (6.28). Recall, that the $t_{\mathbf{d}}$ have to be calculated on the same clusters as the $a^S_{\mathbf{d};\mathbf{r}',\mathbf{d}'}$.[7] The construction of the clusters needed to obtain thermodynamic two-triplon hopping amplitudes in the end follows the line of argument given for the one-triplon case. We have to include one additional step. If we place two triplons in the effective lattice Γ_{eff} we have to check, whether they can interact at all. This can be done by verifying whether the individual zig-zag paths of each of the triplons meet in the given order. If not, there is no chance for them to become correlated. Such individual processes can be discarded, since they are captured by H_1 already.

The discussed approach of considering a finite matrix for the pure two-triplon interaction while considering an (in principal) infinite matrix for the

---

[7] The $a^S_{\mathbf{d};\mathbf{r}',\mathbf{d}'}$ are *not* the thermodynamic amplitudes. Only the $t^S_{\mathbf{d};\mathbf{r}',\mathbf{d}'}$, obtained from the $a^S_{\mathbf{d};\mathbf{r}',\mathbf{d}'}$ by subtracting the one-triplon amplitudes $t_{\mathbf{d}}$ are the thermodynamic amplitudes for which the linked cluster theorem holds.

isolated one-triplon dynamic is well justified. Tab. 6.2 clearly shows, that the interaction energy between two triplons drops rapidly with increasing distance. The interaction can safely be neglected on larger distances.

The splitting of H_{eff} in H_1 and H_2 will be of importance in the sections on spectral densities. As we have seen in chapter 4, an efficient calculation of the effective Green's function by means of continued fraction expansion necessitates the splitting.

6.3.1. Symmetries

As in the one-triplon case, we will use symmetry arguments to derive qualitative aspects of the two-particle spectrum. We begin by calculating the action of the symmetry operators, discussed in section 6.2.2, on the two-triplon states.

We consider the states $|\mathbf{r}, \mathbf{r}'\rangle^S$ and define $\mathbf{d} = \mathbf{r}' - \mathbf{r}$. The action of symmetry operations on $|\mathbf{r}, \mathbf{r}'\rangle$ might again introduce extra phase shifts, since the orientation of singlets on the dimers has to be taken into account. The extra phase shifts are given relative to the ground state. After an operation has been applied it might be necessary to interchange the two triplons in the resulting state such that $\mathbf{d} > 0$. This leads to another minus sign for total spin $S = 1$. We indicate a necessary interchange by $D = 1$, which is 0 otherwise. Thus $(-1)^{SD}$ ensures the correct phase factor. The coordinate system relative to which we define the operations is the same as introduced in section 6.2.2 (see Fig. 6.9 on page 107). We begin with the reflections about the x- and y-axis

- m_x: Reflection about x-axis

$$m_x|\mathbf{r}, \mathbf{r}'\rangle^S = |(r_1, -r_2), (r_1', -r_2')\rangle^S \cdot (-1)^{d_1 + d_2 + SD}$$
$$D = 1, \text{ iff}(-d_1, d_2) > 0 \, , \tag{6.30}$$

- m_y: Reflection about y-axis

$$m_y|\mathbf{r}, \mathbf{r}'\rangle^S = |(-r_1, r_2), (-r_1', r_2')\rangle^S \cdot (-1)^{d_1 + d_2 + SD}$$
$$D = 1, \text{ iff}(d_1, -d_2) > 0 \, , \tag{6.31}$$

- I: Inversion about the origin

$$I|\mathbf{r}, \mathbf{r}'\rangle^S = |-\mathbf{r}', -\mathbf{r}\rangle^S \cdot (-1)^S$$
$$\text{interchange always necessary} \, , \tag{6.32}$$

- σ_u: Reflection about the diagonal u plus translation by $(0, -1)$

$$\sigma_u |\mathbf{r}, \mathbf{r}'\rangle^S = |(-r_2, -r_1 - 1), (-r_2', -r_1' - 1)\rangle^S \cdot (-1)^{SD}$$

$$D = 1, \text{ iff}(d_2, d_1) > 0 , \tag{6.33}$$

- σ_v: Reflection about the diagonal v plus translation by $(0, -1)$

$$\sigma_v |\mathbf{r}, \mathbf{r}'\rangle^S = |(r_2, r_1 - 1), (r_2', r_1' - 1)\rangle^S \cdot (-1)^{SD}$$

$$D = 1, \text{ iff}(-d_2, -d_1) > 0 , \tag{6.34}$$

- R: Rotation of $\pi/2$ about one of the 4-fold axes

$$R|\mathbf{r}, \mathbf{r}'\rangle^S = |(-r_2, r_1 + 1), (-r_2', r_1' + 1)\rangle^S \cdot (-1)^{d_1 + d_2 + SD}$$

$$D = 1, \text{ iff}(d_2, -d_1) > 0 . \tag{6.35}$$

More important to us is the action of these operators on the two-particle momentum states at points of high symmetry such as the Γ point $(\mathbf{K} = \mathbf{0})$

$$m_x |\sigma, \mathbf{0}, \mathbf{d}\rangle^S = (-1)^{d_1 + d_2 + \sigma d_2 + SD} |\sigma, \mathbf{0}, (d_1, -d_2)\rangle^S \tag{6.36}$$

$$m_y |\sigma, \mathbf{0}, \mathbf{d}\rangle^S = (-1)^{d_1 + d_2 + \sigma d_1 + SD} |\sigma, \mathbf{0}, (-d_1, d_2)\rangle^S \tag{6.37}$$

$$R|\sigma, \mathbf{0}, \mathbf{d}\rangle^S = (-1)^{d_1 + d_2 + \sigma + \sigma d_2 + SD} |\sigma, \mathbf{0}, (-d_1, d_2)\rangle^S \tag{6.38}$$

The interchange indicating variable D is the same as in the action on the states $|\mathbf{r}, \mathbf{r}'\rangle^S$ respectively. The calculations are tedious. However, in appendix G we present the detailed calculation for the following symmetry relation as a representative example, which we can use to prove a general double degeneracy at the boundary of the MBZ. At the zone boundary line $K_2 - K_1 = \pi$ (, and $K_1 \in [-\pi, 0],$) of the MBZ we explicitly show ($\bar{\sigma} = 1 - \sigma$, S suppressed for clarity)

$$\sigma_u I |\sigma, \mathbf{K}, (d_1, d_2)\rangle = e^{i\pi\sigma} e^{iK_1 + i\pi(\bar{\sigma}d_1 - \sigma d_2)} |\bar{\sigma}, \mathbf{K}, -(d_2, d_1)\rangle$$

$$\Rightarrow \sigma_u I |\bar{\sigma}, \mathbf{K}, -(d_2, d_1)\rangle = e^{i\pi\bar{\sigma}} e^{iK_1 + i\pi(\bar{\sigma}d_1 - \sigma d_2)} |\bar{\sigma}, \mathbf{K}, (d_1, d_2)\rangle , \tag{6.39}$$

for the combined symmetry $\sigma_u I$, which obviously is a symmetry of the Hamiltonian, too. One clearly sees, that the two states $|\sigma, \mathbf{K}, (d_1, d_2)\rangle \equiv |x\rangle$ and $|\bar{\sigma}, \mathbf{K}, -(d_2, d_1)\rangle \equiv |y\rangle$ span a two-dimensional invariant space under $\sigma_u I$. If we assume $\sigma = 0$ and thus $\bar{\sigma} = 1$ without loss of generality we find

$$\sigma_u I |x\rangle \sim |y\rangle$$

$$\sigma_u I |y\rangle \sim -|x\rangle . \tag{6.40}$$

Thus, up to a prefactor $\sigma_u I$ acts like a 2D rotation $\begin{pmatrix} 0 & -1 \\ 1 & 0 \end{pmatrix}$ on the states $|x\rangle$ and $|y\rangle$. Hence its eigen-vectors are complex with linearly independent real and imaginary parts and so are the simultaneous eigen-vectors of $\sigma_v I$ and H_{eff}. Because H_{eff} is real the real and the imaginary part in fact constitute linearly independent eigen-vectors to the same eigen-value. We thus find a double degeneracy at the mentioned boundary of the MBZ. By similar arguments, the same double degeneracy is concluded for the other parts of the MBZ border.

The double degeneracy at the MBZ border is interesting for analysing experiments, too. Degeneracy reduces the large number of energetically close states helping to resolve the non-degenerate bound states.

The point group symmetry relations (6.36)-(6.38) for $\mathbf{K} = \mathbf{0}$ are also very useful. Consider for the moment that it suffices to represent H_{eff} in the two-triplon sector by a finite matrix, say in the 84 $|\sigma, \mathbf{0}, \mathbf{d}\rangle$ states that suffice to represent H_2 up to 14th order for instance. Then, since H and thus H_{eff} are invariant under the 4mm point symmetry group, the matrix representing H_{eff} splits into various blocks corresponding to the different irreducible representations Γ_1 through Γ_5 of 4mm. The Eqs.(6.36)-(6.38) can be used to obtain the matrices, which represent m_x, m_y and R in the same states which where chosen to represent H_{eff} as matrix. Then, the block structure is easily calculated by simple matrix operations using a computer algebra programme such as MAPLE for instance. The symbolic representation of the matrix elements (polynomials in x here) is preserved. Further calculations in the individual, in general smaller blocks can now be tackled. We will make use of this in the next section.

6.3.2. Results

In this section we consider the full effective Hamiltonian $H_{\text{eff}} = H_0 + H_1 + H_2$ in the two-triplon space. The constant operator H_0 is set to zero without loss of generality. We will not present two-triplon dispersions in this section. We shall rather focus on some bound states at particular $\mathbf{K}$-values of high symmetry. The $\mathbf{K}$-dependence of $S = 1$ bound states will be discussed in section 6.6. It turns out, that we need to consider a few states only (much less than the 84 states needed for a complete representation of H_2 in 14th order), to obtain significant results.

The one-triplon hopping starts in order six, while the two-triplon interaction starts in first order already. Hence, an analytic expansion for the energies of the bound states is possible. At finite order in x only configurations contribute where the two triplons are not too far away from each other. Of course, higher orders imply larger, but still finite distances. In particular, the energies

of the four states which evolve from neighbouring triplons can be computed very well since their interaction is linear. Investigating the matrix elements shows that it is sufficient to study the distances $\mathbf{d} \in \{(0,1),(1,0),(1,\pm 1)\}$ for order 5. To x^{14} only $\mathbf{d} \in \{(1,\pm 2),(2,\pm 1),(0,2),(2,0),(2,\pm 2)\}$ must be added. So, for given total momentum only a finite 8×8 or 24×24 matrix has to be analysed (σ doubles the number of states). For illustration consider the amplitude $t_{(0,1);\mathbf{r},(2,1)}$ (the Fourier transform of $\mathbf{r}$ yields the momentum dependence) connecting $(0,1)$ and $(2,1)$ which is of order (x^4). By second order perturbation one sees that the resulting energy shift is $(x^4)^2/x = x^7$ only (see our argument at the beginning of this section).

Furthermore, the elements connecting shorter distances to longer distances and the elements among longer distances do not need to be known to very high orders. Consider again the process $(0,1) \leftrightarrow (2,1)$. In order x^7 the element $t_{(0,1);\mathbf{r},(2,1)}$ must be known only in x^4 and $t_{(2,1);\mathbf{r},(2,1)}$ only in x^1; in order x^9 the element $t_{(0,1);\mathbf{r},(2,1)}$ must be known only up to x^6 and $t_{(2,1);\mathbf{r},(2,1)}$ only in x^3 and so on.

We have analysed the dispersions in x^5 of the four states bound linearly in x in the MBZ for total spin $S = 0$ and $S = 1$. The results can be found in appendix I. Fukumoto's results are mostly confirmed [101]. In appendix I we compare his results to ours.

As explained in the preceding section we find at particular points of high symmetry $((0,0),(0,\pi),(\pi/2,\pi/2))$ that the matrix representing H_{eff} splits into several blocks corresponding to the different irreducible representations (Γ_1 through Γ_5) of the square point group 4mm, which is the point group of the model (cf. section 6.2.2). At these points the analysis up to x^{14} is carried out.

In practice, the 24×24 matrix, sufficient to compute the series for the energies of the best bound states up to 14th order, splits into 6 blocks H_{eff}^i, $i = 1, \ldots 6$, of various dimensions. From any of these six blocks eigen-energies λ, which start linearly in x, can be extracted as exact polynomials up to order 14. They correspond to the bound states linked to adjacent triplon configurations as discussed in Fig. 6.12. The extraction is facilitated due to the following considerations. We prepare λ as a polynomial with yet unknown coefficients

$$\lambda(x) = \lambda_1 + \lambda_2 x + \lambda_3 x^2 + \ldots + \lambda_{14} x^{13} \ . \tag{6.41}$$

All matrix element of H_{eff}^i are polynomials in x, which have no absolute terms, since we discarded H_0. However, in the matrices H_{eff}^i containing linear eigen-energies, some of the diagonal elements must start linearly in x. Let us focus on a specific block H_{eff}^i which contains a linearly bound state. For our argument to work we divide all matrix elements by x. This leads to the block $\tilde{H}_{\text{eff}}^i$ where some of the diagonal elements have absolute terms now. However, we must not

forget to multiply the resulting eigen-value by x again. This is why we choose Eq. (6.41) for $\lambda(x)$. With E^i denoting the unit matrix of the same dimension as the block $\tilde{H}^i_{\text{eff}}$, we expand the secular equation up to 14th order

$$\det\left(\tilde{H}^i_{\text{eff}}(x) - E^i\lambda(x)\right) = d_1 + d_2 x + d_3 x^2 + \ldots + d_{14}x^{13} \doteq 0 \ . \qquad (6.42)$$

Each coefficient d_i is a function of the unknown coefficients λ_i. Eq. (6.42) is fulfilled up to 13th order if *every* coefficient d_i vanishes. This is used to determine the unknown coefficients λ_i in $\lambda(x)$. They can be determined recursively, starting with λ_1. To illustrate this, we consider a two dimensional block $\tilde{H}^{\text{ex}}_{\text{eff}}$ as an example

$$\tilde{H}^{\text{ex}}_{\text{eff}} = \left(\begin{array}{cc} a(x) & b(x) \\ b(x) & c(x) \end{array}\right) \ . \qquad (6.43)$$

We consider both diagonal elements to start with absolute terms, here a_1 and c_1 (remember, that we have divided by x). Now, from the footnote on page 114 we already now how these terms have to look. For total spin $S = 0, 1, 2$ we have $a_1 = c_1 = -1, -1/2, 1/2$ respectively. Calculating the expansion of the secular equation yields

$$\begin{aligned} 0\doteq\det\left(\begin{array}{cc} a(x) - \lambda(x) & b(x) \\ b(x) & c(x) - \lambda(x) \end{array}\right) &= d_1 + d_2 x + d_3 x^2 + \mathcal{O}(x^3) \\ &= (\lambda_1 - a_1)^2 \\ &+ \left[2(\lambda_1 - a_1)\lambda_2 - (a_2 + c_2)\lambda_1 + a_1 c_2 + a_1 a_2\right] x \\ &+ \left[2(\lambda_1 - a_1)\lambda_3 + \lambda_2^2 - (a_2 + c_2)\lambda_2 - (a_3 + c_3)\lambda_1 + a_1 c_3 + a_2 c_2 + a_1 a_3\right] x^2 \\ &+ \mathcal{O}(x^3) \ . \end{aligned} \qquad (6.44)$$

The vanishing of d_1 implies $\lambda_1 = a_1$. Inserting λ_1 in d_2 yields a linear equation for λ_2. Inserting λ_1 and λ_2 in d_3 yields a linear equation for λ_3 and so on. In this way we can calculate all coefficients λ_i from solving linear equations. Finally, $\lambda(x)$ is multiplied by x to give the eigen-energy. We should not forget to add the absolute term 2 to account for the fact that two triplons have been excited.

We give the linear eigen-energy found in the Γ_3 block of H_{eff} for total spin

$S = 1$ and momentum $\mathbf{K} = \mathbf{0}$ as an example

$$\omega_{\mathrm{lin}}^{\Gamma_3}(x) = 2 - \frac{1}{2}\,x - \frac{5}{4}\,x^2 - \frac{1}{4}\,x^3 - \frac{5}{8}\,x^4 - \frac{57}{64}\,x^5 - \frac{337}{384}\,x^6 - \frac{1087}{1152}\,x^7 - \frac{49745}{27648}\,x^8$$

$$- \frac{1230671}{663552}\,x^9 - \frac{84134083}{31850496}\,x^{10} - \frac{71961335353}{19110297600}\,x^{11} - \frac{6931489716539}{1146617856000}\,x^{12}$$

$$- \frac{41618542755193}{5503765708800}\,x^{13} - \frac{134624403747285691}{9631589990400000}\,x^{14}\ .$$

All other calculated energies of linearly bound states for total spin $S = 0$ and $S = 1$ are given in appendix I.

The extrapolated energies are depicted in Figs. 6.15 ($S = 0$) and 6.16 ($S = 1$) as functions of x. For those energies which stay separated from the two-particle continuum Dlog-Padé approximants are used successfully. The results are stable under changes of the polynomial degrees. The energies close to the continuum (here simply twice the gap Δ between the ground state and the a single triplon at $\mathbf{k} = \mathbf{0}$) are given with less reliability by the truncated series or by a non-defective Dlog-Padé approximant.
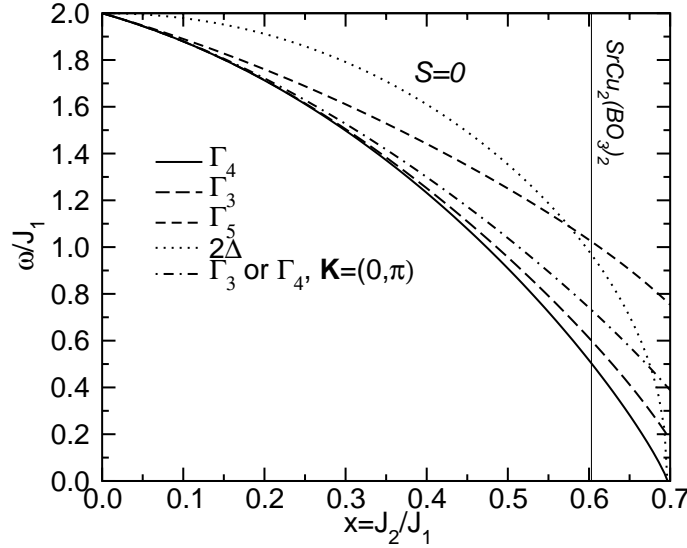
Figure 6.15.: Energy of the lowest lying $S = 0$ states, which start linearly in x, as function of x. The curves refer to $\mathbf{K} = \mathbf{0}$ except the dashed-dotted line. The dotted curve displays the two-triplon continuum at two times the one-triplon gap at $\mathbf{k} = \mathbf{0}$. The lowest two-triplon state gets soft at the same x-value, where the one-triplon dispersion vanishes: x=0.697.

In Figs. 6.15 and 6.16 the modes are sorted in energetically ascending order for small values of x: solid, long dashed, and short dashed curves. The Γ_5

modes are degenerate. The double degeneracy for $\mathbf{K} = (0, \pi)$ does *not* result from the point group but originates from the complex conjugation as explained in the last section. The dashed-dotted curve at $(0, \pi)$ has to be compared to both the solid and the long-dashed curve to assess the dispersion of these two modes from $\mathbf{0}$ to $(0, \pi)$. While for $S = 0$ this dispersion always has the expected behaviour with $\omega(\mathbf{0}) < \omega((0, \pi))$ the energies for $S = 1$ are reversed for small values of x (see also [101]). Only above $x \approx 0.55$ the relation $\omega(\mathbf{0}) < \omega((0, \pi))$ holds for $S = 1$.
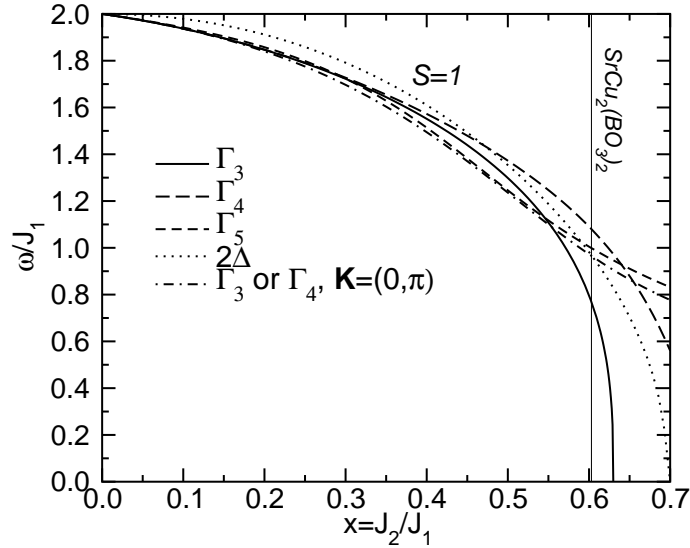
Figure 6.16.: Same as in Fig. 6.15 for $S = 1$. The Γ_3 bound state becomes soft at $x = 0.63$ already.

We do not agree with Ref. [101] that the two lowest states are of s-wave type since this would imply that they are Γ_1. Instead the $S = 0, 1$ states are odd under the reflection m_x and m_y. For $S = 0$, the lowest state is even under the rotation R and the second lowest is odd. For $S = 1$, it is vice-versa. The Γ_5 states can be viewed as being of p-wave type.

For $S = 0$, the lowest mode vanishes at the same x as the one-triplon gap. So, no additional instability occurs for $S = 0$. This provides evidence against a competing singlet phase as presumed in Ref. [85]. There is, however, a salient instability for $S = 1$ (Fig. 6.16) at $x = 0.63$ (the Γ_3 state). This comes as a surprise since one expects binding effects to be largest for $S = 0$ in antiferromagnets.

The singularity at $x = 0.630(5)$ is very stable occurring in all non-defective Dlog-Padé approximants. We should mention however, that we cannot ex-

clude a possible repulsive effect between the Γ_3 state and the continuum of two-triplon states. The plain series result, which stays well below the onset of the continuum for all relevant x-values, might contain "information" on this repulsion. This information is then exaggerated by the Dlog-Padé approximants. It is still intriguing that the instability occurs in almost all approximants.

The softening of the $S = 1$, Γ_3 mode at $x = 0.63$ in Fig. 6.16 implies a level crossing with the single triplon at $x = 0.62$. However, as we have shown in section 6.2.2, the latter is Γ_5 at $\mathbf{k} = \mathbf{0}$ so that both states are of different symmetry. Hence no level repulsion prevents the crossing.[8]

A mode softening like the one at $x = 0.63$ might indicate a 2nd order transition. But, we find the softening of a *bound* mode of two triplons proving significant attraction between triplons. If this attraction extends also to three and more triplons binding them to any total spin, the transition would be 1st order towards a condensate of triplets occurring *below* 0.63. The $S = 1$ bound state is neither parallel ($S = 2$) nor anti-parallel ($S = 0$). The angle being neither zero nor π corroborates a helical order if one adopts a classical view.

This scenario agrees nicely with the findings of Albrecht and Mila [80], which we discussed in the introduction to this chapter. Applying a Schwinger-boson mean field theory, which cannot be expected to be very quantitative, they find a 1st order transition from the dimer phase towards a helical phase at $x = 0.61$. Yet, the scenario cannot be considered to be proven beyond any doubt. Recall, that by perturbation theory Koga and Kawakami [85] find a 1st order transition at $x = 0.677$ into a gapped singlet phase extending up to a 2nd order transition at $x = 0.86$. But our instability occurs at a much lower value of x and the staggered magnetisation at $x = 0.86$ is significantly finite [86] in contradiction to a *second* order phase transition into a phase without long-range order (as mentioned already in Ref. [85]). However, in the light of the instability for $S = 1$ one might interpret the findings by Koga and Kawakami [85] as an indication of the same instability. It is so far not excluded that the bulk triplet condensate (the helical phase) is a singlet or that it can be linked to a singlet [102].

We would also like to reconsider the findings by Läuchli et al. [83] (see also the beginning of this chapter). By exact diagonalisation of clusters containing up to 32 sides they find a possible intermediate phase for $0.68 \leq x \leq 0.70$. Their largest cluster is designed such that it exhibits invariance under the symmetry relations R, m_x and m_y. For this cluster they find various low-lying singlet states well inside the one-triplon gap for x-values within the abovemen-

---

[8] Small values of $\mathbf{K}$ probably mix the states. But at small $\mathbf{K}$ any coupling is presumably too small to be noticed; at larger $\mathbf{K}$ the crossing no longer takes place (cf. energy at $\mathbf{K} = (0, \pi)$ in Fig. 6.16).

tioned possible intermediate range. Two of these singlets have energies very close to the dimer ground state energy. One of these has s-wave symmetry (even under R) the other one has d-wave symmetry (odd under R). They argue, that the d-wave singlet does not seem to be relevant in the thermo-dynamic limit. On the other hand they claim, that the s-wave singlet might combine with the dimer state to yield a two-fold degenerate plaquette singlet ground state.

Although the range of x-values does not agree with our findings, it is rather interesting that they find low energy singlets, i.e. *bound* excitations within the one-triplon gap. However, their lowest excitations are singlets and they discard the d-wave singlet which has the same symmetry $\Gamma_3(xy)$ as our lowest $S = 1$ bound state. A possible scenario might be, that some of their observed singlets within the one-triplon gap are already bound states of our $S = 1$ Γ_3 bound state making it a composite excitation of four triplons. (Obviously it could be a composite of three triplons, too.) This would support the suggested scenario of a triplet-condensate intermediate phase, with the condensated triplets binding to all kinds of total spins, maybe to $S = 0$ most likely.[9]

In conclusion, the transition order and the intermediate phase still deserve further investigation.

We advance and determine J_1 and J_2 for $SrCu_2(BO_3)_2$. We again assume 2.98 meV for the one-triplon gap $\Delta_1(x, J_1)$. By very accurate ESR measurements Nojiri et al. [90] find 4.71 meV (no error given) for the $S = 1$ two-triplon gap $\Delta_2(x, J_1)$. INS data are in the same range (see Fig. 6.45 on page 174 or Fig. 6.46 on page 175). The ratio

$$f(x) := \frac{\Delta_1(x, J_1)}{\Delta_2(x, J_1)} = \frac{2.98}{4.71} \approx 0.633 \tag{6.45}$$

does not depend on J_1 and is used to determine the x-value for $SrCu_2(BO_3)_2$. In Fig. 6.17 we depict $f(x)$ as solid line. It crosses the 0.633 line at $x_0 = 0.603(3)$. The error in the third digit is induced by the experimental error bars. Note that the steep decrease of the bound $S = 1$ state, i.e the steep increase of $f(x)$, enables us to fix x_0 very precisely. Finally, J_1 is fixed by $\Delta_1(x_0, J_1) \doteq 2.98$ meV.

---

[9] In respect thereof Ref. [103] might be interesting. The authors investigate a chain of connected tetrahedrons, each composed of four $S = 1/2$ spins. Depending on the parameter-values the model also exhibits various spin liquid ground states: a simple dimer singlet state (DS) and a plaquette singlet state (PS) amongst others. They find that in the vicinity of the transition DS-PS a dramatic increase in the binding energies between bound singlet-particles, composed of (arbitrarily many) triplon-excitations, triggers the *first*-order phase transition DS-PS.
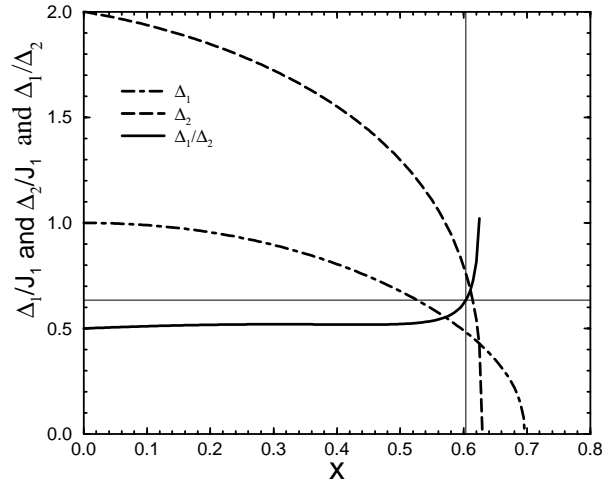
Figure 6.17.: Best Dlog-Padé approximants for the one-triplon gap Δ_1, the $S = 1$ two-triplon gap Δ_2 and their ratio Δ_1/Δ_2 as functions of x. The ratio does not depend on J_1 and is used to determine the x-value that fits the experimental data for $SrCu_2(BO_3)_2$.

The result reads (we drop the index from x_0)

$$J_1 = 6.16(10) \text{ meV} = 71(1) \text{ K}, \qquad x = 0.603(3) \text{ or}$$

$$J_1 = 6.16(10) \text{ meV} = 71(1) \text{ K}, \qquad J_2 = 3.71(7) \text{ meV} = 43(1) \text{ K} . \qquad (6.46)$$

The x-value found is depicted as vertical line in Figs. 6.15 and 6.16. Indeed, $SrCu_2(BO_3)_2$ seems to be very close to the transition point at $x = 0.63$. Note that our values differ from the literature values. However, the one-triplon dispersion is in excellent agreement with the experimental data for our values, as can be seen in Fig. 6.11 on page 113. Unfortunately, the error bars are rather large so that this comparison alone is not a sound evidence for the quality of our values.

Raman scattering [93] provides further support. The energy of the $S = 0$ Γ_3 state matches the energetically lowest resonance at 30cm^{-1} perfectly (see Fig. 6.29 on page 150). The Γ_4 singlet at 25cm^{-1} [10] is forbidden by symmetry since the Raman operator is effectively Γ_3, as we will show in section 6.5. Calculating the next $\Gamma_3, S = 0$ bound state, starting quadratically in x and

---

[10] The small shoulder at about 25cm^{-1} may be a trace of the Γ_4 singlet due to higher order processes or a singlet-triplon excitation.

not shown in Fig. 6.15 since the evaluation is less systematically, yields 45cm^{-1} in good agreement with the experimental 46cm^{-1} line, too.

In conclusion, the perturbative CUT method enabled us to calculate high order series expansions for energy levels in the one- and two-triplon sector. The reliably extrapolated results allow accurate fits to the experimental findings. Thereby, different $T = 0$ experiments (ESR, FIR, INS, Raman) are explained consistently. However, scattering experiments such as Raman or INS provide much more information than just the position of the resonances. In the following sections we will give a detailed description of how the *line shapes* of these experiments can be accessed by a perturbative CUT analysis of the Shastry-Sutherland model. Considerable progress in the understanding of the model and the substance will be achieved.

6.4. Spectral Densities – Preliminaries

The investigations of the preceding sections led to some insights. We were able to compare our results to experimental findings and determined model parameters for $\text{SrCu}_2(\text{BO}_3)_2$. We focused on the *position* of experimentally detected resonances. However, so far we did not address the wealth of information contained in the *line shapes* of available high precision data. We use the approach outlined in chapter 4 to attack these quantities. This short section covers some preparations.

We want to describe the Raman and the inelastic neutron scattering (INS) measurements since they represent clear-cut experiments probing the magnetic subsystem of $\text{SrCu}_2(\text{BO}_3)_2$. They are complementary in the sense that Raman probes the $S = 0$ sector, while INS probes the $S = 1$ sector. However, only an INS experiment can measure dispersions. Raman experiments are restricted to zero momentum states.

The first step in calculating the corresponding spectral densities is to identify realistic observables. They should capture the dominant parts of the experiments, yet they should be simple enough to allow feasible calculations. Therefore, detailed discussions of the chosen observables are included at the beginning of the corresponding subsections 6.5 (Raman) and 6.6 (INS).

In this section we are concerned with general aspects of effective observables for the Shastry-Sutherland model, which do not depend on the specific form of the observable. Our approach is based on the evaluation of the effective zero temperature Green's function (see chapter 4)

$$\mathcal{G} = \left\langle 0 \left| \mathcal{O}_{\text{eff}}^{\dagger} \frac{1}{\omega - H_{\text{eff}}} \mathcal{O}_{\text{eff}} \right| 0 \right\rangle , \tag{6.47}$$

where H_{eff} is the effective Hamiltonian studied in the last section, and $\mathcal{O}_{\text{eff}}$ a given effective observable. The ground state energy is set to zero.

As illustrated in chapter 2, at zero temperature the effective observable decomposes according to

$$\mathcal{O}_{\text{eff}} = \mathcal{O}_{0,0} + \mathcal{O}_{1,0} + \mathcal{O}_{2,0} + \dots \; . \tag{6.48}$$

Acting on the ground state $\mathcal{O}_{0,0}$ is a constant, $\mathcal{O}_{1,0}$ injects one particle (here triplon) into the system, $\mathcal{O}_{2,0}$ injects two triplons and so on. In the following we elaborate on $\mathcal{O}_{1,0}$ and $\mathcal{O}_{2,0}$.

We start by considering locally defined observables, which are then Fourier transformed in a second step. From now on we will call the Fourier transformed observables *global observables*. The basic ideas have been provided in section 3.4.2. However, we again have to take care of the A-B sublattice structure of the Shastry-Sutherland model. On the local level we have

$$\mathcal{O}_{1,0}(\mathbf{r})|0\rangle = \sum_{\mathbf{d}} w_{\mathbf{d}}^{\pi(\mathbf{r})}|\mathbf{r} + \mathbf{d}\rangle \tag{6.49}$$

$$\mathcal{O}_{2,0}(\mathbf{r})|0\rangle = \sum_{\mathbf{d},\mathbf{d}'} w_{\mathbf{d},\mathbf{d}'}^{\pi(\mathbf{r})}|\mathbf{r} + \mathbf{d}, \mathbf{r} + \mathbf{d}'\rangle \; , \tag{6.50}$$

where we again choose to split the amplitudes

$$w_{\mathbf{d}}^{\pi(\mathbf{r})} = \bar{w}_{\mathbf{d}} + e^{i\mathbf{Q}\mathbf{r}} dw_{\mathbf{d}}$$

$$w_{\mathbf{d},\mathbf{d}'}^{\pi(\mathbf{r})} = \bar{w}_{\mathbf{d},\mathbf{d}'} + e^{i\mathbf{Q}\mathbf{r}} dw_{\mathbf{d},\mathbf{d}'} \; . \tag{6.51}$$

The net part is given by $\bar{w} = (w^{\pi(\mathbf{r})=v} + w^{\pi(\mathbf{r})=h})/2$ and the deviation part by $dw = (w^{\pi(\mathbf{r})=v} - w^{\pi(\mathbf{r})=h})/2$, where v (h) means, that the particle injection centre is a vertical (horizontal) dimer. The amplitudes $w^{\pi(\mathbf{r})}$ are available as polynomials in x with rational coefficients by means of the effective observable $\mathcal{O}_{\text{eff}}$ in Eq. (3.36). The global observables are finally obtained by

$$\mathcal{O}_{\mu,0}(\sigma, \mathbf{K}) = \frac{1}{\sqrt{N}} \sum_{\mathbf{r}} e^{i(\mathbf{K}+\sigma\mathbf{Q})\mathbf{r}} \mathcal{O}_{\mu,0}(\mathbf{r}) \; . \tag{6.52}$$

As outlined in section 3.4.2 the action of the global observables on the ground state $|0\rangle$ yields momentum states; here $|\sigma, \mathbf{k}\rangle$ for $\mathcal{O}_{1,0}$ and $|\sigma, \mathbf{K}, \mathbf{d}\rangle$ for $\mathcal{O}_{2,0}$. The full calculations can be found in appendix D. Here we confine ourselves to the results. For the one-triplon observables we find

$$A_{\sigma,\mathbf{k}} = \langle \sigma, \mathbf{k}|\mathcal{O}_{1,0}(\sigma, \mathbf{k})|0\rangle = \sum_{\mathbf{d}} \bar{w}_{\mathbf{d}} \cos[(\mathbf{k} + \sigma\mathbf{Q})\mathbf{d}]$$

$$A_{\bar{\sigma},\mathbf{k}} = \langle \bar{\sigma}, \mathbf{k}|\mathcal{O}_{1,0}(\sigma, \mathbf{k})|0\rangle = \sum_{\mathbf{d}} dw_{\mathbf{d}} \cos[(\mathbf{k} + \sigma\mathbf{Q})\mathbf{d} + \mathbf{Q}\mathbf{d}] \; . \tag{6.53}$$

We assume inversion symmetry to hold about the point of injection $\mathbf{r}$, such that $w_{\mathbf{d}}^{\pi(\mathbf{r})} = w_{-\mathbf{d}}^{\pi(\mathbf{r})}$. In this case we might also restrict to $\mathbf{d} > 0$. For total spin $S = 0$ and $S = 2$ we find

$$A_{\sigma,\mathbf{K},\mathbf{d}} = \langle \sigma, \mathbf{K}, \mathbf{d} | \mathcal{O}_{2,0}(\sigma, \mathbf{K}) | 0 \rangle \tag{6.54}$$

$$= \sum_{\mathbf{r}'} \bar{w}_{\mathbf{r}',\mathbf{r}'+\mathbf{d}} \cos[(\mathbf{K} + \sigma \mathbf{Q})(\mathbf{r}' + \mathbf{d}/2)]$$

$$A_{\bar{\sigma},\mathbf{K},\mathbf{d}} = \langle \bar{\sigma}, \mathbf{K}, \mathbf{d} | \mathcal{O}_{2,0}(\sigma, \mathbf{K}) | 0 \rangle$$

$$= \sum_{\mathbf{r}'} dw_{\mathbf{r}',\mathbf{r}'+\mathbf{d}} \cos[(\mathbf{K} + \sigma \mathbf{Q})(\mathbf{r}' + \mathbf{d}/2) - \mathbf{Q}((\sigma - 1/2)\mathbf{d} - \mathbf{r}')] \ .$$

in the two-triplon sector. The case $S = 1$ is obtained by substituting $\cos \rightarrow \sin$. Again, inversion symmetry about the point of injection $\mathbf{r}$ has been used. However, the two triplons have to be interchanged after inversion. This leads to an additional minus sign in the $S = 1$ channel, ultimately responsible for the sine to appear instead of the cosine (see appendix D).

As in section 3.4.2 we observe that for fixed $\mathbf{k}$ ($\mathbf{K}$) the global effective observables can be pictured as vectors with components $A_{\sigma,\mathbf{k}}$ ($A_{\sigma,\mathbf{K},\mathbf{d}}$) in the basis $\{|\sigma, \mathbf{k}\rangle\}$ ($\{|\sigma, \mathbf{K}, \mathbf{d}\rangle\}$). The one-triplon vector is one-dimensional, while the dimension of the two-triplon vector depends on the perturbation order achieved. The vector components are polynomials in x with real coefficients for arbitrary but fixed momentum $\mathbf{k}$ ($\mathbf{K}$).

So far, the effective observables still depend on the auxiliary quantum number σ. As we will illustrate in the following subsections, the particular experiment under study fixes the ultimate values for $\sigma \in \{0, 1\}$ which has to be inserted into $\mathcal{O}(\sigma, \mathbf{K})$. The Raman-observable for example, for which the first contributions are found in the two-triplon sector, is obtained for $\sigma = 0$. Additionally, a Raman experiment probes the system at total momentum $\mathbf{K} = \mathbf{0}$. Thus, we are left with the rather simple vector components

$$A_{0,\mathbf{0},\mathbf{d}}^{\text{Raman}} = \sum_{\mathbf{r}'} \bar{w}_{\mathbf{r}',\mathbf{r}'+\mathbf{d}} \ \text{and}$$

$$A_{1,\mathbf{0},\mathbf{d}}^{\text{Raman}} = \sum_{\mathbf{r}'} dw_{\mathbf{r}',\mathbf{r}'+\mathbf{d}} \cos[\mathbf{Q}(\mathbf{d}/2 + \mathbf{r}')] \ . \tag{6.55}$$

Note that we need to consider *both* components $A_{0,\dots}$ and $A_{1,\dots}$, although σ has been fixed for the *operator* (re-inspect Eqs. (6.53) and (6.54)).

The observable for the INS experiment is more involved and can be written as a linear combination $a\mathcal{O}(0, \mathbf{K}) + b\mathcal{O}(1, \mathbf{K})$. (Subindex submitted, since this

holds true in the one- and in the two-triplon sector.) Still, we can define vector components $A_{\sigma,\mathbf{K},\mathbf{d}}$ in a fashion similar to that for the Raman observable. This concludes our general considerations on the observables in the Shastry-Sutherland model. We will elaborate on these issues in the following two subsections.

6.5. Raman − $S = 0$

We begin our survey of spectral densities for the Shastry-Sutherland model with the Raman response. In the first subsection we derive the appropriate Raman observable for the Shastry-Sutherland model. The next subsection illustrates in which way the CUT method can be used to obtain a high order series expansion for this observable. In the last subsection the results for the two-triplon energies of section 6.3 and those of the preceding subsection are used to calculate the corresponding Green's function. The model parameters found for $SrCu_2(BO_3)_2$ necessitate the use of extrapolation techniques. Our efforts to be as quantitative as possible will be documented in detail. We will close this section with a discussed comparison of our results to the experimental data.

6.5.1. Raman-Operator

The theory of two-magnon Raman scattering in spin systems closely follows the considerations that lead to the spin Heisenberg model as the effective low energy Hamiltonian of the Hubbard Hamiltonian. The coupling of the vector potential of the light to the electrons is included on the level of the Hubbard model. The vector potential couples to the current operator (and more generally also to the stress tensor). Just as in the derivation of the Heisenberg model a t/U expansion leads to a spin operator expression for the Raman process [104, 105]. For simplicity we consider the leading order $\sim t^2/U$ only[11]

$$\mathcal{R} = \sum_{\mathbf{r},\boldsymbol{\delta}} S_{\mathbf{r}} S_{\mathbf{r}+\boldsymbol{\delta}} \left[\mathbf{A}^i \cdot \boldsymbol{\delta} \right] \left[\mathbf{A}^f \cdot \boldsymbol{\delta} \right] \ , \tag{6.56}$$

where $S_{\mathbf{r}}$ denotes an $S = 1/2$ spin operator acting on site $\mathbf{r}$. Hence, $\mathcal{R}$ is a sum over Heisenberg-type spin-products, where the distances $\boldsymbol{\delta}$ have to be chosen such that the site $\mathbf{r} + \boldsymbol{\delta}$ can be reached by one Hubbard hopping t from

---

[11] Higher order terms can be found in Ref. [105]. As in the case of deriving spin Hamiltonians from the Hubbard model (see e.g. Ref. [106]) one also finds higher products of spin operators (chiral- and four-spin terms for instance) for the Raman operator.

site $\mathbf{r}$. The scalar products $[\cdot, \cdot]$ in $\mathcal{R}$ interrelate the directions of the vector potential $\mathbf{A}^i$ of the incident light and that of the scattered light $\mathbf{A}^f$ to the oriented distance $\boldsymbol{\delta}$ between the two involved sites. The frequency of the light matters, too. For the two-dimensional Shastry-Sutherland model we suppose both vector potentials to be parallel to the plane of the model.

We analyse the case, where $\boldsymbol{\delta}$ connects nearest neighbours, i.e. $\mathcal{R}$ is defined on the inter-dimer bonds on which the perturbation part of the Hamiltonian is defined (see Eq. (6.1) for the definition of nearest neighbour). The Raman operator constructed by next nearest neighbour spins, i.e. spins connected by dimer-bonds, has zero action on the ground state, as can be verified easily.

Fig. 6.18 sketches a portion of the Shastry-Sutherland model and will be used to illustrate the following analysis. The available Raman experiment [93]
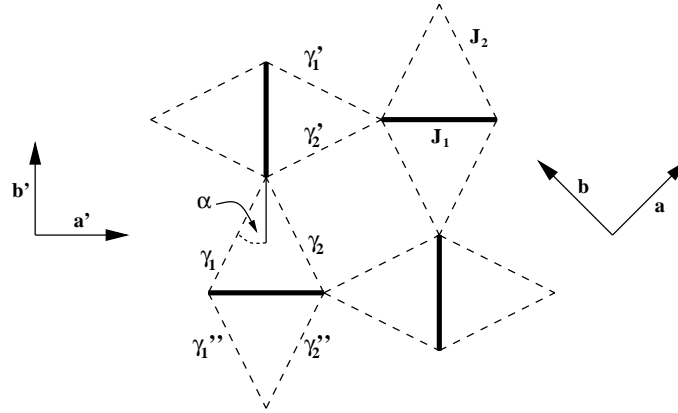
Figure 6.18.: A finite portion of the Shastry-Sutherland model. Nearest neighbour bonds are depicted by dashed lines (see also Fig. 6.2 on page 95). The projections of the fields of the incident and scattered light on these bonds leads to the geometrical understanding of the microscopic coupling-constants γ_i as described in the main text. We analyse the situation for 90° scattering geometries, where the fields of the incident and the scattered light are perpendicular to each other. Only the two depicted polarisations (ab) and (a'b') are experimentally relevant.

probes a $SrCu_2(BO_3)_2$ crystal in the so-called 90° scattering geometry, where $\mathbf{E}^i$ and $\mathbf{E}^f$ are perpendicular to each other ($\mathbf{E} \propto \partial_t \mathbf{A} \parallel \mathbf{A}$). Two different in-plane polarisations (ab) and (a'b') were used (see Fig. 6.18). Calculating the scalar products in Eq. (6.56) for the dashed bonds in Fig. 6.18 in the (ab)-polarisation yields

$$\gamma_1 = \gamma_2 = -\gamma_1' = -\gamma_2' = \gamma \cos\left(\frac{\pi}{4} - \alpha\right) \cos\left(\frac{\pi}{4} + \alpha\right) = \gamma \cos(2\alpha)/2 , \quad (6.57)$$

where γ is a microscopic constant including distances and field-strengths. The

remaining bonds in the lattice are fixed by geometry, for instance $\gamma_1'' = \gamma_2$ and $\gamma_2'' = \gamma_1$. Now, in a $T = 0$ experiment, the initial state of the system is given by singlets on all dimers. In this case, every single spin interacts with a dimer singlet via *equal* bonds (e.g. γ_1 and γ_2), which gives zero; i.e. the effective $T = 0$ Raman operator for the (ab)-polarisation does not create excitations from the ground state.

On the other hand, calculating the projection of the fields on the bonds in the (a'b')-polarisation yields

$$\gamma_1 = -\gamma_2 = -\gamma_1' = \gamma_2' = \gamma \sin(\alpha)\cos(\alpha) = \gamma \sin(2\alpha)/2 \ . \tag{6.58}$$

The above argument does not hold anymore and the effective $T = 0$ operator for this polarisation creates excitations from the ground state. This finding agrees nicely with the experiment [93] where on $T \to 0$ the intensities almost vanish for the (ab)-polarisation but grow for the (a'b')-polarisation. Fig. 6.19 gives a schematic impression of the Raman operator in (a'b')-polarisation.
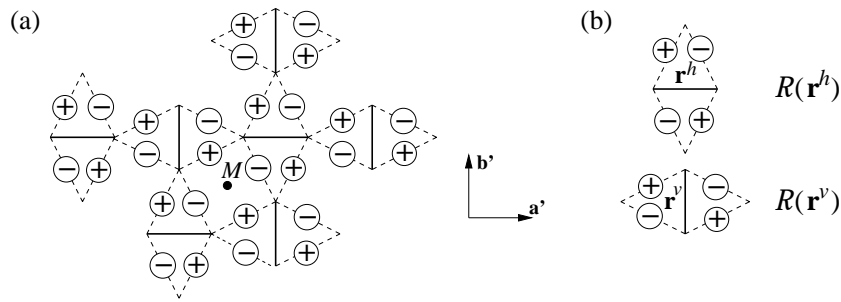
Figure 6.19.: (a) A finite portion of the Raman operator $\mathcal{R}$ corresponding to the (a'b')-polarisation geometry. This operator has a finite action on the ground state of the Shastry-Sutherland model. The operator is a sum over all $S_i S_j$-terms of spins connected by dashed lines. The relative sign of each such term is given in the circles. The point M is used in the discussion of the symmetry of $\mathcal{R}$. It turns out that the chosen operator $\mathcal{R}$ has Γ_3 symmetry; see main text. (b) The operator $\mathcal{R}$ is a sum over two different kinds of *local* operators $\mathcal{R}(\mathbf{r}^{v/h})$, which can be assigned to the position vector of the centre of the corresponding dimer.

We conclude our discussion of the Raman operator by analysing its point symmetries. Fig. 6.19(a) clearly shows, that $\mathcal{R}$ is odd under $m_{x/y}$ (reflection about the x- or y-axis (parallel to $\mathbf{a}'$ and $\mathbf{b}'$), which cross in the centre of one of the dimers). Therefore $\mathcal{R}$ is $\Gamma_3(xy)$ or $\Gamma_4\left(xy\left(x^2 - y^2\right)\right)$. Closer inspection shows, that $\mathcal{R}$ is also odd under R (rotation of $\pi/2$ about the centre of four dimers denoted by M in Fig. 6.19). Thus, $\mathcal{R}$ is Γ_3. We already made use of this result in section 6.3.2.

6.5.2. CUT Implementation

We are now going to tackle the problem of perturbatively calculating the action of the Raman operator $\mathcal{R}$ of the preceding subsection on the ground state $|0\rangle$. Since $\Delta S = 0$ for the Raman process, the minimum number of triplons created is two. According to our results of section 6.4 the two-triplon contribution is given by the amplitudes $w_{\mathbf{n},\mathbf{n'}}^{\pi(\mathbf{r})} = \bar{w}_{\mathbf{n},\mathbf{n'}} + e^{i\mathbf{Qr}}dw_{\mathbf{n},\mathbf{n'}}$ defined by the *local* action

$$\mathcal{R}(\mathbf{r})|0\rangle = \sum_{\mathbf{n},\mathbf{n'}} w_{\mathbf{n},\mathbf{n'}}^{\pi(\mathbf{r})}|\mathbf{r}+\mathbf{n}, \mathbf{r}+\mathbf{n'}\rangle \ . \tag{6.59}$$

Since we have $\mathbf{K} = \sigma = 0$ for the Raman observable, the global operator can be pictured as a sum of these local operators as depicted in Fig. 6.19. Remember the super-index $\pi(\mathbf{r}) \in \{v, h\}$ in $w_{\mathbf{n},\mathbf{n'}}^{\pi(\mathbf{r})}$ reflects the fact that we have two different local operators, depending on whether the operator is assigned to a vertically or horizontally oriented dimer.

We define the net and deviation part of $w_{\mathbf{n},\mathbf{n'}}^{\pi(\mathbf{r})}$ according to

$$\bar{w}_{\mathbf{n},\mathbf{n'}} = (w_{\mathbf{n},\mathbf{n'}}^{v} + w_{\mathbf{n},\mathbf{n'}}^{h})/2$$

$$dw_{\mathbf{n},\mathbf{n'}} = (w_{\mathbf{n},\mathbf{n'}}^{v} - w_{\mathbf{n},\mathbf{n'}}^{h})/2 \ . \tag{6.60}$$

As we will see later on, it suffices to focus on the amplitudes $w_{\mathbf{n},\mathbf{n'}}^{v}$, since the amplitudes $w_{\mathbf{n},\mathbf{n'}}^{h}$ can be calculated from the $w_{\mathbf{n},\mathbf{n'}}^{v}$ by symmetry arguments. We begin by analysing the elementary building block $\mathcal{R}^{\mathrm{el}}(\mathbf{r}^{v})$ of the local Raman operator $\mathcal{R}(\mathbf{r}^{v})$, which is depicted in Fig. 6.20. Again, simple symmetry operations can be used to construct the full local operator from this unit. The microscopic coupling constant γ appearing in $\mathcal{R}$ is proportional to the
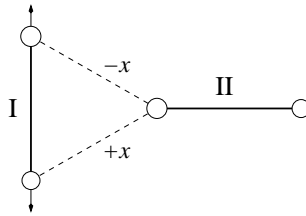

Figure 6.20.: The elementary building block $\mathcal{R}^{\mathrm{el}}$ of the local Raman operator $\mathcal{R}(\mathbf{r}^{v})$. We only need two dimers I and II with $S = 1/2$ spins on their ends (circles). These bonds enter with different signs due to the symmetry of $\mathcal{R}$ (see Fig. 6.19(a)).

coupling-strength x. The remaining numbers entering γ are set to unity.

The elementary operator $\mathcal{R}^{\mathrm{el}}$ can be decomposed with respect to its action on the number of triplons

$$\mathcal{R}^{\mathrm{el}} = T'_{-2} + T'_{-1} + T'_0 + T'_1 + T'_2 \; . \tag{6.61}$$

The elementary cluster depicted in Fig. 6.20 can be in 16 different states which we denote by $|x_{\mathrm{I}}, x_{\mathrm{II}}\rangle$, where $x_{\mathrm{I}}, x_{\mathrm{II}} \in \{s, t^{-1}, t^0, t^1\}$ are singlets or one of the three possible triplons. The operators T' act on these 16 states according to Tab. 6.3. Matrix elements not listed are zero or can be constructed by using ${T'_n}^\dagger = T'_{-n}$. These operators conserve both the total magnetisation m and

$2T'_0$	
$\|s, t^{\pm 1}\rangle \;\longrightarrow$	$-\|t^{\pm 1}, s\rangle$
$\|s, t^0\rangle \;\longrightarrow$	$\|t^0, s\rangle$
$2T'_1$	
$\|s, t^{-1}\rangle \;\longrightarrow$	$\|t^0, t^{-1}\rangle - \|t^{-1}, t^0\rangle$
$\|s, t^0\rangle \;\longrightarrow$	$\|t^1, t^{-1}\rangle - \|t^{-1}, t^1\rangle$
$\|s, t^1\rangle \;\longrightarrow$	$\|t^1, t^0\rangle - \|t^0, t^1\rangle$
$2T'_2$	
$\|s, s\rangle \;\longrightarrow$	$\|t^1, t^{-1}\rangle + \|t^{-1}, t^1\rangle - \|t^0, t^0\rangle$

Table 6.3.: The action of the operators T'_0, T'_1 and T'_2, as they appear in the definition (6.61), on all relevant states of the dimer pair depicted in Fig. 6.20. These operators conserve the total spin S and the total magnetisation m as becomes clear from Tab. 3.1 on page 55. Matrix elements not listed are zero. In practice only the action of T'_2 is of importance, since we consider the lattice to be prepared in the ground state $|0\rangle$.

the total spin S. Therefore, the chosen operator $\mathcal{R}$ complies with the two-magnon Raman process selection rule $\Delta S = 0$. This remains true for the effective operator, since the additional T_i in each operator product $\mathcal{R}^{\mathrm{el}}(\underline{m}; i)$ also conserve S and m (see Eq. (6.62) further down). Since the $T = 0$ ground state is a singlet, our Raman operator is sensitive to singlet excitations only, which agrees with the experimental findings. The conservation of S becomes clearer, if we switch to the $\{|S, m\rangle\}$ basis, where S denotes the total spin and m the total magnetisation associated with S^z_{total}. All possible states in this basis for zero, one and two triplons present in the system are listed in Tab. 3.1 on page 55.

To calculate all $w^{\mathrm{el}, v}_{\mathbf{n}, \mathbf{n}'}$ to a given order, we embed the local operator $\mathcal{R}^{\mathrm{el}}(\mathbf{r}^v)$ at the dimer position $\mathbf{r}^v$ in the ordinary Shastry-Sutherland lattice. Then, the

calculation of the amplitudes w by means of the *effective* observable (3.36)

$$\mathcal{R}^{\text{el}}_{\text{eff}}(\mathbf{r}^v; x) = \sum_{k=0}^{\infty} x^k \sum_{i=1}^{k+1} \sum_{|\underline{m}|=k} \tilde{C}(\underline{m}; i) \mathcal{R}^{\text{el}}(\underline{m}; i) , \quad \text{with}$$

$$\mathcal{R}^{\text{el}}(\underline{m}; i) = T_{m_1} \cdots T_{m_{i-1}} \mathcal{R}^{\text{el}}(\mathbf{r}^v) T_{m_i} \cdots T_{m_k} , \tag{6.62}$$

follows the usual route. The operators T_i already appeared in H_{eff} and conserve both the total spin S and total magnetisation m. After the T_i' for the elementary local Raman observable $\mathcal{R}^{\text{el}}(\mathbf{r}^v)$ are plugged into Eq. (6.62) the action of the corresponding *effective* elementary local observable $\mathcal{R}^{\text{el}}_{\text{eff}}(\mathbf{r}^v)$ on the ground state is evaluated by means of the computer implementation outlined in section 3.5.2. Only those processes $\mathcal{R}^{\text{el}}(\underline{m}; i)$ have to be considered, which start with the T_2' operator, since all T operators of H_{eff} and the remaining T' operators of $\mathcal{R}^{\text{el}}_{\text{eff}}(\mathbf{r}^v)$ give zero when acting on the ground state.

We calculate $\mathcal{R}^{\text{el}}_{2,0}(\mathbf{r}^v)$, the action of $\mathcal{R}^{\text{el}}_{\text{eff}}$ on $|0\rangle$, into the two-triplon sector. There are no contributions in the one-triplon sector due to spin conservation. The actual calculation has been extended to 8th order in x, i.e. we consider all processes of type $\mathcal{R}^{\text{el}}(\underline{m}; i)$ in Eq. (6.62) involving 8 operators T or less plus operator T_2'. Since the T_2' is needed to inject two triplons from the ground state, there are at maximum 8 operators T left to engender the polarisation cloud dressing the injected triplons.

As we have pointed out in section 6.2.1 a single $T_{\pm 1}$ can move one triplon to the adjacent dimer, iff only one of the spins on this end-dimer is connected to the spins on the starting-dimer. A progressive application of T_1 operators leads to a variety of zig-zag paths a single triplon can possibly take through the lattice (see Fig. 6.8 on page 106). Since we want to calculate the two-triplon amplitudes $w_{\mathbf{n},\mathbf{n}'}$ and T_2' already injects two triplons on adjacent dimers, the remaining product of T operators must conserve the number of triplons. The operator T_0 does not lead to a triplon-motion so that we need to consider $T_{\pm 1}$ operators for the construction of the minimum cluster only. In 8th order it suffices to consider 4 T_1 operators, since we need the remaining operators to be T_{-1} operators to annihilate the intermediately created triplons. Hence, the minimum cluster is constructed by considering all zig-zag paths of length 4 for each of the two initially injected triplons.

Fig. 6.21 gives an impression of the size of the minimum cluster needed to calculate all amplitudes to 8th order. The dimer pair, on which the elementary local observable injects triplons can be found in the middle. The left dimer of this dimer-pair is denoted by $\mathbf{r}^v$. We picture the local observable to be attached to this side.
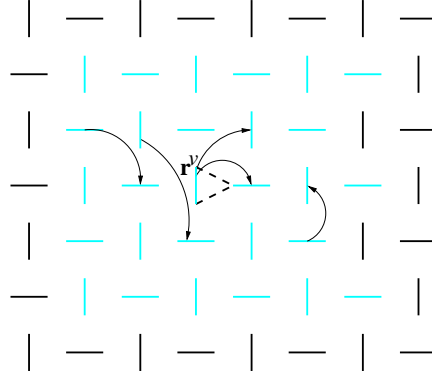
Figure 6.21.: A portion of the Shastry-Sutherland lattice. The effective elementary local Raman operator $\mathcal{R}^{\text{el}}_{2,0}(\mathbf{r}^v)$ injects two triplons on adjacent dimers. One triplon is injected on the dimer $\mathbf{r}^v$ associated with the local Raman operator and another one on the next dimer to the right. The action of $\mathcal{R}^{\text{el}}_{2,0}(\mathbf{r}^v)$ on $|0\rangle$ gives the amplitudes $w^{\text{el},v}_{\mathbf{n},\mathbf{n}'}$, of which we wrote down two in the main text. They are visualised by the two arrows starting from dimer $\mathbf{r}^v$. The calculation of $\mathcal{R}^{\text{el}}_{2,0}(\mathbf{r}^v)$ to 8th order gives rise to many more amplitudes as is indicated by the other arrows. If we consider all calculated amplitudes and stain those dimers cyan (grey), which are positioned at the beginning and at the end of the associated arrows, we obtain the depicted pattern of "unused" black and "used" cyan (grey) dimers. We restrict ourselves to $\mathbf{n}' - \mathbf{n} > 0$.

As for the amplitudes of H_{eff} we calculate only those $w^{\text{el},v}_{\mathbf{n},\mathbf{n}'}$ for which the restriction $\mathbf{d} = \mathbf{n}' - \mathbf{n} > 0$ in $|\mathbf{r} + \mathbf{n}, \mathbf{r} + \mathbf{n}'\rangle$ holds. To give an example of the obtained results we write down two amplitude. With $\mathbf{n} = (n_1, n_2)$ and $\mathbf{n}' = (n_1', n_2')$ we denote $w^{\text{el},v}_{\mathbf{n},\mathbf{n}'} = w^{\text{el},v}_{n_1,n_2;n_1',n_2'}$ and find

$$w^{\text{el},v}_{0,0;1,0} = -\frac{1}{2} + \frac{3}{8}x^2 - \frac{47}{64}x^4 - \frac{7}{32}x^5 + \frac{1495}{576}x^6 + \frac{63863}{27648}x^7 - \frac{1737889}{221184}x^8$$

$$w^{\text{el},v}_{0,0;1,1} = -\frac{1}{8}x^2 - \frac{3}{16}x^3 + \frac{41}{128}x^4 + \frac{551}{512}x^5 - \frac{3179}{18432}x^6 - \frac{1067629}{221184}x^7$$

$$- \frac{11661605}{2654208}x^8 . \tag{6.63}$$

Having calculated $\mathcal{R}^{\text{el}}_{2,0}(\mathbf{r}^v)$ we readily have the result for the *full* local observable $\mathcal{R}_{2,0}(\mathbf{r}^v)$ by symmetry. The latter is the sum of the elementary building block depicted in Fig. 6.20 and its counterpart obtained by reflecting the figure at the axis sketched by the arrows in Fig. 6.20. The observable $\mathcal{R}_{2,0}(\mathbf{r}^v)$ is odd

under this operation. The symmetry operation m_y yields

$$m_y|0\rangle = |0\rangle \quad \text{and}$$

$$m_y|\mathbf{r}, \mathbf{r}'\rangle = m_y|r_1, r_2; r_1', r_2'\rangle = (-1)^{r_1+r_2+r_1'+r_2'}|-r_1, r_2; -r_1', r_2'\rangle . \qquad (6.64)$$

Then, assuming $\mathbf{r}^v = (0,0)$ without loss of generality, the amplitudes $\tilde{w}_{\mathbf{n},\mathbf{n}'}^{\text{el},v}$ of the reflected part of the elementary observable are given by

$$\tilde{w}_{n_1,n_2;n_1',n_2'}^{\text{el},v} = - \langle n_1, n_2; n_1', n_2'|m_y \mathcal{R}_{\text{eff}}^{\text{el}}(\mathbf{r}^v)m_y^\dagger|0\rangle$$

$$= (-1)^{SD+n_1+n_2+n_1'+n_2'+1}\langle -n_1, n_2; -n_1', n_2'|\mathcal{R}_{\text{eff}}^{\text{el}}(\mathbf{r}^v)|0\rangle$$

$$= (-1)^{n_1+n_2+n_1'+n_2'+1} \begin{cases} w_{-n_1',n_2';-n_1,n_2}^{\text{el},v} , & \text{triplons interchanged} \\ w_{-n_1,n_2;-n_1',n_2'}^{\text{el},v} , & \text{otherwise.} \end{cases}$$

$$(6.65)$$

Since, after reflection, the two triplons can be connected by a negative distance $\mathbf{d}$ (see above for definition), it might be necessary to interchange these triplons. This introduces an extra minus sign, if the total spin S of the two-triplon state is odd. Since the Raman observable injects only $S = 0$ states, the product SD can be dropped altogether. We still have to distinguish the two cases. The amplitudes of the full vertical local observable $\mathcal{R}_{2,0}(\mathbf{r}^v)$ are finally given by

$$w_{\mathbf{n},\mathbf{n}'}^v = w_{\mathbf{n},\mathbf{n}'}^{\text{el},v} + \tilde{w}_{\mathbf{n},\mathbf{n}'}^{\text{el},v} . \qquad (6.66)$$

To calculate the *global* Raman observable $\mathcal{R}_{2,0}(\sigma, K)$ we still need the corresponding amplitudes $w_{\mathbf{n},\mathbf{n}'}^h$ of the *horizontal* local observable $\mathcal{R}_{2,0}(\mathbf{r}^h)$ since they also contribute to the $\bar{w}_{\mathbf{n},\mathbf{n}'}$ and $dw_{\mathbf{n},\mathbf{n}'}$ (cf. Eqs. (6.54) and (6.60)). Again, the $w_{\mathbf{n},\mathbf{n}'}^h$ can be obtained from the $w_{\mathbf{n},\mathbf{n}'}^v$ by a simple symmetry argument. Consider $\mathcal{D}$ to denote the operation which turns the lattice at $\pi/2$ about the dimer-centre $\mathbf{r}^v$. The associated vertical dimer becomes a horizontal dimer which we address by $\mathbf{r}^h$ after the operation. We have

$$\mathcal{D}|0\rangle = |0\rangle \quad \text{and}$$

$$\mathcal{D}|\mathbf{r}, \mathbf{r}'\rangle = \mathcal{D}|r_1, r_2; r_1'r_2'\rangle = (-1)^{r_1+r_2+r_1'+r_2'}|-r_2, r_1; -r_2', r_1'\rangle . \qquad (6.67)$$

A short look at Fig. 6.19 shows that

$$\mathcal{R}_{\text{eff}}(\mathbf{r}^h) = -\mathcal{D}^\dagger \mathcal{R}_{\text{eff}}(\mathbf{r}^v)\mathcal{D} . \qquad (6.68)$$

and in analogy to our symmetry reasoning from above we find (again $\mathbf{r}^v = (0,0)$ without loss of generality)

$$
\begin{aligned}
w^h_{n_1, n_2; n'_1, n'_2} &= -\langle n_1, n_2; n'_1, n'_2 | \mathcal{D} \mathcal{R}_{\text{eff}}(\mathbf{r}^v) \mathcal{D}^\dagger | 0 \rangle \\
&= (-1)^{n_1 + n_2 + n'_1 + n'_2 + 1} \langle n_2, -n_1; n'_2, -n'_1 | \mathcal{R}_{\text{eff}}(\mathbf{r}^v) | 0 \rangle \\
&= (-1)^{n_1 + n_2 + n'_1 + n'_2 + 1} \left\{ \begin{array}{ll} w^v_{n'_2, -n'_1; n_2, -n_1} \ , & \text{triplons interchanged} \\ w^v_{n_2, -n_1; n'_2, -n'_1} \ , & \text{otherwise.} \end{array} \right.
\end{aligned}
$$
(6.69)

We now have all the ingredients necessary to calculate the action of $\mathcal{R}_{2,0}(\sigma, K)$ on the ground state by means of Eq. (6.54) of section 6.4. As we have outlined there, we prefer to express our results in the language of vector components

$$
A_{\sigma', \mathbf{K}, \mathbf{d}} = \langle \sigma', \mathbf{K}, \mathbf{d} | \mathcal{R}_{2,0}(\sigma, \mathbf{K}) | 0 \rangle \ . \tag{6.70}
$$

The wave vector of visible laser light is in the vicinity of 10^5 cm^{-1}, while the typical Brillouin dimension of a crystal is about 10^8 cm^{-1}. Thus Raman scattering provides information about excitations in the immediate neighbourhood of $\mathbf{K} = \mathbf{0}$ only. Hence, $\mathbf{K}$ in Eq. (6.70) can be set to zero. Moreover, the auxiliary quantum number $\sigma \in \{0, 1\}$, which was introduced to account for possible extra phase shifts between the two sublattices of the Shastry-Sutherland model, can also be set to zero. We end up with the Raman vector components (see Eqs. (6.55))

$$
A_{0, \mathbf{0}, \mathbf{d}} = \sum_{\mathbf{n}} \bar{w}_{\mathbf{n}, \mathbf{n} + \mathbf{d}}
$$

$$
A_{1, \mathbf{0}, \mathbf{d}} = \sum_{\mathbf{n}} dw_{\mathbf{n}, \mathbf{n} + \mathbf{d}} \cos \left[\mathbf{Q} (\mathbf{n} + \mathbf{d}/2) \right] \ , \tag{6.71}
$$

with

$$
\bar{w}_{\mathbf{n}, \mathbf{n}'} = (w^v_{\mathbf{n}, \mathbf{n}'} + w^h_{\mathbf{n}, \mathbf{n}'})/2
$$

$$
dw_{\mathbf{n}, \mathbf{n}'} = (w^v_{\mathbf{n}, \mathbf{n}'} - w^h_{\mathbf{n}, \mathbf{n}'})/2 \ . \tag{6.72}
$$

We want to close this subsection by giving some examples $(\mathbf{d} = (d_1, d_2))$

$$
A_{0, \mathbf{0}, 1, 0} = -1/2 + \frac{1}{2} x^2 - \frac{95}{64} x^4 - \frac{37}{64} x^5 + \frac{2491}{384} x^6 + \frac{67241}{9216} x^7 - \frac{12024629}{442368} x^8
$$

$$
A_{0, \mathbf{0}, 1, 1} = -\frac{1}{4} x^2 - \frac{3}{8} x^3 + \frac{29}{32} x^4 + \frac{177}{64} x^5 - \frac{17083}{9216} x^6 - \frac{901703}{55296} x^7 - \frac{2526421}{331776} x^8
$$

$$
A_{0, \mathbf{0}, 1, 2} = \frac{5}{128} x^4 + \frac{43}{512} x^5 - \frac{1985}{18432} x^6 - \frac{137357}{221184} x^7 - \frac{203695}{1327104} x^8 \tag{6.73}
$$

All $A_{1,\mathbf{0},\mathbf{d}}$ happen to be zero. In the following subsection we evaluate the results and compare them to experimental data.

6.5.3. Results

A first physically relevant quantity we can already construct from the above findings is the relative spectral weight of the Raman operator in the two-triplon channel. The *total* weight I_{tot} (momentum- and energy-integrated) of the Raman operator per dimer is given by the sum rule

$$I_{\text{tot}} = \langle 0|(\mathcal{R}(\mathbf{r}))^2|0\rangle - \langle 0|\mathcal{R}(\mathbf{r})|0\rangle^2 = 3/2, \qquad (6.74)$$

where $\mathcal{R}(\mathbf{r})$ is the local Raman operator assigned to a vertical or horizontal dimer. It obviously does not matter if we choose $\mathbf{r}$ to be a vertical or a horizontal dimer. The results of the preceding section, in particular those for the decomposition of $\mathcal{R}^{\text{el}}(\mathbf{r})$ into the ladder operators T_i' (Eq. (6.61)), show, that $\mathcal{R}(\mathbf{r})|0\rangle$ has no overlap with $|0\rangle$. Therefore, the second term in Eq. (6.74) is zero. It is straightforward to calculate the first term which finally yields the given result.

The corresponding weight I_2 contained in the two-triplon part of $\mathcal{R}(\mathbf{r})$ is given by (set $\mathbf{r}^v = (0,0)$)

$$I_2 = \langle 0|\left(\mathcal{R}_{2,0}(\mathbf{r}^v)\right)^2|0\rangle = \sum_{\mathbf{n},\mathbf{n}'} |\langle \mathbf{n}, \mathbf{n}'|\mathcal{R}_{\text{eff}}(\mathbf{r}^v)|0\rangle|^2 = \sum_{\mathbf{n},\mathbf{n}'} \left(w_{\mathbf{n},\mathbf{n}'}^v\right)^2$$

$$= 3/2 - 3x^2 + \frac{273}{32}x^4 + \frac{21}{16}x^5 - \frac{6155}{192}x^6 - \frac{44053}{2304}x^7 + \frac{365857}{3072}x^8 . \qquad (6.75)$$

Again, the specific choice of $\mathbf{r}$ does not matter, and we fix $\mathbf{r}$ to be a vertical dimer. We first calculate the squares of the amplitudes w^v in Eq. (6.75), drop all terms of order 9 and higher, since the original results have been obtained to order 8 only, and perform the sum which leads to the given plain series result. The resulting relative intensity I_2/I_{tot} is depicted as solid grey line in Fig. 6.22. All other lines correspond to Padé or Dlog-Padé approximants. The extrapolations deviate strongly at the relevant value ($x = 0.603$, the vertical line in Fig. 6.22). However, we can be sure, that the two-triplon part of the Raman operator covers 55% to 60% of the total weight. A closer inspection of all plotted extrapolation suggests an accumulation of approximants at about 60%.

We now commence the evaluation of the effective two-triplon Green's func-
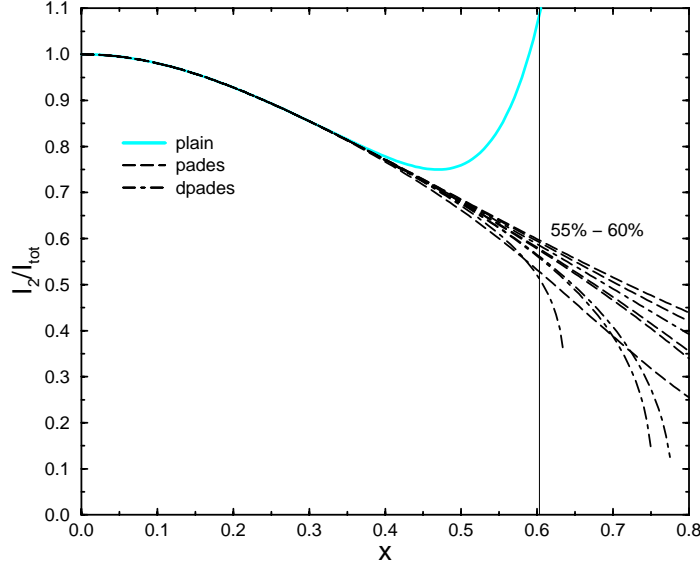
Figure 6.22.: Relative intensity of the two-triplon part of the Raman operator. The plain series result is depicted as solid cyan (grey) line. Various Padé and Dlog-Padé approximants are shown by dashed and dashed-dotted lines. In the vicinity of $x = 0.603$, the $SrCu_2(BO_3)_2$-relevant value (vertical line), the deviations of the various approximants amongst each other are rather strong already.

tion for the Raman operator at $\mathbf{K} = \mathbf{0}$ and $\sigma = 0$

$$\mathcal{G}^{\mathcal{R}}(\omega; x) = \left\langle 0 \left| \mathcal{R}_{2,0}^{\dagger}(0, \mathbf{0}; x) \frac{1}{\omega - [H_1(0, \mathbf{0}; x) + H_2(0, \mathbf{0}; x)]} \mathcal{R}_{2,0}(0, \mathbf{0}; x) \right| 0 \right\rangle$$

$$= \frac{\sum_{\mathbf{d} > 0} \left(A_{0,\mathbf{0},\mathbf{d}}(x) \right)^2}{\omega - a_0 - \cfrac{b_1^2}{\omega - a_1 - \cfrac{b_2^2}{\omega - \cdots}}} \ . \tag{6.76}$$

All $A_{1,\mathbf{0},\mathbf{d}}$ evaluate to zero. As explained in detail in chapter 4 we are going to evaluate $\mathcal{G}^{\mathcal{R}}$ by utilising the continued fraction technique. The coefficients a_i and b_i in Eq. (6.76) are obtained from repeated action of $H_1 + H_2$ on the state $|\text{Init}\rangle = \mathcal{R}_{2,0}(0, \mathbf{0}; x)|0\rangle$.

The vector components A of $\mathcal{R}_{2,0}$ and the matrix elements t of H_1 and H_2 have to be extrapolated to warrant quantitative results. We begin by examin-

ing the amplitudes w, from which the vector components A are constructed. The extrapolation of the matrix elements t of H_1 and H_2 is treated thereafter.

Fig. 6.23 shows $w_{0,0;1,0}^v$ (lower curves) and $w_{0,0;1,1}^v$ (upper curves) as functions of x. The dashed lines correspond to the plain series results, while the solid lines represent various Padé approximants to the series. For x-values of interest ($x \approx 0.6$) the latter give very reliable estimates. The plain series start to deviate from the extrapolations at about $x \approx 0.4$.
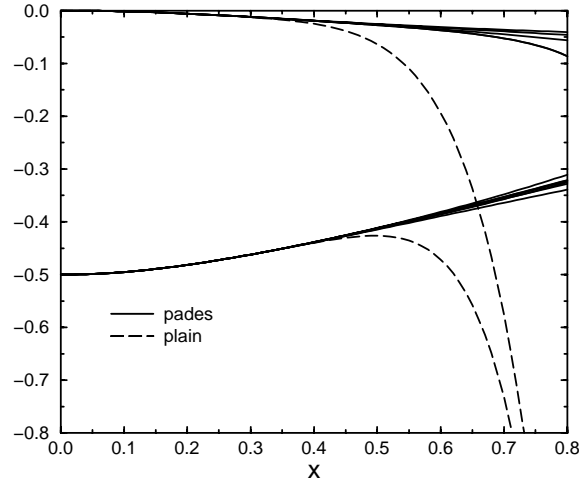
Figure 6.23.: The dashed lines represent the plain series results for $w_{0,0;1,0}^v$ (lower curve) and $w_{0,0;1,1}^v$ (upper curve). Solid lines are various Padé approximants. They give reliable estimates in the regime of interest ($x \approx 0.6$).

Amplitudes w corresponding to larger distances **d** drop to zero rapidly as illustrated in Tab. 6.4. Basically, only the two amplitudes depicted in Fig. 6.23 have to be extrapolated carefully. The remaining amplitudes are small enough to rely on the plain series results.

After all calculated amplitudes have been inspected and extrapolated as described or found to be small enough to abstain from an extrapolation, they are added according to Eq. (6.72) and (6.71) to yield the vector components we are going to use in the evaluation of the Green's function.

We could have added the amplitudes prior to extrapolation and extrapolate the resulting vector components. In fact, this leads to very small quantitative changes only. It really does not matter, in which order the two operations are executed.

i,j	$|w^v_{0,0;i,j}|$; $x = 0.4$	$|w^v_{0,0;i,j}|$; $x = 0.6$
1,0	$4.40 \cdot 10^{-1}$	$4.71 \cdot 10^{-1}$ $(3.81 \cdot 10^{-1})$
1,1	$2.50 \cdot 10^{-2}$	$1.93 \cdot 10^{-1}$ $(3.53 \cdot 10^{-2})$
2,1	$8.51 \cdot 10^{-4}$	$5.48 \cdot 10^{-3}$ $(5.12 \cdot 10^{-3})$
2,2	$2.64 \cdot 10^{-5}$	$4.12 \cdot 10^{-4}$
3,0	$6.96 \cdot 10^{-8}$	$1.78 \cdot 10^{-6}$
3,2	$3.48 \cdot 10^{-8}$	$8.92 \cdot 10^{-7}$

Table 6.4.: The amplitudes $w^v_{\mathbf{n},\mathbf{n}+\mathbf{d}}$ drop off rapidly with increasing distance $\mathbf{d}$. The values given in this table correspond to the plain series results at $x = 0.4$ (left column) and $x = 0.6$ (right column). The values in parentheses in the right column result from Padé approximants as depicted in Fig. 6.23. The values for larger distances are small enough to abstain from approximations.

We continue and show how the matrix elements of H_1 and H_2 can be extrapolated. The matrix representing H_1 in $\{|\sigma, \mathbf{K}, \mathbf{d}\rangle\}$ depends on the *one*-triplon hopping amplitudes $\bar{t}_{\mathbf{r}}$ (net part) and $dt_{\mathbf{r}}$ (deviation part) only. The one-triplon amplitudes have been calculated up to 15th order. They represent different physics than the pure two-triplon hopping amplitudes (calculated up to 14th order), which constitute H_2. We therefore choose to extrapolate the one-triplon and the two-triplon amplitudes separately.

Since the number of matrix elements in H_1 and H_2 is much larger than the number of components in $|\text{Init}\rangle$ we resort to the method of optimised perturbation theory (OPT) introduced in chapter 5. OPT has the convenient property to be additive; i.e. it does not matter if we apply OPT to the hopping amplitudes, of which the matrix elements of H_{eff} are linear combinations, or if we apply OPT directly to the matrix elements. The result is the same. For the one-triplon part H_1 we decide to use the first alternative, since we can check the quality of the extrapolation with our previous result for the one-triplon energy $\omega(\mathbf{k})$.

Fig. 6.24 shows $\omega(\mathbf{k})$ for $\mathbf{k} = (0,0)$ (one-triplon gap) and $\mathbf{k} = (\pi, 0)$ at $x = 0.603$. The curves are plotted as functions of the OPT-parameter α_1 used to optimise all one-triplon hopping amplitudes that build up $\omega(\mathbf{k})$. Using the minimal sensitivity criterion we find two possible values for α_1. Since the first extremum yields values much larger than those found in section 6.2.3 we decide in favour of the second extremum which gives $\alpha_1 \approx -0.2$. Using this value and plotting $\omega(\mathbf{k} = (0,0))$ and $\omega(\mathbf{k} = (\pi, 0))$ now as functions of x we obtain the solid grey curves in Fig. 6.25. Disappointingly these curves do not yield better results than the plain series depicted as solid black lines (just beneath the grey lines) in comparison with the most reliable Dlog-Padé approximants
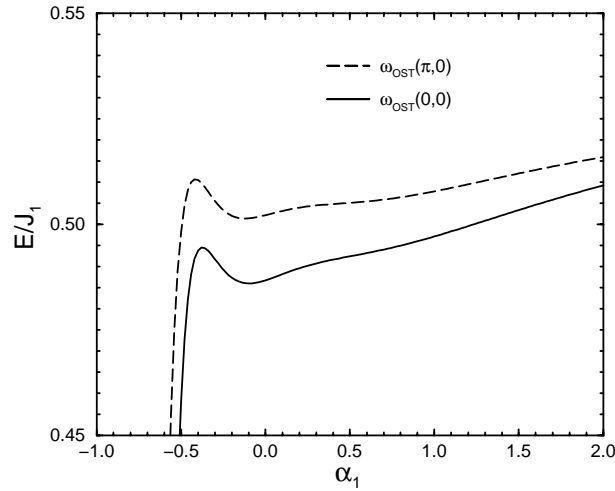
Figure 6.24.: OPT results for the one-triplon energy $\omega(\mathbf{k})$ at the depicted $\mathbf{k}$-values as functions of the OPT-parameter α_1. The curves shown correspond to $x = 0.603$. One clearly sees well expressed extrema at about the same α_1-value for both curves. We decide for $\alpha_1 = -0.2$.

shown as dashed lines. However, we stick to this technique to be sure that none of the one-triplon amplitudes diverges, which would ultimately lead to a diverging matrix element in H_{eff}. This could spoil the final results. Moreover, at $x \approx 0.6$ the deviation from the approximants is negligible.

We move on to the interaction part H_2. As explained in section 6.3 we represent H_{eff}, H_1 and H_2 by 84×84 matrices and use $H_2 = H_{\text{eff}} - H_1$. The matrix elements of H_{eff} and H_1 are cut down to 14th order to account for the fact that the two-particle hopping amplitudes, building up the matrix elements of H_2, have been calculated to 14th order only. For H_2 we resort to the second alternative and apply the OPT procedure directly to the matrix elements.

After all matrix elements of H_2 have been optimised with yet not determined OPT parameter α_2 we add the result to the optimised H_1 ($\alpha_1 = -0.2$) and plot some of the lowest eigen-values of the resulting Hamiltonian for $\mathbf{K} = \mathbf{0}$ and $x = 0.603$ as function of α_2. Fig. 6.26 shows two well separated lowest bound states and three more states. The depicted result is obtained by exactly diagonalising the resulting Hamiltonian H_{eff} at discrete values for α_2 (points). The exact diagonalisation is left to the computer algebra programme MAPLE. The results depicted in Fig. 6.26 do not change visibly, if we extend the basis to incorporate 14 further distances (those positive distances, which correspond
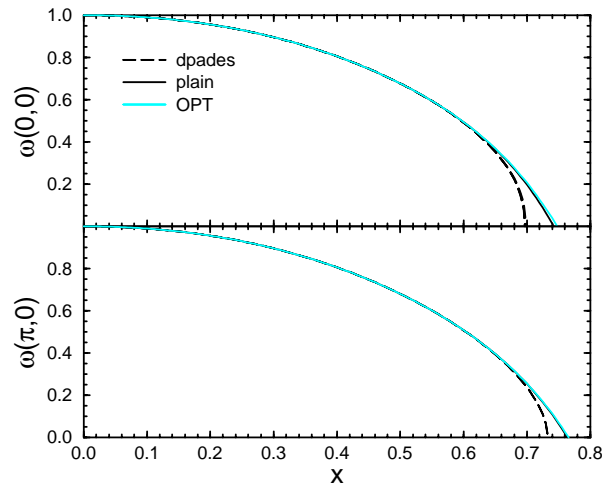
Figure 6.25.: The solid cyan (grey) lines depict the OPT results for the one-triplon energy $\omega(\mathbf{k})$ with OPT parameter $\alpha_1 = -0.2$ as function of x. The upper panel shows the one-triplon gap $\omega(0,0)$, the lower panel shows $\omega(\pi,0)$. Solid black lines correspond to the plain series results. They lie very close to the OPT results. Dashed lines depict the most reliable Dlog-Padé approximants.

to the dimers just outside the triangle depicted in Fig. 6.26 on page 147). This is easily understood. Expanding the basis does not lead to any new interaction terms, since they are already captured by the minimum basis of 84 states (42 distances). The basis expansion merely captures a larger part of the H_1 matrix, which may lead to changes within the continuum of states. But, this continuum is rather narrow (width: 0.029 in units of J_1) for the chosen x-value ($x = 0.603$) and all energies depicted in Fig. 6.26 correspond to bound state, which are mainly effected by triplon-triplon interactions captured by H_2.

Fig. 6.26 shows well pronounced extrema for the two lowest well separated bound states at about $0.9 \leq \alpha_2 \leq 1.2$. There is another extremum in the upper bands, falling in the same range. The two horizontal lines show the most reliable Dlog-Padé values for the two lowest energies at $x = 0.603$ and $\mathbf{K} = \mathbf{0}$ (see also Fig. 6.15 on page 124). A reasonable agreement is achieved for $\alpha_2 = 1.0$, which agrees nicely with the range given by the minimal sensitivity criterion.

Fig. 6.27 shows some eigen-values of $H_1 + H_2$ (84×84 matrix; exact diagonalisation as above) with the final OPT parameters $\alpha_1 = -0.2$ (H_1) and $\alpha_2 = 1.0$ (H_2) as functions of x for $\mathbf{K} = \mathbf{0}$. The solid lines are our previous
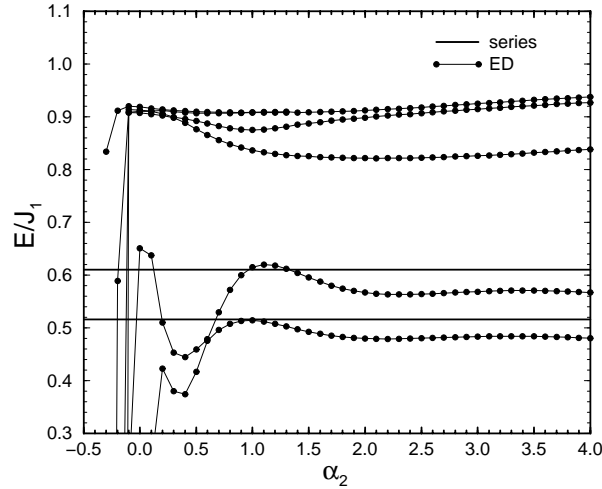
Figure 6.26.: Some eigen-values of H_{eff} with OPT parameter $\alpha_1 = -0.20$ for H_1 as function of the OPT parameter α_2 for H_2. The spectrum is obtained by exact diagonalisation of the 84×84 matrix representing $H_1 + H_2$ at $\mathbf{K} = \mathbf{0}$ and $x = 0.603$ at discrete values of α_2 (points). The horizontal lines correspond to the most reliable Dlog-Padé approximants of the two lowest eigen-values at $x = 0.603$. We detect well pronounced extrema of the two lower bands peaking at the values suggested by the approximants. A good OPT extrapolation can be achieved with $\alpha_2 = 1.0$.

Dlog-Padé results also depicted in Fig 6.15 on page 124. The agreement, especially for the two lowest eigen-values is excellent up to $x \approx 0.7$ where the $S = 0$ two-triplon gap closes.

Now, that we have calculated and extrapolated all quantities needed for the Green's function $\mathcal{G}^{\mathcal{R}}$ (Eq. (6.76)) we commence evaluating the continued fraction as outlined in chapter 4. In Fig. 6.28 we show the first nine continued fraction coefficients a_i and b_i for $x = 0.603$ and $\mathbf{K} = \mathbf{0}$. The width Δ_{cont} of the continuum at the chosen values for $\mathbf{K}$ and x is ≈ 0.029 in units of J_1. Since $\Delta_{\text{cont}} = 4b_{i=\infty}$ (see chapter 4) we expect the b_i depicted in Fig. 6.28 to be very small. However, the lower panel shows strong periodic increases in b_i after a fraction depth of five, although the coefficients have converged to small values before. The pattern seems to repeat itself if one enlarges the fraction depth. The coefficients a_i show a similar behaviour. An analogous consideration (see text below Eq. (4.8) on page 83) shows that $a_{i=\infty} \approx 0.47$. The repetitive algorithm of the continued fraction technique seems to produce rounding errors. Therefore, the algorithm does not produce states, which are
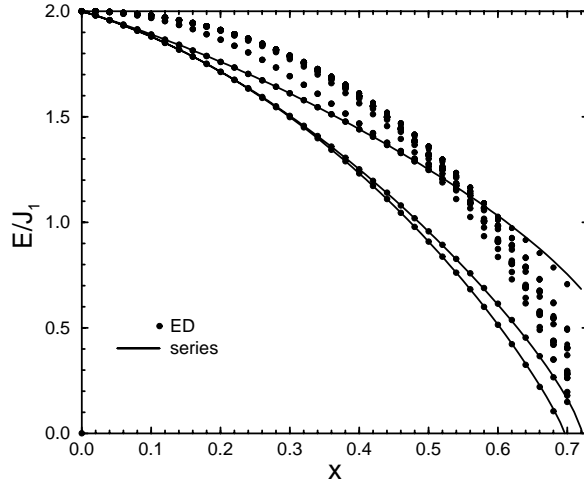
Figure 6.27.: Some eigen-values of $H_1 + H_2$ with OPT parameters $\alpha_1 = -0.20$ (H_1) and $\alpha_2 = 1.0$ (H_2) as function of x. The spectrum is obtained by exact diagonalisation of the 84×84 matrix representing $H_1 + H_2$ at $\mathbf{K} = \mathbf{0}$ for discrete values of x (points). The result agrees nicely with the energies obtained from Dlog-Padé approximant (solid lines) of the series results.

orthogonal to all the preceding states (see chapter 4). The algorithm gets trapped in a loop through the Hilbert space and starts to produce the same states and thus the same coefficients a_i and b_i on and on . We conclude, that all *relevant* information is captured in the depicted leading coefficients.

We evaluate the corresponding spectral density

$$S(\omega, \mathbf{0}; x) = -\frac{1}{\pi} \mathrm{Im}\mathcal{G}^{\mathcal{R}}(\omega, \mathbf{0}; x) \qquad (6.77)$$

at fixed x and $\mathbf{K} = \mathbf{0}$ by introducing an artificial broadening δ through $\omega \to \omega + i\delta$. Technically this is not necessary. However, the experiment has an intrinsic line broadening of approximately 2% in, which we model by $\delta = 0.02$ in units of J_1. Fig. 6.29 shows the experimental data [93] for the (a', b')-polarisation at a temperature well below the one-triplon gap as filled diamonds. The solid lines are the broadened spectral densities $S(\omega, \mathbf{0}; x)$ at $x = 0.603$ and $J_1 = 6.10$ meV$= 49.20$ cm^{-1}, which corresponds to the parameter values we have found in section 6.3.2. The black solid curve depicts the result for $\alpha_2 = 1.0$, while the grey solid curve is the corresponding result for $\alpha_2 = 1.3$. One clearly sees that the sensitivity of the spectral density S with respect to the OPT parameter α_2 for H_2 is not very strong. All depicted results have
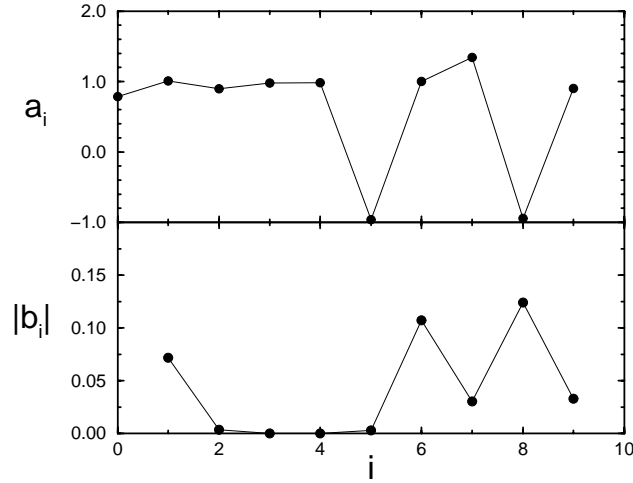
Figure 6.28.: Continued fraction coefficients a_i (upper panel) and b_i (lower panel) up to fraction depth nine at $\mathbf{K} = \mathbf{0}$ and $x = 0.603$.

been multiplied by a factor to account for the unknown numbers in the coupling constant γ (Eq. (6.58)). The factor is chosen such, that the theoretical result displays approximately the same weight as can be found in the first three peaks of the experiment.

The one-triplon gap of $\approx 24\text{cm}^{-1}$ gives a two-triplon continuum position of $\approx 48\text{cm}^{-1}$. Then, the first two peaks can be identified to be Γ_3 bound states, while the third peak is a Γ_3 anti-bound state (recall, that $\mathcal{R}$ has Γ_3 symmetry). The fourth experimentally observed peak is not captured within the investigated two-particle sector. Most probably this peak arises from three-triplon processes. The first peak at $\approx 30\text{cm}^{-1}$ corresponds to the upper one of the two well isolated lowest bound states depicted in Fig. 6.27. Its position, shape and weight fits the experiment perfectly. The positions of the remaining peaks deviate from the experimental centre positions by less than 7%. The weight distribution between the second and the third peak slightly differs from the experimental finding. However, the overall agreement must be consider good.

The sensitivity of the spectral density S with respect to changes in the parameters is tested by calculating S for $x = 0.635$ and $J = 7.325$ meV= 59.080 cm^{-1}, the parameter set suggested by Totsuka et al. [96]. The result is depicted by the dashed line in Fig. 6.29. The parameter modification cer-
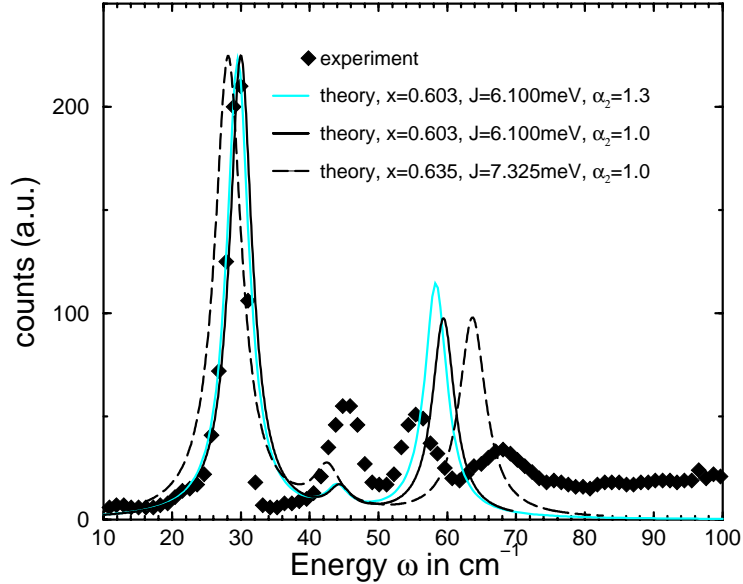
Figure 6.29.: Spectral density of the Raman operator $\mathcal{R}$ for two different sets of model parameters (lines) as given in the legend. The diamonds are data points from a Raman experiment on a $SrCu_2(BO_3)_2$ single crystal kindly provided by P. Lemmens. The experiment was performed at temperatures well below the one-triplon gap in the $(a'b')$-polarisation geometry. The solid lines results from inserting our parameter set from section 6.3.2. The cyan (grey) solid line results from choosing $\alpha_2 = 1.3$ as OPT value for H_2, while the black solid lines results from $\alpha_2 = 1.0$. The α_2-dependence of the results is rather weak. The dashed curve corresponds to the parameter set suggested by Totsuka et al. [96] for $\alpha_2 = 1.0$.

tainly influences S in the wrong direction. The two upper peaks have drifted apart. From the comparisons made in Fig. 6.29 it is justified to claim, that our parameter set leads to a somewhat better fit to the experimental finding.

It might be possible to find better suited parameters for this particular experiment. However, since we hope to find a parameter set that explains *all* available low temperature data at the same time, we are inclined to accept small cut-backs in specific experiments. One should also bear in mind, that the Raman operator we used to model the real process is a first order approximation only. Deviations of the spectral density S from the experiment can therefore not only be reduced to the choice of possibly wrong parameters[12].

---

[12] Modifications of the model Raman operator can lead to changes in the weight distribution between the different peaks. The peak positions, however, are entirely fixed by the

The confidence in our model parameters will be enhanced even more by comparing the results for the model INS spectral density to the appropriate experiment. We will tackle this issue in the next section. It will be our last topic.

6.6. Inelastic Neutron Scattering $-$ $S = 1$

We again start by defining a suitable operator describing an INS measurement performed on the Shastry-Sutherland model. The CUT-implementation and related calculational details are similar to those for the Raman operator. We will therefore profit from the detailed descriptions provided in the preceding subsection. The results and the comparison to experimental findings can again be found at the end of the subsection on hand.

6.6.1. INS-Operator

The differential cross section of neutrons inelastically scattered from magnetic excitations in spin lattices with momentum transfer $\mathbf{q}$ and energy transfer ω is essentially proportional to the magnetic dynamic structure factor[13] (see Ref. [107] for an overview)

$$
S(\omega, \mathbf{q}) = -\frac{1}{\pi} \mathrm{Im} \mathcal{G}^{\mathcal{F}}(\omega, \mathbf{q})
$$

$$
= -\frac{1}{\pi} \mathrm{Im} \left\langle 0 \left| \mathcal{F}^{\dagger}(\mathbf{q}) \frac{1}{\omega - (H - E_0)} \mathcal{F}(\mathbf{q}) \right| 0 \right\rangle , \quad \text{with} \qquad (6.78)
$$

$$
\mathcal{F}(\mathbf{q}) = \sum_i S^z(\mathbf{x}_i) e^{i\mathbf{q}\mathbf{x}_i} . \qquad (6.79)
$$

Here $S^z(\mathbf{x}_i)$ is the z-component of the spin located at the position $\mathbf{x}_i$. The latter is an element of the lattice Γ (see Fig. 6.31(a) on page 155). The sum in Eq. (6.79) is taken over all lattice sites i. Thus $\mathcal{F}(\mathbf{q})$ is proportional to the discrete Fourier transform of the local magnetic moments. We have to address two important points

(A) An INS experiment can probe any momentum transfer $\mathbf{q}$, i.e. $\mathbf{q}$ is not necessarily restricted to lie within the magnetic Brillouin zone (MBZ),

---

Hamiltonian.

[13] At this point the nomenclature differs in the literature. Some authors prefer to call $\mathcal{F}(\mathbf{q})$ the dynamic structure factor. We favour the given notation.

but can be any vector in the dual space. However, the excitations of the Shastry-Sutherland model are labelled by the total (crystal) momentum $\mathbf{K} \in \mathrm{MBZ}$. We thus have to fold back all $\mathbf{q} \notin \mathrm{MBZ}$. This is always possible, since the reduction $\mathbf{q} = \mathbf{K} + \mathbf{K}_0$, with $\mathbf{K} \in \mathrm{MBZ}$, holds for all $\mathbf{K}_0$ element of the reciprocal lattice. For some given $\mathbf{q}$ we shall denote by $\mathbf{K}(\mathbf{q})$ the corresponding value within the MBZ. Obviously $\mathbf{K} = \mathbf{q}$ for $\mathbf{q} \in \mathrm{MBZ}$. The quantum number σ is not changed by the back-folding process as will become clear in Eq. (6.87).

(B) The position vectors $\mathbf{x}_i \in \Gamma$ in Eq. (6.79) address each spin in the lattice and should not be confused with the vectors $\mathbf{r} \in \Gamma_{\mathrm{eff}}$ we introduced to denote the position of the dimer centres, see Fig. 6.31(a) on page 155.

Bearing these two points in mind we construct an operator $\mathcal{N}$ defined for the quantum numbers $\mathbf{K} = \mathbf{K}(\mathbf{q})$ and $\mathbf{r}$ such, that $\mathcal{N}(\mathbf{K}, \mathbf{r})$ and $\mathcal{F}(\mathbf{q}, \mathbf{x})$ have the same action on the ground state $|0\rangle$.

Let us begin by calculating the action of the "reference" operator $\mathcal{F}$ on the ground state. The action of $\mathcal{F}(\mathbf{q})$ on a *single* dimer composed of the two spins 0 and 1 in the singlet state $|s\rangle$ leads to the state $|t^0\rangle$, which is the $S^z = 0$ triplet-(triplon-)state of the dimer. A short calculation yields

$$\mathcal{F}(\mathbf{q})|s\rangle = \frac{1}{2}(e^{i\mathbf{q}x_0} - e^{i\mathbf{q}x_1})|t^0\rangle \; , \qquad (6.80)$$

where x_0 and x_1 are the position vectors of the two spins on the dimer. The minus sign for the second exponential appears, because we choose the orientation of the singlet $|s\rangle$ for the particular dimer according to

$$|s\rangle = \frac{1}{\sqrt{2}} \left(\uparrow_0 \downarrow_1 - \downarrow_0 \uparrow_1 \right) \; , \qquad (6.81)$$

where the indices on the arrows indicate the number of the spin. If we were to reverse the orientation of the singlet, the minus sign in Eq. (6.80) would appear in front of the first exponential.

For the rest of our discussion we fix the singlet orientation on the dimers according to

$$\frac{1}{\sqrt{2}} \left(\uparrow_{\mathrm{top/left}} \downarrow_{\mathrm{bottom/right}} - \downarrow_{\mathrm{top/left}} \uparrow_{\mathrm{bottom/right}} \right) \; , \qquad (6.82)$$

for the vertical dimers with top and bottom spin and for the horizontal dimers with left and right spin. With $|\mathbf{r}\rangle$ denoting the state with one t^0-triplet (triplon)

on dimer $\mathbf{r}$ and singlets on all other dimers we find (see Fig. 6.30 for notational details)

$$
\begin{aligned}
\mathcal{F}(\mathbf{q})|0\rangle &= \frac{1}{2}\left\{\ldots + \left(e^{i\mathbf{q}\mathbf{x}_0} - e^{i\mathbf{q}\mathbf{x}_1}\right)|\mathbf{r}_\mathrm{I}\rangle + \left(e^{i\mathbf{q}\mathbf{x}_2} - e^{i\mathbf{q}\mathbf{x}_3}\right)|\mathbf{r}_\mathrm{II}\rangle + \ldots\right\} \\
&= i\left\{\ldots + e^{i\mathbf{q}(\mathbf{x}_0+\mathbf{x}_1)/2}\sin(\mathbf{q}\boldsymbol{\delta}_v)|\mathbf{r}_\mathrm{I}\rangle + e^{i\mathbf{q}(\mathbf{x}_2+\mathbf{x}_3)/2}\sin(\mathbf{q}\boldsymbol{\delta}_h)|\mathbf{r}_\mathrm{II}\rangle + \ldots\right\} \\
&= i\sin(\mathbf{q}\boldsymbol{\delta}_v)\sum_{\mathbf{r}^v} e^{i\mathbf{q}\mathbf{r}^v}|\mathbf{r}^v\rangle + i\sin(\mathbf{q}\boldsymbol{\delta}_h)\sum_{\mathbf{r}^h} e^{i\mathbf{q}\mathbf{r}^h}|\mathbf{r}^h\rangle\ . \qquad (6.83)
\end{aligned}
$$

The sums in the last line run over all vertical dimers $\mathbf{r}^v$ and horizontal dimers $\mathbf{r}^h$ respectively. We continue and define an appropriate *local* operator $\mathcal{N}(\mathbf{r})$ using the distances $\mathbf{r}\in\Gamma_\mathrm{eff}$ instead of $\mathbf{x}\in\Gamma$

$$
\mathcal{N}(\mathbf{r}) = S_0^z(\mathbf{r}) - S_1^z(\mathbf{r})\ , \qquad (6.84)
$$

where we have introduced the sub-indices 0 and 1 to distinguish the two spins on dimer $\mathbf{r}$.[14] Since $\mathcal{N}(\mathbf{r})$ does not contain an interaction of spins there will be no difference in the action on the ground state for horizontal or vertical dimers. Once we have decided whether the operators for the upper spins or
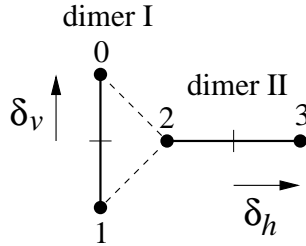
Figure 6.30.: Two adjacent dimers with $S = 1/2$ spins at their ends depicted by filled circles. Roman numerals denote dimers, Arabic numerals denote spins. The position vectors $\mathbf{x}_i$ end on the spins, while the vectors $\mathbf{r}_\mathrm{I/II}$ end on the dimer centres indicated by thin short lines. Note that $(\mathbf{x}_0 + \mathbf{x}_1)/2 = \mathbf{r}_\mathrm{I}$ and likewise for $\mathbf{r}_\mathrm{II}$. In the main text we denote by $|\mathbf{r}_\mathrm{I/II}\rangle$ the state where a t^0-triplon is located on the dimer addressed by the vector $\mathbf{r}_\mathrm{I/II}$, while all other dimers are in the singlet state. The difference vectors $\boldsymbol{\delta}_{v/h}$ are also shown, with $\boldsymbol{\delta}_v = (\mathbf{x}_0 - \mathbf{x}_1)/2$ for instance.

the lower spins on the vertical dimers have a negative sign, we still have to choose whether the operators for the left or the right spins on the horizontal dimers enter with a negative sign. For the rest of our considerations we fix

---

[14] Note that the operator $S_0^z(\mathbf{r}) + S_1^z(\mathbf{r})$ does not inject any triplons at all when acting on the ground state $|0\rangle$.

the lower spin operator on the vertical dimers and the right spin operator on the horizontal dimers to carry the minus sign. With $|\nu\rangle$, $\nu \in \{s, t^{-1}, t^0, t^1\}$, denoting the state of dimer $\mathbf{r}$ we get

$$\mathcal{N}(\mathbf{r})|s\rangle = T_1'|s\rangle = |t^0\rangle \equiv |\mathbf{r}\rangle. \tag{6.85}$$

There are no other processes. As outlined in section 6.4 we construct the global observable $\mathcal{N}(\sigma, \mathbf{q}) = \mathcal{N}(\sigma, \mathbf{K}(\mathbf{q}))$ from the local one by

$$\mathcal{N}(\sigma, \mathbf{q}) \sim \sum_r e^{i(\mathbf{K}(\mathbf{q}) + \sigma \mathbf{Q})\mathbf{r}} \mathcal{N}(\mathbf{r}) \ . \tag{6.86}$$

Since the neutrons can transfer an arbitrary momentum into the system, we cannot fix $\sigma \in \{0, 1\}$ to one of its values as we did for the Raman operator. We should rather consider

$$\mathcal{N}(\mathbf{q}) = a(\mathbf{q})\mathcal{N}(\sigma = 0, \mathbf{q}) + b(\mathbf{q})\mathcal{N}(\sigma = 1, \mathbf{q}) \ . \tag{6.87}$$

The microscopic situation *on* each dimer, not captured by the position vectors $\mathbf{r}$, which are too coarse, are correctly accounted for, if we choose

$$a(\mathbf{q}) = i \left[\sin\left(\mathbf{q}\boldsymbol{\delta}_v\right) + \sin\left(\mathbf{q}\boldsymbol{\delta}_h\right)\right]/2$$
$$b(\mathbf{q}) = i \left[\sin\left(\mathbf{q}\boldsymbol{\delta}_v\right) - \sin\left(\mathbf{q}\boldsymbol{\delta}_h\right)\right]/2 \ . \tag{6.88}$$

We can immediately prove this, by again calculating the action on the ground state $|0\rangle$. If we choose all vertical dimers to be addressed by vectors $\mathbf{r}^v = (r_1^v, r_2^v)$, with $r_1^v + r_2^v$ even, then the components of the vectors $\mathbf{r}^h$ for horizontal dimers add up to odd integers and we find ($\mathbf{Q} = (\pi, \pi)$)

$$\mathcal{N}(\mathbf{q})|0\rangle = \sum_{\mathbf{r}} \left(e^{i\mathbf{K}(\mathbf{q})\mathbf{r}}(a(\mathbf{q}) + b(\mathbf{q})e^{i\mathbf{Q}\mathbf{r}}\right)|\mathbf{r}\rangle$$

$$= (a(\mathbf{q}) + b(\mathbf{q})) \sum_{\mathbf{r}^v} e^{i\mathbf{K}(\mathbf{q})\mathbf{r}^v}|\mathbf{r}^v\rangle + (a(\mathbf{q}) - b(\mathbf{q})) \sum_{\mathbf{r}^h} e^{i\mathbf{K}(\mathbf{q})\mathbf{r}^h}|\mathbf{r}^h\rangle$$

$$= \mathcal{F}(\mathbf{q})|0\rangle \ . \tag{6.89}$$

The last identity is trivial for $\mathbf{q} \in$ MBZ, since we can identify $\mathbf{K}(\mathbf{q}) = \mathbf{q}$ in this case. For larger $\mathbf{q}$ the momenta $\mathbf{K}(\mathbf{q})$ in the exponents have to be folded back to the MBZ as outlined in point (A) after Eq. (6.79).

To be more specific and to allow a comparison to measurements on $SrCu_2(BO_3)_2$ we have to turn to the microscopic details. Fig. 6.31(a) shows the abstracted real space lattice Γ of $SrCu_2(BO_3)_2$ where the $S = 1/2$ copper

ions are depicted as filled grey circles connected by grey lines building up the dimers. The inter-dimer super exchange path via the borate group is indicated as dashed grey line for one dimer pair only. All relevant atomic distances and angles taken from Ref. [76] are given. From them, the remaining distances and angles can be reconstructed. The vectors **a** and **b** are the primitive vectors of
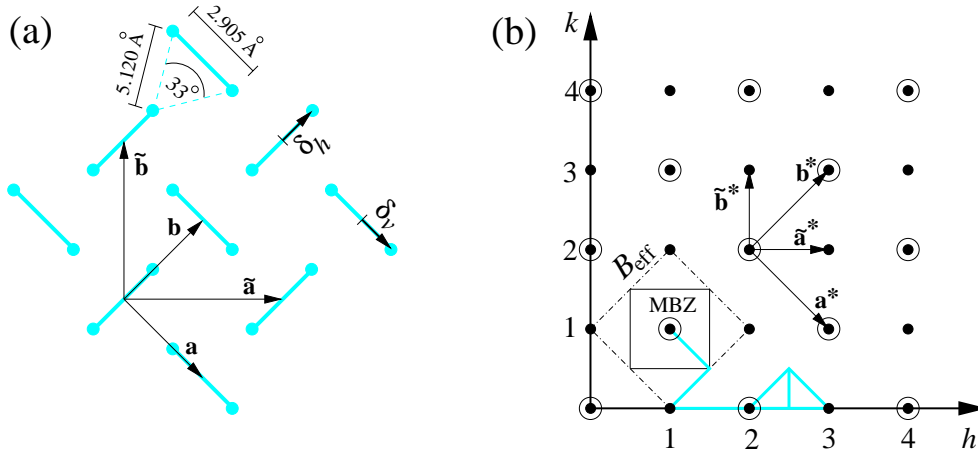
Figure 6.31.: (a) A portion of the Shastry-Sutherland model. The cyan (grey) circles denote $S = 1/2$ spins (copper ions). The set of all these circles is the direct lattice Γ. The primitive vectors **a** and **b** constitute the effective direct lattice Γ_{eff}, while the vectors $\tilde{\mathbf{a}}$ and $\tilde{\mathbf{b}}$ constitute the lattice Γ_{AF}, which takes the A-B-structure of the dimers into account. Mapping the model to the substance $SrCu_2(BO_3)_2$ necessitates the introduction of microscopic distances. Since both dimers (horizontal and vertical) have the same lengths, the given numbers are sufficient to calculate all other distances of interest.
(b) A sketch of the dual space of the Shastry-Sutherland model. The primitive vectors $\mathbf{a}^*$ and $\mathbf{b}^*$ constitute the dual lattice Γ_{eff}^*, denoted by open circles. The vectors $\tilde{\mathbf{a}}^*$ and $\tilde{\mathbf{b}}^*$ constitute Γ_{AF}^* denoted by small filled circles. The dashed-dotted lines denote the outer boundaries of a possible Brillouin zone B_{eff} of Γ_{eff}^*. The magnetic Brillouin zone MBZ is the square within B_{eff}. The components along the primitive vectors $\tilde{\mathbf{a}}^*$ and $\tilde{\mathbf{b}}^*$ of an arbitrary vector $\mathbf{q} = (h, k)$ of the dual space can be read off the given axes. The thick cyan (grey) lines denote different routes through dual space along which INS measurements have been performed [89, 108].

the effective lattice Γ_{eff}, which is the lattice we used in all our calculations so far. The vectors $\tilde{\mathbf{a}}$ and $\tilde{\mathbf{b}}$ span the true unit cell accounting for the A-B structure of Γ_{eff}. They are the primitive vectors of the lattice Γ_{AF}, which should be viewed to have a basis containing two dimers, one vertical and one horizontal. For convenience we choose **a** proportional to (1,0) and **b** proportional to (0,1).

Then, including the real distances, a little geometry yields

$$\mathbf{a} = 6.360\text{Å} \begin{pmatrix} 1 \\ 0 \end{pmatrix}, \quad \mathbf{b} = 6.360\text{Å} \begin{pmatrix} 0 \\ 1 \end{pmatrix}$$

$$\mathbf{a}^* = \frac{2\pi}{6.360\text{Å}} \begin{pmatrix} 1 \\ 0 \end{pmatrix}, \quad \mathbf{b}^* = \frac{2\pi}{6.360\text{Å}} \begin{pmatrix} 0 \\ 1 \end{pmatrix} . \tag{6.90}$$

The remaining vectors depicted in Fig. 6.31 follow from

$$\tilde{\mathbf{a}} = \mathbf{a} + \mathbf{b}, \qquad \tilde{\mathbf{b}} = \mathbf{b} - \mathbf{a}$$

$$\tilde{\mathbf{a}}^* = (\mathbf{a}^* + \mathbf{b}^*)/2, \quad \tilde{\mathbf{b}}^* = (\mathbf{b}^* - \mathbf{a}^*)/2 . \tag{6.91}$$

The vectors $\mathbf{a}^*$, $\mathbf{b}^*$ and $\tilde{\mathbf{a}}^*$, $\tilde{\mathbf{b}}^*$ span the reciprocal lattices Γ^*_{eff} and Γ^*_{AF} respectively. Fig. 6.31(b) shows Γ^*_{eff} as open circles, while small filled circles denote Γ^*_{AF}. To explain the experimental findings [89, 108], we need to decompose an arbitrary vector $\mathbf{q}$ of the dual space according to

$$\mathbf{q} = h\tilde{\mathbf{a}}^* + k\tilde{\mathbf{b}}^* . \tag{6.92}$$

In Fig. 6.31(b) $\mathbf{q}$ can be pictured to be any point of the h-k plane. The dashed-dotted line in Fig. 6.31(b) denotes a possible Brillouin zone B_{eff} of Γ^*_{eff}. The magnetic Brillouin zone (MBZ) is given by the square limited by a solid line and corresponds to the Wigner-Seitz cell of Γ^*_{AF}. All total (crystal) momenta $\mathbf{K}$ lie within this square. Since we prefer to represent direct space variables (like $\mathbf{r}$ and $\mathbf{d}$) in the $\{\mathbf{a}, \mathbf{b}\}$-basis, we decompose $\mathbf{K}$ according to

$$\mathbf{K} = K_1 \frac{\mathbf{a}^*}{2\pi} + K_2 \frac{\mathbf{b}^*}{2\pi} \dot{\equiv} \mathbf{q} = h\tilde{\mathbf{a}}^* + k\tilde{\mathbf{b}}^* . \tag{6.93}$$

We immediately obtain the mapping from $\mathbf{q}$ measured in units of $\tilde{\mathbf{a}}^*$ and $\tilde{\mathbf{b}}^*$ to $\mathbf{K} \in B_{\text{eff}}$ as

$$K_1 = \pi((h - k) \bmod 2)$$

$$K_2 = \pi((h + k) \bmod 2) . \tag{6.94}$$

We still have to be careful and represent all $\mathbf{K}$ by vectors within the MBZ$\subset$ B_{eff}, which can be done by standard back-folding.[15]

---

[15] The fact, that the MBZ contains only half the number of states as there should be according to the direct lattice, is compensated by introducing the quantum number $\sigma \in \{0, 1\}$ in the momentum states $|\sigma, \mathbf{K}\rangle$ and $|\sigma, \mathbf{K}, \mathbf{d}\rangle$.

The grey lines in Fig. 6.31(b) denote routes through dual space, where actual measurements have been performed [89, 108]. To illustrate the mapping $\mathbf{q} \leftrightarrow \mathbf{K}$ consider the route (h, k): $(2, 0) \rightarrow (2.5, 0) \rightarrow (2.5, 0.5)$, which translates to the reduced points (K_1, K_2): $(0, 0) \rightarrow (\pi/2, \pi/2) \rightarrow (0, \pi)$. We will reconsider this route in the explanation of the experimental findings.

By inserting the microscopic distances given in Fig. 6.31 we calculate the scalar products $\mathbf{q}\boldsymbol{\delta}_{v/h}$, which appear in the operator prefactors $a(\mathbf{q})$ and $b(\mathbf{q})$ (see Eq. (6.87))

$$\mathbf{q}\boldsymbol{\delta}_v = \left(h\tilde{\mathbf{a}}^* + k\tilde{\mathbf{b}}^* \right) \frac{2.905\text{Å}}{2} \begin{pmatrix} 1 \\ 0 \end{pmatrix} = 0.717(h - k)$$

$$\mathbf{q}\boldsymbol{\delta}_h = \left(h\tilde{\mathbf{a}}^* + k\tilde{\mathbf{b}}^* \right) \frac{2.905\text{Å}}{2} \begin{pmatrix} 0 \\ 1 \end{pmatrix} = 0.717(h + k) \ . \tag{6.95}$$

We can now summarise our findings. The $T = 0$ operator describing an INS experiment performed on $SrCu_2(BO_3)_2$ as captured by the Shastry-Sutherland model reads

$$\mathcal{N}(\mathbf{q}) = \mathcal{N}(h, k) = a(\mathbf{q})\mathcal{N}(\sigma = 0, \mathbf{q}) + b(\mathbf{q})\mathcal{N}(\sigma = 1, \mathbf{q}) \tag{6.96}$$

$$= \sum_r e^{i\mathbf{K}(\mathbf{q})\mathbf{r}} \left(a(\mathbf{q}) + b(\mathbf{q})e^{i\mathbf{Q}\mathbf{r}} \right) \mathcal{N}(\mathbf{r}), \quad \text{with} \tag{6.97}$$

$$\mathcal{N}(\mathbf{r})|0\rangle = |\mathbf{r}\rangle \ ,$$

$$\mathbf{r} = r_1\mathbf{a} + r_2\mathbf{b}$$

$$\mathbf{K} = K_1\mathbf{a}^* + K_2\mathbf{b}^* \in \text{MBZ}, \quad \text{where}$$

$$K_1 = \pi((h - k) \bmod 2)$$

$$K_2 = \pi((h + k) \bmod 2), \quad \text{from}$$

$$\mathbf{q} = h\tilde{\mathbf{a}}^* + k\tilde{\mathbf{b}}^*, \quad \text{and}$$

$$a(\mathbf{q}) = i[\sin(0.717(h - k)) + \sin(0.717(h + k))]/2$$

$$b(\mathbf{q}) = i[\sin(0.717(h - k)) - \sin(0.717(h + k))]/2 \ . \tag{6.98}$$

Inserting the *effective* local operator $\mathcal{N}_{\text{eff}}(\mathbf{r})$ into the second equation gives the effective global observable $\mathcal{N}_{\text{eff}}(\mathbf{q})$. We elaborate on this issue in the next subsection.

We can already present a rough sketch of the dynamic structure factor for $SrCu_2(BO_3)_2$ without any complicated computations. For inter-dimer ex-

change $x = 0$ the one-triplon dynamic structure factor reduces to (no disper-
sion, and the states $|\mathbf{r}\rangle$ are exact eigen-states)

$$S(\mathbf{q}) = \langle 0|\mathcal{N}(\mathbf{q})^{\dagger}\mathcal{N}(\mathbf{q})\ |0\rangle = \sum_{\mathbf{r}} |\langle \mathbf{r}|\mathcal{N}(\mathbf{q})|0\rangle|^2$$

$$\sim \sin^2\left[0.717(h - k)\right] + \sin^2\left[0.717(h + k)\right]\ . \tag{6.99}$$

We show the resulting structure factor in Fig. 6.32. In part (b) the experi-

(a)   (b)
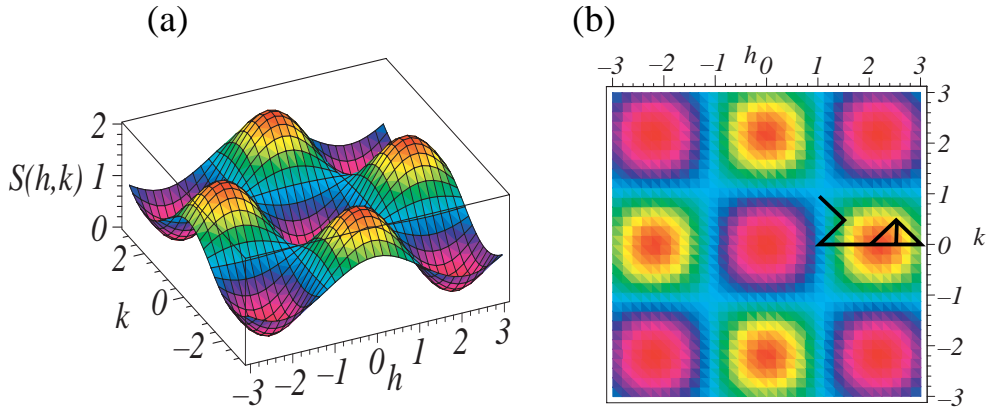
Figure 6.32.: The one-triplon structure factor S according to Eq. (6.99) as function of the components h and q of an arbitrary vector $\mathbf{q}$ in dual space, for inter dimer coupling $x = 0$. Although the isolated dimer model is rather simple, the depicted function is a very good approximation to what can be measured (cf. beginning of section 6.6.3). In (b) we show S viewed from the top. The solid black lines denote a path through dual space on which INS measurements have been performed. The experiments were done close to the hot spot in the vicinity of $(h, k) = (2, 0)$.

mentally followed routes through dual space have been included as solid black lines. One clearly sees, that the measurement has been performed in the region of the $x = 0$ one-triplon hot spot at about $(h, k) = (2, 0)$.

6.6.2. CUT Implementation

In this subsection we show how the action of the global INS observable $\mathcal{N}(\mathbf{q})$ on the ground state $|0\rangle$ can be calculated perturbatively for a *finite* inter dimer exchange $x > 0$. We restrict our considerations to the one- and two-triplon sector. In this case the effective *local* observable leads to (see also section 6.4

or section 6.5.2 on the implementation of the Raman operator)

$$\mathcal{N}_{1,0}(\mathbf{r})|0\rangle = \sum_{\mathbf{n}} w_{\mathbf{n}}^{\pi(\mathbf{r})}|\mathbf{r}+\mathbf{n}\rangle,$$

$$\mathcal{N}_{2,0}(\mathbf{r})|0\rangle = \sum_{\mathbf{n},\mathbf{n}'} w_{\mathbf{n},\mathbf{n}'}^{\pi(\mathbf{r})}|\mathbf{r}+\mathbf{n},\mathbf{r}+\mathbf{n}'\rangle, \text{ with}$$

$$w_{\mathbf{n}(,\mathbf{n}')}^{\pi(\mathbf{r})} = \bar{w}_{\mathbf{n},(\mathbf{n}')} + e^{i\mathbf{Q}\mathbf{r}}dw_{\mathbf{n}(,\mathbf{n}')}, \text{ and}$$

$$\bar{w}_{\mathbf{n}(,\mathbf{n}')} = (w_{\mathbf{n}(,\mathbf{n}')}^{v} + w_{\mathbf{n}(,\mathbf{n}')}^{h})/2,$$

$$dw_{\mathbf{n}(,\mathbf{n}')} = (w_{\mathbf{n}(,\mathbf{n}')}^{v} - w_{\mathbf{n}(,\mathbf{n}')}^{h})/2 , \tag{6.100}$$

where the super indices v and h apply when the corresponding amplitude has been calculated for $\mathbf{r}$, the location of the operator, denoting a vertical or horizontal dimer respectively. Again, we calculate the w^v only and obtain the w^h from a symmetry argument. The corresponding effective local operator is readily given by

$$\mathcal{N}_{\text{eff}}(\mathbf{r}^v; x) = \sum_{k=0}^{\infty} x^k \sum_{i=1}^{k+1} \sum_{|\underline{m}|=k} \tilde{C}(\underline{m}; i)\mathcal{N}(\underline{m}; i) , \quad \text{with}$$

$$\mathcal{N}(\underline{m}; i) = T_{m_1} \cdots T_{m_{i-1}}\mathcal{N}(\mathbf{r}^v)T_{m_i} \cdots T_{m_k} , \tag{6.101}$$

where the operators T_i belong to the effective Hamiltonian H_{eff}. As we have already seen in the last subsection the local operator $\mathcal{N}$ can be decomposed with respect to its action on the number of triplons

$$\mathcal{N} = T'_{-1} + T'_1 . \tag{6.102}$$

We do not have to decompose the local INS operator $\mathcal{N}(\mathbf{r})$ into two elementary building blocks as we did for the local Raman operator. This is because there are no spin-spin products in $\mathcal{N}(\mathbf{r})$ linking different dimers.

In a computer implementation of Eq. (6.101) we have to consider only those operator products $\mathcal{N}(\underline{m}; i)$, which start with T'_1, since the action of all other possible operators in $\mathcal{N}(\underline{m}; i)$ on the ground state is zero. Thus, each virtual process $\mathcal{N}(\underline{m}; i)$, weighted by $\tilde{C}(\underline{m}; i)$, starts by injecting one t^0-triplon on the operator site $\mathbf{r}$, which acquires a dynamics controlled by the Hamiltonian. Also, further triplons might be created. The consequences for the size and shape of the clusters in a given order are analogous to those we have discussed for the Raman operator. The same applies to the actual computer implementation.

Since all T_i conserve the total spin S and the total magnetisation m, $\mathcal{N}_{\text{eff}}(\mathbf{r})$, and thus $\mathcal{N}_{\text{eff}}(\mathbf{q})$, lead to $S = 1$ excitations from the ground state.[16]

The largest amplitude in the one-triplon sector is $w^v_{\mathbf{n}=(0,0)}$ for which we find

$$w^v_{0,0} = 1 - \frac{1}{2}\,x^2 - \frac{1}{2}\,x^3 - \frac{3}{32}\,x^4 + \frac{29}{64}\,x^5 + \frac{449}{1536}\,x^6 - \frac{5219}{6912}\,x^7 - \frac{376885}{221184}\,x^8 \;. \quad (6.103)$$

As we did for the Raman operator we focus on those two-triplon amplitudes $w_{\mathbf{n},\mathbf{n}'}$ for which $\mathbf{n}' - \mathbf{n} > 0$ holds. We give two examples $(\mathbf{n}, \mathbf{n}' = n_1, n_2; n'_1, n'_2)$

$$w^v_{0,0;1,0} = \frac{1}{2}\,x + \frac{1}{4}\,x^2 - \frac{3}{16}\,x^3 - \frac{13}{32}\,x^4 - \frac{131}{256}\,x^5 - \frac{61}{512}\,x^6 - \frac{4721}{18432}\,x^7 - \frac{68317}{55296}\,x^8$$

$$w^v_{0,0;1,1} = -\frac{1}{16}\,x^3 - \frac{3}{64}\,x^4 - \frac{7}{256}\,x^5 + \frac{13}{512}\,x^6 - \frac{269}{1024}\,x^7 - \frac{597149}{589824}\,x^8 \;.$$

$$\quad (6.104)$$

The corresponding amplitudes w^h of the local INS operator acting on a horizontal dimer are again obtained from the w^v by turning the whole lattice at $\pi/2$ about the dimer-centre r^v. In section 6.5.2 we denoted this operation by $\mathcal{D}$. We have

$$\mathcal{N}_{\text{eff}}(\mathbf{r}^h) = \mathcal{D}\mathcal{N}_{\text{eff}}(\mathbf{r}^v)\mathcal{D}^\dagger \;, \quad (6.105)$$

and a calculation analogous to that which led to Eq. (6.69) in section 6.5.2 gives

$$w^h_{n_1,n_2} = (-1)^{n_1+n_2} w^v_{n_2,-n_1}$$

$$w^h_{n_1,n_2;n'_1,n'_2} = \begin{cases} (-1)^{n_1+n_2+n'_1+n'_2+1}\; w^v_{n'_2,-n'_1;+n_2,-n_1} \;, & \text{triplons interchanged} \\ (-1)^{n_1+n_2+n'_1+n'_2}\; w^v_{n_2,-n_1;+n'_2,-n'_1} \;, & \text{otherwise.} \end{cases}$$

$$\quad (6.106)$$

Interchanging the triplons in the two-triplon sector leads to an extra minus here since the states involved have total spin $S = 1$.

We calculated all amplitudes accessible in an 8th order calculation. Inserting them into Eqs. (6.100) readily gives the action of the effective local operator $\mathcal{N}_{\text{eff}}(\mathbf{r})$ on the ground state as perturbative result in x. Inserting $\mathcal{N}_{\text{eff}}(\mathbf{r})$ into Eq. (6.97) of the preceding subsection finally yields the 8th order

---

[16] At first T'_1 injects one t^0 triplon at $\mathbf{r}$ from the ground state. All other dimers are in the singlet state. Therefore, the full state is $S = 1$ and $m = 0$. The action of the remaining T_i operators conserves these quantum numbers.

result for the global operator $\mathcal{N}_{\text{eff}}(\mathbf{q})$. We again give the results in form of the vector components

$$A_{\sigma,\mathbf{q}} = \langle \sigma, \mathbf{q} | \mathcal{N}_{1,0}(\mathbf{q}) | 0 \rangle \quad \text{for the one-triplon sector, and}$$

$$A_{\sigma,\mathbf{q},\mathbf{d}} = \langle \sigma, \mathbf{q}, \mathbf{d} | \mathcal{N}_{2,0}(\mathbf{q}) | 0 \rangle \quad \text{for the two-triplon sector.} \tag{6.107}$$

By using Eqs. (6.53) and (6.54) of section 6.4 in combination with Eq. (6.96) of the preceding subsection we find

$$A_{0,\mathbf{q}} = \sum_{\mathbf{n}} e^{-i\mathbf{K}(\mathbf{q})\mathbf{n}} \left[a(\mathbf{q}) \bar{w}_{\mathbf{n}} + b(\mathbf{q}) dw_{\mathbf{n}} \right]$$

$$A_{1,\mathbf{q}} = \sum_{\mathbf{n}} e^{-i(\mathbf{K}(\mathbf{q})+\mathbf{Q})\mathbf{n}} \left[a(\mathbf{q}) dw_{\mathbf{n}} + b(\mathbf{q}) \bar{w}_{\mathbf{n}} \right]$$

$$A_{0,\mathbf{q},\mathbf{d}} = \sum_{\mathbf{n}} e^{-i\mathbf{K}(\mathbf{q})(\mathbf{n}+\mathbf{d}/2)} \left[a(\mathbf{q}) \bar{w}_{\mathbf{n},\mathbf{n}+\mathbf{d}} + b(\mathbf{q}) dw_{\mathbf{n},\mathbf{n}+\mathbf{d}} \right]$$

$$A_{1,\mathbf{q},\mathbf{d}} = \sum_{\mathbf{n}} e^{-i(\mathbf{K}(\mathbf{q})+\mathbf{Q})(\mathbf{n}+\mathbf{d}/2)} \left[a(\mathbf{q}) dw_{\mathbf{n},\mathbf{n}+\mathbf{d}} + b(\mathbf{q}) \bar{w}_{\mathbf{n},\mathbf{n}+\mathbf{d}} \right] . \tag{6.108}$$

There are only two vector components in the one-triplon sector for fixed $\mathbf{q}$. We calculated all A accessible in computations up to 8th order in x. Hence, all quantities needed to elaborate on the structure factor are provided. We turn to this issue in the following subsection.

6.6.3. Results

We start by presenting results for the one-triplon sector and write down the two $\mathbf{q}$-dependent vector components up to 6th order in x

$$\frac{A_{0,\mathbf{q}}}{a(\mathbf{q})} = \frac{A_{1,\mathbf{q}}}{b(\mathbf{q})} = \tag{6.109}$$

$$1 - \frac{1}{2}x^2 - \frac{1}{2}x^3 - \frac{3}{32}x^4 + \frac{29}{64}x^5 + \left(\frac{449}{1536} - \frac{23}{288} \cos(K_1(\mathbf{q})) \cos(K_2(\mathbf{q})) \right) x^6 .$$

For $x = 0$ we re-obtain the one-triplon structure factor Eq. (6.99) of the last subsection

$$S(\mathbf{q}; x = 0) = A_{0,\mathbf{q}}^2 + A_{1,\mathbf{q}}^2 = a^2(\mathbf{q}) + b^2(\mathbf{q})$$

$$= \frac{1}{2} \sin^2[0.717(h+k)] + \frac{1}{2} \sin^2[0.717(h-k)] . \tag{6.110}$$

Up to 5th order we have $S(\mathbf{q}; x) = S(\mathbf{q}; 0)f(x)$ with $f(x)$ being a polynomial in x. Thus, to this order, the qualitative shape of the one-triplon structure factor depicted in Fig. 6.32 does not change if we switch on x. The positions of the extrema stay fixed, only the slopes vary with x. It is not before the 6th order, that the extremal positions become sensitive to x. This was to be expected, since the one-triplon dispersion does not start before the 6th order. Hence, Fig. 6.32 already gives a very good approximation of what can be measured in the one-triplon channel.

To calculate the relative weight I_1 of the one-triplon contribution it is more convenient to work in direct space. We again use the sum rule

$$I_{\text{tot}} = \langle 0|\mathcal{N}^2(\mathbf{r})|0\rangle - \langle 0|\mathcal{N}(\mathbf{r})|0\rangle^2 = 1 \qquad (6.111)$$

to obtain the total weight of the operator per dimer. The second term in Eq. (6.111) vanishes, the first is easily calculated. The one-triplon contribution is given by

$$I_1 = \langle 0|\mathcal{N}_{1,0}(\mathbf{r}^v)|0\rangle = \sum_{\mathbf{n}} (w_{\mathbf{n}}^v)^2$$

$$= 1 - x^2 - x^3 + \frac{1}{16}\,x^4 + \frac{45}{32}\,x^5 + \frac{713}{768}\,x^6 - \frac{6461}{3456}\,x^7 - \frac{458353}{110592}\,x^8 \; . \quad (6.112)$$

The result does not depend on whether we choose $\mathbf{r}$ to be a vertical or horizontal dimer. This plain series result is depicted as solid grey curve in Fig. 6.33. The other lines correspond to Padé or Dlog-Padé approximants as indicated. At the value of interest at about $x \approx 0.6$ the various approximants fan out considerably. However, there are two Dlog-Padés with intriguing singularities very close to $x = 0.697$, the value where we found the one-triplon gap to close (cf. section 6.2.3). We decide in favour of these approximants.

The vanishing of the one-triplon *weight* at the x-value where the one-triplon *gap* vanishes is plausible. In section 6.3.2 we found an $S = 1$ two-triplon bound state to become soft at $x_c = 0.63$, which we interpreted as a signal for a transition into a triplet-condensate phase. Most probably the elementary excitations in this new regime cannot be captured by triplons, but rather by more complicated quasi-particles composed of two or more triplons. Thus, the relative weight of one-triplon processes should vanish. For x-values just above $x_c = 0.63$ single triplons might still be observable due to the proximity to the dimer-singlet phase and we can still measure what has been the one-triplon gap in the dimer-singlet phase. In this scenario the softening of this gap is accompanied by the vanishing of the one-triplon weight.
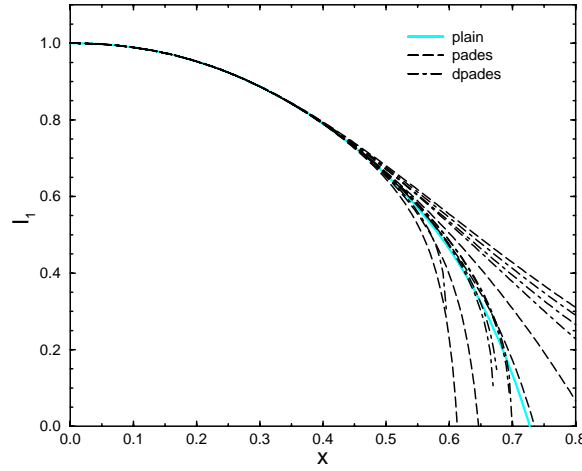
Figure 6.33.: One-triplon weight as function of x. The cyan (grey) curve corresponds to the plain series result, which is compared to various Padé (dashed) and Dlog-Padé (dashed-dotted) approximants. Two of the latter show intriguing singularities at $x = 0.6965$, which is exactly the point, where the one-triplon gap vanishes. Thus we assume that they are the most reliable estimates of this quantity.

The calculation for the two-triplon contribution follows the same line

$$I_2 = \langle 0|\mathcal{N}_{2,0}(\mathbf{r}^v)|0\rangle = \sum_{\mathbf{n},\mathbf{n'}}(w^v_{\mathbf{n},\mathbf{n'}})^2$$

$$= x^2 + x^3 - \frac{1}{2}\,x^4 - 2\,x^5 - \frac{43}{16}\,x^6 - \frac{27}{32}\,x^7 + \frac{967}{4608}\,x^8 \,, \qquad (6.113)$$

with the result again depicted as solid cyan/grey line in Fig. 6.34. The spread of the approximant is comparable to what we found for the one-triplon sector. The scale is different. There is an accumulation of approximants in the middle of the extremal curves, which should give a reasonable estimate. We choose the Dlog-Padé [3,2] approximant which is depicted as thick dashed-dotted line in Fig. 6.34.

Fig. 6.35 shows the combined picture. The lowest, dashed-dotted curve is the two-triplon contribution discussed in the preceding paragraph. The one-triplon contribution is depicted as dashed line. Adding both gives the black solid line. The horizontal solid grey line is the total weight of the INS operator. For $x = 0$ one clearly sees, that the exact one-triplon excitations contain the full weight. They loose weight as x increases and the two-triplon
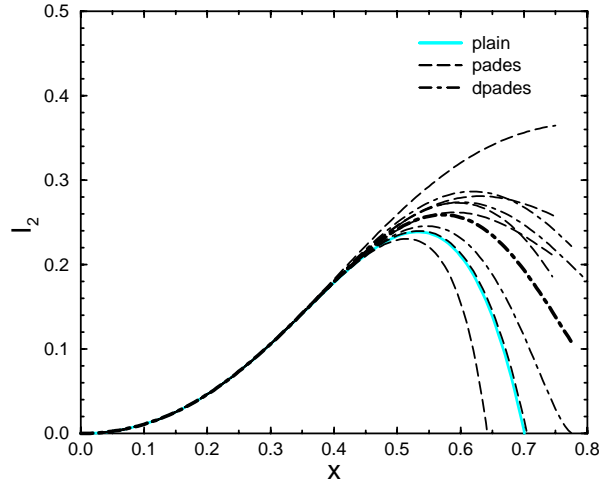
Figure 6.34.: Two-triplon weight as function of x. The plain series result (cyan/grey curve) is compared to various Padé (dashed) and Dlog-Padé (dashed-dotted) approximants. We choose the Dlog-Padé [3,2] approximant (thick dashed-dotted) as a conservative estimate.

states start to contribute. The sum of the relative one- and two-triplon weights essentially constitutes the full weight for $x \leq 0.3$. Beyond this value multi-triplon contributions become important. However, at $x = 0.603$ (the vertical line in Fig. 6.35) the two lowest excitation sectors still hold about 75% of the total weight.

Fig. 6.36 is a copy of Fig. 2 in Ref. [89] and renders a qualitative comparison of the results depicted in Fig. 6.35 to the experimental findings possible. The authors depict the measured scattering rate at $\mathbf{q} = (2.0) \equiv \mathbf{K} = (0,0)$ for two temperatures (1.7K and 24K) as function of the transferred energy. The solid line is a fit to the data [89]. The one-triplon gap for $SrCu_2(BO_3)_2$ is approximately 3 meV≈33 K. At a temperature of 24K the system no longer shows an appreciable response. The low temperature data, however, show a weight distribution very similar to our result. The one-triplon contribution I contains approximately twice the weight of the two-triplon contributions II. The rest III, which lies in energy-ranges too large to be accessible by two-triplon states, does not seem to carry more than 25% of the total weight, which is in very good accordance with our estimates. However, one must be careful with the significance of this comparison. The measurement shows data for a specific $\mathbf{q}$-value only. But the main features should be covered since most of the weight distributed in the $\mathbf{q} = (h, k)$-plane accumulates in the vicinity of
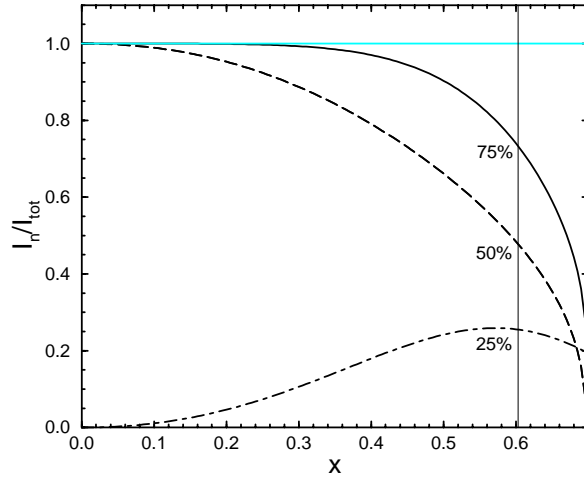
Figure 6.35.: Relative one- (dashed) and two-triplon (dashed-dotted) weights as function of x taken from Fig. 6.33 and Fig. 6.34 respectively. Their sum is depicted as solid line. The cyan (grey) horizontal line is the total weight of INS-operator $\mathcal{N}$ as obtained from the sum rule. At the value of interest ($x = 0.603$, vertical line) the (one-) two-triplon states contribute with approximately (50%) 25% to the total weight. Their sum makes up approximately 75%. The remaining weight is distributed amongst states of higher triplon numbers.

the hot spot (2,0) as verified in Fig. 6.32.

We turn to the calculation of the dynamic structure factor for the two-triplon sector at $x > 0$. We again use the continued fraction technique to obtain the effective Green's function

$$\mathcal{G}^{\mathcal{N}}(\omega, \mathbf{q}; x) = \left\langle 0 \left| \mathcal{N}_{2,0}^{\dagger}(\mathbf{q}; x) \frac{1}{\omega - [H_1(\mathbf{K}(\mathbf{q}; x) + H_2(\mathbf{K}(\mathbf{q}; x)]} \mathcal{N}_{2,0}(\mathbf{q}; x) \right| 0 \right\rangle$$

$$= \cfrac{\sum_{\sigma, \mathbf{d} > 0} (A_{\sigma, \mathbf{q}, \mathbf{d}}(x))^2}{\omega - a_0 - \cfrac{b_1^2}{\omega - a_1 - \cfrac{b_2^2}{\omega - \cdots}}} \ . \tag{6.114}$$

To get reliable results for $x \approx 0.6$ we have to extrapolate the effective quantities appearing on the right hand side. Again OPT will be the method of choice. We begin by seeking a suitable OPT parameter α_w for the amplitudes $w_{\mathbf{n}, \mathbf{n}'}$ building up the vector components $A_{\sigma, \mathbf{q}, \mathbf{d}}$. For the effective Hamiltonian, determining the coefficients a_i and b_i, we use the splitting $H_{\text{eff}} = H_1 + H_2$ in
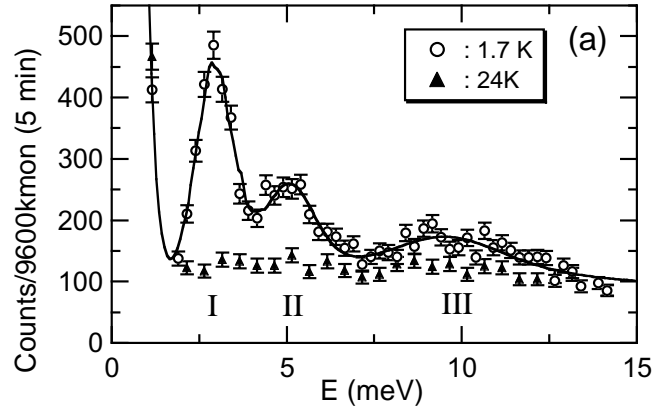
Figure 6.36.: This image is a copy of Fig. 2 in Ref. [89]. It shows an energy scan at $\mathbf{q} = (2, 0)$ at temperatures 1.7K (open circles) and 24K (filled triangles). The low temperature response shows a one-triplon peak (I) at about 3 meV, a two-triplon peak (II) at about 5 meV and some remaining response (III) outside the energy range accessible by two-triplon states. The weight distribution between these distinguishable responses resembles the theoretical findings depicted in Fig. 6.35.

a pure one-triplon part H_1 and a pure two-triplon part H_2. Part H_1, which is independent of the total spin S, has been optimised in section 6.5.3 already (result: $\alpha_1 = -0.20$). Part H_2 will be treated here for total spin $S = 1$.

We begin with the extrapolation of the operator amplitudes. Fig. 6.37 shows three different w^v amplitudes of the effective local INS operator $\mathcal{N}_{2,0}(\mathbf{r}^v)$ acting on $|0\rangle$ as function of the OPT parameter α_w at $x = 0.6$. The first well pronounced extrema can be found in the range $-0.5 \leq \alpha_w \leq -0.25$. Choosing $\alpha_w = -0.25$ leads to Fig. 6.38 where we depict $w^v_{0,0;1,0}$ (upper curves) and $w^v_{0,0;1,1}$ (lower curves) as function of x. The OPT approximants with $\alpha_w = -0.25$ are given by the solid grey lines, which we compare to the plain series results (solid black lines) and various Padé and Dlog-Padé approximants (dashed and dashed-dotted lines). Unfortunately, the spread of the latter is very large and does not allow quantitative estimates. The OPT approximants are close to the plain series and can be considered to constitute reasonable estimates. However, since the modulus of the amplitudes w is small and drops rapidly with increasing distances $\mathbf{d}$ (see Tab. 6.5) the error should be less than 15% at $x \approx 0.6$. Applying OPT with $\alpha_w = -0.25$ to all amplitudes w gives the extrapolated vector components $A_{\sigma,\mathbf{q},\mathbf{d}}$ as they appear in the numerator of Eq. (6.114).

We continue and investigate the OPT extrapolation of H_{eff}. We again
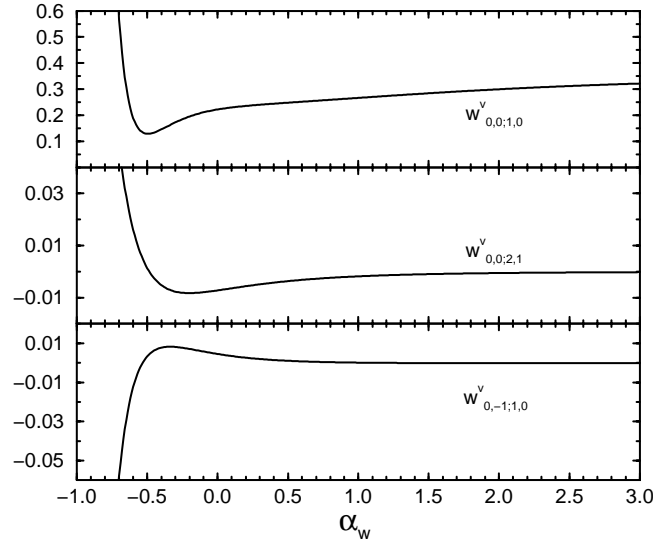
Figure 6.37.: Some INS operator amplitudes w^v as functions of the OPT parameter α_w for $x = 0.6$. All depicted amplitudes show well pronounced extrema in the range $-0.5 \leq \alpha_w \leq -0.25$. We choose $\alpha_w = -0.25$, which should optimise all amplitudes w^v equally well.

i, j	$|w^v_{0,0;i,j}|$; $x = 0.4$	$|w^v_{0,0;i,j}|$; $x = 0.6$
1,0	$2.11 \cdot 10^{-1}$	$2.24 \cdot 10^{-1}$ $(1.81 \cdot 10^{-1})$
1,1	$6.47 \cdot 10^{-3}$	$4.49 \cdot 10^{-2}$ $(7.67 \cdot 10^{-2})$
2,1	$4.51 \cdot 10^{-4}$	$6.97 \cdot 10^{-3}$ $(7.54 \cdot 10^{-3})$
2,2	$3.94 \cdot 10^{-6}$	$9.50 \cdot 10^{-5}$ $(2.95 \cdot 10^{-4})$

Table 6.5.: The amplitudes $w^v_{\mathbf{n},\mathbf{n+d}}$ for the INS operator $\mathcal{N}_{2,0}(\mathbf{r}^v)$ drop off rapidly with increasing distance $\mathbf{d}$. The values given in this table correspond to the plain series results at $x = 0.4$ (left column) and $x = 0.6$ (right column). The values in parentheses in the right column are obtained by using OPT with $\alpha_w = -0.25$.

choose to represent H_{eff}, H_1 and H_2 in the basis of 84 states, which we used several times now. $\mathcal{B}_{\mathrm{rem}} = \{|\sigma = 0, \mathbf{d}\rangle, |\sigma = 1, \mathbf{d}\rangle\}$ (see earlier consideration in subsection 6.5.3). The matrix elements of $H_2 = H_{\mathrm{eff}} - H_1(\alpha_1 = -0.20)$, where H_{eff} and H_1 have been truncated to contain order 14 terms at maximum (see the analogous procedure for the Raman operator), are subject to the OPT method with undetermined OPT parameter α_2. Subsequently $H_2(\alpha_2; \mathbf{K}(\mathbf{q}), x)$ and $H_1(\alpha_1 = -0.20; \mathbf{K}(\mathbf{q}), x)$ are added again to yield the extrapolated effect-
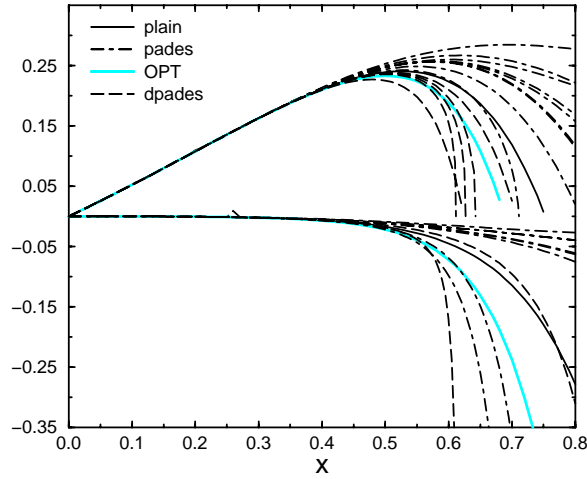
Figure 6.38.: Solid black curves denote the plain series results for $w^v_{0,0;1,0}$ (top) and $w^v_{0,0;1,1}$ (bottom). The optimised series results with OPT parameter $\alpha_w = -0.25$ are depicted as solid cyan (grey) curves. They are compared to various Padé (dashed-dotted) and Dlog-Padé (dashed) approximants. The collection of all depicted approximants spreads heavily. The optimised series can be considered to give reasonable estimates.

ive Hamiltonian $H_{\text{eff}}(\alpha_2; \mathbf{K}(\mathbf{q}), x)$.

Fig. 6.39 shows some eigen-values of $H_{\text{eff}}(\alpha_2; \mathbf{K}(\mathbf{q}), x)$ for $x = 0.6$ and $\mathbf{K} = (0,0)$ as function of α_2. The horizontal line corresponds to the best Dlog-Padé approximant of the lowest eigen-value (see also Fig. 6.16 on page 125 in section 6.3.2) for the given values. The analogous result for $\mathbf{K} = (0, \pi)$ is depicted in Fig. 6.40. The results are again obtained by using MAPLE to diagonalise the remaining 84×84 matrix for discrete values of α_2 (points in both of the figures). As for the Raman operator we extended the basis by adding 14 further distances and noticed no visible changes to the depicted results. An inspection of Figs. 6.39 and 6.40 shows a well pronounced minimum of the lowest eigen-energy at $\alpha_2 \approx 1.00$ for both depicted $\mathbf{K}$-values. However, Fig. 6.39 illustrates, that the energy for this eigen-states seems to be too low for the extremal α_2-value. Since higher eigen-energies seem to have stationary points at lower α_2 values, we decide to choose $\alpha_2 = 0.80$, which should yield reasonable energy values for *all* eigen-states. In Fig. 6.41 we depict the exact diagonalisation results (MAPLE) for

$$H_{\text{eff}}(\mathbf{K}(\mathbf{q}), x) = H_1(\alpha_1 = -0.20; \mathbf{K}(\mathbf{q}), x) + H_2(\alpha_2 = 0.80; \mathbf{K}(\mathbf{q}), x) \quad (6.115)$$
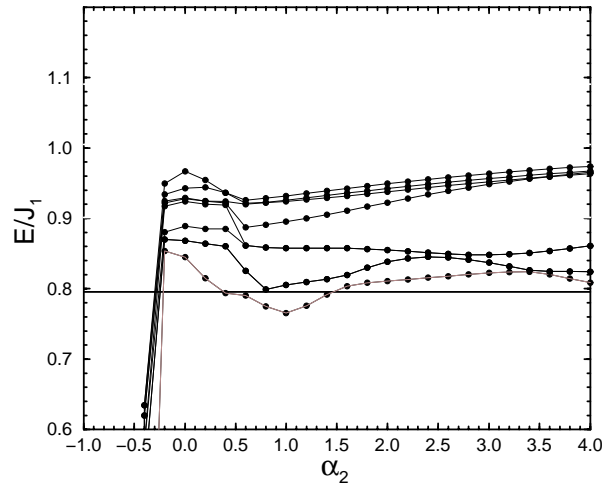
Figure 6.39.: Some eigen-energies of the effective Hamiltonian H_{eff} including the two lowest lying ones as function of the OPT parameter α_2 used to optimise the pure two-particle part H_2 of $H_{\text{eff}} = H_1 + H_2$. The results are obtained by using MAPLE to numerically diagonalise the 84×84 matrix representing H_{eff} for fixed $x = 0.6$ and $\mathbf{K} = (0,0)$ at discrete values of α_2 (points). The horizontal solid line is the corresponding value of the most reliable Dlog-Padé approximant of the lowest lying state in the $S = 1$ one channel, see also Fig. 6.16 in section 6.3.2. Choosing $\alpha_2 = 0.80$, which is close to the value where many levels show extremal behaviour, should lead to a uniform optimisation of all eigen-energies.

at $\mathbf{K} = (0,0)$ as function of x (points). The result is compared to the best Dlog-Padé approximants of the lowest eigen-energies (cf. Fig. 6.16 on page 125). The agreement is good, though not perfect. Especially the sharp drop of the lowest eigen-energy cannot be reproduced.

With all effective quantities being optimised we now calculate the effective two-triplon Green's function (6.114) for various momenta $\mathbf{q}$ at $x = 0.603$. The resulting form of the coefficients a_i and b_i show a similar behaviour to that for the Raman operator depicted in Fig 6.28. We can learn nothing new from them: the continued fraction can be truncated after the leading coefficients. We choose fraction depth 8.

The corresponding two-triplon dynamic structure factor

$$S(\omega, \mathbf{q}) = -\frac{1}{\pi}\text{Im}\mathcal{G}^{\mathcal{N}}(\omega, \mathbf{q}) \tag{6.116}$$

is again calculated by introducing an artificial broadening δ through $\omega \rightarrow \omega + i\delta$ in $\mathcal{G}^{\mathcal{N}}$ to model the experimental broadening. We choose $\delta = 0.02$
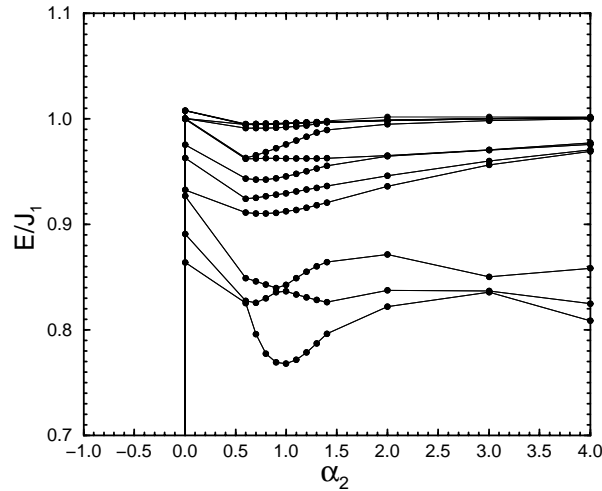
Figure 6.40.: The same as Fig. 6.39 with $x = 0.6$ and $\mathbf{K} = (0, \pi)$. The extremal positions are comparable to those found in Fig. 6.39.

in units of J_1. Fig. 6.42 shows S for $x = 0.603$ and $J_1 = 6.16$ meV at $\mathbf{q} = (2.0, 0) \equiv \mathbf{K} = (0, 0)$ (red) and at $\mathbf{q} = (2.5, 0.5) \equiv \mathbf{K} = (0, \pi)$ (blue) as function of the energy ω. The depicted structure factors have been multiplied by a constant number to ease the comparison with the experimental findings shown in Fig. 6.43 [108]. The number has been chosen such that the dominant peak at 4.8 meV for $\mathbf{q} = (2.0, 0)$ yields the same number of counts the experiment gave in a 10 minute measurement (see ordinate-label of Fig. 6.43). The agreement of the theoretical structure factor with the measured one in Fig. 6.43 is very good. All main structures of the experimental data can be found. For $\mathbf{q} = (2.0, 0)$ we obtain the main peak at $\omega = 4.8$ meV and a second peak at about $\omega = 5.7$ meV, whereas the experiment gives 4.75 meV and 5.6 meV. The weight distribution between these two peaks is in very good agreement with the experiment. The theoretical main peak shows a shoulder on the high energy side. This resembles the asymmetry of the experimental main peak, which displays a double maximum structure.

The theoretical positions $\omega = 5.5$ meV and $\omega = 5.9$ meV of the two peaks found for $\mathbf{q} = (2.5, 0.5)$ compare reasonable well with the experimental positions 5.6 meV and 6.25 meV. Our result for the position of the higher peak differs stronger from the experimental position than the other positions. Interestingly, our peak at 5.9 meV is below the two-triplon continuum (6.0 meV -
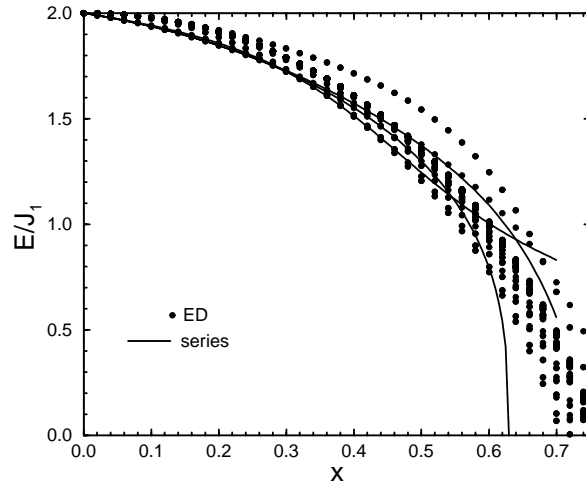
Figure 6.41.: Some eigen-energies of $H_{\text{eff}} = H_1 + H_2$ including the lowest levels as function of x for $\mathbf{K} = (0,0)$. The matrix elements of H_1 and H_2 have been optimised with OPT parameters $\alpha_1 = -0.20$ and $\alpha_2 = 0.80$ respectively. The points are obtained by diagonalising the $84{\times}84$ matrix representing H_{eff} at discrete values of x. The solid curves represent the most reliable Dlog-Padé approximants for three different eigen-energies that we are able to obtain as series (see also Fig. 6.16 in section 6.3.2).

6.2 meV), while the experimental one seems to be slightly above. We assume, that the continued fraction technique runs into difficulties here, where a weakly (anti-)bound state crosses the continuum as function of the total momentum $\mathbf{q}$. It could also be the extrapolations that cause inaccuracies like this. Otherwise, the calculation seems to give very good results. Especially the overall weight distribution is excellent.

In Fig. 6.44 we compare the spectral densities obtained from inserting our parameter set $(x, J_1) = (0.603, 6.16 \text{ meV})$ (solid lines) to the corresponding densities obtained from inserting $(x, J_1) = (0.635, 7.325 \text{ meV})$ the parameter set suggested by Totsuka et al. [96] (dashed lines). The agreement of the latter curves with the experimental data is not as good as for our parameter set.

Let us take a look at the measured dispersions. In Fig. 6.45 we show a copy of Fig. 3 in Ref. [89]. It depicts the energy and momentum resolved data collected in an INS experiment from the year 2000. The solid lines in the one- and two-triplon energy ranges should be considered to be guides to the eye. The two-triplon line suggests a very strong dispersive behaviour. A more recent high precision measurement of the two-triplon spectrum [108] is
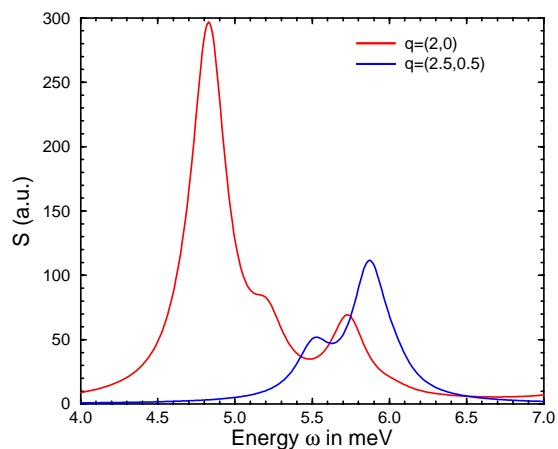
Figure 6.42.: The perturbatively obtained two-triplon dynamic structure factor for $(x, J_1) = (0.603, 6.16 \text{ meV})$ and $\mathbf{q} = (2,0) \equiv \mathbf{K} = (0,0)$ (red / light grey) and $\mathbf{q} = (2.5, 0.5) \equiv \mathbf{K} = (0, \pi)$ (blue / dark grey). The line shapes and weight distribution agree nicely with those detected experimentally (Fig. 6.43).
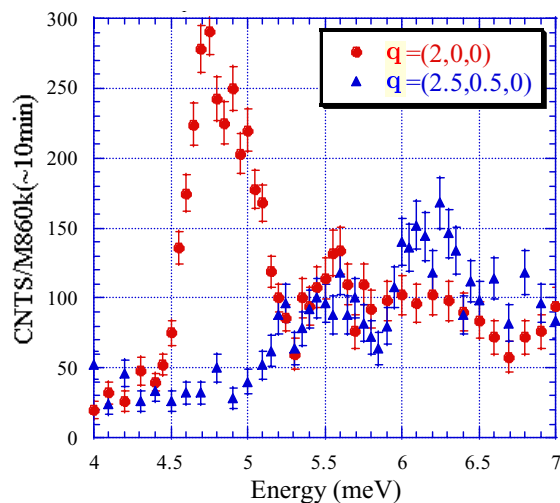
Figure 6.43.: High precision INS measurement results kindly provided by A. Nafumi and coworkers [108]. This image shows the low temperature INS response of $SrCu_2(BO_3)_2$ as function of energy for $\mathbf{q} = (2,0)$ (circles) and $\mathbf{q} = (2.5, 0.5)$ (triangles). The agreement with our perturbative results depicted in Fig. 6.42 is very good.
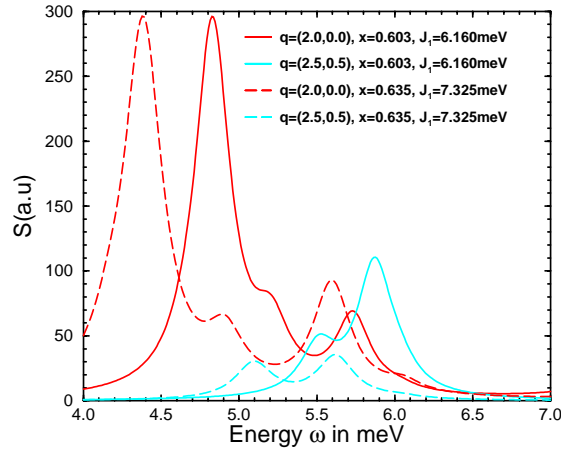
Figure 6.44.: Same as in Fig. 6.42. Additionally plotted are the spectral densities obtained for the parameter set $(x, J_1) = (0.635, 7.325 \text{ meV})$ taken from Ref. [96] (dashed lines).

depicted as colour plot in Fig. 6.46.

To be able to compare with the large amount of data depicted in Fig. 6.46, we calculated the two-triplon structure factor S along the triangle $\mathbf{q} = (2, 0) \leftrightarrow (2.5, 0) \leftrightarrow (2.5, 0.5) \leftrightarrow (2, 0)$ (see also Fig. 6.31(b)) in dual space for 150 equivalently spaced momenta $\mathbf{q}$. Each of these slices is multiplied by the same number which we used for the structure factors depicted in Fig. 6.42. The result is shown in Fig. 6.47. Figs. 6.46 and 6.47 can be compared directly. The first striking feature is the excellent agreement in the lower part of the spectrum. The weight distribution throughout the whole covered $\mathbf{q}$-space matches the experiment perfectly. The energy ranges are in astonishing agreement, too. Clearly visible is a slightly stretched hot spot located at $\mathbf{q} = (2, 0)$. There is a region at about $\mathbf{q} = (2.5, 0.5)$ where the measurement is not sensitive to magnetic excitations. The experiment shows a second rather flat band at a constant energy of about 5.5 meV, which is also visible in Fig. 6.47, though only very weakly. In the upper part of the spectrum the experiment shows yet another area of significant intensity at an energy between 6 meV and 6.3 meV and momentum $\mathbf{q} \approx (2.5, 0.5)$. This oval shaped island of intensity can be found in Fig. 6.47, too, though slightly too low in energy. We already discussed this energy mismatch in Fig. 6.42. Experimentally, this region of intensity seems to be connected by a thin bridge of intensity to another active area on the left, close to $\mathbf{q} = (2, 0)$ at energy 5.8 meV. This bridge might be the single dispersing state with weak intensity clearly visible in Fig. 6.47.
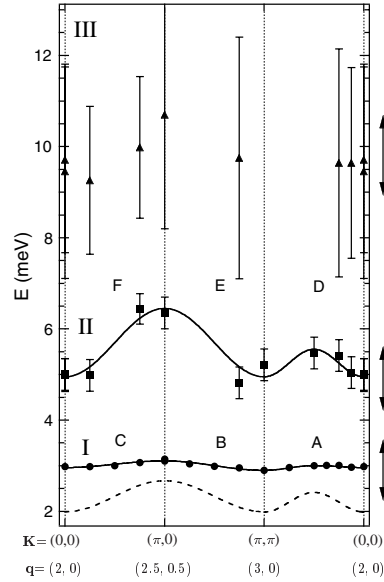
Figure 6.45.: Dispersion of magnetic excitations in $SrCu_2(BO_3)_2$ as measured by INS at low temperatures (from Ref. [89]). A sample energy scan for $\mathbf{q} = (2, 0)$ is given in Fig. 6.36. The density of measured points in the two-triplon energy range (II) is low. The solid line is a guide to the eye, but it suggests strongly dispersive two-triplon states. Our results (Fig. 6.47) in comparison to recently obtained high resolution data (Fig. 6.43 and Fig. 6.46) suggest a different interpretation. Also depicted are the rather flat one-triplon band (I) and the higher multi-particle response (III).

The theoretical results yield even more information. For fixed $\mathbf{q}$ we have chosen to represent the effective Hamiltonian H_{eff} as a 84×84 matrix. This matrix is diagonalised at 150 different $\mathbf{q}$-values.[17] Those states, which contribute with a considerable weight to the INS structure factor, are depicted as thin solid lines in Fig. 6.47. We would like to emphasise that the knowledge of the spectral density is essential to identify the relevant states. The thick dashed lines in the upper part of Fig. 6.47 denote the calculated lower and upper bounds of the two-triplon continuum.

The area of high intensity at about 5 meV to the left and right side of the figure is essentially composed of four states partly degenerate at the points of high symmetry (vertical lines). The dispersion width of these four states is about 0.5 meV. An important result is that these states traverse the insensitive area between the low energy hot spots to the left and right of Fig. 6.47 in a

---

[17] The enlarged 112×112 matrix (see earlier discussions) incorporates larger parts of the band-diagonal pure one-triplon part H_1 of H_{eff} but no new H_2-elements. Diagonalising this larger matrix leads to now visible changes in the energy levels of (anti-)bound states, which is important in this discussion.
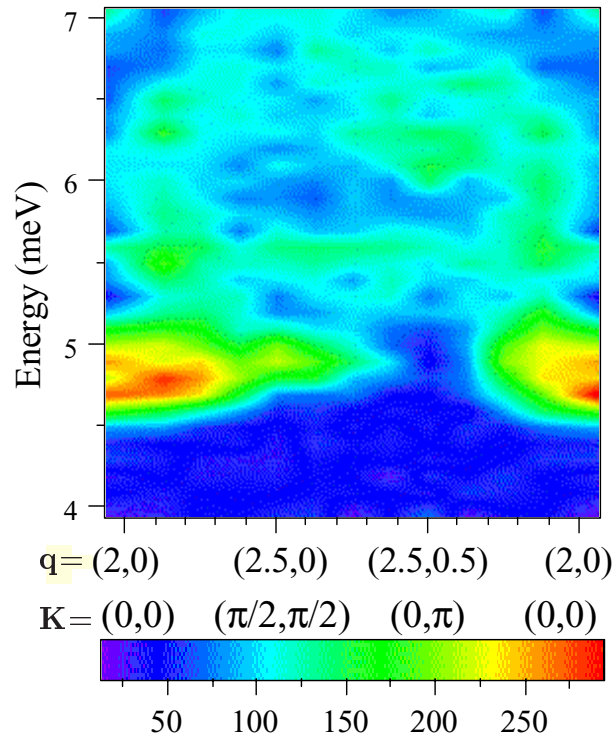
Figure 6.46.: High precision INS measurement results from Ref. [108]. Corresponding energy scans are depicted in Fig. 6.43. The chosen path through reciprocal space differs from the one in the earlier experiment depicted in Fig. 6.45. Still, some branches can be compared. These new results suggest moderate dispersions in contradiction to the lines depicted in Fig. 6.45. However, there is a **q**-range in the vicinity of (2.5,0.5) were the experiment is not sensitive to the lowest magnetic excitations leaving room for further speculations. Our results in Fig. 6.47 clarify the dispersive behaviour of the two-triplon states.

straight fashion *without* dispersing to higher energies. Because of the lack of resolution, the experimental data gives no conclusive evidence for this behaviour. The theoretical calculation is indispensable to clarify this point. The speculations about very strongly dispersing states in the two-triplon sector, as indicated in the left panel of Fig. 6.45 for instance, can be ruled out. Still, there are states dispersing considerably, especially when compared to the two nearly dispersionless one-triplon states. But the scenario is not as drastic as considered so far.

From our discussion it should be clear that the knowledge of energy levels alone might not suffice. The possibility to calculate spectral densities and (or)
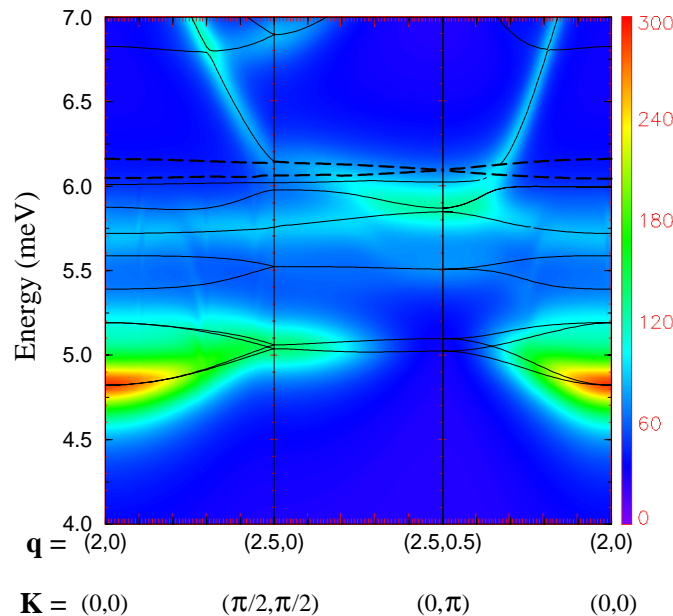
Figure 6.47.: Calculated two-triplon structure factor for the INS experiment. The thin solid lines are eigen-energies of H_{eff} corresponding to states which show an appreciable intensity. The upper and lower boundaries of the two-triplon continuum are depicted as thick dashed lines. This figure can be directly compared to the experimental findings depicted in Fig. 6.46. Of particular interest are the rather flat energy levels connecting the areas of high intensity in the energy range 4.7 meV to 5.2 meV. They do not show any significant dispersion in the **q**-range, where the experiment is insensitive. We are thus able to settle the question of whether there are strongly dispersing modes in the low energy spectrum of $SrCu_2(BO_3)_2$.

spectral weights is essential to gain a deeper understanding.

The two very dispersive states in the upper energy range seem to have no correspondence in the experimental data. We do not quite understand this feature yet. It might be connected to some level repulsion effects difficult to track. It is also conceivable that the experiment is not able to resolve these modes for a technical reason, or simply because of superpositions with the three-particle response.

6.7. Shastry-Sutherland Model – Summary

In this last section we give a comprehensive summary of this rather extensive chapter. Hoping to present a systematic approach we restructure our discussions and results so as to highlight the most significant findings.

In section 6.1 we introduce the two-dimensional $S = 1/2$ Shastry-Sutherland model as a particularly transparent spin liquid system. The model has two coupling constants: J_1 (intra-dimer coupling) and J_2 (inter-dimer coupling), for which we define the ratio $x = J_1/J_2$. The perturbative approach to the model is controlled by the limit of isolated dimers ($x = 0$), which serves as starting point for our calculations. Each dimer is represented by a *single* site in the effective lattice Γ_{eff}, on which the effective Hamiltonian H_{eff} and observables $\mathcal{O}_{\text{eff}}$ act. Due to the orthogonal arrangement of dimers Γ_{eff} exhibits an A-B sublattice structure. Starting in the limit of isolated dimers ($x = 0$), the ground state of H_{eff} is given by singlets on all sites of Γ_{eff}. The elementary excitations, i.e. the quasi-particles, are single triplets (triplons) on one of the sites of Γ_{eff}.

For positive, i.e. antiferromagnetic, couplings the model exhibits three quantum mechanical phases: an extended dimer-singlet regime for weak inter-dimer coupling, an intermediate phase, the nature of which is unclear, and a long-ranged Néel-type phase for weak intra-dimer coupling.

Many authors agree on an upper critical value of $x_c \approx 0.7$ for the dimer phase [77, 83, 85–87]. The upper value for the intermediate phase is an unsettled issue, but it is expected to be smaller than $x = 0.9$ [80, 85–87].

We show that $SrCu_2(BO_3)_2$, a layered compound of $Cu(BO_3)$-planes, is an experimental realization of the Shastry-Sutherland model. At low temperatures the magnetic properties of $SrCu_2(BO_3)_2$ are governed by $S = 1/2$ spins on the Cu^{2+} ions, for which the in-plane interactions exhibit the same topology as the two-dimensional Shastry-Sutherland model. Strong geometrical inter-layer frustration legitimates a two-dimensional treatment.

Using perturbative continuous unitary transformation, we systematically investigate the spectral properties of the Shastry-Sutherland model by exploiting high order results for H_{eff} and $\mathcal{O}_{\text{eff}}$. In the following we summarise our findings by discussing the symmetries, the one-triplon dynamics, the two-triplon dynamics, the Raman and the INS spectral densities of the model point by point.

Symmetries

The two-dimensional space group of the Shastry-Sutherland model is p4mm with underlying point group 4mm, of which the irreducible representations

are $\Gamma_1(1)$, $\Gamma_2(x^2 - y^2)$, $\Gamma_3(xy)$, $\Gamma_4(xy(x^2 - y^2))$ and $\Gamma_5(x, y)$. Polynomials in brackets give the transformation behaviour.

The one-triplon dispersion splits into two bands. The corresponding states transform like the two-dimensional Γ_5 representation. At $\mathbf{k} = \mathbf{0}$ and at the borders of the MBZ the bands are degenerate. Due to the geometrical frustration of the lattice, one-triplon motion is strongly suppressed (see also Ref. [97]). The one-triplon dispersion starts in 6th order only and is rather flat. This is verified experimentally (INS) [89]. Triplon hopping along the $\mathbf{a}$ and $\mathbf{b}$ axes (see Fig. 6.31 on page 155) can take place on one kind of the sublattices only. Likewise, at $\mathbf{k} = \mathbf{0}$ the triplon lives on either sublattice A or B only.

Two-triplon *correlated* hopping is much less restricted. Here the dispersion sets in in third order already. Thus, two-triplon modes are expected to show a stronger dispersion than the one-triplon modes (see also Ref. [93]). An older INS measurement confirms this scenario [89]. However, a more recent experiment shows rather flat bands in the two-triplon sector, too [108]. We will come back to this point in the summary of our findings for the INS spectral density. Again, symmetry arguments reveal a general double degeneracy at the borders of the MBZ.

At points of high symmetry ($\mathbf{K} = (0, 0), (0, \pi)$) the matrix representing H_{eff} in the two-triplon sector splits into various blocks corresponding to the irreducible representations Γ_1 through Γ_5 of the 4mm point group. Thus, the transformation behaviour of states, corresponding to a specific block, is fixed. For total spin $S = 0$ and momentum $\mathbf{K} = \mathbf{0}$ the energetically lowest two-triplon bound state is found in the Γ_4 block for instance. Equivalently, the lowest bound state is Γ_3 for $S = 1$.

Finally, we show that the observable $\mathcal{R}$, modelling the leading two-magnon Raman process, has Γ_3 symmetry. Thus, the states excited by $\mathcal{R}$ are Γ_3 states.

One-Triplon Dynamics

The one-triplon hopping amplitudes are calculated up to 15th order on finite clusters. For fixed momentum $\mathbf{k}$ a 2×2 matrix represents H_{eff} in momentum space. The two resulting dispersive one-triplon bands are nearly degenerate. Their splitting starts in 10th order in x and can be neglected for all practical purposes. At $\mathbf{k} = \mathbf{0}$ we obtain the one-triplon gap, which vanishes at $x = 0.697$ signalising the ultimate breakdown of the dimer phase. This finding is in perfect agreement with the result obtained by Zheng et al. [86].

The one-triplon dispersion is compared to the INS experiment on $SrCu_2(BO_3)_2$ [89]. Due to the large error bars of the experiment, it is not possible to unambiguously fix the model parameters from the one-triplon dispersion alone.

Two-Triplon Dynamics

The two-triplon hopping amplitudes are calculated up to 14th order on finite clusters. For fixed total momentum $\mathbf{K}$ the relative distances $\mathbf{d}$ between the two triplons are the only remaining quantum numbers. At points of high symmetry ($\mathbf{K} = (0,0), (0,\pi)$) we calculate various bound states of two, *linearly* interacting triplons. It turns out that we need to consider only 12 relative distances for results up to 14th order in x, i.e. for fixed $\mathbf{K}$, $H_{\text{eff}}(\mathbf{d})$ is a 24×24 matrix (we introduce an additional quantum number $\sigma \in \{0,1\}$ to account for the sublattice structure). The point group symmetries are exploited to extract the energies of the linearly bound states as exact 14th order polynomials from this matrix. Their dispersion is analysed in 5th order. Fukumoto's results are mostly confirmed [101].

At $\mathbf{K} = \mathbf{0}$ the lowest $S = 0$ bound state becomes soft at $x = 0.695$, which is the value where the one-triplon gap vanishes, too. However, for $S = 1$ we find that the Γ_3 mode already vanishes at $x = 0.63$, signalising the ultimate breakdown of the dimer phase at a smaller value than considered so far [77, 83, 85–87]. A softening of an $S = 1$ mode might indicate the transition into a triplet condensate, if the corresponding increase in binding energy extends to higher triplon sectors, too. Calculations in higher triplon sectors are necessary to confirm these suggestions. In chapter 2 we outlined how such a calculation could be approached within the framework of perturbative CUTs.

Fitting the theoretical results for the one- and two-triplon gap to the corresponding measured quantities of $\text{SrCu}_2(\text{BO}_3)_2$ (one-triplon gap: INS [89], ESR [90], FIR [91]; two-triplon gap: INS [89]) allows to determine the model-parameters: $x = 0.603(3)$, $J_1 = 6.16(10)$ meV. The resulting predictions of our theory compare excellently to the residual collection of experimental data. The one-triplon gap is in good agreement with the INS measurement. Additionally, two of the Γ_3 two-triplon bound states for $S = 0$ yield the same energy (error less than 3%) as the two lowest resonances in the Raman experiment.

Raman

We identify the observable modelling the two-magnon Raman process to leading order in a t^2/U expansion. By considering the microscopic structure of this observable we prove that a Raman experiment will produce a significant response in the (a'b') scattering geometry only. This has been observed in the experiment on $\text{SrCu}_2(\text{BO}_3)_2$ [93].

The *effective* observable is calculated up to 8th order in x. At $x = 0$ the two-triplon excitations comprise the full energy and momentum-integrated weight of the Raman process. Their relative weight drops with increasing x and

exhausts about 55% of the full weight at $x = 0.603$, the value we specified for $SrCu_2(BO_3)_2$.

We substitute our model parameters in the calculated spectral density and compare the result to the experiment. The positions of the calculated resonances are given by the effective Hamiltonian and yield no new information. They are identified as $S = 0$, Γ_3, two-triplon (anti-)bound states, and are thus given as weighted δ-functions. A comparison to the experiment [93] is eased by introducing an artificial broadening comparable to the systematic broadening of the experiment ($\approx 2\%$ here). The Raman data show four well defined resonances with a characteristic weight distribution. The three energetically lowest resonances are captured within the two-triplon approximation. The fourth peak must be attributed to three-triplon processes. The weight distribution of our theoretical result agrees nicely with the experimental finding. As in the experiment, the lowest resonance is the most dominant feature comprising about 50% of the full two-triplon weight, the shape fits the experiment excellently. The distribution of weight for the remaining two resonances shows some discrepancies but can be considered satisfying.

INS

The effective INS observable is calculated up to 8th order in x. At $x = 0$ the total energy and momentum integrated weight of the complete effective INS observable is fully seized by its one-triplon contribution. For increasing x the relative one-triplon weight decreases, while the two-triplon weight increases. The sum of the relative one- and two-triplon weights constitute the full weight up to $x \approx 0.3$. At $x = 0.603$ their relative weights still add up to about 75% of the full weight, where the two-triplon contributions accounts for approximately 25%. This finding agrees nicely with an INS energy scan of $SrCu_2(BO_3)_2$ performed at the Γ-point [89].

While we are content with a qualitative treatment of the energy and momentum resolved one-triplon spectral density, we strive for a quantitative analysis of the two-triplon sector. With novel high-resolution INS data at our disposal [108], we calculate the spectral densities for 150 different momentum vectors along the same path through dual space as used for the experimental investigation. We again use our model parameters determined beforehand. The resulting spectral density is in very good agreement with the measured scattering intensity, particularly so in the lower two-triplon energy range. Here, the shape and extension of the experimental intensity image provided is captured very well. Many structures at intermediate energies can also be found in the theoretical result, although the accuracy drops towards higher energies (the range above the two-triplon continuum).

The novel INS data [108] must be compared to the older measurement [89]. While the latter suggests the existence of strongly dispersing two-triplon modes in comparison to the rather flat one-triplon dispersion, the new, high-resolution experiment does not confirm this scenario. On the contrary, the two-triplon modes seem to be rather flat, too. However, and this is important, the high-resolution measurement has a "blind" region in the lower energy range at about $\mathbf{K} = (0, \pi)$. Here the experiment is insensitive to magnetic excitations, so the dispersing modes cannot be tracked through this momentum range. The theoretical calculation confirms that the matrix elements are very small in this region. However, the position of the dispersive bound states is given by the Hamiltonian and can thus be tracked theoretically without flaw. The calculation shows that they traverse the mentioned momentum-range without dramatic changes in their energy. Thus, the two-triplon modes *are* rather flat. The average band width is about 0.5 meV, which is still large compared to the one-triplon band width of about 0.15 meV. But it is much smaller than the 1.5 meV suggested by the former experiment. We also calculate the dispersion of energetically higher bands. They show a similar qualitative behaviour, exhibiting the same average band width.

7. Summary

In this chapter we summarise our findings. Let us do so by considering the pure methodical part separately from the application part. We wish to discuss the advantages and caveats of perturbative CUTs.

Method

We introduce perturbative CUTs as a systematic and controlled calculational method well suited to tackle low temperature properties of gapped spin (liquid) systems defined on a lattice.

The initial Hamiltonian (or observable) is unitarily mapped onto an *effective* operator H_{eff} ($\mathcal{O}_{\text{eff}}$) in a continuous fashion. The initial Hamiltonian must allow a perturbative decomposition

$$H = U + xV \ , \tag{7.1}$$

such that the unperturbed part U has an equidistant spectrum bounded from below. Moreover, we must be able to decompose the perturbing part V into ladder operators T_n

$$V = \sum_{n=-N}^{N} T_n \ , \ \text{with} \ \ N \in \mathbb{N} \ \ \text{and} \ \ [U, T_n] = nT_n \ . \tag{7.2}$$

The difference between two successive levels of U is the energy of a *quasi-particle*. These quasi-particles become renormalised by the transformation and appear as dressed particles in the effective problem.

If the system under study complies with these requirements the transformation can be constructed such that the mapping onto H_{eff} is *exact* to some maximum order in x. Moreover, the effective Hamiltonian commutes with the number of quasi-particles, i.e. $[H_{\text{eff}}, U] = 0$. Hence, H_{eff} is *block-diagonal* with respect to the number of quasi-particles. This property is crucial, since it renders high order calculations for multi-particle properties possible. Independently from our considerations this has also been found by Hamer and co-workers [28]. They show that a transformation of the initial Hamiltonian onto

a block-diagonal problem allows to use the linked-cluster expansion method to obtain high order series expansions for two-particle properties.

The task of defining U amounts to identifying appropriate quasi-particles for the system. This might not always be possible. In this case the method cannot be applied. Moreover, V connects sectors of different quasi-particle numbers. If the initial problem is such that this difference is a large number, say larger than three or four, it becomes difficult to obtain high order results. This is simply because of the increased Hilbert space dimension, which imposes computational difficulties in the computer implementation. We simply run out of memory. Lower orders obviously reduce the accuracy of the results. The same effect can be observed by increasing the dimensionality of the problem. However, geometrical frustration might help to reduce this problem, by imposing constraints to the actual states which the system can occupy.

Assuming that a (perturbative) transformation to an effective problem is possible for the initial system such that H_{eff} conserves the number of quasi-particles, we can deduce a variety of useful properties for the effective Hamiltonian and observables.

Two important results need to be mentioned. At first we find that the effective Hamiltonian and observables decompose into n-particle irreducible operators, which are defined on the *full Hilbert space* of H_{eff}. The problem splits into different sectors uniquely characterised by the number of quasi-particles. The zero-particle irreducible part H_0 of H_{eff} measures the ground state energy, no matter how many particles are present. Similarly H_1, the irreducible one-particle part of H_{eff}, measures one-particle energies. Pure two-particle interactions are captured by H_2 and so on. This constitutes a clear and systematic way in which the spectral properties of the effective system can be attacked.

Although effective *observables* $\mathcal{O}_{\text{eff}}$ (not the Hamiltonian) generally do not conserve the number of quasi-particles, a similar decomposition holds true. Zero-temperature observables, for instance, can be split into irreducible parts injecting non, one, two, etc. particles in the system, allowing the determination of the relative contributions of these individual sectors to the full process. A useful property with regard to the question of whether the initially defined quasi-particles constitute a reasonable choice for the effective systems. This question can be answered positively, if a *small* number of quasi-particles suffice to capture a large part of the full weight.

The second point we would like to mention is that an evaluation of the irreducible operators on *finite clusters* suffices to yield results for the thermodynamic system, if the analysis is truncated at a finite maximum order and if the Hamiltonian comprises interactions of finite range only. This is shown by

promoting the property of *cluster additivity* on the level of operators and by evaluating this property for the irreducible n-particle operators.

Let us turn to the evaluation of the effective quantities. The states, on which the resulting effective operators act, can be uniquely characterised by the number of quasi-particles and their position in the lattice. The effective problem can thus be analysed in *real space*.

The effective operators are given by a *high order* series expansion in the (small) perturbation parameter x ensuring *quantitative results*. In each order a sequence of virtual excitations in the number and position of the initial particles emulates the polarisation cloud dressing the initial particles in the effective problem – a straightforward and traceable effective picture emerges.

However, the evaluation of the effective operators on finite clusters in real space should be discussed carefully. The dynamics of systems, which exhibit *long-ranged correlations*, might not be fully captured by the finite clusters. Even the largest clusters for the highest possible orders might be too small. This is a serious problem in particular for the treatment of gapless systems with algebraically decreasing correlations. Although the perturbative starting point ($x = 0$) is given by the gapped system U, one might be interested in a gapless system reached at some finite value of x. This problem can be partly overcome by using extrapolation techniques. However, judging the reliability of the extrapolated results can be a difficult issue.

For systems not hampered by the discussed difficulties the high order perturbation scheme can be used successfully to quantitatively calculate zero-one- and two-particle energies. We also indicate how calculations in sectors of higher particle numbers can be tackled.

We also show that the calculation of high order series expansions for the effective observables leads to the possibility to obtain quantitative results for the corresponding spectral densities. By using the continued fraction technique [63–67] for the Green's function composed of H_{eff} and $\mathcal{O}_{\mathrm{eff}}$ we are able to quantitatively calculate two-particle spectral densities of interest.

Again, the truncation in real space (finite clusters) is the crucial factor, which limits the accuracy of the results. Necessary extrapolations are particularly difficult for the involved quantities. We address this problem in a separate chapter where we introduce an extrapolation technique called optimised perturbation theory, which is based on the principle of minimal sensitivity [70].

We would like to conclude this section by discussing some general aspects. As mention at the beginning of this section we need the initial Hamiltonian to allow a perturbative decomposition. For systems, not offering a "natural" decomposition, a splitting must be introduced by force. The actual system of interest can then be reached by extrapolating the results to the corresponding

parameter value. Now, besides the need to extrapolate, the "artificial" split-ting might bias the results in an unwanted fashion. Particularly delicate are situations in which the starting-regime belongs to a different universality class or has a different symmetry group than the system we are finally interested in.

Moreover, the starting-limit defines the (gapped) *starting-regime* ($x = 0$). The softening of energy-modes at a critical value x_c signals the breakdown of the perturbative approach. Although this constitutes a method to calculate an upper critical x-value for the starting-phase, we cannot make any predictions for the new, emergent phase. We can only touch single points of gapless regimes. It is not possible at all to analyse the phase-transition points between two gapless phases. For these kinds of problems renormalisation techniques constitute a better suited approach.

Application

Although it is a two-dimensional system the Shastry-Sutherland model consti-tutes a well-suited example to illustrate the application of perturbative CUTs. Due to strong geometrical frustration, the used Hilbert space is considerably decreased. Additionally, we have rather short correlation lengths (typically a few sites) in the dimer-singlet phase, the regime we investigate. The calcula-tions on finite clusters thus constitute a safe approach.

The dimer-singlet phase is characterised by singlets on all dimers, which is the exact ground state of the system for x not too large. The limit of isolated dimers ($x = 0$) is the perturbative starting point. Here the elementary excitations are given by single triplets (triplons) on the dimers. The triplons are the quasi-particles of our approach. They become dressed as soon as the inter-dimer coupling is switched on ($x > 0$).

We start by analysing the symmetries of the model and calculate the one-triplon dispersion, which splits into two bands. The results are obtained up to 15th order in x. At zero momentum and at the borders of the magnetic Brillouin zone the two branches fall onto each other leading to a two-fold degenerate dispersion. Ignoring the band splitting, our findings are in perfect agreement with the numerical findings by Zheng et al. [86, 98]. They use the cluster expansion method to also obtain results up to 15th order. Miyahara and Ueda perturbatively calculated the one-triplon gap up to 4th order [77]. We can verify their results and find that the one-triplon gap vanishes at $x \approx 0.7$. This value marks the upper critical value for the dimer-singlet phase. It is in very good agreement with the upper critical values determined by other authors [77, 83, 85–87].

Next we analyse the two-triplon energies. The dispersion of linearly bound two-triplon states is evaluated up to 5th order in x. The results can be partly

compared to a perturbative expansion up to 5th order by Fukumoto [101]. Some of his 5th order terms show deviations from our results. Totsuka et al. also use perturbation theory to calculate the two-triplon dispersion up to 3rd order [96]. Unfortunately their results do not allow a direct comparison to our findings.

At total momentum $\mathbf{K} = (0, 0)$ and $\mathbf{K} = (0, \pi)$ we calculate the energies of the linearly bound two-triplon states as 14th order polynomials in x for total spin $S = 0$ and $S = 1$. The symmetries of the corresponding states can be classified according to the irreducible representations Γ_1 through Γ_5 of the 4mm point group of the model. An interesting feature is the softening of the Γ_3 two-triplon mode for $S = 1$ at $x = 0.63$, signalling a transition into a new phase at a smaller value than considered so far (see above and Refs. [77, 83, 85–87]). Our considerations about the nature of this phase require further investigations. However, by comparing our results to the experimental data for $SrCu_2(BO_3)_2$, an experimental realization of the model, we show that a sound determination of the parameters is eased, if the two-triplon spectrum can be used, too.

Furthermore, the identification of the relevant Raman and neutron scattering observables renders a quantitative comparison to the corresponding experiments possible [89, 93, 108]. We show, that our parameter set leads to an excellent agreement. Our findings for the neutron scattering intensity in particular lead to interesting insights into the spectral properties of the Shastry-Sutherland model and its experimental realization $SrCu_2(BO_3)_2$. One of the intriguing features of $SrCu_2(BO_3)_2$ are strong dispersive two-triplon modes in comparison to a rather flat one-triplon dispersions. Speculations, based on the experimental facts alone, suggest *very* large dispersions in the two-triplon sector. In combination with novel experimental data [108], we are able to show that the two-triplon states show moderate dispersions only. This constitutes a fine example of the virtue that lies in the combination of theoretical and experimental efforts.

At the end of this section we would like to very shortly discuss alternative approaches to the Shastry-Sutherland model. Unfortunately, quantum Monte Carlo calculations cannot be applied due to the frustration induced sign problem. Exact diagonalisation methods [77–79, 83, 96] are difficult to use here, since not only the number of considered sites but also the topology of the corresponding finite clusters affect the finite size scaling. Renormalisation methods have been used successfully to investigate the critical behaviour of the Shastry-Sutherland model [80–82]. An important result is that an intermediate phase *must* exist between the dimer-singlet phase at small x-values and a Néel-type phase at larger x-values.

So far, perturbation theory seems to be the only available approach to obtain quantitative results for measurable properties of the Shastry-Sutherland model [77, 85–87, 96, 101, 109]. With regard to this point, high order perturbation theories in particular constitute a valuable tool for these kind of systems.

Outlook

We would like to address two methodical points that deserve further attention. The possibility to calculate *many-particle properties* by perturbative CUTs for suitable systems constitutes an interesting perspective. Further work in this direction might be rewarding. For the Shastry-Sutherland model in particular the calculation of three- and four-triplon bound states might shed some light on the intermediate phase. It would be interesting to see, if triplets composed of a larger number of triplons are also subject to increased binding energies. This would give strong evidence for a triplet-condensate phase as intermediate regime supporting the findings of renormalisation approaches [81, 82].

We constructed the mapping to an effective model perturbatively. That means that all operators, the Hamiltonian H, the generator η and the observables $\mathcal{O}$, are given in a series of some small parameter x. Then a calculation up to a certain order describes processes of a certain *finite* range only, which leads to the discussed problems for systems comprising long-ranged correlations.

This problem can be overcome by performing the continuous unitary transformation directly on the level of the n-particle irreducible operators. An ansatz for the effective Hamiltonian is chosen comprising for instance all possible irreducible n-particle terms and similar terms creating and annihilating particles. This ansatz is inserted in the flow equation (1.11). Comparison of the coefficients $t_{j_1\dots;i_1\dots}$ and $\partial_\ell t_{j_1\dots;i_1\dots}$ in front of the terms $e^\dagger_{j_1}\dots e_{i_1}\dots$ (see Eq. (2.6)) yields coupled non-linear differential equations. These differential equations represent renormalisation equations for the problem under study. This type of transformation might be called *self-similar* since the kind of terms retained stays the same. It would be interesting to see, if such an approach, extending the applicability beyond finite range processes, can be applied successfully to gapless systems. For our considerations gapless spin systems in particular, such as the spin 1/2 Heisenberg model on a square lattice, constitute interesting testing grounds. An illustrative application of the self-similar approach to spinless fermions in one dimension can be found in Refs. [45, 50].

A. Three-Particle Irreducible Interaction

Here we complete the formulae for the irreducible 3-particle interaction which was given in Eq. (2.17). The corrections A_0, A_1 and A_2 result from H_0, H_1 and H_2, respectively, as given in (2.8). They read

$$A_0 \;=\; E_0^A[\delta_{j_1 i_1}\tilde{\delta}_{j_2 j_3; i_2 i_3} + \delta_{j_1 i_2}\tilde{\delta}_{j_2 j_3; i_1 i_3} + \delta_{j_1 i_3}\tilde{\delta}_{j_2 j_3; i_1 i_2}]$$

(A.1)

$$\begin{aligned}
A_1 \;=\;\; & t^A_{j_1; i_1}\tilde{\delta}_{j_2 j_3; i_2 i_3} + t^A_{j_1; i_2}\tilde{\delta}_{j_2 j_3; i_1 i_3} + t^A_{j_1; i_3}\tilde{\delta}_{j_2 j_3; i_1 i_2} + \\
& t^A_{j_2; i_1}\tilde{\delta}_{j_1 j_3; i_2 i_3} + t^A_{j_2; i_2}\tilde{\delta}_{j_1 j_3; i_1 i_3} + t^A_{j_2; i_3}\tilde{\delta}_{j_1 j_3; i_1 i_2} + \\
& t^A_{j_3; i_1}\tilde{\delta}_{j_1 j_2; i_2 i_3} + t^A_{j_3; i_2}\tilde{\delta}_{j_1 j_2; i_1 i_3} + t^A_{j_3; i_3}\tilde{\delta}_{j_1 j_2; i_1 i_2}
\end{aligned}$$

(A.2)

$$\begin{aligned}
A_2 \;=\;\; & \delta_{j_1 i_1}\tilde{t}^A_{j_2 j_3; i_2 i_3} + \delta_{j_1 i_2}\tilde{t}^A_{j_2 j_3; i_1 i_3} + \delta_{j_1 i_3}\tilde{t}^A_{j_2 j_3; i_1 i_2} + \\
& \delta_{j_2 i_1}\tilde{t}^A_{j_1 j_3; i_2 i_3} + \delta_{j_2 i_2}\tilde{t}^A_{j_1 j_3; i_1 i_3} + \delta_{j_2 i_3}\tilde{t}^A_{j_1 j_3; i_1 i_2} + \\
& \delta_{j_3 i_1}\tilde{t}^A_{j_1 j_2; i_2 i_3} + \delta_{j_3 i_2}\tilde{t}^A_{j_1 j_2; i_1 i_3} + \delta_{j_3 i_3}\tilde{t}^A_{j_1 j_2; i_1 i_2}
\end{aligned}$$

(A.3)

where we used the shorthands

$$\begin{aligned}
\tilde{\delta}_{j_1 j_2; i_1 i_2} \;&:=\; \delta_{j_1 i_1}\delta_{j_2 i_2} + \delta_{j_1 i_2}\delta_{j_2 i_1} \\
\tilde{t}^A_{j_1 j_2; i_1 i_2} \;&:=\; t^A_{j_1 j_2; i_1 i_2} + t^A_{j_1 j_2; i_2 i_1} + t^A_{j_2 j_1; i_1 i_2} + t^A_{j_2 j_1; i_2 i_1}.
\end{aligned}$$

(A.4)

While the actual formulae are lengthy the underlying principle is straightforward (see main text). Note that in concrete realizations it is often advantageous to denote only one representative of the states which do not change on interchange of particles ($|ji\rangle = |ij\rangle$). Furthermore, certain problems allow to

exploit higher particular symmetries like spin rotation symmetry. Then additional permutation symmetries among the various quantum numbers constituting the multi-index can be exploited leading to the appearance of exchange-parity factors.

Let us briefly discuss an example. In this thesis we focus on dimer spin systems for which the elementary excitations or quasi-particles are given by triplets (triplons). The corresponding effective Hamiltonians H_{eff} act on states which are uniquely characterised by the number and the position of these triplons. If H_{eff} conserves the total spin S, the triplon exchange parity is fixed and we find (see text below Eq. (3.47) on page 57)

$$|\mathbf{r}, \mathbf{r}'\rangle^S = (-1)^S |\mathbf{r}', \mathbf{r}\rangle^S , \tag{A.5}$$

where $|\mathbf{r}, \mathbf{r}'\rangle^S$ denotes the state of total spin S composed of two triplons at the positions $\mathbf{r}$ and $\mathbf{r}'$.

B. Coefficients

In this appendix we present the leading coefficients C (6th order) and $\tilde{C}$ (4$^{\text{th}}$ order) for the effective Hamiltonian

$$H_{\text{eff}}(x) = U + \sum_{k=1}^{\infty} x^k \sum_{\substack{|\underline{m}|=k \\ M(\underline{m})=0}} C(\underline{m})T(\underline{m}) , \quad \text{with}$$

$$T(\underline{m}) = T_{m_1}T_{m_2}\dots T_{m_k} \tag{B.1}$$

and for effective observables respectively

$$\mathcal{O}_{\text{eff}}(x) = \sum_{k=0}^{\infty} x^k \sum_{i=1}^{k+1} \sum_{|\underline{m}|=k} \tilde{C}(\underline{m};i)\mathcal{O}(\underline{m};i) , \quad \text{with}$$

$$\mathcal{O}(\underline{m};i) = T_{m_1}\cdots T_{m_{i-1}}\mathcal{O}T_{m_i}\cdots T_{m_k} . \tag{B.2}$$

We consider the case where the perturbation V in $H = U + xV$ can be decomposed according to

$$V = T_{-2} + T_{-1} + T_0 + T_1 + T_2. \tag{B.3}$$

Thus, V can create or annihilate two particles at most. We denote the set of all coefficients C and $\tilde{C}$ needed in this case by $(-2,-1,0,1,2)_C$ and $(-2,-1,0,1,2)_{\tilde{C}}$ respectively. The sets $(-1,0,1)_{C/\tilde{C}}$ and $(-2,0,2)_{C/\tilde{C}}$ can be extracted from the given coefficients.[1] One simply has to drop all those coefficients, which contain entries m_i not part of the chosen set. We have calculated the various sets to higher orders than presented here.[2] All calculated coefficients are available on our websites [62].

---

[1] It is easily verified, that the sets $(-1,0,1)_{C/\tilde{C}}$ can be obtained from the sets $(-2,0,2)_{C/\tilde{C}}$ by multiplying all coefficients in $(-2,0,2)_{C/\tilde{C}}$ by 2^{k-1}, where $k = |\underline{m}|$ is the order.

[2] $(-2,-1,0,1,2)_C$: 10$^{\text{th}}$ order,
$(-1,0,1)_C$: 15$^{\text{th}}$ order,
$(-2,-1,0,1,2)_{\tilde{C}}$: 8$^{\text{th}}$ order and
$(-1,0,1)_{\tilde{C}}$: 11$^{\text{th}}$ order.

The coefficients are presented in form of tables. Coefficients not listed are zero or can be obtained by making use of the symmetry relations (cf. Eqs. (3.15), (3.16), (3.34) and (3.35))

$$C(\underline{m}) = C(-m_k, -m_{k-1} \ldots, -m_1)$$

$$C(\underline{m}) = C(-m_1, -m_2, \ldots, -m_k)(-1)^{|\underline{m}|+1}$$

$$\tilde{C}(\underline{m}; i) = \tilde{C}((-m_k, -m_{k-1} \ldots, -m_1); |\underline{m}| - i + 2)$$

$$\tilde{C}(\underline{m}; i) = \tilde{C}((-m_1, -m_2, \ldots, -m_k); i)(-1)^{|\underline{m}|} , \tag{B.4}$$

with $\underline{m} = (m_1, m_2, \ldots, m_k)$.

$\underline{m}$	$C(\underline{m})$	$\underline{m}$	$C(\underline{m})$	$\underline{m}$	$C(\underline{m})$	$\underline{m}$	$C(\underline{m})$	$\underline{m}$	$C(\underline{m})$
$|\underline{m}| = 1$		$|\underline{m}| = 4$		$|\underline{m}| = 5$		$|\underline{m}| = 5$		$|\underline{m}| = 5$	
0	1	200-2	1/8	020-20	3/32	11-2-22	1/8	20-11-2	1/8
$|\underline{m}| = 2$		21-1-2	1/12	020-1-1	-1/4	11-2-11	1/8	210-1-2	1/36
1-1	1	22-2-2	1/16	021-2-1	-11/72	11-11-2	1/4	211-2-2	1/48
2-2	1/2	2-22-2	-1/8	021-1-2	-1/18	11-1-21	-1/2	21-21-2	1/12
$|\underline{m}| = 3$		2-11-2	1/4	022-2-2	-5/128	120-2-1	1/9	220-2-2	1/64
01-1	-1/2	$|\underline{m}| = 5$		02-21-1	7/24	120-1-2	1/18	2-202-2	3/64
02-2	-1/8	0001-1	-1/8	02-22-2	9/128	121-2-2	1/24	2-20-22	-1/64
10-1	1	0002-2	-1/128	02-2-22	-3/128	12-21-2	1/6	2-211-2	-1/4
11-2	1/2	0010-1	3/4	02-2-11	-1/12	12-2-21	-1/3	2-2-1-12	1/8
1-21	-1	0011-2	7/32	02-10-1	-5/8	12-10-2	1/12	2-101-2	1/4
20-2	1/4	001-21	-5/16	02-11-2	-1/4	1-202-1	1	2-1-2-12	1/4
$|\underline{m}| = 4$		001-10	-3/8	02-1-21	7/24	1-20-12	-1/2	$|\underline{m}| = 6$	
001-1	1/4	0020-2	3/64	1000-1	1	1-211-1	1/4	00001-1	1/16
002-2	1/32	002-20	-3/128	1001-2	1/2	1-212-2	0	00002-2	1/512
010-1	-1	002-1-1	7/32	100-21	-1	1-21-22	1/4	00010-1	-1/2
011-2	-3/8	0100-1	-3/2	1010-2	1/4	1-21-11	3/4	00011-2	-15/128
01-21	1/4	0101-2	-5/8	101-1-1	1/2	1-221-2	-1/2	0001-21	5/64
01-10	1/2	010-21	7/8	102-2-1	1/3	1-22-21	1	0001-10	1/4
020-2	-1/8	010-10	3/2	102-1-2	1/6	1-2-212	-1/6	00020-2	-1/64
02-20	1/16	0110-2	-1/4	10-201	1	1-2-102	-1/4	0002-20	1/128
02-1-1	-3/8	011-20	7/16	10-22-1	-1	1-101-1	3/4	0002-1-1	-15/128
100-1	1	011-1-1	-5/8	10-2-12	1/2	1-102-2	7/32	00100-1	3/2
101-2	1/2	012-2-1	-7/18	10-11-1	-3/2	1-10-22	-3/32	00101-2	17/32
10-21	-1	012-1-2	-11/72	10-12-2	-5/8	1-10-11	-1/4	0010-21	-3/4
110-2	1/4	01-201	1/8	10-1-22	3/8	1-111-2	-5/8	0010-10	-3/2
11-1-1	1/2	01-210	-3/8	10-1-11	1/2	1-120-2	-1/4	00110-2	11/64
12-2-1	1/3	01-22-1	1/2	1100-2	1/8	1-1-202	0	0011-20	-45/128
12-1-2	1/6	01-2-12	-1/24	110-1-1	1/4	1-1-1-12	1/8	0011-1-1	17/32
1-22-1	-1	01-11-1	9/8	111-2-1	1/6	2000-2	1/16	0012-2-1	17/54
1-2-12	1/2	01-12-2	35/96	111-1-2	1/12	201-1-2	1/24	0012-1-2	85/864
1-11-1	-1	01-1-22	-19/96	112-2-2	1/16	202-2-2	1/32	001-201	1/2
1-12-2	-3/8	01-1-11	-3/8	11-21-1	-5/8	20-22-2	-3/32	001-210	1/64
1-1-22	1/8	0200-2	-3/32	11-22-2	-1/4	20-2-22	1/32	001-22-1	-13/24

$\underline{m}$	$C(\underline{m})$	$\underline{m}$	$C(\underline{m})$	$\underline{m}$	$C(\underline{m})$	$\underline{m}$	$C(\underline{m})$	$\underline{m}$	$C(\underline{m})$
$|\underline{m}|=6$		$|\underline{m}|=6$		$|\underline{m}|=6$		$|\underline{m}|=6$		$|\underline{m}|=6$	
001-2-12	53/288	01-202-1	0	02-20-11	-7/384	10-211-1	5/8	11-1-22-1	-1/2
001-100	3/8	01-20-12	-1/6	02-210-1	95/144	10-212-2	3/16	11-1-2-12	1/4
001-11-1	-29/32	01-211-1	-2/3	02-211-2	85/384	10-21-22	1/16	11-1-11-1	-7/8
001-12-2	-301/1152	01-212-2	-15/64	02-21-21	-53/192	10-21-11	3/8	11-1-12-2	-3/8
001-1-22	179/1152	01-21-22	37/192	02-220-2	33/512	10-220-1	-1	11-1-1-22	1/4
001-1-11	7/32	01-21-11	13/24	02-22-20	-27/512	10-221-2	-1/2	11-1-1-11	3/8
00200-2	3/64	01-220-1	7/8	02-22-1-1	85/384	10-22-21	1	1200-2-1	1/27
0020-20	-3/64	01-221-2	1/3	02-2-202	7/512	10-2-212	-1/6	1200-1-2	1/54
0020-1-1	11/64	01-22-21	-5/16	02-2-211	23/384	10-2-221	-1/3	1201-2-2	1/72
0021-2-1	85/864	01-22-10	-11/12	02-2-101	31/144	10-2-102	-1/4	120-21-2	1/18
0021-1-2	43/1728	01-2-212	-1/144	02-2-12-1	-11/64	10-2-111	-1/2	120-2-21	-1/9
0022-2-2	17/1024	01-2-221	-25/288	02-2-1-12	23/384	10-101-1	3/2	120-10-2	1/36
002-200	3/256	01-2-102	-1/36	02-100-1	-7/8	10-102-2	17/32	1210-2-2	1/96
002-21-1	-197/1152	01-2-111	-1/6	02-101-2	-3/8	10-10-22	-9/32	121-20-2	1/48
002-22-2	-29/1024	01-2-120	31/144	02-10-21	7/12	10-10-11	-1/2	121-1-2-1	1/36
002-2-22	7/1024	01-101-1	-1	02-110-2	-5/32	10-110-1	-2	121-1-1-2	1/72
002-2-11	-23/1152	01-102-2	-329/1152	02-11-20	11/32	10-111-2	-7/8	122-2-2-1	1/45
002-10-1	17/32	01-10-22	53/384	02-11-1-1	-3/8	10-11-21	5/4	122-2-1-2	1/90
002-11-2	11/64	01-10-11	3/16	02-12-2-1	-17/72	10-120-2	-3/8	122-1-2-2	1/120
002-1-21	-65/288	01-110-1	33/16	02-12-1-2	-7/72	10-12-1-1	-7/8	12-201-2	1/6
002-1-10	-45/128	01-111-2	73/96	02-1-201	-5/36	10-1-202	-1/8	12-20-21	-1/3
01000-1	-2	01-11-21	-49/48	02-1-22-1	5/12	10-1-211	-1/8	12-210-2	1/12
01001-2	-7/8	01-11-10	-27/16	02-1-2-12	-11/96	10-1-12-1	3/4	12-22-2-1	1/9
0100-21	23/16	01-120-2	151/576	02-1-11-1	5/6	10-1-1-12	-1/8	12-22-1-2	1/18
0100-10	3	01-12-20	-149/384	02-1-12-2	113/384	11000-2	1/16	12-2-22-1	-1/3
01010-2	-3/8	01-12-1-1	73/96	02-1-1-22	-67/384	1100-1-1	1/8	12-2-2-12	1/6
0101-20	17/16	01-1-202	47/576	02-1-1-11	-7/24	1101-2-1	1/12	12-2-11-1	-5/9
0101-1-1	-7/8	01-1-211	17/96	10000-1	1	1101-1-2	1/24	12-2-12-2	-17/72
0102-2-1	-5/9	01-1-220	113/1152	10001-2	1/2	1102-2-2	1/32	12-2-1-22	11/72
0102-1-2	-17/72	01-1-101	7/16	1000-21	-1	110-21-1	-3/8	12-2-1-11	2/9
010-201	-5/8	01-1-12-1	-31/48	10010-2	1/4	110-22-2	-5/32	12-100-2	1/24
010-210	-3/4	01-1-1-12	17/96	1001-1-1	1/2	110-2-22	3/32	12-11-2-1	1/18
010-22-1	9/8	02000-2	-1/16	1002-2-1	1/3	110-2-11	1/8	12-11-1-2	1/36
010-2-12	-7/18	0200-20	3/32	1002-1-2	1/6	110-11-2	1/8	12-12-2-2	1/48
010-11-1	39/16	0200-1-1	-5/32	100-201	1	110-1-21	-1/4	12-1-21-1	-17/72
010-12-2	269/288	0201-2-1	-7/72	100-22-1	-1	1110-2-1	1/18	12-1-22-2	-7/72
010-1-22	-181/288	0201-1-2	-11/288	100-2-12	1/2	1110-1-2	1/36	12-1-2-22	1/18
010-1-11	-17/48	0202-2-2	-7/256	100-11-1	-2	1111-2-2	1/48	12-1-2-11	5/72
01100-2	-5/32	020-21-1	73/288	100-12-2	-7/8	111-21-2	1/12	12-1-11-2	1/12
0110-20	11/32	020-22-2	39/512	100-1-22	5/8	111-2-21	-1/6	12-1-1-21	-1/6
0110-1-1	-3/8	020-2-22	-17/512	100-1-11	1	111-10-2	1/24	1-2002-1	-1
0111-2-1	-17/72	020-2-11	-17/288	10100-2	1/8	111-1-1-1	1/12	1-200-12	1/2
0111-1-2	-7/72	020-10-1	-3/8	1010-1-1	1/4	1120-2-2	1/64	1-2011-1	3/8
0112-2-2	-9/128	020-11-2	-5/32	1011-2-1	1/6	112-20-2	1/32	1-2012-2	5/16
011-21-1	5/6	020-1-21	2/9	1011-1-2	1/12	112-2-1-1	1/16	1-201-22	-9/16
011-22-2	113/384	0210-2-1	-13/216	1012-2-2	1/16	112-1-2-1	1/24	1-201-11	-11/8
011-2-22	-67/384	0210-1-2	-5/216	101-21-1	-7/8	112-1-1-2	1/48	1-2021-2	1/2
011-2-11	-7/24	0211-2-2	-19/1152	101-22-2	-3/8	11-201-1	17/32	1-202-21	-1
011-10-1	-7/8	021-20-1	-17/72	101-2-22	1/4	11-202-2	11/64	1-20-212	1/6
011-11-2	-3/8	021-21-2	-7/72	101-2-11	3/8	11-20-22	-5/64	1-20-102	1/4
011-1-21	7/12	021-2-21	19/144	101-10-1	1/2	11-20-11	-5/32	1-2101-1	-7/16
011-1-10	17/16	021-10-2	-11/288	101-11-2	1/4	11-211-2	-3/8	1-2102-2	-5/32
0120-2-1	-4/27	021-1-20	43/864	101-1-21	-1/2	11-21-21	1/2	1-210-22	7/32
0120-1-2	-13/216	021-1-1-1	-7/72	1020-2-1	1/9	11-220-2	-5/32	1-210-11	11/16
0121-2-2	-25/576	0220-2-2	-3/256	1020-1-2	1/18	11-22-1-1	-3/8	1-2111-2	1/4
012-20-1	-5/9	022-20-2	-7/256	1021-2-2	1/24	11-2-202	-1/32	1-2120-2	1/16
012-21-2	-17/72	022-2-20	17/512	102-20-1	1/3	11-2-12-1	1/4	1-21-202	-3/16
012-2-21	103/288	022-2-1-1	-9/128	102-21-2	1/6	11-101-2	1/4	1-21-12-1	1/2
012-2-10	17/27	022-1-2-1	-25/576	102-2-21	-1/3	11-10-21	-1/2	1-21-1-12	-1/2
012-10-2	-7/72	022-1-1-2	-19/1152	102-10-2	1/12	11-110-2	1/8	1-2201-2	-1/2
012-1-20	85/432	02-201-1	-211/1152	102-1-1-1	1/6	11-11-1-1	1/4	1-2210-2	-1/4
012-1-1-1	-17/72	02-202-2	-1/32	10-202-1	1	11-12-2-1	1/6	1-222-1-2	-1/6
01-2001	-9/16	02-20-22	3/512	10-20-12	-1/2	11-12-1-2	1/12	1-22-22-1	1

$\underline{m}$	$C(\underline{m})$	$\underline{m}$	$C(\underline{m})$
$|\underline{m}| = 6$		$|\underline{m}| = 6$	
1-22-2-12	-1/2	2011-2-2	1/96
1-22-11-1	1	201-21-2	1/24
1-22-12-2	3/8	201-10-2	1/48
1-22-1-22	-1/8	2020-2-2	1/128
1-22-1-11	0	202-20-2	1/64
1-2-2012	1/18	202-1-1-2	1/96
1-2-2102	1/12	20-202-2	3/64
1-2-222-1	-1/3	20-20-22	-1/64
1-2-22-12	1/6	20-211-2	-5/32
1-2-2-122	1/24	20-220-2	-1/16
1-2-1002	1/8	20-2-1-12	1/32
1-2-112-1	-1/2	20-101-2	1/8
1-2-11-12	1/4	20-110-2	1/16
1-2-121-1	1/24	20-12-1-2	1/24
1-2-122-2	1/12	20-1-2-12	1/8
1-2-12-22	-5/24	20-1-12-2	-5/32
1-2-12-11	-13/24	20-1-1-22	3/32
1-2-1-222	1/16	2100-1-2	1/108
1-2-1-112	1/12	2101-2-2	1/144
1-1001-1	-1/2	210-21-2	1/36
1-1002-2	-15/128	2110-2-2	1/192
1-100-22	5/128	211-1-1-2	1/144
1-1011-2	17/32	212-2-1-2	1/180
1-1020-2	11/64	212-1-2-2	1/240
1-10-202	3/64	21-201-2	1/12
1-10-1-12	5/32	21-22-1-2	1/36
1-1101-2	-7/8	21-2-2-12	1/12
1-1110-2	-3/8	21-2-12-2	-7/72
1-112-1-2	-17/72	21-2-1-22	1/18
1-11-2-12	-7/24	21-11-1-2	1/72
1-11-11-1	2	21-12-2-2	1/96
1-11-12-2	71/96	21-1-22-2	-11/288
1-11-1-22	-43/96	21-1-2-22	5/288
1-11-1-11	-3/4	21-1-11-2	1/24
1-1200-2	-5/32	2200-2-2	1/256
1-121-1-2	-7/72	221-1-2-2	1/320
1-122-2-2	-9/128	222-2-2-2	1/384
1-12-21-1	31/48	22-22-2-2	1/128
1-12-22-2	83/384	22-2-22-2	-7/256
1-12-2-22	-41/384	22-2-2-22	3/256
1-12-2-11	-3/16	22-2-11-2	1/32
1-12-11-2	-3/8	22-11-2-2	1/192
1-1-2002	-1/32	22-1-21-2	1/48
1-1-21-12	-1/8	2-2002-2	-1/64
1-1-221-1	-11/48	2-2011-2	11/64
1-1-222-2	-25/384	2-20-1-12	5/64
1-1-22-22	19/384	2-2101-2	-3/8
1-1-2-222	-1/128	2-21-2-12	-1/12
1-1-2-112	-1/72	2-21-12-2	49/192
1-1-10-12	-3/8	2-21-1-22	-9/64
1-1-111-1	-1/2	2-22-22-2	1/16
1-1-112-2	-19/96	2-22-2-22	-3/128
1-1-11-22	23/96	2-22-11-2	-5/32
1-1-121-2	5/24	2-2-21-12	-3/32
1-1-1-212	-5/72	2-2-222-2	-1/64
1-1-1-102	-1/8	2-2-10-12	-1/4
20000-2	1/32	2-2-112-2	-17/192
2001-1-2	1/48	2-2-121-2	1/24
2002-2-2	1/64	2-1001-2	1/4
200-22-2	-1/16	2-10-2-12	1/4
200-2-22	1/32	2-11-11-2	1/8
200-11-2	1/16	2-12-21-2	1/12
2010-1-2	1/72	2-1-221-2	-1/4
		2-1-111-2	-3/8

i	$\underline{m}$	$\tilde{C}(\underline{m};i)$
	$|\underline{m}| = 0$	
1		1/1
	$|\underline{m}| = 1$	
1	1	-1/1
1	2	-1/2
	$|\underline{m}| = 2$	
1	01	1/1
1	02	1/4
1	10	-1/1
1	11	1/2
1	12	1/6
1	1-2	1/2
1	1-1	-1/2
1	20	-1/4
1	21	1/3
1	22	1/8
1	2-2	-1/8
1	2-1	-1/1
2	11	-1/1
2	12	-1/2
2	1-2	1/2
2	1-1	1/1
2	22	-1/4
2	2-2	1/4
	$|\underline{m}| = 3$	
1	001	-1/1
1	002	-1/8
1	010	2/1
1	011	-1/4
1	012	-1/18
1	01-2	1/2
1	01-1	1/4
1	020	1/4
1	021	-1/9
1	022	-1/32
1	02-2	1/32
1	02-1	1/1
1	101	-1/2
1	102	-1/12
1	10-2	1/4
1	10-1	-1/1
1	110	3/4
1	111	-1/6
1	112	-1/24
1	11-2	-3/8
1	11-1	-1/2
1	120	5/36
1	121	-1/12
1	122	-1/40
1	12-2	-3/8
1	12-1	1/2
1	1-20	-3/4
1	1-21	1/4
1	1-22	5/8
1	1-2-2	1/24
1	1-2-1	1/6
1	1-10	3/4
1	1-11	3/2
1	1-12	-1/4
1	1-1-2	1/12
1	1-1-1	1/2
1	201	-1/3
1	202	-1/16

i	$\underline{m}$	$\tilde{C}(\underline{m};i)$
	$|\underline{m}| = 3$	
1	20-2	-1/8
1	20-1	-1/1
1	211	-1/8
1	212	-1/30
1	21-2	-1/2
1	21-1	0/1
1	220	3/32
1	221	-1/15
1	222	-1/48
1	22-2	-1/16
1	22-1	1/3
1	2-20	3/32
1	2-21	1/1
1	2-22	3/16
1	2-2-2	1/16
1	2-2-1	1/3
1	2-11	1/2
1	2-12	-1/6
1	2-1-2	1/6
1	2-1-1	-3/8
2	101	1/1
2	102	1/4
2	10-2	1/4
2	10-1	1/1
2	111	1/2
2	112	1/6
2	11-2	1/2
2	11-1	-1/2
2	121	1/3
2	122	1/8
2	12-2	-1/8
2	12-1	-1/1
2	1-21	-1/1
2	1-22	-1/8
2	1-2-2	1/8
2	1-2-1	1/3
2	1-11	-1/2
2	1-12	1/2
2	1-1-2	1/6
2	1-1-1	1/2
2	202	1/8
2	20-2	1/8
2	212	1/12
2	21-2	1/4
2	222	1/16
2	22-2	-1/16
2	2-22	-1/16
2	2-2-2	1/16
2	2-12	1/4
2	2-1-2	1/12
3	011	1/1
3	012	1/2
3	01-2	-1/2
3	01-1	-1/1
3	021	1/4
3	022	1/8
3	02-2	-1/8
3	02-1	-1/4
3	102	-1/2
3	10-2	1/2
3	112	-1/4
3	11-2	1/4
3	122	-1/6

i	$\underline{m}$	$\tilde{C}(\underline{m};i)$
	$|\underline{m}| = 3$	
3	12-2	1/6
3	1-22	1/2
3	1-2-2	-1/2
3	1-12	1/4
3	1-1-2	-1/4
4	001	1/1
4	002	1/8
4	012	-4/9
4	01-2	0/1
	$|\underline{m}| = 4$	
1	0001	1/1
1	0002	1/16
1	0010	-3/1
1	0011	1/8
1	0012	1/54
1	001-2	1/2
1	001-1	-1/8
1	0020	-3/16
1	0021	1/27
1	0022	1/128
1	002-2	-1/128
1	002-1	-1/1
1	0100	3/1
1	0101	1/4
1	0102	1/36
1	010-2	1/4
1	010-1	3/4
1	0110	-1/2
1	0111	1/18
1	0112	1/96
1	011-2	7/32
1	011-1	3/2
1	0120	-7/108
1	0121	1/48
1	0122	1/200
1	012-2	7/8
1	012-1	-1/4
1	01-20	-5/4
1	01-21	-5/16
1	01-22	-9/8
1	01-2-2	1/72
1	01-2-1	1/12
1	01-10	-1/2
1	01-11	-5/2
1	01-12	1/8
1	01-1-2	1/24
1	01-1-1	1/2
1	0200	3/16
1	0201	1/9
1	0202	1/64
1	020-2	3/64
1	020-1	1/1
1	0210	-5/27
1	0211	1/32
1	0212	1/150
1	021-2	1/2
1	021-1	1/8
1	0220	-1/32
1	0221	1/75
1	0222	1/288
1	022-2	3/32
1	022-1	-1/9
1	02-20	-1/32

i	$\underline{m}$	$\tilde{C}(\underline{m};i)$
	$|\underline{m}| = 4$	
1	02-21	-1/1
1	02-22	-5/32
1	02-2-2	1/32
1	02-2-1	1/3
1	02-10	1/1
1	02-11	-3/8
1	02-12	1/18
1	02-1-2	1/6
1	02-1-1	7/32
1	1001	1/2
1	1002	1/24
1	100-2	1/8
1	100-1	-3/2
1	1010	-5/4
1	1011	1/12
1	1012	1/72
1	101-2	-5/8
1	101-1	-3/4
1	1020	-1/9
1	1021	1/36
1	1022	1/160
1	102-2	-13/32
1	102-1	-1/2
1	10-20	-1/2
1	10-21	7/8
1	10-22	21/32
1	10-2-2	1/96
1	10-2-1	1/18
1	10-10	9/4
1	10-11	7/4
1	10-12	1/4
1	10-1-2	1/36
1	10-1-1	1/4
1	1101	1/6
1	1102	1/48
1	110-2	-1/4
1	110-1	0/1
1	1110	-11/36
1	1111	1/24
1	1112	1/120
1	111-2	-1/8
1	111-1	1/2
1	1120	-13/288
1	1121	1/60
1	1122	1/240
1	112-2	5/16
1	112-1	-1/6
1	11-20	21/32
1	11-21	3/4
1	11-22	-7/16
1	11-2-2	1/48
1	11-2-1	1/6
1	11-10	-3/4
1	11-11	-1/1
1	11-12	1/12
1	11-1-2	1/12
1	11-1-1	-5/8
1	1201	1/12
1	1202	1/80
1	120-2	-1/8
1	120-1	1/2
1	1210	-19/144
1	1211	1/40

i	$\underline{m}$	$\tilde{C}(\underline{m};i)$	i	$\underline{m}$	$\tilde{C}(\underline{m};i)$	i	$\underline{m}$	$\tilde{C}(\underline{m};i)$	i	$\underline{m}$	$\tilde{C}(\underline{m};i)$
	$|\underline{m}|=4$			$|\underline{m}|=4$			$|\underline{m}|=4$			$|\underline{m}|=4$	
1	1212	1/180	1	1-1-1-1	1/12	1	22-11	-5/32	2	10-12	-1/2
1	121-2	1/4	1	2001	1/3	1	22-12	1/30	2	10-1-2	1/18
1	121-1	1/18	1	2002	1/32	1	22-1-2	-1/6	2	10-1-1	1/4
1	1220	-19/800	1	200-2	-3/32	1	22-1-1	1/16	2	1101	-1/2
1	1221	1/90	1	200-1	-1/1	1	2-201	-1/1	2	1102	-1/12
1	1222	1/336	1	2011	1/16	1	2-202	-1/8	2	110-2	1/4
1	122-2	7/144	1	2012	1/90	1	2-20-2	1/32	2	110-1	-1/1
1	122-1	-1/12	1	201-2	-1/2	1	2-20-1	1/3	2	1111	-1/6
1	12-20	-11/32	1	201-1	-1/8	1	2-211	-5/16	2	1112	-1/24
1	12-21	-1/2	1	2020	-5/64	1	2-212	1/18	2	111-2	-3/8
1	12-22	-13/144	1	2021	1/45	1	2-21-2	1/6	2	111-1	-1/2
1	12-2-2	1/16	1	2022	1/192	1	2-21-1	31/96	2	1121	-1/12
1	12-2-1	-7/18	1	202-2	-3/64	1	2-220	11/64	2	1122	-1/40
1	12-10	1/4	1	202-1	-1/3	1	2-221	1/9	2	112-2	-3/8
1	12-11	-2/9	1	20-20	9/64	1	2-222	1/64	2	112-1	1/2
1	12-12	1/24	1	20-21	1/1	1	2-22-2	11/128	2	11-21	1/4
1	12-1-2	-11/72	1	20-22	7/64	1	2-22-1	1/1	2	11-22	5/8
1	12-1-1	-1/8	1	20-2-2	1/64	1	2-2-21	-1/3	2	11-2-2	1/24
1	1-201	1/8	1	20-2-1	1/9	1	2-2-22	-5/128	2	11-2-1	1/6
1	1-202	-3/8	1	20-11	3/8	1	2-2-2-2	1/192	2	11-11	3/2
1	1-20-2	1/48	1	20-12	1/6	1	2-2-2-1	1/45	2	11-12	-1/4
1	1-20-1	1/6	1	20-1-2	1/18	1	2-2-11	-11/96	2	11-1-2	1/12
1	1-210	-11/16	1	20-1-1	-1/4	1	2-2-12	-1/2	2	11-1-1	1/2
1	1-211	-7/8	1	2101	1/8	1	2-2-1-2	1/90	2	1201	-1/3
1	1-212	1/12	1	2102	1/60	1	2-2-1-1	1/16	2	1202	-1/16
1	1-21-2	1/12	1	210-2	-1/4	1	2-101	-3/4	2	120-2	-1/8
1	1-21-1	-1/1	1	210-1	1/4	1	2-102	1/12	2	120-1	-1/1
1	1-220	27/32	1	2111	1/30	1	2-10-2	1/12	2	1211	-1/8
1	1-221	1/6	1	2112	1/144	1	2-10-1	-5/8	2	1212	-1/30
1	1-222	1/48	1	211-2	1/16	1	2-111	1/6	2	121-2	-1/2
1	1-22-2	-7/16	1	211-1	5/18	1	2-112	1/48	2	121-1	0/1
1	1-22-1	1/2	1	2120	-31/900	1	2-11-2	-1/4	2	1221	-1/15
1	1-2-20	-13/288	1	2121	1/72	1	2-11-1	1/2	2	1222	-1/48
1	1-2-21	-1/6	1	2122	1/280	1	2-120	-11/36	2	122-2	-1/16
1	1-2-22	5/16	1	212-2	13/72	1	2-121	1/24	2	122-1	1/3
1	1-2-2-2	1/240	1	212-1	-1/8	1	2-122	1/120	2	12-21	1/1
1	1-2-2-1	1/60	1	21-20	1/4	1	2-12-2	1/8	2	12-22	3/16
1	1-2-11	1/2	1	21-21	1/8	1	2-12-1	3/8	2	12-2-2	1/16
1	1-2-12	-1/24	1	21-22	-19/72	1	2-1-21	7/24	2	12-2-1	1/3
1	1-2-1-2	1/120	1	21-2-2	1/24	1	2-1-22	1/8	2	12-11	1/2
1	1-2-1-1	1/24	1	21-2-1	-11/72	1	2-1-2-2	1/120	2	12-12	-1/6
1	1-101	-2/1	1	21-11	-11/18	1	2-1-2-1	1/24	2	12-1-2	1/6
1	1-102	1/8	1	21-12	1/16	1	2-1-11	1/2	2	12-1-1	-3/8
1	1-10-2	1/24	1	21-1-2	-1/18	1	2-1-12	-5/16	2	1-201	1/1
1	1-10-1	1/2	1	21-1-1	-1/2	1	2-1-1-2	1/48	2	1-202	1/8
1	1-110	11/4	1	2201	1/15	1	2-1-1-1	1/6	2	1-20-2	1/16
1	1-111	1/4	1	2202	1/96	2	1001	-1/1	2	1-211	3/8
1	1-112	1/36	1	220-2	0/1	2	1002	-1/8	2	1-212	-1/6
1	1-11-2	1/4	1	220-1	1/3	2	100-2	1/8	2	1-21-2	1/6
1	1-11-1	11/8	1	2211	1/48	2	100-1	1/1	2	1-21-1	-1/2
1	1-120	-1/2	1	2212	1/210	2	1011	-1/4	2	1-221	-1/3
1	1-121	1/18	1	221-2	1/6	2	1012	-1/18	2	1-222	-1/16
1	1-122	1/96	1	221-1	1/32	2	101-2	1/2	2	1-22-2	-3/16
1	1-12-2	47/96	1	2220	-11/576	2	101-1	1/4	2	1-22-1	-1/1
1	1-12-1	5/4	1	2221	1/105	2	1021	-1/9	2	1-2-21	-1/3
1	1-1-20	-1/9	1	2222	1/384	2	1022	-1/32	2	1-2-22	1/16
1	1-1-21	-1/2	1	222-2	1/32	2	102-2	1/32	2	1-2-2-2	1/48
1	1-1-22	-31/96	1	222-1	-1/15	2	102-1	1/1	2	1-2-2-1	1/15
1	1-1-2-2	1/160	1	22-20	-3/64	2	10-21	-1/1	2	1-2-11	0/1
1	1-1-2-1	1/36	1	22-21	-1/3	2	10-22	-1/32	2	1-2-12	1/2
1	1-1-11	-5/8	1	22-22	-1/16	2	10-2-2	1/32	2	1-2-1-2	1/30
1	1-1-12	-7/8	1	22-2-2	-5/128	2	10-2-1	1/9	2	1-2-1-1	1/8
1	1-1-1-2	1/72	1	22-2-1	-1/3	2	10-11	-1/4	2	1-101	1/1

i	$\underline{m}$	$\tilde{C}(\underline{m};i)$	i	$\underline{m}$	$\tilde{C}(\underline{m};i)$	i	$\underline{m}$	$\tilde{C}(\underline{m};i)$	i	$\underline{m}$	$\tilde{C}(\underline{m};i)$
	$|\underline{m}| = 4$			$|\underline{m}| = 4$			$|\underline{m}| = 4$			$|\underline{m}| = 4$	
2	1-102	-1/4	2	2-1-2-2	1/80	3	10-2-2	1/8	3	1-1-11	1/4
2	1-10-2	1/12	2	2-1-12	3/16	3	10-2-1	1/3	3	1-1-12	-1/4
2	1-111	-1/2	2	2-1-1-2	1/48	3	10-11	-1/2	3	1-1-1-2	-1/12
2	1-112	-1/12	3	0101	-1/1	3	10-12	1/2	3	2002	1/16
2	1-11-2	1/4	3	0102	-1/4	3	10-1-2	1/6	3	200-2	1/16
2	1-11-1	-3/2	3	010-2	-1/4	3	10-1-1	1/2	3	2012	1/24
2	1-121	-1/6	3	010-1	-1/1	3	1102	1/8	3	201-2	1/8
2	1-122	-1/24	3	0110	1/1	3	110-2	1/8	3	2022	1/32
2	1-12-2	-5/8	3	0111	-1/2	3	1111	1/4	3	202-2	-1/32
2	1-12-1	-1/4	3	0112	-1/6	3	1112	1/12	3	20-22	-1/32
2	1-1-21	-1/2	3	011-2	-1/2	3	111-2	1/4	3	20-2-2	1/32
2	1-1-22	3/8	3	011-1	1/2	3	111-1	-1/4	3	20-12	1/8
2	1-1-2-2	1/40	3	0120	1/4	3	1121	1/6	3	20-1-2	1/24
2	1-1-2-1	1/12	3	0121	-1/3	3	1122	1/16	3	2112	1/36
2	1-1-11	1/2	3	0122	-1/8	3	112-2	-1/16	3	211-2	1/12
2	1-1-12	3/8	3	012-2	1/8	3	112-1	-1/2	3	2122	1/48
2	1-1-1-2	1/24	3	012-1	1/1	3	11-21	-1/2	3	212-2	-1/48
2	1-1-1-1	1/6	3	01-20	1/4	3	11-22	-1/16	3	21-22	-1/48
2	2002	-1/16	3	01-21	1/1	3	11-2-2	1/16	3	21-2-2	1/48
2	200-2	1/16	3	01-22	1/8	3	11-2-1	1/6	3	21-12	1/12
2	2012	-1/36	3	01-2-2	-1/8	3	11-11	-1/4	3	21-1-2	1/36
2	201-2	1/4	3	01-2-1	-1/3	3	11-12	1/4	3	221-2	1/16
2	2022	-1/64	3	01-10	1/1	3	11-1-2	1/12	3	2222	1/64
2	202-2	1/64	3	01-11	1/2	3	11-1-1	1/4	3	222-2	-1/64
2	20-22	-1/64	3	01-12	-1/2	3	1202	1/12	3	22-22	-1/64
2	20-2-2	1/64	3	01-1-2	-1/6	3	120-2	1/12	3	22-2-2	1/64
2	20-12	-1/4	3	01-1-1	-1/2	3	1212	1/18	3	22-12	1/16
2	20-1-2	1/36	3	0201	-1/4	3	121-2	1/6	3	2-21-2	-1/16
2	2102	-1/24	3	0202	-1/16	3	121-1	-1/6	3	2-22-2	1/64
2	210-2	1/8	3	020-2	-1/16	3	1221	1/9	3	2-2-22	1/64
2	2112	-1/48	3	020-1	-1/4	3	1222	1/24	3	2-2-12	-1/16
2	211-2	-3/16	3	0211	-1/8	3	122-2	-1/24	3	2-11-2	1/4
2	2122	-1/80	3	0212	-1/24	3	122-1	-1/3	3	2-1-12	1/4
2	212-2	-3/16	3	021-2	-1/8	3	12-21	-1/3	4	0011	-1/1
2	21-22	5/16	3	021-1	1/8	3	12-22	-1/24	4	0012	-1/2
2	21-2-2	1/48	3	0220	1/16	3	12-2-2	1/24	4	001-2	1/2
2	21-12	-1/8	3	0221	-1/12	3	12-2-1	1/9	4	001-1	1/1
2	21-1-2	1/24	3	0222	-1/32	3	12-11	-1/6	4	0021	-1/8
2	2202	-1/32	3	022-2	1/32	3	12-12	1/6	4	0022	-1/16
2	220-2	-1/16	3	022-1	1/4	3	12-1-2	1/18	4	002-2	1/16
2	2212	-1/60	3	02-20	1/16	3	1-202	-1/4	4	002-1	1/8
2	221-2	-1/4	3	02-21	1/4	3	1-20-2	-1/4	4	0101	2/1
2	2222	-1/96	3	02-22	1/32	3	1-212	-1/6	4	0102	1/1
2	222-2	-1/32	3	02-2-2	-1/32	3	1-21-2	-1/2	4	010-2	-1/1
2	22-22	3/32	3	02-2-1	-1/12	3	1-21-1	1/2	4	010-1	-2/1
2	22-2-2	1/32	3	02-11	1/8	3	1-222	-1/8	4	0111	3/4
2	22-12	-1/12	3	02-12	-1/8	3	1-22-2	1/8	4	0112	3/8
2	22-1-2	1/12	3	02-1-2	-1/24	3	1-22-1	1/1	4	011-2	-3/8
2	2-202	1/16	3	02-1-1	-1/8	3	1-2-21	1/1	4	011-1	-3/4
2	2-212	-1/12	3	1001	1/1	3	1-2-22	1/8	4	0121	4/9
2	2-21-2	1/12	3	1002	1/4	3	1-2-2-2	-1/8	4	0122	2/9
2	2-222	-1/32	3	100-2	1/4	3	1-2-11	1/2	4	012-2	-2/9
2	2-22-2	-3/32	3	100-1	1/1	3	1-2-12	-1/2	4	012-1	-4/9
2	2-2-22	1/32	3	1011	1/2	3	1-2-1-2	-1/6	4	01-21	0/1
2	2-2-2-2	1/96	3	1012	1/6	3	1-102	-1/8	4	01-22	0/1
2	2-2-12	1/4	3	101-2	1/2	3	1-10-2	-1/8	4	01-2-2	0/1
2	2-2-1-2	1/60	3	101-1	-1/2	3	1-112	-1/12	4	01-2-1	0/1
2	2-102	-1/8	3	1021	1/3	3	1-11-2	-1/4	4	01-11	-3/4
2	2-112	-1/24	3	1022	1/8	3	1-11-1	1/4	4	01-12	-3/8
2	2-11-2	1/8	3	102-2	-1/8	3	1-122	-1/16	4	01-1-2	3/8
2	2-122	-1/48	3	102-1	-1/1	3	1-12-2	1/16	4	01-1-1	3/4
2	2-12-2	-5/16	3	10-21	-1/1	3	1-1-22	1/16	4	0201	1/4
2	2-1-22	3/16	3	10-22	-1/8	3	1-1-2-2	-1/16	4	0202	1/8

i	$\underline{m}$	$\tilde{C}(\underline{m};i)$	i	$\underline{m}$	$\tilde{C}(\underline{m};i)$
	$|\underline{m}| = 4$			$|\underline{m}| = 4$	
4	020-2	-1/8	4	1-11-2	-3/4
4	020-1	-1/4	4	1-122	1/4
4	0211	5/36	4	1-12-2	-1/4
4	0212	5/72	4	1-1-22	0/1
4	021-2	-5/72	4	1-1-2-2	0/1
4	021-1	-5/36	4	1-1-12	1/4
4	0221	3/32	4	1-1-1-2	-1/4
4	0222	3/64	4	201-2	1/24
4	022-2	-3/64	4	202-2	1/32
4	022-1	-3/32	5	0001	-1/1
4	02-21	-3/32	5	0002	-1/16
4	02-22	-3/64	5	0011	7/8
4	02-2-2	3/64	5	0012	13/27
4	02-2-1	3/32	5	001-2	-1/1
4	02-11	3/4	5	001-1	-7/8
4	02-12	3/8	5	0021	19/216
4	02-1-2	-3/8	5	0022	7/128
4	02-1-1	-3/4	5	002-2	-7/128
4	1002	-1/2	5	002-1	7/8
4	100-2	1/2	5	0102	-7/9
4	1012	-1/4	5	010-2	1/1
4	101-2	1/4	5	0112	-7/32
4	101-1	1/2	5	011-2	21/32
4	1022	-1/6	5	011-1	-5/4
4	102-2	1/6	5	0122	-23/225
4	102-1	1/3	5	012-2	-7/9
4	10-22	1/2	5	012-1	-11/36
4	10-2-2	-1/2	5	01-22	1/1
4	10-12	1/2	5	01-2-2	1/9
4	10-1-2	-1/2	5	01-12	3/4
4	1102	-1/8	5	01-1-2	-1/4
4	110-2	1/8	5	021-2	-11/36
4	1112	-1/12	5	022-2	-5/64
4	111-2	1/12			
4	1122	-1/16			
4	112-2	1/16			
4	11-22	3/16			
4	11-2-2	-3/16			
4	11-12	-1/4			
4	11-1-2	1/4			
4	1202	-1/18			
4	120-2	1/18			
4	1212	-1/24			
4	121-2	1/24			
4	1222	-1/30			
4	122-2	1/30			
4	12-22	-1/6			
4	12-2-2	1/6			
4	12-12	-1/12			
4	12-1-2	1/12			
4	1-202	-1/2			
4	1-20-2	1/2			
4	1-212	1/8			
4	1-21-2	-1/8			
4	1-222	1/2			
4	1-22-2	-1/2			
4	1-2-22	-1/6			
4	1-2-2-2	1/6			
4	1-2-12	-1/4			
4	1-2-1-2	1/4			
4	1-102	-1/8			
4	1-10-2	1/8			
4	1-112	3/4			

C. H_1 and H_2 – Momentum States

To account for a possible A-B type sublattice structure we choose the following two-triplon momentum states

$$|\sigma, \mathbf{K}, \mathbf{d}\rangle^S = \frac{1}{\sqrt{N}} \sum_{\mathbf{r}} e^{i(\mathbf{K}+\sigma\mathbf{Q})(\mathbf{r}+\mathbf{d}/2)}|\mathbf{r}, \mathbf{r}+\mathbf{d}\rangle^S \,, \qquad (C.1)$$

with $\sigma = 1 - \bar{\sigma} \in \{0, 1\}$ and $\mathbf{Q} = (\pi, \pi)$. For a motivation see section 6.2.3. The one-particle hopping amplitudes are split into a net and a deviation part according to

$$t_{\mathbf{d}}^{\pi(\mathbf{r})} = \bar{t}_{\mathbf{d}} + e^{i\mathbf{Q}\mathbf{r}}dt_{\mathbf{d}} \,, \qquad (C.2)$$

where the super-index $\pi(r) = A, B$ allows to distinguish whether the hopping started on a site of type A or type B. For the two-triplon amplitudes we use a similar splitting

$$t_{\mathbf{d};\mathbf{r}',\mathbf{d}'}^{\pi(\mathbf{r})} = \bar{t}_{\mathbf{d};\mathbf{r}',\mathbf{d}'} + e^{i\mathbf{Q}\mathbf{r}}dt_{\mathbf{d};\mathbf{r}',\mathbf{d}'} \,. \qquad (C.3)$$

In these and all the following equations one retrieves the corresponding equations for the simple lattice (without A-B structure) by setting the deviation part to zero. In this appendix we assume the model to have inversion symmetry.

C.1. H_1

We begin by calculating the action of H_1 on the states $|\sigma, \mathbf{K}, \mathbf{d}\rangle^S$. Because of inversion symmetry we have $t_{\mathbf{d}}^{\pi(\mathbf{r})} = t_{-\mathbf{d}}^{\pi(\mathbf{r})}$, hence

$$H_1|\sigma, \mathbf{K}, \mathbf{d}\rangle^S = \qquad\qquad\qquad\qquad\qquad\qquad\qquad\qquad (C.4)$$

$$\frac{1}{\sqrt{N}} \sum_{\mathbf{r}} e^{i(\mathbf{K}+\sigma\mathbf{Q})(\mathbf{r}+\mathbf{d}/2)} \sum_{\substack{\mathbf{d}' \\ \mathbf{d}'\neq\mathbf{d}}} \left[(\bar{t}_{\mathbf{d}'} + e^{i\mathbf{Q}\mathbf{r}}dt_{\mathbf{d}'})|\mathbf{r}+\mathbf{d}', \mathbf{r}+\mathbf{d}\rangle^S \right.$$

$$\left. +(\bar{t}_{\mathbf{d}'} + e^{i\mathbf{Q}(\mathbf{r}+\mathbf{d})}dt_{\mathbf{d}'})|\mathbf{r}, \mathbf{r}+\mathbf{d}-\mathbf{d}'\rangle^S \right] \,.$$

199

Note that H_1 moves only one of the two triplons. However, since we cannot know which one has been moved, we have to add the amplitudes for both of the possible processes in the first line. We first treat the part proportional to $\bar{t}_{\mathbf{d}'}$. Substituting $\mathbf{r} \to \mathbf{r} - \mathbf{d}'$ for the first of the resulting states on the right hand side yields

$$\text{Part}_1 = \frac{1}{\sqrt{N}} \sum_{\mathbf{r},\mathbf{d}'} \bar{t}_{\mathbf{d}'} \left[e^{iX} + e^{iY} \right] |\mathbf{r}, \mathbf{r} + \mathbf{d} - \mathbf{d}'\rangle^S , \quad \text{with}$$

$$X = (\mathbf{K} + \sigma\mathbf{Q})(\mathbf{r} - \mathbf{d}' + \mathbf{d}/2)$$

$$Y = (\mathbf{K} + \sigma\mathbf{Q})(\mathbf{r} + \mathbf{d}/2) . \tag{C.5}$$

We rewrite the exponents

$$X = (\mathbf{K} + \sigma\mathbf{Q})(\mathbf{r} + (\mathbf{d} - \mathbf{d}')/2) - (\mathbf{K} + \sigma\mathbf{Q})\mathbf{d}'/2$$

$$Y = (\mathbf{K} + \sigma\mathbf{Q})(\mathbf{r} + (\mathbf{d} - \mathbf{d}')/2) + (\mathbf{K} + \sigma\mathbf{Q})\mathbf{d}'/2 , \tag{C.6}$$

and obtain

$$\text{Part}_1 = 2 \sum_{\mathbf{d}'} \bar{t}_{\mathbf{d}'} \cos[(\mathbf{K} + \sigma\mathbf{Q})\mathbf{d}'/2] \frac{1}{\sqrt{N}} \sum_{\mathbf{r}} e^{i(\mathbf{K}+\sigma\mathbf{Q})(\mathbf{r}+(\mathbf{d}-\mathbf{d}')/2)} |\mathbf{r}, \mathbf{r} + \mathbf{d} - \mathbf{d}'\rangle^S$$

$$= 2 \sum_{\mathbf{d}'} \bar{t}_{\mathbf{d}'} \cos[(\mathbf{K} + \sigma\mathbf{Q})\mathbf{d}'/2] |\sigma, \mathbf{K}, \mathbf{d} - \mathbf{d}'\rangle^S . \tag{C.7}$$

The calculation is somewhat more involved for the second part proportional to $dt_{\mathbf{d}'}$. We can use Eq. (C.5) if we substitute $\bar{t}_{\mathbf{d}'}$ by $dt_{\mathbf{d}'}$. One triplon starts hopping from position $\mathbf{r}$, while the other one starts from position $\mathbf{r} + \mathbf{d}$. This gives additional phase factors

$$\text{Part}_2 = \frac{1}{\sqrt{N}} \sum_{\mathbf{r},\mathbf{d}'} dt_{\mathbf{d}'} \left[e^{iX} + e^{iY} \right] |\mathbf{r}, \mathbf{r} + \mathbf{d} - \mathbf{d}'\rangle^S , \quad \text{with}$$

$$X = (\mathbf{K} + \sigma\mathbf{Q})(\mathbf{r} + (\mathbf{d} - \mathbf{d}')/2) - (\mathbf{K} + \sigma\mathbf{Q})\mathbf{d}'/2 + \mathbf{Q}\mathbf{r} - \mathbf{Q}\mathbf{d}'$$

$$Y = (\mathbf{K} + \sigma\mathbf{Q})(\mathbf{r} + (\mathbf{d} - \mathbf{d}')/2) + (\mathbf{K} + \sigma\mathbf{Q})\mathbf{d}'/2 + \mathbf{Q}\mathbf{r} + \mathbf{Q}\mathbf{d} . \tag{C.8}$$

Making use of $\sigma = 1 - \bar{\sigma}$, $\exp(i\pi n) = \exp(-i\pi n)$ and $\exp(2i\pi n) = 1$ for integer n we can rewrite the exponents. Some calculation yields

$$X = (\mathbf{K} + \bar{\sigma}\mathbf{Q})(\mathbf{r} + (\mathbf{d} - \mathbf{d}')/2) - (\mathbf{K} + \bar{\sigma}\mathbf{Q})\mathbf{d}'/2 + (\sigma - 1/2)\mathbf{Q}\mathbf{d}$$

$$Y = (\mathbf{K} + \bar{\sigma}\mathbf{Q})(\mathbf{r} + (\mathbf{d} - \mathbf{d}')/2) + (\mathbf{K} + \bar{\sigma}\mathbf{Q})\mathbf{d}'/2 - (\sigma - 1/2)\mathbf{Q}\mathbf{d} . \tag{C.9}$$

Thus, Part$_2$ finally reads

$$\text{Part}_2 = 2\sum_{\mathbf{d}'} dt_{\mathbf{d}'} \cos[(\mathbf{K} + \bar{\sigma}\mathbf{Q})\mathbf{d}'/2 - (\sigma - 1/2)\mathbf{Q}\mathbf{d}]|\bar{\sigma}, \mathbf{K}, \mathbf{d} - \mathbf{d}'\rangle^S . \quad \text{(C.10)}$$

Adding Part$_1$ and Part$_2$ gives the full action of H_1 on the states $|\sigma, \mathbf{K}, \mathbf{d}\rangle$. As explained in the main text, we can restrict the distances to $\mathbf{d} > 0$ in $|\sigma, \mathbf{K}, \mathbf{d}\rangle$ exploiting the exchange parity of a pair of triplons: $(-1)^S$. However, since the sum over $\mathbf{d}'$ in Part$_1$ and Part$_2$ runs over positive and negative values we need to make use of Eq. (3.49), which leads to the appearance of signum functions in the final expression

$$H_1|\sigma, \mathbf{K}, \mathbf{d}\rangle^S =$$

$$2\sum_{\mathbf{d}'} \bar{t}_{\mathbf{d}'} \cos[(\mathbf{K} + \sigma\mathbf{Q})\mathbf{d}'/2][\text{sgn}(\mathbf{d} - \mathbf{d}')]^S|\sigma, \mathbf{K}, |\mathbf{d} - \mathbf{d}'|\rangle^S+ \quad \text{(C.11)}$$

$$2\sum_{\mathbf{d}'} dt_{\mathbf{d}'} \cos[(\mathbf{K} + \bar{\sigma}\mathbf{Q})\mathbf{d}'/2 - (\sigma - 1/2)\mathbf{Q}\mathbf{d}][\text{sgn}(\mathbf{d} - \mathbf{d}')]^S|\bar{\sigma}, \mathbf{K}, |\mathbf{d} - \mathbf{d}'|\rangle^S .$$

The result for the simple lattice (without A-B structure) is given by the part proportional to $\bar{t}_{\mathbf{d}'}$.

C.2. H_2

Before we calculate the action of H_2 on $|\sigma, \mathbf{K}, \mathbf{d}\rangle^S$ we derive an important symmetry relation for the two-particle amplitudes, which we will use later. We have

$$t^{\pi(r)}_{\mathbf{d};\mathbf{r}',\mathbf{d}'} = \bar{t}_{\mathbf{d};\mathbf{r}',\mathbf{d}'} + e^{i\mathbf{Q}\mathbf{r}}dt_{\mathbf{d};\mathbf{r}',\mathbf{d}'} = \langle \mathbf{r}'', \mathbf{r}'' + \mathbf{d}'|H_2|\mathbf{r}, \mathbf{r} + \mathbf{d}\rangle , \quad \text{(C.12)}$$

with $\mathbf{r}' = \mathbf{r}''-\mathbf{r}$. In contrast to the one-triplon amplitudes the two-triplon amplitudes depend on the total spin S. We drop S in the intermediate calculations for simplicity.

The thermodynamic hopping amplitude $t_{\mathbf{d};\mathbf{r}',\mathbf{d}'}$ is associated with a fixed constellation of initial and final triplon pairs. We define a configuration CON by the set of four positions given by these two pairs CON = $\{\mathbf{r}, \mathbf{r}+\mathbf{d}, \mathbf{r}'', \mathbf{r}''+\mathbf{d}'\}$. Let $\mathbf{s}$ denote the middle of this configuration $\mathbf{s} = (\max(\text{CON}) - \min(\text{CON}))/2$ (see Eq. (3.48) on page 57 for a definition of $>$ between vectors). Note that $\mathbf{s}$ may denote a point in the middle between lattice sites. Reflecting a configuration about $\mathbf{s}$ and interchanging the triplon positions in both initial and final

triplon pairs (possible minus signs due to the inflection cancel!), gives

$$\bar{t}_{\mathbf{d};\mathbf{r}',\mathbf{d}'} + e^{i\mathbf{Q}\mathbf{r}} dt_{\mathbf{d};\mathbf{r}',\mathbf{d}'} = \langle \mathbf{r}'', \mathbf{r}'' + \mathbf{d}' | H_2 | \mathbf{r}, \mathbf{r} + \mathbf{d} \rangle$$

$$\xrightarrow{\text{infl./interch.}} \langle 2\mathbf{s} - \mathbf{r}'' - \mathbf{d}', 2\mathbf{s} - \mathbf{r}'' | H_2 | 2\mathbf{s} - \mathbf{r} - \mathbf{d}, 2\mathbf{s} - \mathbf{r} \rangle$$

$$= \bar{t}_{\mathbf{d};\mathbf{d}-\mathbf{d}'-\mathbf{r}',\mathbf{d}'} + e^{i\mathbf{Q}(2\mathbf{s}-\mathbf{r}-\mathbf{d})} dt_{\mathbf{d};\mathbf{d}-\mathbf{d}'-\mathbf{r}',\mathbf{d}'} \ . \qquad \text{(C.13)}$$

With $\exp(2i\pi n) = 1$ and $\exp(i\pi n) = \exp(-i\pi n)$ for integer n we conclude

$$\bar{t}_{\mathbf{d};\mathbf{r}',\mathbf{d}'} = \bar{t}_{\mathbf{d};\mathbf{d}-\mathbf{d}'-\mathbf{r}',\mathbf{d}'}$$

$$dt_{\mathbf{d};\mathbf{r}',\mathbf{d}'} = e^{i\mathbf{Q}\mathbf{d}} dt_{\mathbf{d};\mathbf{d}-\mathbf{d}'-\mathbf{r}',\mathbf{d}'} \ . \qquad \text{(C.14)}$$

From the second equation we can conclude that $(\mathbf{d} = (d_1, d_2))$

$$dt_{\mathbf{d};(\mathbf{d}-\mathbf{d}')/2,\mathbf{d}'} = -dt_{\mathbf{d};(\mathbf{d}-\mathbf{d}')/2,\mathbf{d}'} \ , \quad \text{for } d_1 + d_2 \text{ odd} \ . \qquad \text{(C.15)}$$

We continue and calculate the action of H_2 on the momentum states

$$H_2 | \sigma, \mathbf{K}, \mathbf{d} \rangle = \qquad\qquad\qquad\qquad\qquad\qquad\qquad\qquad \text{(C.16)}$$

$$\frac{1}{\sqrt{N}} \sum_{\mathbf{r}} e^{i(\mathbf{K}+\sigma\mathbf{Q})(\mathbf{r}+\mathbf{d}/2)} \sum_{\mathbf{r}',\mathbf{d}'} \left(\bar{t}_{\mathbf{d};\mathbf{r}',\mathbf{d}'} + e^{i\mathbf{Q}\mathbf{r}} dt_{\mathbf{d};\mathbf{r}',\mathbf{d}'} \right) |\mathbf{r} + \mathbf{r}', \mathbf{r} + \mathbf{r}' + \mathbf{d}' \rangle \ .$$

We again proceed by calculating the part proportional to $\bar{t}_{\mathbf{d};\mathbf{r}',\mathbf{d}'}$ at first. Substituting $\mathbf{r} \to \mathbf{r} - \mathbf{r}'$ yields

$$\text{Part}_1 = \sum_{\mathbf{r}',\mathbf{d}'} \bar{t}_{\mathbf{d};\mathbf{r}',\mathbf{d}'} e^{-i(\mathbf{K}+\sigma\mathbf{Q})(\mathbf{r}'+(\mathbf{d}'-\mathbf{d})/2)} |\sigma, \mathbf{K}, \mathbf{d}' \rangle \ . \qquad \text{(C.17)}$$

We split the sum over $\mathbf{r}'$ in three parts

$$\sum_{\mathbf{r}'} a_{\mathbf{r}'} = a_{(\mathbf{d}-\mathbf{d}')/2} + \sum_{\mathbf{r}'>(\mathbf{d}-\mathbf{d}')/2} a_{\mathbf{r}'} + \sum_{\mathbf{r}'<(\mathbf{d}-\mathbf{d}')/2} a_{\mathbf{r}'}$$

$$= a_{(\mathbf{d}-\mathbf{d}')/2} + \sum_{\mathbf{r}'>(\mathbf{d}-\mathbf{d}')/2} a_{\mathbf{r}'} + \sum_{\mathbf{r}'>(\mathbf{d}-\mathbf{d}')/2} a_{\mathbf{d}-\mathbf{d}'-\mathbf{r}'} \qquad \text{(C.18)}$$

By introducing the shorthand $\mathbf{R}(\mathbf{r}') = \mathbf{r}' + (\mathbf{d}' - \mathbf{d})/2$ and making use of symmetry relation (C.14) we are left with

$$\langle \sigma, \mathbf{K}, \mathbf{d}' | H_2 | \sigma, \mathbf{K}, \mathbf{d} \rangle_{\text{Part}_1}$$

$$= \bar{t}_{\mathbf{d};(\mathbf{d}-\mathbf{d}')/2,\mathbf{d}'} + \sum_{\mathbf{r}'>(\mathbf{d}-\mathbf{d}')/2} \bar{t}_{\mathbf{d};\mathbf{r}',\mathbf{d}'} e^{-i(\mathbf{K}+\sigma\mathbf{Q})\mathbf{R}(\mathbf{r}')} + \bar{t}_{\mathbf{d};\mathbf{d}-\mathbf{d}'-\mathbf{r}',\mathbf{d}'} e^{i(\mathbf{K}+\sigma\mathbf{Q})\mathbf{R}(\mathbf{r}')}$$

$$= \bar{t}_{\mathbf{d};(\mathbf{d}-\mathbf{d}')/2,\mathbf{d}'} + 2 \sum_{\mathbf{r}'>(\mathbf{d}-\mathbf{d}')/2} \bar{t}_{\mathbf{d};\mathbf{r}',\mathbf{d}'} \cos[(\mathbf{K}+\sigma\mathbf{Q})\mathbf{R}(\mathbf{r}')] \ . \qquad \text{(C.19)}$$

We now turn to the second part proportional to $dt_{\mathbf{d};\mathbf{r}',\mathbf{d}'}$, which reads (recall $\bar{\sigma} = 1 - \sigma$)

$$\text{Part}_2 = \frac{1}{\sqrt{N}} \times$$

$$\times \sum_{\mathbf{r},\mathbf{r}',\mathbf{d}'} dt_{\mathbf{d};\mathbf{r}',\mathbf{d}'} e^{i(\mathbf{K}+\sigma\mathbf{Q})(\mathbf{r}-\mathbf{r}'+\mathbf{d}/2)+i\mathbf{Q}(\mathbf{r}-\mathbf{r}')-i(\mathbf{K}+\bar{\sigma}\mathbf{Q})(\mathbf{r}+\mathbf{d}'/2)+i(\mathbf{K}+\bar{\sigma}\mathbf{Q})(\mathbf{r}+\mathbf{d}'/2)} |\mathbf{r}, \mathbf{r}+\mathbf{d}'\rangle$$

$$= \sum_{\mathbf{r}',\mathbf{d}'} dt_{\mathbf{d};\mathbf{r}',\mathbf{d}'} e^{-i(\mathbf{K}+\bar{\sigma}\mathbf{Q})(\mathbf{r}'+(\mathbf{d}'-\mathbf{d})/2)+i(\sigma-1/2)\mathbf{Q}\mathbf{d}} |\bar{\sigma}, \mathbf{K}, \mathbf{d}'\rangle \ . \tag{C.20}$$

The last identity is not obvious, but we abstain from giving the rather tedious explicit calculation. As for Part_1 we split the $\mathbf{r}'$-sum. The case $\mathbf{r}' = (\mathbf{d} - \mathbf{d}')/2$ leads to

$$dt_{\mathbf{d};(\mathbf{d}-\mathbf{d}')/2,\mathbf{d}'} e^{i(\sigma-1/2)\mathbf{Q}d} = dt_{\mathbf{d};(\mathbf{d}-\mathbf{d}')/2,\mathbf{d}'} \cos(\mathbf{Q}\mathbf{d}/2) \ , \tag{C.21}$$

since $dt_{\mathbf{d};(\mathbf{d}-\mathbf{d}')/2,\mathbf{d}'} = 0$ for $d_1 + d_2$ odd as we have shown in Eq. (C.15). Using the symmetry relation (C.14) and the short hand $\mathbf{R}(\mathbf{r}')$ again we finally obtain

$$\langle \bar{\sigma}, \mathbf{K}, \mathbf{d}' | H_2 | \sigma, \mathbf{K}, \mathbf{d} \rangle_{\text{Part}_2} \tag{C.22}$$

$$= dt_{\mathbf{d};(\mathbf{d}-\mathbf{d}')/2,\mathbf{d}'} \cos(\mathbf{Q}\mathbf{d}/2)$$

$$+ \sum_{\mathbf{r}'>(\mathbf{d}-\mathbf{d}')/2} dt_{\mathbf{d};\mathbf{r}',\mathbf{d}'} e^{-i(\mathbf{K}+\bar{\sigma}\mathbf{Q})\mathbf{R}(\mathbf{r}')+i(\sigma-1/2)\mathbf{Q}\mathbf{d}} + dt_{\mathbf{d};\mathbf{d}-\mathbf{d}'-\mathbf{r}',\mathbf{d}'} e^{i(\mathbf{K}+\bar{\sigma}\mathbf{Q})\mathbf{R}(\mathbf{r}')+i(\sigma-1/2)\mathbf{Q}\mathbf{d}}$$

$$= dt_{\mathbf{d};(\mathbf{d}-\mathbf{d}')/2,\mathbf{d}'} \cos(\mathbf{Q}\mathbf{d}/2)$$

$$+ \sum_{\mathbf{r}'>(\mathbf{d}-\mathbf{d}')/2} dt_{\mathbf{d};\mathbf{r}',\mathbf{d}'} e^{-i(\mathbf{K}+\bar{\sigma}\mathbf{Q})\mathbf{R}(\mathbf{r}')+i(\sigma-1/2)\mathbf{Q}\mathbf{d}} + dt_{\mathbf{d};\mathbf{r}',\mathbf{d}'} e^{i\mathbf{Q}\mathbf{d}} e^{i(\mathbf{K}+\bar{\sigma}\mathbf{Q})\mathbf{R}(\mathbf{r}')+i(\sigma-1/2)\mathbf{Q}\mathbf{d}}$$

$$= dt_{\mathbf{d};(\mathbf{d}-\mathbf{d}')/2,\mathbf{d}'} \cos(\mathbf{Q}\mathbf{d}/2)$$

$$+ \sum_{\mathbf{r}'>(\mathbf{d}-\mathbf{d}')/2} dt_{\mathbf{d};\mathbf{r}',\mathbf{d}'} e^{-i(\mathbf{K}+\bar{\sigma}\mathbf{Q})\mathbf{R}(\mathbf{r}')+i(\sigma-1/2)\mathbf{Q}\mathbf{d}} + dt_{\mathbf{d};\mathbf{r}',\mathbf{d}'} e^{i(\mathbf{K}+\bar{\sigma}\mathbf{Q})\mathbf{R}(\mathbf{r}')-i(\sigma-1/2)\mathbf{Q}\mathbf{d}}$$

$$= dt_{\mathbf{d};(\mathbf{d}-\mathbf{d}')/2,\mathbf{d}'} \cos(\mathbf{Q}\mathbf{d}/2)$$

$$+ 2 \sum_{\mathbf{r}'>(\mathbf{d}-\mathbf{d}')/2} dt_{\mathbf{d};\mathbf{r}',\mathbf{d}'} \cos[(\mathbf{K} + \bar{\sigma}\mathbf{Q})\mathbf{R}(\mathbf{r}') - (\sigma - 1/2)\mathbf{Q}\mathbf{d}] \ . \tag{C.23}$$

In conclusion, Part_1 connects states of equal σ, while Part_2 connects states of different σ. We write down the complete result in dependence of the total spin

S

$$^S\langle\sigma,\mathbf{K},\mathbf{d}'|H_2|\sigma,\mathbf{K},\mathbf{d}\rangle^S = \bar{t}^S_{\mathbf{d};(\mathbf{d}-\mathbf{d}')/2,\mathbf{d}'} +$$

$$2\sum_{\mathbf{r}'>(\mathbf{d}-\mathbf{d}')/2}\bar{t}^S_{\mathbf{d};\mathbf{r}',\mathbf{d}'}\cos\left[(\mathbf{K}+\sigma\mathbf{Q})\left(\mathbf{r}'+(\mathbf{d}'-\mathbf{d})/2\right)\right]\ ,$$

$$^S\langle\bar{\sigma},\mathbf{K},\mathbf{d}'|H_2|\sigma,\mathbf{K},\mathbf{d}\rangle^S = dt^S_{\mathbf{d};(\mathbf{d}-\mathbf{d}')/2,\mathbf{d}'}\cos(\mathbf{Q}\mathbf{d}/2) + \tag{C.24}$$

$$2\sum_{\mathbf{r}'>(\mathbf{d}-\mathbf{d}')/2}dt^S_{\mathbf{d};\mathbf{r}',\mathbf{d}'}\cos\left[(\mathbf{K}+\bar{\sigma}\mathbf{Q})\left(\mathbf{r}'+(\mathbf{d}'-\mathbf{d})/2\right)-\mathbf{Q}\mathbf{d}(\sigma-1/2)\right]\ .$$

The sum runs over $\mathbf{r}' \in \mathbb{Z}$ only. Again, the corresponding result for the simple lattice, without A-B structure, is given by the part proportional to the net amplitudes $\bar{t}$.

D. $\mathcal{O}_{1,0}$ and $\mathcal{O}_{2,0}$ – Momentum States

For the calculations in this appendix we assume a translational invariant lattice with A-B sublattice structure. We assume inversion symmetry in addition to render real results possible.

We consider the one- and two-particle injecting parts of a locally acting effective $T = 0$ observable

$$\mathcal{O}_{1,0}(\mathbf{r})|0\rangle = \sum_{\mathbf{d}} w_{\mathbf{d}}^{\pi(\mathbf{r})}|\mathbf{r} + \mathbf{d}\rangle \tag{D.1}$$

$$\mathcal{O}_{2,0}(\mathbf{r})|0\rangle = \sum_{\mathbf{d},\mathbf{d}'} w_{\mathbf{d},\mathbf{d}'}^{\pi(\mathbf{r})}|\mathbf{r} + \mathbf{d}, \mathbf{r} + \mathbf{d}'\rangle \ , \tag{D.2}$$

where we again choose to split the amplitudes into a net part and a deviation part

$$w_{\mathbf{d}}^{\pi(\mathbf{r})} = \bar{w}_{\mathbf{d}} + e^{i\mathbf{Q}\mathbf{r}}dw_{\mathbf{d}}$$

$$w_{\mathbf{d},\mathbf{d}'}^{\pi(\mathbf{r})} = \bar{w}_{\mathbf{d},\mathbf{d}'} + e^{i\mathbf{Q}\mathbf{r}}dw_{\mathbf{d},\mathbf{d}'} \ . \tag{D.3}$$

The global observables are obtained by

$$\mathcal{O}_{\mu,0}(\sigma, \mathbf{K}) = \frac{1}{\sqrt{N}} \sum_{\mathbf{r}} e^{i(\mathbf{K}+\sigma\mathbf{Q})\mathbf{r}}\mathcal{O}_{\mu,0}(\mathbf{r}) \ , \tag{D.4}$$

with $\mu = 1, 2$. Note that $\mathbf{K}$ is the total crystal momentum within the magnetic Brillouin zone and $\sigma \in \{0, 1\}$ is an additional quantum number needed to account for the sublattice structure (for a motivation see section 6.2.3). In the one-particle case we shall rather write $\mathbf{k}$ instead of $\mathbf{K}$. We further define $\mathbf{Q} = (\pi, \pi)$. The case of a simple lattice, not showing the A-B sublattice structure, is retrieved by setting the deviation part to zero in these and the following equations.

In section D.1 we focus on $\mathcal{O}_{1,0}$. The two-triplon case is dealt with in section D.2.

D.1. $\mathcal{O}_{1,0}$

The action of $\mathcal{O}_{1,0}(\sigma, \mathbf{k})$ on the ground state splits into two parts

$$\mathcal{O}_{1,0}(\sigma, \mathbf{k})|0\rangle = \underbrace{\frac{1}{\sqrt{N}} \sum_{\mathbf{r},\mathbf{d}} e^{i(\mathbf{k}+\sigma\mathbf{Q})\mathbf{r}} \bar{w}_{\mathbf{d}}|\mathbf{r}+\mathbf{d}\rangle}_{\mathcal{A}}$$

$$+ \underbrace{\frac{1}{\sqrt{N}} \sum_{\mathbf{r},\mathbf{d}} e^{i(\mathbf{k}+\sigma\mathbf{Q})\mathbf{r}} e^{i\mathbf{Q}\mathbf{r}} dw_{\mathbf{d}}|\mathbf{r}+\mathbf{d}\rangle}_{\mathcal{B}} \ . \tag{D.5}$$

Substituting $\mathbf{r} \to \mathbf{r} - \mathbf{d}$ and re-arranging the sums readily gives a simple expression for the first part

$$\mathcal{A} = \sum_{\mathbf{d}} e^{-i(\mathbf{k}+\sigma\mathbf{Q})\mathbf{d}} \bar{w}_{\mathbf{d}} \frac{1}{\sqrt{N}} \sum_{\mathbf{r}} e^{i(\mathbf{k}+\sigma\mathbf{Q})\mathbf{r}} |\mathbf{r}\rangle$$

$$= \sum_{\mathbf{d}} e^{-i(\mathbf{k}+\sigma\mathbf{Q})\mathbf{d}} \bar{w}_{\mathbf{d}} |\sigma, \mathbf{k}\rangle \ . \tag{D.6}$$

For the definition of $|\sigma, \mathbf{k}\rangle$ ($|\mathbf{k}\rangle$) see Eq. (6.17) (Eq. (3.40)). With $\bar{\sigma} = 1 - \sigma$ and by exploiting $\exp(i\sigma\mathbf{Q}\mathbf{r}) = \exp(-i\sigma\mathbf{Q}\mathbf{r})$ we find a similar expression for the second part

$$\mathcal{B} = \sum_{\mathbf{d}} e^{-i(\mathbf{k}+(\sigma+1)\mathbf{Q})\mathbf{d}} dw_{\mathbf{d}} |\bar{\sigma}, \mathbf{k}\rangle \ . \tag{D.7}$$

We finally end up with

$$\mathcal{O}_{1,0}(\sigma, \mathbf{k})|0\rangle = \sum_{\mathbf{d}} e^{-i(\mathbf{k}+\sigma\mathbf{Q})\mathbf{d}} \left[\bar{w}_{\mathbf{d}}|\sigma, \mathbf{k}\rangle + e^{-i\mathbf{Q}\mathbf{d}} dw_{\mathbf{d}}|\bar{\sigma}, \mathbf{k}\rangle \right] \ . \tag{D.8}$$

Projecting on the resulting momentum states yields

$$\langle\sigma, \mathbf{k}|\mathcal{O}_{1,0}(\sigma, \mathbf{k})|0\rangle = \sum_{\mathbf{d}} \bar{w}_{\mathbf{d}} e^{-i(\mathbf{k}+\sigma\mathbf{Q})\mathbf{d}}$$

$$\langle\bar{\sigma}, \mathbf{k}|\mathcal{O}_{1,0}(\sigma, \mathbf{k})|0\rangle = \sum_{\mathbf{d}} dw_{\mathbf{d}} e^{-i(\mathbf{k}+\sigma\mathbf{Q})\mathbf{d}-i\mathbf{Q}\mathbf{d}} \ . \tag{D.9}$$

Using inversion symmetry about the point of injection $\mathbf{r}$ shows, that $w_\mathbf{d}^{\pi(\mathbf{r})} = w_{-\mathbf{d}}^{\pi(\mathbf{r})}$ and thus

$$\langle \sigma, \mathbf{k} | \mathcal{O}_{1,0}(\sigma, \mathbf{k}) | 0 \rangle = \sum_\mathbf{d} \bar{w}_\mathbf{d} \cos[(\mathbf{k} + \sigma\mathbf{Q})\mathbf{d}]$$

$$\langle \bar{\sigma}, \mathbf{k} | \mathcal{O}_{1,0}(\sigma, \mathbf{k}) | 0 \rangle = \sum_\mathbf{d} dw_\mathbf{d} \cos[(\mathbf{k} + \sigma\mathbf{Q})\mathbf{d} + \mathbf{Q}\mathbf{d}] . \qquad \text{(D.10)}$$

We might also restrict to $\mathbf{d} > 0$ if desired. The case of the simple translational invariant lattice is given by the parts proportional to the net amplitudes $\bar{w}$.

D.2. $\mathcal{O}_{2,0}$

The action of $\mathcal{O}_{2,0}(\sigma, \mathbf{K})$ on the ground state is also split into two parts

$$\mathcal{O}_{2,0}(\sigma, \mathbf{K}) | 0 \rangle = \underbrace{\frac{1}{\sqrt{N}} \sum_\mathbf{r} e^{i(\mathbf{K}+\sigma\mathbf{Q})\mathbf{r}} \sum_{\mathbf{r}',\mathbf{d}} \bar{w}_{\mathbf{r}',\mathbf{r}'+\mathbf{d}} | \mathbf{r} + \mathbf{r}', \mathbf{r} + \mathbf{r}' + \mathbf{d} \rangle}_{\mathcal{A}'}$$

$$+ \underbrace{\frac{1}{\sqrt{N}} \sum_\mathbf{r} e^{i(\mathbf{K}+\sigma\mathbf{Q})\mathbf{r}} \sum_{\mathbf{r}',\mathbf{d}} dw_{\mathbf{r}',\mathbf{r}'+\mathbf{d}} e^{i\mathbf{Q}\mathbf{r}} | \mathbf{r} + \mathbf{r}', \mathbf{r} + \mathbf{r}' + \mathbf{d} \rangle}_{\mathcal{B}'} .$$

$$\text{(D.11)}$$

Substituting $\mathbf{r} \to \mathbf{r} - \mathbf{r}'$ yields

$$\mathcal{A}' = \sum_{\mathbf{r}',\mathbf{d}} \bar{w}_{\mathbf{r}',\mathbf{r}'+\mathbf{d}} e^{-i(\mathbf{K}+\sigma\mathbf{Q})\mathbf{r}'} \frac{1}{\sqrt{N}} \sum_\mathbf{r} e^{i(\mathbf{K}+\sigma\mathbf{Q})\mathbf{r}} | \mathbf{r}, \mathbf{r} + \mathbf{d} \rangle$$

$$= \sum_{\mathbf{r}',\mathbf{d}} \bar{w}_{\mathbf{r}',\mathbf{r}'+\mathbf{d}} e^{-i(\mathbf{K}+\sigma\mathbf{Q})\mathbf{r}'} e^{-i(\mathbf{K}+\sigma\mathbf{Q})\mathbf{d}/2} \underbrace{\frac{1}{\sqrt{N}} \sum_\mathbf{r} e^{i(\mathbf{K}+\sigma\mathbf{Q})\mathbf{r}} e^{i(\mathbf{K}+\sigma\mathbf{Q})\mathbf{d}/2} | \mathbf{r}, \mathbf{r} + \mathbf{d} \rangle}_{|\sigma,\mathbf{K},\mathbf{d}\rangle}$$

$$= \sum_{\mathbf{r}',\mathbf{d}} \bar{w}_{\mathbf{r}',\mathbf{r}'+\mathbf{d}} e^{-i(\mathbf{K}+\sigma\mathbf{Q})(\mathbf{r}'+\mathbf{d}/2)} |\sigma, \mathbf{K}, \mathbf{d} \rangle . \qquad \text{(D.12)}$$

The definition of $|\sigma, \mathbf{K}, \mathbf{d}\rangle$ ($|\mathbf{K}, \mathbf{d}\rangle$) can be found in Eq. (6.25) (Eq. (3.47)). If we apply the same operations that lead to the second line of the last equation

to part $\mathcal{B}'$ we obtain

$$\mathcal{B}' = \sum_{\mathbf{r}',\mathbf{d}} dw_{\mathbf{r}',\mathbf{r}'+\mathbf{d}} e^{-i(\mathbf{K}+\sigma\mathbf{Q})(\mathbf{r}'+\mathbf{d}/2)-i\mathbf{Q}\mathbf{r}'} \underbrace{\frac{1}{\sqrt{N}} \sum_{\mathbf{r}} e^{i(\mathbf{K}+\sigma\mathbf{Q})(\mathbf{r}+\mathbf{d}/2)+i\mathbf{Q}\mathbf{r}} |\mathbf{r},\mathbf{r}+\mathbf{d}\rangle}_{Y} .$$
(D.13)

Let us take a closer look at the exponent in Y. If we once more recall $\exp(i\sigma\mathbf{Q}\mathbf{r}) = \exp(-i\sigma\mathbf{Q}\mathbf{r})$ and $\bar{\sigma} = 1 - \sigma$ we can expand the exponent

$$i\mathbf{K}(\mathbf{r}+\mathbf{d}/2) \overset{!}{-} i\sigma\mathbf{Q}\mathbf{r} + i\mathbf{Q}\mathbf{r} + i\sigma\mathbf{Q}\mathbf{d}/2$$

$$= i\mathbf{K}(\mathbf{r}+\mathbf{d}/2) + i(1-\sigma)\mathbf{Q}\mathbf{r} + i(1-\sigma)\mathbf{Q}\mathbf{d}/2 + i(\sigma-1/2)\mathbf{Q}\mathbf{d}$$

$$= i(\mathbf{K}+\bar{\sigma}\mathbf{Q})(\mathbf{r}+\mathbf{d}/2) + i(\sigma-1/2)\mathbf{Q}\mathbf{d} .$$
(D.14)

In other words,

$$Y = e^{i(\sigma-1/2)\mathbf{Q}\mathbf{d}} |\bar{\sigma}, \mathbf{K}, \mathbf{d}\rangle ,$$
(D.15)

so that we end up with

$$\mathcal{B}' = \sum_{\mathbf{r}',\mathbf{d}} dw_{\mathbf{r}',\mathbf{r}'+\mathbf{d}} e^{-i(\mathbf{K}+\sigma\mathbf{Q})(\mathbf{r}'+\mathbf{d}/2)} e^{i\mathbf{Q}((\sigma-1/2)\mathbf{d}-\mathbf{r}')} |\bar{\sigma}, \mathbf{K}, \mathbf{d}\rangle .$$
(D.16)

We may summarise our findings by projecting onto the final states

$$\langle \sigma, \mathbf{K}, \mathbf{d} | \mathcal{O}_{2,0}(\sigma, \mathbf{K}) | 0 \rangle = \sum_{\mathbf{r}'} \bar{w}_{\mathbf{r}',\mathbf{r}'+\mathbf{d}} e^{-i(\mathbf{K}+\sigma\mathbf{Q})(\mathbf{r}'+\mathbf{d}/2)}$$
(D.17)

$$\langle \bar{\sigma}, \mathbf{K}, \mathbf{d} | \mathcal{O}_{2,0}(\sigma, \mathbf{K}) | 0 \rangle = \sum_{\mathbf{r}'} dw_{\mathbf{r}',\mathbf{r}'+\mathbf{d}} e^{-i(\mathbf{K}+\sigma\mathbf{Q})(\mathbf{r}'+\mathbf{d}/2)+i\mathbf{Q}((\sigma-1/2)\mathbf{d}-\mathbf{r}')}$$
(D.18)

We finally want to use inversion symmetry about the point of particle injection $\mathbf{r}$ to derive real results. The symmetry yields

$$w^{\pi(\mathbf{r})}_{\mathbf{r}',\mathbf{r}'+\mathbf{d}} = w^{\pi(\mathbf{r})}_{-\mathbf{r}'-\mathbf{d},-\mathbf{r}'}(-1)^S ,$$
(D.19)

where S is the total spin of the two-triplon states under study. Note that the triplons need to be interchanged after inversion, which leads to an additional minus sign for odd total spin (see also Eq. (6.32) in section 6.3.1). For the right hand side of Eq. (D.17) we thus find

$$\sum_{\mathbf{r}'} \bar{w}_{\mathbf{r}',\mathbf{r}'+\mathbf{d}} e^{-i(\mathbf{K}+\sigma\mathbf{Q})(\mathbf{r}'+\mathbf{d}/2)} , \quad \mathbf{r}' \to -\mathbf{r}'-\mathbf{d}$$

$$= \sum_{\mathbf{r}'} \bar{w}_{-\mathbf{r}'-\mathbf{d},-\mathbf{r}'} e^{i(\mathbf{K}+\sigma\mathbf{Q})(\mathbf{r}'+\mathbf{d}/2)}$$

$$= \sum_{\mathbf{r}'} \bar{w}_{\mathbf{r}',\mathbf{r}'+\mathbf{d}}(-1)^S e^{i(\mathbf{K}+\sigma\mathbf{Q})(\mathbf{r}'+\mathbf{d}/2)} .$$
(D.20)

Similarly for the right hand side of Eq. (D.18)

$$\sum_{\mathbf{r}'} dw_{\mathbf{r}',\mathbf{r}'+\mathbf{d}} e^{-i(\mathbf{K}+\sigma\mathbf{Q})(\mathbf{r}'+\mathbf{d}/2)+i\mathbf{Q}((\sigma-1/2)\mathbf{d}-\mathbf{r}')} \ , \quad \mathbf{r}' \to -\mathbf{r}' - \mathbf{d}$$

$$= \sum_{\mathbf{r}'} dw_{-\mathbf{r}'-\mathbf{d},-\mathbf{r}'} e^{i(\mathbf{K}+\sigma\mathbf{Q})(\mathbf{r}'+\mathbf{d}/2)+i\mathbf{Q}((\sigma-1/2)\mathbf{d}+\mathbf{r}'+\mathbf{d})} \tag{D.21}$$

$$= \sum_{\mathbf{r}'} dw_{\mathbf{r}',\mathbf{r}'+\mathbf{d}}(-1)^S e^{i(\mathbf{K}+\sigma\mathbf{Q})(\mathbf{r}'+\mathbf{d}/2)-i\mathbf{Q}((\sigma-1/2)\mathbf{d}-\mathbf{r}')} \tag{D.22}$$

The last identity can be understood by taking a closer look at the the second part of the exponent in Eq. (D.21)

$$i\mathbf{Q}[(\sigma - 1/2)\mathbf{d} + \mathbf{r}' + \mathbf{d}] \tag{D.23}$$

$$\overset{!}{=} i\mathbf{Q}[-\sigma\mathbf{d} + \mathbf{d}/2 + \mathbf{r}']$$

$$= -i\mathbf{Q}[(\sigma - 1/2)\mathbf{d} - \mathbf{r}'] \ .$$

Thus, for even total spin S we finally obtain

$$\langle\sigma, \mathbf{K}, \mathbf{d}|\mathcal{O}_{2,0}(\sigma, \mathbf{K})|0\rangle = \sum_{\mathbf{r}'} \bar{w}_{\mathbf{r}',\mathbf{r}'+\mathbf{d}} \cos[(\mathbf{K} + \sigma\mathbf{Q})(\mathbf{r}' + \mathbf{d}/2)]$$

$$\langle\bar{\sigma}, \mathbf{K}, \mathbf{d}|\mathcal{O}_{2,0}(\sigma, \mathbf{K})|0\rangle =$$

$$\sum_{\mathbf{r}'} dw_{\mathbf{r}',\mathbf{r}'+\mathbf{d}} \cos[(\mathbf{K} + \sigma\mathbf{Q})(\mathbf{r}' + \mathbf{d}/2) - \mathbf{Q}((\sigma - 1/2)\mathbf{d} - \mathbf{r}')] \ . \tag{D.24}$$

The cosine-function has to be replaced by the sine-function in the case of odd S. Here an additional global imaginary unit i appears, which one can always get rid of by suitably re-defining the momentum states. The corresponding result for the simple translational invariant lattice is given by the parts proportional to the net amplitudes $\bar{w}$.

E. One-Triplon Hopping Amplitudes

In this appendix we prove some properties of the one-triplon hopping amplitudes for the Shastry-Sutherland model. We begin by showing that the deviation part $dt_{\mathbf{d}}$ of $t_{\mathbf{d}}^{\pi(\mathbf{r})} = \bar{t}_{\mathbf{d}} + dt_{\mathbf{d}}$ with $\mathbf{d} = (d_1, d_2)$ vanishes for $d_1 = d_2$. Introducing the shorthand $\mathbf{d}$ odd (even), iff $(d_1 + d_2)$ odd (even), (the same for $\mathbf{r} = (r_1, r_2)$) we further show that $dt_{\mathbf{d}}$ vanishes for $\mathbf{d}$ odd.

1) At first we show that $dt_{\mathbf{d}}=0$, iff $d_1 = d_2$.
With Eq. (6.12) (the σ_v symmetry) we have

$$t_{\mathbf{d}}^{\pi(\mathbf{r})} = t_{d_2,d_1}^{\pi(\mathbf{r}-(0,1))} \ . \tag{E.1}$$

Splitting both sides according to Eq. (6.6) we get

$$\bar{t}_{\mathbf{d}} + e^{iQ\mathbf{r}}dt_{\mathbf{d}} = \bar{t}_{d_2,d_1} + e^{iQ(\mathbf{r}-(0,1))}dt_{d_2,d_1} \ , \tag{E.2}$$

leading to

$$\bar{t}_{\mathbf{d}} + dt_{\mathbf{d}} = \bar{t}_{d_2,d_1} - dt_{d_2,d_1} \ , \quad \text{for } \mathbf{r} \text{ even and} \tag{E.3}$$

$$\bar{t}_{\mathbf{d}} - dt_{\mathbf{d}} = \bar{t}_{d_2,d_1} + dt_{d_2,d_1} \ , \quad \text{for } \mathbf{r} \text{ odd.} \tag{E.4}$$

Taking the difference of both equations yields

$$dt_{d_1,d_2} = -dt_{d_2,d_1} \ , \tag{E.5}$$

which proves $dt_{\mathbf{d}}=0$, iff $d_1 = d_2$. In particular $dt_{\mathbf{0}} = 0$.

2) We now show that $dt_{\mathbf{d}} = 0$, iff $\mathbf{d}$ is odd.

According to Eq. (6.5) we have

$$
\begin{aligned}
t_{\mathbf{d}}^{\pi(\mathbf{r})} &= \langle \mathbf{r} + \mathbf{d} | H_{\text{eff}} | \mathbf{r} \rangle \\
&= \langle \mathbf{r} | H_{\text{eff}} | \mathbf{r} + \mathbf{d} \rangle = t_{-\mathbf{d}}^{\pi(\mathbf{r}+\mathbf{d})} \\
&= t_{\mathbf{d}}^{\pi(\mathbf{r}+\mathbf{d})}
\end{aligned}
\tag{E.6}
$$

since H_{eff} has only real matrix elements in this basis (cf. Eq. (3.18)) and inversion symmetry holds. The last equality follows from Eq. (6.10). Splitting both sides according to Eq. (6.6) yields

$$
\begin{aligned}
\bar{t}_{\mathbf{d}} + e^{iQ\mathbf{r}} dt_{\mathbf{d}} &= \bar{t}_{\mathbf{d}} + e^{iQ\mathbf{r}} e^{iQ\mathbf{d}} dt_{\mathbf{d}} \\
\Rightarrow dt_{\mathbf{d}} &= e^{iQ\mathbf{d}} dt_{\mathbf{d}} \\
\Rightarrow dt_{\mathbf{d}} &= 0 \quad \text{for } \mathbf{d} \text{ odd.}
\end{aligned}
\tag{E.7}
$$

This proves the assertion.

F. Degeneracy of ω

Here we will show that the one-triplon dispersion (6.21) of the Shastry-Sutherland model is two-fold degenerate at particular points (lines) of the magnetic Brillouin zone (MBZ). We will do so by showing that the square root

$$\sqrt{(a_0 - a_1)^2 + 4b^2} \tag{F.1}$$

in Eq. (6.21) vanishes. We will use the shorthand $\mathbf{r}$ odd (even), iff $(r_1 + r_2)$ odd (even).

F.1. $\mathbf{k} = 0$

F.1.1. $b \overset{!}{=} 0$

For $\mathbf{k} = 0$ Eq. (6.20) gives

$$\frac{b}{2} = \sum_{\substack{\mathbf{r} > 0 \\ \mathbf{r}\ \text{even}}} dt_{\mathbf{r}} = \sum_{\substack{r_1 = 0 \\ r_2 > 0 \\ \mathbf{r}\ \text{even}}} dt_{\mathbf{r}} + \sum_{\substack{r_1 > 0 \\ r_2 = 0 \\ \mathbf{r}\ \text{even}}} dt_{\mathbf{r}} + \sum_{\substack{r_1 > 0 \\ r_2 > 0 \\ \mathbf{r}\ \text{even}}} dt_{\mathbf{r}} + \sum_{\substack{r_1 > 0 \\ r_2 < 0 \\ \mathbf{r}\ \text{even}}} dt_{\mathbf{r}}$$

$$= I_1 + I_2 + I_3 + I_4 \ . \tag{F.2}$$

We rewrite the first and the third sum on the right hand side of Eq. (F.2)

$$I_1 = \sum_{\substack{r_1 > 0 \\ r_2 = 0 \\ \mathbf{r}\ \text{even}}} dt_{-r_2, r_1} \ \text{and}\ I_3 = \sum_{\substack{r_1 > 0 \\ r_2 < 0 \\ \mathbf{r}\ \text{even}}} dt_{-r_2, r1} \ . \tag{F.3}$$

From Eq. (6.13) (the R symmetry) we deduce

$$dt_{r_1, r_2} = -dt_{-r_2, r_1} \ ,$$

and see that $I_1 = -I_2$ and $I_3 = -I_4$. Hence we find $b = 0$.

F.1.2. $(a_0 - a_1) \overset{!}{=} 0$

For $\mathbf{k} = 0$ we have (cf. Eq. (6.19))

$$\frac{a_0 - a_1}{2} = \sum_{\mathbf{r} > 0} \bar{t}_{\mathbf{r}} \left[1 - \cos(\pi(r_1 + r_2))\right] = 2 \sum_{\substack{\mathbf{r} > 0 \\ \mathbf{r} \text{ odd}}} \bar{t}_{\mathbf{r}} \ , \tag{F.4}$$

and by recalling that $dt_{\mathbf{r}} = 0$ for $\mathbf{r}$ odd, Eq. (6.13) yields

$$\bar{t}_{r_1, r_2} = -\bar{t}_{-r_2, r_1} \ , \tag{F.5}$$

so that we can use the same splitting as in Eq. (F.2). Thus the energy-degeneracy at $\mathbf{k} = 0$ is due to the rotational symmetry R.

F.2. $k_1 + k_2 = \pi$

F.2.1. $b \overset{!}{=} 0$

Making use of $dt_{\mathbf{r}} = dt_{-\mathbf{r}}$, which follows from Eq. (6.10), we have for $k_2 = \pi - k_1$

$$\begin{aligned}
\frac{b}{4} &= \sum_{\substack{\mathbf{r} \\ \mathbf{r} \text{ even}}} dt_{\mathbf{r}} \cos(k_1(r_1 - r_2) + \pi r_2) \\
&= \sum_{\substack{r_1, r_2 \\ \mathbf{r} \text{ even}}} dt_{r_2, r_1} \cos(k_1(r_2 - r_1)) \cos(\pi r_1) \ .
\end{aligned} \tag{F.6}$$

In the last step we choose to re-arrange the sum and observe that if $\mathbf{r}$ is even we have r_1 and r_2 both odd or both even. In both cases the identity

$$\cos(\pi r_1) = \cos(\pi r_2) \tag{F.7}$$

holds. Inserting relation (E.5) in the last row of Eq. (F.6) we end up with

$$\frac{b}{4} = -\sum_{\substack{\mathbf{r} \\ \mathbf{r} \text{ even}}} dt_{\mathbf{r}} \cos(k_1(r_1 - r_2)) \cos(\pi r_2) \ , \tag{F.8}$$

resulting in $b = -b$ and thus $b = 0$.

F.2.2. $(a_0 - a_1) \overset{!}{=} 0$

In analogy to section F.1.2 we have here

$$
\begin{aligned}
\frac{a_0 - a_1}{4} &= \sum_{\mathbf{r}} \bar{t}_{\mathbf{r}} \left[\cos(\mathbf{kr}) - \cos(\mathbf{kr} + \pi(r_1 + r_2)) \right] \\
&= 2 \sum_{\mathbf{r} \text{ odd}} \bar{t}_{\mathbf{r}} \cos(k_1(r_1 - r_2) + \pi r_2) \\
&= 2 \sum_{\mathbf{r} \text{ odd}} \bar{t}_{r_2,r_1} \cos(k_1(r_2 - r_1)) \cos(\pi r_1) \\
&= -2 \sum_{\mathbf{r} \text{ odd}} \bar{t}_{r_1,r_2} \cos(k_1(r_1 - r_2)) \cos(\pi r_2) , \quad\quad (\text{F.9})
\end{aligned}
$$

where the last but one equality follows from Eq. (6.12) (the σ_v symmetry), i.e $\bar{t}_{r_1,r_2} = \bar{t}_{r_2,r_1}$, and from the fact that if $\mathbf{r}$ is odd we have that r_1 odd and r_2 even or r_1 even and r_2 odd. From that we see $\cos(\pi r_1) = -\cos(\pi r_2)$.
The degeneracy at the remaining three borders of the magnetic Brillouin zone can be shown analogously. It is interesting to note that the calculations necessarily involved glide line operations. The degeneracies can thus not be explained by considering point group symmetries only.

G. Symmetry Relation for $|\sigma, \mathbf{K}, \mathbf{d}\rangle^S$

In this appendix we show that the combined effect of the symmetries σ_u and I on the states

$$|\sigma, \mathbf{K}, \mathbf{d}\rangle^S = \frac{1}{\sqrt{N}} \sum_{\mathbf{r}=(r_1, r_2)} \left[e^{i(\mathbf{K}+\sigma\mathbf{Q})(\mathbf{r}+\mathbf{d}/2)} |\mathbf{r}, \mathbf{r}+\mathbf{d}\rangle^S \right] \tag{G.1}$$

at the boundary of the MBZ, $K_2 - K_1 = \pi$, is captured by

$$\sigma_u I |\sigma, \mathbf{K}, \mathbf{d}\rangle^S = e^{iK_1 + i\pi(\sigma + \bar{\sigma}d_1 - \sigma d_2 + SD)} |\bar{\sigma}, \mathbf{K}, -(d_2, d_1)\rangle^S$$

$$D = 1, \text{ iff } (d_2, d_1) > 0 . \tag{G.2}$$

We begin by observing that (see Eqs. (6.32) and (6.33))

$$\sigma_u I |\mathbf{r}, \mathbf{r} + \mathbf{d}\rangle^S = \sigma_u| - \mathbf{r} - \mathbf{d}, -\mathbf{r}\rangle^S \cdot (-1)^S$$

$$= |(r_2 + d_2, r_1 + d_1 - 1), (r_2, r_1 - 1)\rangle^S \cdot (-1)^{S(1+\tilde{D})=SD} , \tag{G.3}$$

with $\tilde{D} = 1$, iff $-(d_2, d_1) > 0$, or equivalently $D = 1$, iff $(d_2, d_1) > 0$. We thus have

$$\sigma_u I |\sigma, \mathbf{K}, \mathbf{d}\rangle^S = (-1)^{SD} \sum_{r_1, r_2} \left[e^{i(\mathbf{K}+\sigma\mathbf{Q})(\mathbf{r}+\mathbf{d}/2)} \times \right.$$

$$\left. \times |(r_2 + d_2, r_1 + d_1 - 1), (r_2, r_1 - 1)\rangle^S \right] . \tag{G.4}$$

We can write $(-1)^{SD}$ as $\exp(i\pi SD)$. Further progress is made by substituting $r_1 \to r_2 - d_1 + 1$ and $r_2 \to r_1 - d_2$. This yields

$$\sigma_u I |\sigma, \mathbf{K}, \mathbf{d}\rangle^S = e^{i\pi SD} \sum_{r_1, r_2} \left[e^{i(\mathbf{K}+\sigma\mathbf{Q})(r_2 - d1/2 + 1, r_1 - d_2/2)} |\mathbf{r}, \mathbf{r} - (d_2, d_1)\rangle^S \right] . \tag{G.5}$$

Let us focus on the exponent E of the exponential function under the sum. With $\bar{\sigma} = 1 - \sigma$ and $Q = (\pi, \pi)$ we can write

$$E = \underbrace{i(\mathbf{K} + \bar{\sigma}\mathbf{Q})(\mathbf{r} - (d_2, d_1)/2)}_{E'}$$

$$- i(\mathbf{K} + \bar{\sigma}\mathbf{Q})(\mathbf{r} - (d_2, d_1)/2) + i(\mathbf{K} + \sigma\mathbf{Q})(r_2 - d_1/2 + 1, r_1 - d_2/2)$$

$$= E' + i\mathbf{K}(r_2 - r_1 + d_2/2 - d_1/2 + 1, r_1 - r_2 + d_1/2 - d_2/2)$$

$$- i\bar{\sigma}\pi(r_1 + r_2 - d_1/2 - d_2/2) + i\sigma\pi(r_2 + r_1 - d_1/2 - d_2/2 + 1)$$

$$= E' + i\mathbf{K}(r_2 - r_1 + d_2/2 - d_1/2 + 1, r_1 - r_2 + d_1/2 - d_2/2)$$

$$- i\pi(r_1 + r_2 - d_1/2 - d_2/2) + i\sigma\pi(2r_1 + 2r_2 - d_1 - d_2 + 1) \qquad \text{(G.6)}$$

With $K_2 = \pi + K_1$ and $\exp(2i\sigma\pi n) = 1$ for integer n the expression simplifies to

$$E = E' + iK_1 + i\pi(\sigma + \bar{\sigma}d_1 - \sigma d_2) , \qquad \text{(G.7)}$$

which proves the assertion.

H. Ground State Energy

As in the main text $|0\rangle$ denotes the particle vacuum, which is the ground state of $H(x = 0) = U$. In this appendix we show that under certain conditions $|0\rangle$ is also the ground state of $H(x > 0)$. Then $E_0(x) = E(x; \ell = \infty) = \langle 0|H_{\text{eff}}(x)|0\rangle$ is the ground state energy.

To clarify this on general grounds we write down the flow equation (3.1) for the matrix elements of H, Q and η in the eigen-basis $\{|n\rangle\}$ of the particle counting operator Q. Our choice for η is given by Eq. (3.5). We first observe that $|0\rangle$ is a single, unique state, so that $E(x; \ell) = H_{00} = \langle 0|H|0\rangle$ is a number. A sketch of the situation for $N = 1$ is given in Fig. 3.1 on page 47.

For our purposes it suffices to survey the flow of the first column of matrix elements in H

$$\frac{\partial H_{i0}}{\partial \ell} = -\text{sgn}(q_i - q_0)(H_{ii}H_{i0} - H_{i0}E)$$

$$+ \sum_{k \neq i,0} (\text{sgn}(q_i - q_k) - \text{sgn}(q_0 - q_k))H_{ik}H_{k0} . \tag{H.1}$$

Note that in the chosen basis H_{nm} can be a sub-matrix of H containing more than one matrix element. For large but finite ℓ we expect the H_{nm} connecting states with different numbers of quasi-particles $(n \neq m)$ to be very small. Hence we can neglect the sum in Eq. (H.1) whose addends are squares in these entities. We end up with

$$\frac{\partial H_{i0}}{\partial \ell} = (E - H_{ii})H_{i0} , \text{ for } \ell \gg 1 . \tag{H.2}$$

Since we know that H_{i0} must vanish for $\ell \to \infty$ for all $i > 0$ we find that

$$(E - H_{ii}) \leq 0 , \text{ for } \ell \to \infty \tag{H.3}$$

for all $i > 0$. Hence $E_0(x) = E(x; \ell = \infty)$ is the ground state energy. For this argument to work we need blocks of low quasi-particle number like H_{11} to be connected to the ground state. An unconnected block (like H_{22} in the

$N = 1$ example in Fig. 3.1) can have arbitrarily low energies. The argument of Eqs. (H.2) and (H.3) becomes meaningless, because the connecting block H_{20} is zero.

For vanishing perturbation parameter x it is clear that E is the ground state. On physical grounds we expect a finite x to modify the energy levels in a smooth and quantitative way, not to generate qualitative, mercurial changes. In this perspective Eq. (H.3) protects E_0 against energy levels in blocks of low quasi-particle numbers connected to the ground state. For larger x higher blocks, not connected to the ground state, may produce energy levels dropping below E_0. This scenario corresponds to a phase transition and the perturbative approach breaks down. Yet the approach can be used to find an upper estimate x_c to which the phase we have started in extends.

I. Two-Triplon Energies

In this appendix we compile some results for the two-triplon energies of the Shastry-Sutherland model.

I.1. Bound State Energies up to 14$^{\text{th}}$ Order

We begin by giving the 14$^{\text{th}}$ order results for the energies of the linearly bound states at total momentum $\mathbf{K} = (0,0)$ and $\mathbf{K} = (0,\pi)$ for $S = 0$ and $S = 1$ as depicted in Figs. 6.15 and 6.15 respectively. The symmetries of the corresponding states are given as indices.

I.1.1. $S = 0$, $\mathbf{K} = (0,0)$

$$\omega_{\Gamma_4}(x) = 2 - x - 2\,x^2 - x^3 + \frac{3}{8}\,x^4 + \frac{23}{16}\,x^5 - \frac{37}{64}\,x^6 - \frac{3593}{768}\,x^7 - \frac{12109}{4608}\,x^8$$

$$+ \frac{62261}{5184}\,x^9 + \frac{1392949559}{79626240}\,x^{10} - \frac{31969538107}{1194393600}\,x^{11} - \frac{31775088956269}{382205952000}\,x^{12}$$

$$+ \frac{637813109001179}{22932357120000}\,x^{13} + \frac{20605943642943311131}{6421059993600000}\,x^{14} \,, \tag{I.1}$$

$$\omega_{\Gamma_3}(x) = 2 - x - 2\,x^2 - x^3 + \frac{7}{8}\,x^4 + \frac{43}{16}\,x^5 - \frac{25}{64}\,x^6 - \frac{2435}{256}\,x^7 - \frac{12659}{1536}\,x^8$$

$$+ \frac{98741}{3456}\,x^9 + \frac{949469191}{15925248}\,x^{10} - \frac{39313719143}{597196800}\,x^{11} - \frac{371668244803807}{1146617856000}\,x^{12}$$

$$- \frac{31302358410107}{2548039680000}\,x^{13} + \frac{9400924284794617963}{6421059993600000}\,x^{14} \,, \tag{I.2}$$

$$\omega_{\Gamma_5}(x) = 2 - x - x^2 + \frac{1}{8}\,x^4 - \frac{1}{16}\,x^5 - \frac{53}{192}\,x^6 - \frac{13}{768}\,x^7 + \frac{377}{6912}\,x^8 - \frac{2341}{13824}\,x^9$$

$$- \frac{2366921}{5308416}\,x^{10} - \frac{415612943}{2388787200}\,x^{11} - \frac{33486987683}{127401984000}\,x^{12}$$

$$- \frac{4533115819027}{5733089280000}\,x^{13} - \frac{92584505133810481}{57789539942400000}\,x^{14} \,. \tag{I.3}$$

I.1.2. $S = 0$, $\mathbf{K} = (0, \pi)$

$$
\omega_{\Gamma_3/\Gamma_4}(x) = 2 - x - 2\,x^2 + \frac{9}{8}\,x^4 - \frac{5}{16}\,x^5 - \frac{449}{192}\,x^6 + \frac{1645}{2304}\,x^7 + \frac{70427}{13824}\,x^8
$$
$$
- \frac{452555}{165888}\,x^9 - \frac{364407181}{26542080}\,x^{10} + \frac{20932260889}{2388787200}\,x^{11}
$$
$$
+ \frac{43212785310413}{1146617856000}\,x^{12} - \frac{1082384121586093}{34398535680000}\,x^{13}
$$
$$
- \frac{6423538821754896467}{57789539942400000}\,x^{14} \ . \tag{I.4}
$$

I.1.3. $S = 1$, $\mathbf{K} = (0, 0)$

$$
\omega_{\Gamma_3}(x) = 2 - \frac{1}{2}\,x - \frac{5}{4}\,x^2 - \frac{1}{4}\,x^3 - \frac{5}{8}\,x^4 - \frac{57}{64}\,x^5 - \frac{337}{384}\,x^6 - \frac{1087}{1152}\,x^7 - \frac{49745}{27648}\,x^8
$$
$$
- \frac{1230671}{663552}\,x^9 - \frac{84134083}{31850496}\,x^{10} - \frac{71961335353}{19110297600}\,x^{11} - \frac{6931489716539}{1146617856000}\,x^{12}
$$
$$
- \frac{41618542755193}{5503765708800}\,x^{13} - \frac{134624403747285691}{9631589990400000}\,x^{14} \ , \tag{I.5}
$$
$$
\omega_{\Gamma_4}(x) = 2 - \frac{1}{2}\,x - \frac{5}{4}\,x^2 - \frac{1}{4}\,x^3 - \frac{3}{8}\,x^4 - \frac{5}{64}\,x^5 - \frac{15}{128}\,x^6 - \frac{1}{384}\,x^7 - \frac{8677}{27648}\,x^8
$$
$$
- \frac{248747}{663552}\,x^9 - \frac{61964869}{53084160}\,x^{10} - \frac{28161170261}{19110297600}\,x^{11} - \frac{1286215153651}{382205952000}\,x^{12}
$$
$$
- \frac{722520360562511}{137594142720000}\,x^{13} - \frac{694140469564491133}{57789539942400000}\,x^{14} \ , \tag{I.6}
$$
$$
\omega_{\Gamma_5}(x) = 2 - \frac{1}{2}\,x - \frac{3}{4}\,x^2 - \frac{1}{2}\,x^3 - \frac{25}{8}\,x^4 - \frac{441}{64}\,x^5 - \frac{3023}{192}\,x^6 - \frac{121721}{4608}\,x^7
$$
$$
- \frac{34775}{6144}\,x^8 + \frac{11768317}{55296}\,x^9 + \frac{38294096717}{31850496}\,x^{10} + \frac{83630268980713}{19110297600}\,x^{11}
$$
$$
+ \frac{650630140801309}{57330892800}\,x^{12} + \frac{348272518978158487}{22932357120000}\,x^{13}
$$
$$
- \frac{4990505545003648955371}{115579079884800000}\,x^{14} \ . \tag{I.7}
$$

I.1.4. $S = 1$, $\mathbf{K} = (0, \pi)$

$$\omega_{\Gamma_3/\Gamma_4}(x) = 2 - \frac{1}{2}x - \frac{5}{4}x^2 - \frac{3}{4}x^3 - \frac{15}{8}x^4 - \frac{189}{64}x^5 - \frac{71}{24}x^6 + \frac{16555}{4608}x^7$$
$$+ \frac{521443}{18432}x^8 + \frac{57239671}{663552}x^9 + \frac{23845114583}{159252480}x^{10} + \frac{62475412451}{3822059520}x^{11}$$
$$- \frac{1111196843333209}{1146617856000}x^{12} - \frac{61012927483426099}{15288238080000}x^{13}$$
$$- \frac{18791746943890357267}{2063912140800000}x^{14} \ . \tag{I.8}$$

I.2. Dispersions, $\mathbf{K} = (K_1, K_2)$

We identify four different dispersions for the linearly bound states. They are analysed up to 5th order in x. We define the shorthands

$$u := \cos(K_1)\cos(K_2) \ ,$$
$$v := \cos(K_1) + \cos(K_2) \ ,$$
$$s := \sqrt{1 + (\cos(K_1) - \cos(K_2))^2} \ .$$

I.2.1. $S = 0$

$$\omega_{1/2}(x; \mathbf{K}) = 2 - x - 2\,x^2 - \frac{1}{2}\,x^3\,(1 + u) + \frac{1}{8}\,x^4\,(7 - v^2 + 2\,u^2 \mp vs)$$

$$+ \frac{1}{16}\,x^5 \Bigg(10 - 2\,v^2 + 23\,u + 2\,u\,(v^2 + 2\,u)$$

$$- 4\,u^3 \pm \frac{v\,(-6 - 2\,v^2 + 9\,u + 2\,u\,(v^2 - 4\,u))}{s} \Bigg) , \qquad (\text{I.9})$$

$$\omega_3(x; \mathbf{K}) = 2 - x - x^2 + \frac{1}{2}\,x^3\,(u - 1) + \frac{1}{8}\,x^4\,(-5 + 6\,u - 2\,u^2 + 2\,(\cos(K_1))^2)$$

$$+ x^5 \left(-\frac{3}{8} + \frac{1}{16}\,u + \frac{1}{4}\,(\cos(K_2))^2\,(3 - u) - \frac{1}{2}\,u^2 + \frac{1}{4}\,u^3 \right) , \quad (\text{I.10})$$

$$\omega_4(x; \mathbf{K}) = 2 - x - x^2 + \frac{1}{2}\,x^3\,(u - 1) + \frac{1}{8}\,x^4\,(-5 + 6\,u - 2\,u^2 + 2\,(\cos(K_2))^2)$$

$$+ x^5 \left(-\frac{3}{8} + \frac{1}{16}\,u + \frac{1}{4}\,(\cos(K_2))^2\,(3 - u) - \frac{1}{2}\,u^2 + \frac{1}{4}\,u^3 \right) . \quad (\text{I.11})$$

I.2.2. $S = 1$

$$\omega_{1/2}(x; \mathbf{K}) = 2 - \frac{1}{2}\,x - \frac{5}{4}\,x^2 + \frac{1}{4}\,x^3\,(u - 2) + \frac{1}{16}\,x^4\,(-v^2 + 13\,u + 2\,u^2 - 19 \mp vs)$$

$$- \frac{1}{64}\,x^5 \Bigg(118 - 119\,u + 20\,v^2 + 4\,u\,(v^2 - 14\,u) - 8\,u^3$$

$$\pm \frac{v\,(11 + 20\,v^2 - 2\,u\,(39 - 2\,v^2 + 8\,u))}{s} \Bigg) , \qquad (\text{I.12})$$

$$\omega_3(x; \mathbf{K}) = 2 - \frac{1}{2}\,x - \frac{3}{4}\,x^2 - \frac{1}{4}\,x^3\,(1 + u) + \frac{1}{16}\,x^4\,(-35 + 2\,(\cos(K_1))^2 - 15\,u - 2\,u^2)$$

$$+ x^5 \left(-\frac{175}{64}\,u - \frac{137}{32} + \frac{1}{8}\,(\cos(K_1))^2\,(7 + u) - \frac{3}{4}\,u^2 - \frac{1}{8}\,u^3 \right) ,$$
$$(\text{I.13})$$

$$\omega_4(x; \mathbf{K}) = 2 - \frac{1}{2}\,x - \frac{3}{4}\,x^2 - \frac{1}{4}\,x^3\,(1 + u) + \frac{1}{16}\,x^4\,(-35 + 2\,(\cos(K_2))^2 - 15\,u - 2\,u^2)$$

$$+ x^5 \left(-\frac{175}{64}\,u - \frac{137}{32} + \frac{1}{8}\,(\cos(K_1))^2\,(7 + u) - \frac{3}{4}\,u^2 - \frac{1}{8}\,u^3 \right) .$$
$$(\text{I.14})$$

I.3. Comparison to Other Results

Fukumoto calculated two-triplon hopping amplitudes up to 5th order in x, which are listed in Tab. I in Ref. [101]. He considered the four different amplitudes (see Eqs. (6.5) and (6.26) for notation)

$$1n \equiv t^h_{(1,0);(0,0),(1,0)} - t^h_{(0,0)} \ ,$$

$$2n \equiv t^h_{(1,-1);(0,0),(1,-1)} - t^h_{(0,0)} \ ,$$

$$3n \equiv t^h_{(0,2);(0,0),(0,2)} - t^h_{(0,0)} \ ,$$

$$4n \equiv t^v_{(2,1);(0,0),(2,1)} - t^v_{(0,0)} \ .$$

We compare his results to ours in Tab. I.1 for total spin $S = 0$, 1 and 2. Deviations are found for all 5th order terms in the amplitudes 1n and 2n. Otherwise there are no deviations.

	S	Fukumoto's results	our results
1n	0	$-x + \frac{1}{2}x^2 + x^3 + \frac{9}{8}x^4 - \frac{1}{16}x^5$	$-x + \frac{1}{2}x^2 + x^3 + \frac{9}{8}x^4 - \frac{3}{16}x^5$
	1	$-\frac{1}{2}x + x^2 + \frac{7}{8}x^3 - \frac{9}{16}x^4 - x^5$	$-\frac{1}{2}x + x^2 + \frac{7}{8}x^3 - \frac{9}{16}x^4 - \frac{65}{64}x^5$
	2	$\frac{1}{2}x + \frac{1}{2}x^2 - \frac{1}{8}x^3 - \frac{9}{16}x^4 - \frac{1}{16}x^5$	$\frac{1}{2}x + \frac{1}{2}x^2 - \frac{1}{8}x^3 - \frac{9}{16}x^4 - \frac{3}{64}x^5$
2n	0	$-\frac{1}{2}x^3 + \frac{45}{32}x^5$	$-\frac{1}{2}x^3 + \frac{49}{32}x^5$
	1	$-\frac{1}{4}x^3 - \frac{3}{8}x^4 - \frac{3}{16}x^5$	$-\frac{1}{4}x^3 - \frac{3}{8}x^4 - \frac{11}{64}x^5$
	2	$\frac{1}{4}x^3 + \frac{3}{8}x^4 + \frac{3}{8}x^5$	$\frac{1}{4}x^3 + \frac{3}{8}x^4 + \frac{23}{64}x^5$
3n	0	$-x^2 - \frac{3}{2}x^3 + \frac{7}{4}x^4 + \frac{289}{32}x^5$	$-x^2 - \frac{3}{2}x^3 + \frac{7}{4}x^4 + \frac{289}{32}x^5$
	1	$-\frac{1}{2}x^2 - \frac{3}{4}x^3 + \frac{1}{8}x^4 + \frac{129}{64}x^5$	$-\frac{1}{2}x^2 - \frac{3}{4}x^3 + \frac{1}{8}x^4 + \frac{129}{64}x^5$
	2	$\frac{1}{2}x^2 + \frac{3}{4}x^3 - \frac{1}{8}x^4 - \frac{49}{64}x^5$	$\frac{1}{2}x^2 + \frac{3}{4}x^3 - \frac{1}{8}x^4 - \frac{49}{64}x^5$
4n	0	$-\frac{1}{4}x^4 - \frac{17}{32}x^5$	$-\frac{1}{4}x^4 - \frac{17}{32}x^5$
	1	$-\frac{1}{8}x^4 - \frac{17}{64}x^5$	$-\frac{1}{8}x^4 - \frac{17}{64}x^5$
	2	$\frac{1}{8}x^4 + \frac{17}{64}x^5$	$\frac{1}{8}x^4 + \frac{17}{64}x^5$

Table I.1.: Comparison of Fukumoto's results for some particular two-triplon hopping amplitudes [101] to our results. Deviations are marked magenta (grey).

Bibliography

[1] L. D. Landau and E. M. Lifshitz, *Statistical Physics Part 2* (Pergamon Press, Oxford, 1980)

[2] A. A. Abrikosov, L. P. Gor'kov and I. Y. Dzyaloshinskii, *Quantum Field Theoretical Methods in Statistical Physics* (Pergamon Press, Oxford, 1965)

[3] W. Marshall, Proc. Roy. Soc. Lond. **A232**, 48 (1955)

[4] D. C. Mattis, *The Theory of Magnetism I* (Springer-Verlag, Berlin, 1988)

[5] J. Bardeen, L. N. Cooper and J. R. Schrieffer, Phys. Rev. **108**, 1175 (1957)

[6] L. D. Faddeev and L. A. Takhtajan, Phys. Lett. **85A**, 375 (1981)

[7] Chapter 6, of *The Many-Body Problem*, edited by D. C. Mattis (World Scientific, Singapore, 1993)

[8] A. Auerbach, *Interacting Electrons and Quantum Magnetism* (Springer, New York, 1994)

[9] M. E. Fisher, Rev. Mod. Phys. **46**, 597 (1974)

[10] B. S. Shastry and B. Sutherland, Physica **108B**, 1069 (1981)

[11] A. Messiah, *Quantum Mechanics* (North-Holland, Amsterdam, 1961), Vol. 2

[12] H. L. Davis, Phys. Rev. **129**, 789 (1960)

[13] M. H. Boon, Nouvo Cim. **21**, 885 (1961)

[14] T. Arai and B. Goodman, Phys. Rev. **155**, 514 (1967)

[15] M. Parrinello, M. Scirè and T. Arai, Lett. Nouvo Cim. **6**, 138 (1973)

[16] M. Parrinello and T. Arai, Phys. Rev. B **10**, 265 (1974)

[17] C. J. Hamer, J. B. Kogut and L. Susskind, Phys. Rev. D **19**, 3091 (1979)

[18] C. J. Hamer and A. C. Irving, Nucl. Phys. B **230**, 336 (1984)

[19] L. P. Kadanoff and M. Kohmoto, J. Phys. A **14**, 1291 (1981)

[20] L. G. Marland, J. Phys. A **14**, 2047 (1981)

[21] M. P. Gelfand and R. R. P. Singh, Adv. Phys. **49**, 93 (2000)

[22] W. Zheng, J. Oitmaa and C. J. Hamer, Phys. Rev. B **43**, 8321 (1991)

[23] M. P. Gelfand, Solid State Commun. **98**, 11 (1996)

[24] R. R. P. Singh, Phys. Rev. B **53**, 11582 (1996)

[25] C. Knetter, A. Bühler, E. Müller-Hartmann and G. S. Uhrig, Phys. Rev. Lett. **85**, 3958 (2000)

[26] C. Knetter, K. P. Schmidt, M. Grüninger and G. S. Uhrig, Phys. Rev. Lett. **87**, 167204 (2001)

[27] S. Trebst *et al.*, Phys. Rev. Lett. **85**, 4373 (2000)

[28] W. Zheng *et al.*, Phys. Rev. B **63**, 144410 (2001)

[29] K. P. Schmidt, C. Knetter and G. Uhrig, Europhys. Lett. **56**, 877 (2001)

[30] M. Windt *et al.*, Phys. Rev. Lett. **87**, 127002 (2001)

[31] M. Grüninger *et al.*, J. Phys. Chem. Solids **63**, 2167 (2002)

[32] W. Zheng, C. Hamer and R. Singh, cond-mat/0211346, accepted by Phys. Rev. Lett. (2003)

[33] F. J. Wegner, Ann. Physik **3**, 77 (1994)

[34] S. D. Głazeck and K. G. Wilson, Phys. Rev. D **48**, 5863 (1993)

[35] S. D. Głazeck and K. G. Wilson, Phys. Rev. D **49**, 4214 (1994)

[36] J. Stoer and R. Bulirsch, *Einführung in die Numerische Mathematik II* (Springer-Verlag, Berlin, 1973)

[37] W. Magnus, Commun. Pure Appl. Math. **7**, 649 (1954)

[38] S. Klarsfeld and J. A. Otep, Phys. Rev. A **39**, 3270 (1989)

[39] S. Blanes, F. Casas, J. A. Oteo and J. Ros, J. Phys. A: Math. Gen. **31**, 259 (1998)

[40] H. Fröhlich, Phys. Roy. Soc. Lond. **A215**, 291 (1952)

[41] P. Lenz and F. Wegner, Nucl. Phys. B **482**, 693 (1996)

[42] A. Mielke, Eur. Phys. J. B **5**, 605 (1998)

[43] I. Grote, E. Körding and F. Wegner, J. Low Temp. Phys. **126**, 1385 (2002)

[44] K. G. Wilson, Rev. Mod. Phys. **47**, 773 (1975)

[45] C. Heidbrink and G. Uhrig, Eur. Phys. J. B **30**, 443 (2002)

[46] S. K. Kehrein, A. Mielke and P. Neu, Z. Phys. B **99**, 269 (1996)

[47] A. Kabel and F. Wegner, Z. Phys. – Cond. Mat. **103**, 555 (1997)

[48] S. Kehrein, Phys. Rev. Lett. **83**, 4914 (1999)

[49] S. Kehrein, Nucl. Phys. B **592**, 512 (2001)

[50] C. Heidbrink and G. Uhrig, Phys. Rev. Lett. **88**, 146401 (2002)

[51] M. P. Gelfand, R. R. P. Singh and D. A. Huse, J. Stat. Phys. **59**, 1093 (1990)

[52] G. S. Uhrig and B. Normand, Phys. Rev. B **58**, R14705 (1998)

[53] W. Zheng *et al.*, Phys. Rev. B **63**, 144411 (2001)

[54] R. R. P. Singh and W. Zheng, Phys. Rev. B **59**, 9911 (1999)

[55] K. P. Schmidt and G. Uhrig, cond-mat/0211627, submitted to Phys. Rev. Lett. (Nov. 2002)

[56] C. Knetter, K. Schmidt and G. S. Uhrig, Physica B **312**, 527 (2002)

[57] C. Knetter and G. S. Uhrig, Eur. Phys. J. B **13**, 209 (2000)

[58] C. Knetter, *Störungstheorie mit Hilfe von Flußgleichungen angewendet auf dimerisierte Spinmodelle* (Diploma thesis, University of Cologne, 1999) available at `www.thp.Uni-Koeln.de/˜ck` or `/˜gu`

[59] C. Knetter and G. S. Uhrig, Phys. Rev. B **63**, 94401 (2001)

[60] J. Stein, J. Stat. Phys. **88**, 487 (1997)

[61] A. H. W. Brenig, Phys. Rev. B **65**, 140407 (2002)

[62] `www.thp.Uni-Koeln.de/˜ck` or `www.thp.Uni-Koeln.de/˜gu`

[63] R. Zwanzig, in *Lectures in Theoretical Physics*, edited by W. E. Brittin, B. W. Downs and J.Downs (Interscience, New York, 1961), Vol. 3

[64] H. Mori, Prog. Theor. Phys. **34**, 399 (1965)

[65] E. R. Gagliano and C. A. Balseiro, Phys. Rev. Lett. **26**, 2999 (1987)

[66] D. G. Pettifor and D. L. Weaire, *The Recursion Method and its Applications*, Vol. 58 of *Springer Series in Solid State Sciences*, edited by M. Cardona, P. Fulde and H.-J. Queisser (Springer-Verlag, Berlin, 1985)

[67] V. S. Viswanath and G. Müller, *The Recursion Method; Application to Many-Body Dynamics*, Vol. m23 of *Lecture Notes in Physics* (Springer-Verlag, Berlin, 1994)

[68] K. P. Schmidt, C. Knetter, M. Grüninger and G. Uhrig, Phys. Rev. Lett. **90**, 167201 (2003)

[69] *Phase Transitions and Critical Phenomena*, edited by C. Domb and J. L. Lebowitz (Academic Press, London, 1983), Vol. 13

[70] P. M. Stevenson, Phys. Rev. D **23**, 2916 (1981)

[71] C. Bender and T. Wu, Phys. Rev. **184**, 1231 (1969)

[72] C. K. Majumdar and D. K. Ghosh, J. Math. Phys. **10**, 1388 (1969)

[73] P. M. van den Broek, Phys. Lett. **77A**, 261 (1980)

[74] B. S. Shastry and B. Sutherland, Phys. Rev. Lett. **47**, 964 (1981)

[75] K. Ueda and S. Miyahara, J. Phys. Soc. Jpn. **69**, Suppl. A, 326 (2000)

[76] R. W. Smith and D. A. Keszler, J. Solid State Chem. **93**, 430 (1991)

[77] S. Miyahara and K. Ueda, Phys. Rev. Lett. **82**, 3701 (1999)

[78] S. Miyahara and K. Ueda, J. Phys. Soc. Jpn. **69**, Suppl. B, 72 (2000)

[79] U. Löw and E. Müller-Hartmann, J. Low Temp. Phys. **127**, 290 (2002)

[80] M. Albrecht and F. Mila, Europhys. Lett. **34**, 145 (1996)

[81] C. Chung, J. Marston and S. Sachdev, Phys. Rev. B **64**, 134407 (2001)

[82] D. Carpentier and L. Balents, Phys. Rev. B **65**, 024427 (2002)

[83] A. Läuchli, S. Wessel and M. Sigrist, Phys. Rev. B **66**, 014401 (2002)

[84] T. Munehisa and Y. Munehisa, J. Phys. Soc. Jpn. **72**, 160 (2003)

[85] A. Koga and N. Kawakami, Phys. Rev. Lett. **84**, 4461 (2000)

[86] W. Zheng, C. Hamer and J. Oitmaa, Phys. Rev. B **60**, 6608 (1999)

[87] W. Zheng, J. Oitmaa and C. Hamer, Phys. Rev. B **65**, 014408 (2002)

[88] H. Kageyama *et al.*, Phys. Rev. Lett. **82**, 3168 (1999)

[89] H. Kageyama *et al.*, Phys. Rev. Lett. **84**, 5876 (2000)

[90] H. Nojiri *et al.*, J. Phys. Soc. Jpn. **68**, 2906 (1999)

[91] T. Rõõm *et al.*, Phys. Rev. B **61**, 14342 (2000)

[92] K. Kodama *et al.*, J. Phys.: Condens. Matter **14**, L319 (2002)

[93] P. Lemmens *et al.*, Phys. Rev. Lett **85**, 2605 (2000)

[94] E. Müller-Hartmann *et al.*, Phys. Rev. Lett. **84**, 1808 (2000)

[95] K. Kodama *et al.*, Science **298**, 395 (2002)

[96] K. Totsuka, S.Miyahara and K. Ueda, Phys. Rev. Lett. **86**, 520 (2001)

[97] S. Miyahara and K. Ueda, Phys. Rev. B **61**, 3417 (2000)

[98] W. Zheng, C. Hamer and J. Oitmaa, cond-mat/9811030; the coefficients for the one-triplon dispersion calculated perturbatively from the limit of isolated dimers can only be found in the cond-mat version. The article has been published in Phys. Rev. B **60**, 6608 (1999) without the coefficients.

[99] C. Knetter, E. Müller-Hartmann and G. S. Uhrig, J. Phys.: Condens. Matter **12**, 9069 (2000)

[100] T. Momoi and K. Totsuka, Phys. Rev. B **61**, 3231 (2000)

[101] Y. Fukumoto, J. Phys. Soc. Jpn. **69**, 2755 (2000)

[102] On large systems even the Néel state can be approximated by $S = 0$ states, cf. S. Liang, B. Douçot and P. W. Anderson, Phys. Rev. Lett. **61**, 365 (1988)

[103] K. Totsuka and H.-J. Mikeska, Phys. Rev. B **66**, 054435 (2002)

[104] P. A. Fleury and R. Loudon, Phys. Rev. **166**, 514 (1968)

[105] B. S. Shastry and B. I. Shraiman, Phys. Rev. Lett. **65**, 1068 (1990)

[106] E. Müller-Hartmann and A. Reischl, Eur. Phys. J. B **28**, 173 (2002)

[107] S. Lovesey, in *Dynamics of Solids and Liquids by Neutron Scattering*, Vol. 3 of *Topics in Current Physics*, edited by S. Lovesey and T. Springer (Springer-Verlag, Berlin, 1977)

[108] N. Aso, private communication (2001); unpublished data

[109] T. Momoi and K. Totsuka, Phys. Rev. B **61**, 3231 (2000)

Kurze Zusammenfassung

In der vorliegenden Arbeit beschreiben wir einen neuartigen störungstheoretischen Zugang zu niedrigdimensionalen Vielteilchensystemen, der auf kontinuierlichen unitären Transformationen aufbaut. Im Speziellen betrachten wir auf Gittern definierte Ausgangssysteme, die eine perturbative Darstellung erlauben. Diese muss so geartet sein, dass der ungestörte Anteil des Ausgangshamiltonians ein äquidistantes Spektrum hat. Der Abstand zwischen zwei benachbarten Niveaus wird als Quasiteilchen bezeichnet. In diesem Fall führt die perturbativ, bis zu einer bestimmten Maximalordung ausgeführte Transformation auf ein effektives System, dessen Hamiltonoperator die Quasiteilchenzahl erhält.

Dieselbe Transformation kann verwendet werden, um auch andere Observablen auf ihre effektiven Gegenstücke abzubilden. Am Ende liegen alle effektiven Operatoren als Reihenentwicklungen im Störparameter vor. Die einzelnen Glieder dieser Entwicklungen sind Produkte von Leiteroperatoren, die auf die ursprünglichen Quasiteilchen wirken. In diesem Sinne kann die Wirkung der effektiven Operatoren auf Zustände berechnet werden, welche eineindeutig durch die Anzahl der Quasiteilchen und deren Position im Gitter beschrieben sind; die Berechnungen können also im Ortsraum durchgeführt werden.

Die den effektiven Operatoren zugrundeliegende mathematische Struktur wird ausführlich dargelegt. Ferner werden alle benötigen Details einer computergestützten Implementierung der Methode erläutert, welche störungstheoretische Berechnungen zu hohen Ordnungen ermöglicht.

Neben der Möglichkeit, quantitative Berechnungen für Mehrteilchenenergien durchzuführen, ist die durch die perturbative Transformation ermöglichte quantitative Berechnung von spektralen Dichten für verschiedene experimentell relevante Observablen von entscheidender konzeptioneller Bedeutung.

Die Arbeit umfaßt eine ausführlich beschriebene Anwendung der Methode auf das zweidimensionale Shastry-Sutherland Modell, ein stark frustriertes Quantenspinsystem ($S = 1/2$), das durch die Substanz $SrCu_2(BO_3)_2$ eine experimentelle Realisierung erfahren hat. Der Ausgangspunkt unserer störungstheoretischen Analyse ist der Limes starker Dimerisierung, für den der Grundzustand durch Singuletts auf den Dimeren gegeben ist. Die elementaren Anregungen, oder Quasiteilchen, werden durch einzelne, zu Tripletts aufgebrochene Singuletts dargestellt. Wir erläutern quantitative Berechnungen der Ein- und Zwei-Triplett Energien, sowie der spektralen Dichten des Raman- und Neutronen-Streu-Operators. Die Ergebnisse für die spektralen Dichten im Besonderen stellen neuartige Befund dar. Der Vergleich dieser Größen mit experimentellen Daten führt zu interessanten Einsichten über die spektralen Eigenschaften niedrigdimensionaler Quantenspinsysteme.

Abstract

In this thesis we describe a novel perturbative approach to low-dimensional quantum many-particle systems, which is based on continuous unitary transformations. We consider systems, which are defined on a lattice and allow a perturbative decomposition. The unperturbed part must have an equidistant spectrum – the difference between two successive levels is called a quasi-particle. In this case the perturbative transformation leads to an effective Hamiltonian, which conserves the number of particles. The same transformation is used to also derive the effective counterparts of other, experimentally relevant observables.

The effective operators are obtained as series expansions in the (small) perturbation parameter. In each order we find a set of products of ladder-operators, which act on states uniquely defined by the number of quasi-particles and their position in the lattice. Thus all calculations can be done in real space.

The mathematical structure of the effective operators is extensively analysed. We additionally give all details necessary to implement the method on a computer, which allows the calculation of the effective quantities up to high orders.

The method facilitates quantitative calculations of multi-particle excitations and spectral densities of experimentally relevant observables.

We include a comprehensive application of the method to the two-dimensional Shastry-Sutherland model, a strongly frustrated quantum spin system. The model has experience an experimental realization by $SrCu_2(BO_3)_2$. The limit of strong dimerization serves as starting point. Here the ground state is given by singlets on all dimers – a single triplet constitutes an elementary excitation, i.e. quasi-particle. We quantitatively calculate the one- and two-triplet energies as well as the spectral densities of the Raman and neutron scattering operators. The findings for the spectral densities in particular represent new results. Comparing them to experimental data leads to interesting insights into the spectral properties of low-dimensional quantum spin systems.

Danksagungen

Erklärung

Ich versichere, daß ich die von mir vorgelegte Dissertation selbständig angefertigt, die benutzten Quellen und Hilfsmittel vollständig angegeben und die Stellen der Arbeit - einschließlich Tabellen, Karten und Abbildungen -, die anderen Werken im Wortlaut oder dem Sinn nach entnommen sind, in jedem Einzelfall als Entlehnung kenntlich gemacht habe; daß diese Dissertation noch keiner anderen Fakultät oder Universität zur Prüfung vorgelegen hat; daß sie - abgesehen von unten angegebenen Teilpublikationen - noch nicht veröffentlicht worden ist sowie, daß ich eine solche Veröffentlichung vor Abschluß des Promotionsverfahrens nicht vornehmen werde. Die Bestimmungen dieser Promotionsordnung sind mir bekannt. Die von mir vorgelegte Dissertation ist von Herrn Privat-Dozent Dr. Götz S. Uhrig betreut worden.

Köln, den 17. April 2003

Teilpublikationen

- C. Knetter und G.S. Uhrig, *Perturbation theory by flow equations: dimerized and frustrated S=1/2 chain*, Eur. Phys. J. B **13**, 209 (2000)

- C. Knetter, E. Müller-Hartmann und G.S. Uhrig, *Symmetries and triplet dispersion in a modified Shastry-Sutherland model for $SrCu_2(BO_3)_2$*, J. Phys.: Condens. Matter **12**, 9069 (2000)

- E. Müller-Hartmann, R.R.P. Singh, C. Knetter und G.S. Uhrig, *Exact demonstration of magnetization plateaus and first-order dimer-Neél phase transitions in a modified Shastry-Sutherland model for $SrCu_2(BO_3)_2$*, Phys. Rev. Lett. **84**, 1808 (2000)

- C. Knetter, A. Bühler, E. Müller-Hartmann und G.S. Uhrig, *Dispersion and symmetry of bound states in the Shastry-Sutherland model*, Phys. Rev. Lett. **85**, 3958 (2000)

- C. Knetter und G.S. Uhrig, *Triplet dispersion in CuGeO₃: Perturbative analysis*, Phys. Rev. B **63**, 94401 (2001)

- K.P. Schmidt, C. Knetter und G.S. Uhrig, *Raman response in antiferromagnetic two-leg S=1/2 Heisenberg ladders*, Europhys. Lett. **56**, pp 877 (2001)

- C. Knetter, K.P. Schmidt, M. Grüninger und G.S. Uhrig, *Fractional and integer excitations in quantum antiferromagnetic spin 1/2 ladders*, Phys. Rev. Lett. **87**, 167204 (2001)

- M. Windt, M. Grüninger, T. Nunner, C. Knetter, K.P. Schmidt und G.S. Uhrig *et al.*, *Observation of two-magnon bound states in the two-leg ladders of $(Ca, La)_{14}Cu_{24}O_{41}$*, Phys. Rev. Lett. **87**, 127002 (2001)

- C. Knetter, A. Bühler, R. Singh, E. Müller-Hartmann und G.S. Uhrig, *$SrCu_2(BO_3)_2$ - a two-dimensional spin liquid*, Can. J. Phys. **79**, 1565 (2001)

- C. Knetter, K.P. Schmidt und G.S. Uhrig, *Multi-particle excitations and spectral densities in quantum spin-systems*, Physica B **312**, 527 (2002)

- M. Grüninger, M. Windt, T. Nunner, C. Knetter, K.P. Schmidt, G.S. Uhrig, T. Kopp, A. Freimuth, U. Ammerahl, B. Büchner und A. Revcolevschi, *Optical spectroscopy of $(La, Ca)_{14}Cu_{24}O_{41}$ spin ladders: comparison of experiment and theory*, Physica B **312**, 617 (2002)

- M. Grüninger, M. Windt, T. Nunner, C. Knetter, K.P. Schmidt, G.S. Uhrig, T. Kopp, A. Freimuth, U. Ammerahl, B. Büchner und A. Revcolevschi, *Magnetic excitations in two-leg spin 1/2 ladders: experiment and theory*, J. Phys. Chem. Solids **63**, 2167 (2002)

- K.P. Schmidt, C. Knetter und G.S. Uhrig, *Novel Extrapolation for Strong Coupling Expansions*, Acta Physica Polonica B **34**, 1481 (2003)

- K.P. Schmidt, C. Knetter, M. Grüninger und G.S. Uhrig, *Charge order induced sharp Raman peak in $Sr_{14}Cu_{24}O_{41}$*, Phys. Rev. Lett. **90**, 167201 (2003)

Lebenslauf

Persönliche Daten

Name:	Christian Knetter
Geburtsdatum:	1. Februar 1972
Geburtsort:	Troisdorf
Familienstand:	ledig
Staatsangehörigkeit:	deutsch

Schulbildung

1978-1982	Grundschule Neuenrade
1982–1991	Albert-Schweitzer-Gymnasium Plettenberg
Juni 1991	Abitur

Hochschulstudium

Okt. 1993	Immatrikulation an der Universität zu Köln, Studiengang: Physik, Diplom
Juni 1996	Vordiplom
Juni 1999	Abschluss der Diplomarbeit bei Prof. Dr. E. Müller-Hartmann
seit Juli 1999	Anfertigung der vorliegenden Dissertation unter Anleitung von Priv. Doz. Dr. G. S. Uhrig

Arbeitsverhältnisse

1998–1999	Studentische Hilfskraft am Institut für Theoretische Physik der Universität zu Köln
Seit 1999	Wissenschaftlicher Mitarbeiter am Institut für Theoretische Physik der Universität zu Köln